



University of Tehran

Print ISSN: 2322-2093

Online ISSN: 2423-6691

Volume 55, Number 1, June 2022

Civil Engineering Infrastructures Journal

CEIJ

Available online at
<http://ceij.ut.ac.ir/>

Civil Engineering Infrastructures Journal (CEIJ)

Semiannual Publication

Editor – in - Charge

Soltani, N., Professor
nsoltani@ut.ac.ir

Editor – in – Chief

Tabesh, M., Professor
mtabesh@ut.ac.ir

Executive Manager and Contact Person

Akhtari, N.
cej@ut.ac.ir

Published by:

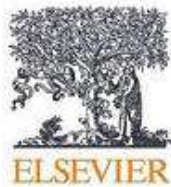


University of Tehran
College of Engineering

Indexed by:



Web of Science (ESCI)



Scopus

Civil Engineering Infrastructures
Journal (CEIJ)
College of Engineering
University of Tehran
P.O. Box: 11155-4563
Tehran, Iran.
Tel/ Fax: +98-21-88956097
Email: ceij@ut.ac.ir
Web Site: www.ceij.ir

Editorial Board

Askari, F., Associate Professor, International Institute of Earthquake Engineering and Seismology, Iran.

Aslani, F., Associate Professor, University of Western Australia, Australia.

Babazadeh, A., Associate Professor, University of Tehran, Iran.

Behnamfar, F., Associate Professor, Isfahan University of Technology, Iran.

EskandariGhadi, M., Professor, University of Tehran, Iran.

Fatahi, B., Associate Professor, University of Technology Sydney, Australia.

Gupta, R., Professor, Visvesvaraya National Institute of Technology, India.

Heravi, Gh.R., Professor, University of Tehran, Iran.

Kerachian, R., Professor, University of Tehran, Iran.

Mahmoudzadeh Kani, I., Professor, University of Tehran, Iran.

Mazza, F., Professor, University of Calabria, Italy.

Moghadas Nejad, F., Professor, Amirkabir University of Technology, Iran.

Moridpour, S., Associate Professor, RMIT University, Australia.

Motamed, R., Associate Professor, University of Nevada, USA.

Salehi Neyshabouri, A.A., Professor, Tarbiat Modarres University, Iran.

Nourani, V., Professor, University of Tabriz, Iran.

Ouhadi, V.R., Professor, Bu-Ali Sina University, Iran.

Shafei, B., Associate Professor, Iowa State University, USA.

Naderpajouh, N., Associate Professor, University of Sydney, Australia.

Shekarchizadeh, M., Professor, University of Tehran, Iran.

Shafieezadeh, A., Associate Professor, Ohio State University, USA.

Tanyimboh, T., Associate Professor, University of the Witwatersrand, South Africa.

Touran, A., Professor, Northeastern University, USA.

Towhata, I., Professor, University of Tokyo, Japan.

Zahraei, S.M., Professor, University of Tehran, Iran.

Advisory Board

Ahmadi, M.T., Professor, Tarbiat Modarres University, Iran.

Behnia, K., Associate Professor, University of Tehran, Iran.

Benekohal, R.F., Professor, University of Illinois, USA.

Gatmiri, B., Professor, University of Tehran, Iran.

Mobasher, B., Professor, Arizona State University, USA.

Motavali, M., Professor, Structural Engineering Research Laboratory, EMPA, Switzerland.

Rahimian, M., Professor, University of Tehran, Iran.

Saiidi, M., Professor, University of Nevada, Reno, USA.

Sorooshian, S., Professor, University of California, USA.

CONTENTS

Volume 55, Number 1, June 2022

Research Papers

- Predicting Compression Strength of Reinforced Concrete Columns 1**
Confined by FRP Using Meta-Heuristic Methods
Mohammadzadeh, M.R. and Esfandnia, F.
- A Laboratory Study on the Potentiodynamic Polarization and Transport 19**
Properties of Binary Concrete with Silica Fume and Zeolite
Sobhani, J., Najimi, M. and Pourkhorshidi, A.R.
- Development of the Fragility Curves for Conventional Reinforced Concrete..... 31**
Moment Resistant Frame Structures in Qods Town, Qom City, Iran
Deghani, E. and Soltanimohajer, M.
- Simulation of Near-Fault Seismic Ground Motions of 03 November, 2002..... 43**
Denali Earthquake Using Modified Semi-Empirical Approach
Rajaram, C. and Pradeep Kumar, R.
- Influences of Polyvinyl Alcohol Fiber Addition on the Specimen Size Effect..... 59**
and Energy Absorption of Self-Consolidating Concrete
Abbasi Nattaj Omrani, I., Ardeshir-Behrestaghi, A. and Saeedian, A.
- Reduction Factors for Laterally Loaded Pile Groups Accounting for Pile..... 75**
Cross Sections and Soil Properties
Talebi, A. and Derakhshani, A.
- Developing a Hybrid ANN-Jaya Procedure for Backcalculation of Flexible..... 89**
Pavements Moduli
Ghanizadeh, A.R., Heidarabadizadeh, N. and Khalifeh, V.
- The Effect of Hydrophobic Amorphous Carbon Powder on the Compressive Strength,..... 109**
Water Absorption and Rheological Attributes of Cement Mortar
Haji Hossein, A.R., Bigdeli, H.R., Mokhtari, F., Jahantab, S. and Habibnejad Korayem, A.
- Collapse Probability Assessment of a 4-Story RC Frame under 121**
Post-Earthquake Fire Scenario
Moradi, M., Tavakoli, H.R. and Abdollahzade, G.H.R.
- Developing Performance Levels for Concrete Bridge Bents with a Focus on..... 139**
the Joint Region
Bahrani, M.K., Nooralizadeh, A., Sharifi, M. and Karami, N.
- Spatial Transferability of a Daily Activity Type and Duration MDCEV Model..... 161**
Nohekhan, A., Samimi, A. and Zahedian, S.
- Damage Detection in Truss Bridges under Moving Load Using Time 183**
History Response and Members Influence Line Curves
Kordi, A. and Mahmoudi, M.



Predicting Compression Strength of Reinforced Concrete Columns Confined by FRP Using Meta-Heuristic Methods

Mohammadizadeh, M.R.^{1*} and Esfandnia, F.²

¹ Associate Professor, Department of Civil Engineering, University of Hormozgan, Bandar Abbas, Iran.

² Ph.D. Candidate, Department of Civil Engineering, University of Hormozgan, Bandar Abbas, Iran.

© University of Tehran 2021

Received: 10 Jun. 2020;

Revised: 16 May 2021;

Accepted: 25 May 2021

ABSTRACT: There are several methods to predict the compression strength of reinforced concrete columns confined by FRP, such as experimental methods, theory of elasticity and plasticity. Meanwhile, due to its good potential and high accuracy in predicting different problems, the soft computing techniques has attracted considerable attentions. Soft computing includes methods and programs to deal with complex computational problems. The objective of this study is to evaluate and compare the performance of four methods of Least Squares Support Vector Machine (LS-SVM), the Weight Least Squares Support Vector Machine (WLS-SVM), Adaptive Neuro-Fuzzy Inference System (ANFIS) and Particle Swarm Optimization - Adaptive Network based Fuzzy Inference System (PSO-ANFIS) for predicting the compression strength of reinforced concrete columns confined by FRP. A total of 95 laboratory data are selected for use in these methods. The Root Mean Square Error (RMSE) and the correlation coefficient of the results are used to validate and compare the performance of the methods. The results of the study show that the PSO-ANFIS method with the RMSE of 4.610 and the coefficient of determination of $R^2 = 0.9677$ predicts compression strength of reinforced concrete columns confined by FRP with high accuracy and therefore, it can be a good alternative to time-consuming and costly laboratory methods.

Keywords: ANFIS, Compression Strength, FRP-Confined Columns, LS-SVM, PSO-ANFIS, WLS-SVM.

1. Introduction

There are a variety of methods, such as using prefabricated concrete systems, making steel veneers, or composite sheets made of fiber-reinforced polymers (FRPs) for strengthening of reinforced concrete columns. FRPs are among the most desirable materials for repair due to their

high weight-to-strength ratio, anti-corrosion properties, ease of installation and reasonable price. These materials increase the service life of the structure. In order to ensure that large deformations subjected to pre-damage load, in order to achieve sufficient strength in reinforced concrete columns, these columns require lateral confinement. Therefore, when transversal

* Corresponding author E-mail: mrz_mohammadizadeh@hormozgan.ac.ir

reinforcement in reinforced concrete columns is not sufficient, FRP is used for confinement of the columns externally (Haji et al., 2018). Many laboratory studies have examined the strengthening techniques using FRP, some of which can be mentioned (Galal et al., 2005; Chellapandian et al., 2017; Bengar and Shahmansouri, 2020; Choi et al., 2015; Ribeiro et al., 2018; Zeng et al., 2017). Eid et al. (2017) proposed a model based on analytical methods. Comparison of the obtained results showed that the analytical model presented in this study has a very good adaptation with laboratory results and finite element method.

The soft computing techniques have good remarkable accuracy in estimating the relationships between different parameters. Many studies on soft computing in civil engineering have been used to solve complex problems, such as the works conducted by Kamgar et al. (2020), Kar and Pandit (2020), Nematzadeh et al. (2020), Shahmansouri et al. (2019), Shahmansouri et al. (2020), Yasi and Mohammadzadeh (2018), Chou et al. (2019), Kazemi Elaki et al. (2016), Nir et al. (2019) and Taban et al. (2021). Khatibinia and Mohammadzadeh (2017) presented a model for determining the bonding of FRP polymer fibers and building elements. This model was based on ANFIS simulation, and while confirming the accuracy of the ANFIS method, their results in predicting the bonding of FRP polymer fibers and building elements show that the use of the ANFIS model and meta-heuristic models such as PSO and GA can significantly improve the prediction accuracy.

Azimipour et al. (2020) investigated the compressive strength of self-compacting concretes with a high volume of fly ash using linear and nonlinear algorithms in SVM. The results showed that in the case of considering the appropriate input parameters and a wide range of data to obtain the appropriate kernel performance coefficient, the results of the prediction for SVM-RBF method are more accurate than

other SVM methods. Naderpour et al. (2019) provided a relationship to predict the compression strength of reinforced concrete columns confined by FRP using Artificial Neural Networks (ANN). Cascardi et al. (2017) studied the prediction of the compression strength of reinforced concrete columns confined by FRP in circular columns using ANN. The results of this study showed that ANN can be used to predict the compression strength of reinforced concrete columns confined by FRP.

To predict the compression strength of reinforced concrete columns confined by FRP, two different techniques including FRP reinforcing effect and the simultaneous FRP reinforcing effect are considered. In this study, methods have been developed to predict the compression strength of reinforced concrete columns confinement by FRP and transverse reinforcement. For this purpose, a set of experimental data is used for training and testing in the proposed methods. This database includes 95 specimens of FRP-confined columns obtained from different studies. There are 7 input parameters including column height, compressive strength of concrete core without confinement, FRP modulus of elasticity, cross-sectional area of longitudinal reinforcement, yield stress in longitudinal reinforcements, compressive stress due to FRP and shear reinforcement. Here, to estimate the stable stress in the FRP-reinforced columns by soft computational techniques such as Least Squares Support Vector Machine (LS-SVM) method, Weight Least Squares Support Vector Machine (WLS-SVM) and so on, Adaptive Network based Fuzzy Inference System (PSO-ANFIS) are used. Finally, the results of the proposed methods are compared with other available methods.

2. Confinement Stress of FRP Wrap

As the axial pressure is applied to a confined concrete column, the concrete core expands. This expansion and increase in

lateral volume is limited by the surrounding wrap. Therefore, a kind of passive lateral pressure is applied to the middle concrete by the wrap, which is called the confining compressive stress. The distribution of confining compressive stresses in circular sections is quite uniform. Considering the equilibrium of the stresses applied on the repellent material and also regardless of the tangential stresses along the longitudinal direction of the column sample, it can be written that (Purba and Mufti, 1999):

$$f_{lf} = \frac{2 \times t_f \times f_{yf}}{D}, f_{ls} = \frac{2 \times A_{st} \times f_{ys}}{s \times d_c} \quad (1)$$

where D and d_c : are the diameter of column and the diameter of the core, respectively. f_{lf} and f_{ls} : are the compression strength of reinforced concrete columns confined by FRP and transverse reinforcement, respectively. Also t_f : is the thickness of the FRP wrap, f_{yf} : is the maximum tensile stress of FRP, A_{st} : is the cross-sectional area of the transverse reinforcement, f_{ys} : is the yielding stress of the transverse reinforcement and s : is the distance between the transverse reinforcements. The performance manner of concrete, FRP layer and shear reinforcement have been shown in Figure 1. The maximum tensile stress of FRP has been calculated in Eq. (2).

$$f_{yf} = E_f \varepsilon_f \quad (2)$$

where E_f : is the elastic modulus of the FRP wrap in line with the fibers around the column and ε_f : is the ultimate strain of FRP under tension.

The value of ε_f is determined by the Flat Coupon Tensile Test. Laboratory observations show that at the moment of failure, the measured tensile strain of the wrap is less than the value of ε_f . Lam and Teng (2003) used Eq. (3) to calculate the failure strain in the sample of wrapped cylindrical columns with FRP sheets.

$$\varepsilon_{h,wrap} = k_e \varepsilon_f \quad (3)$$

where $\varepsilon_{h,wrap}$: is the circular failure strain of the FRP wrap. k_e : is also the FRP efficiency factor. The value of this coefficient depends on the type of FRP composite.

According to ACI 440.2R-17 (2017), the maximum normal force (P_n) in an element confined by FRP layer, can be calculated using the following equations for elements non-prestressed by existing steel rebar and steel-tie reinforcement, respectively:

$$\phi P_n = 0.85 \phi [0.85 f'_c (A_g - A_{st}) + f_y A_{st}] \quad (4)$$

$$\phi P_n = 0.8 \phi [0.85 f'_c (A_g - A_{st}) + f_y A_{st}] \quad (5)$$

in which A_g and A_{st} : represent the gross and total area of the longitudinal reinforcement, respectively. f_y : denotes the steel reinforcement yield strength and f'_c : represents the maximum compressive strength in confined concrete as follows:

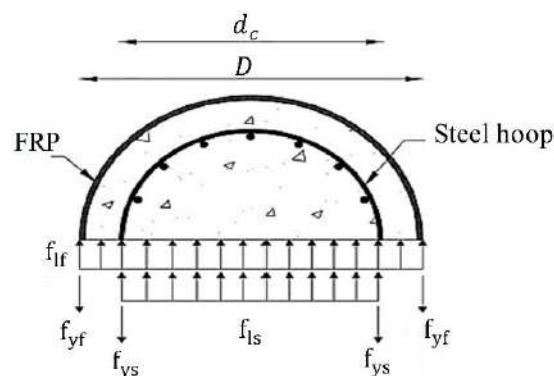


Fig. 1. Mechanism of distribution of concrete stress confined by FRP and transverse reinforcements

$$f'_c = f'_c + \psi_f 3.3k_a f_{lf} \quad (6)$$

in which ψ_f : denotes the reduction factor, which is 0.95, f'_c : represents the compressive strength of unconfined concrete, k_a : is the geometric dependent efficiency factor and f_{lf} : denotes the maximum confinement pressure (Eq. (1)).

3. Laboratory Data

Initially, a laboratory data set consisting of 135 samples (circular columns of reinforced concrete subjected to axial load) was selected (Chastre and Silva, 2010; Demers and Neale, 1999; Benzaid et al., 2010; Matthys et al., 2005; Eid et al., 2009; Abdelrahman and El-Hacha, 2012; Mostofinejad and Torabian, 2015; Silva, 2011; Hadi et al., 2017; Hadi, 2010; Issa et al., 2009; Moshiri et al., 2015; Yin et al., 2015; Hadi, 2006). After collecting the experimental data, the data were excluded to 95 experimental data. Based on Table 1, 12 variables were first gathered from the

references. However, according to the existing algorithms, by calculating the other two parameters using Eq. (1), the number of input parameters was reduced to seven parameters (Table 1). The changes calculated in 95 laboratory data have been shown in Table 2. In order to increase the performance of the LS-SVM, WLS-SVM, ANFIS and PSO-ANFIS methods in the training phase, the values of the input parameters using Eq. (7) are considered in the range [0.1-0.9].

$$S_{I,i} = S_{I,\min} + \left[(S_{I,\max} - S_{I,\min}) \times \frac{D_{I,i} - D_{I,\min}}{D_{I,\max} - D_{I,\min}} \right] \quad (7)$$

where $S_{I,i}$: is the I-th normalized input parameters for the i -th set of parameters in the data. $S_{I,\max}$ and $S_{I,\min}$: are the maximum and minimum values of $S_{I,i}$ for $1 \leq i \leq 95$ the sets of parameter in the data. The values of $D_{I,i}$, $D_{I,\min}$ and $D_{I,\max}$: are the I-th input parameter in the i -th set of the data, minimum and maximum of the data.

Table 1. Description of input and output parameters

Symbol	Parameters
$D(m)$	Concrete section diameter
$L(m)$	Column height
$f'_{co}(MPa)$	Maximum compressive strength of concrete core
$t_f(mm)$	FRP wrap thickness
$E_f(GPa)$	FRP wrap elasticity module
$f_{yf}(MPa)$	Maximum FRP tensile stress
$A_s(mm^2)$	The cross-sectional area of longitudinal reinforcement
$f_y(MPa)$	Yield stress of longitudinal reinforcement
$f_{ys}(MPa)$	Yield stress of transverse reinforcement
$s(m)$	The distance between the transverse reinforcement
$d_b(mm)$	The diameter of the concrete core
$f'_{cu}(MPa)$	Ultimate compressive strength of the columns

Table 2. Statistical description of input and output parameters in the present study

Input parameter	$L(m)$	$f'_{co}(MPa)$	$E_f(GPa)$	$A_{s1}(mm^2)$	$f_y(MPa)$	$f_{yf}(MPa)$	$f_{ys}(MPa)$	$f'_{cu}(MPa)$
Minimum	0.3	25	0	0	0	0	0	26.35
Maximum	2	75	480	2493.8	620	41.8	7.17	164.11
Average	0.95	39.58	102.56	806.53	404.74	11.01	2.38	68.37
Standard deviation	0.45	12.08	87.32	615.36	160.36	9.46	2.11	30.81
Coefficient of variation	0.47	0.3	0.85	0.76	0.4	0.86	0.89	0.45

4. Methods

4.1. Least Squares Support Vector Machine

Strong theoretical evidences show the capability of modeling high non-linear systems based on small sample in Support Vector Machines (SVMs) (Vapnik and Lerner, 1963). The approaches is based on Structural Risk Minimization (SRM) rules (Park and Ang, 1985). Suykens et al. (1999) proposed the Least Squares Support Vector Machine (LS-SVM) to fix the problems of SVM, including the slow training velocity in the large-scale problem.

Consider a set of training data $\{(x_1, y_1) \cdots (x_n, y_n)\} \subset X$, where X implies the input patterns space. The error quadratic norm is considered as the loss function of LS-SVM in the regression modelling of LS-SVM. The optimization problem is expressed as below (Suykens and Vandewalle, 1999):

$$\min J(\omega, \xi) = \frac{1}{2} \omega^2 + \frac{1}{2} C \sum_{i=1}^n \xi_i^2 \quad (8)$$

By considering the equality restriction:

$$y_i = \omega^T \phi(x_i) + b + \xi_i; i = 1, 2, \dots, n \quad (9)$$

Hence, the LS-SVM regression model is defined as below:

$$y(x) = \omega^T \phi(x) + b \quad (10)$$

in Eq. (8), C : denotes the punishment factor to meet tradeoff between the LS-SVM model complexities. The Lagrange function for the optimization problem is:

$$L(\omega, b, \xi_i, \alpha) = \frac{1}{2} \|\omega\|^2 + C \sum_{i=1}^n \xi_i^2 - \sum_{i=1}^n \alpha_i \left[\omega^T \phi(x_i) + b + \xi_i - y_i \right] \quad (11)$$

where $\alpha_i (i=1, 2, \dots, n)$: denotes the Lagrange

multipliers. By eliminating ω and ξ , the Karush–Khun–Tucker (KKT) conditions is:

$$\begin{bmatrix} 0 & 1 & \cdots & 1 \\ 1 & K(x_1, x_1 + \frac{1}{C}) & \cdots & K(x_1, x_n) \\ \vdots & \vdots & \ddots & \vdots \\ 1 & K(x_1, x_n) & \cdots & K(x_n, x_n + \frac{1}{C}) \end{bmatrix} \begin{bmatrix} b \\ \alpha \end{bmatrix} = \begin{bmatrix} 0 \\ y_1 \\ \vdots \\ y_n \end{bmatrix} \quad (12)$$

where $K(\cdot, \cdot)$: represents the so-called kernel function. Based on the Mercer's condition, a kernel $K(\cdot, \cdot)$ is chosen, such that:

$$K(x, \bar{x}) = \langle \phi(x), \phi(\bar{x}) \rangle_H \quad (13)$$

in fact, the high dimensional feature spaces are described by $K(\cdot, \cdot)$. Therefore, the following LS-SVM model is concluded:

$$y(x) = \sum_{i=1}^n \alpha_i K(x, x_i) + b \quad (14)$$

4.2. Weighted Least Squares-Support Vector Machine

The WLS-SVM regression can be defined as the following optimization in the first weight space by training dataset of N samples $[(x_k, y_k)]_{k=1}^n$ with input data $x_i \in R^d$ and output data $y_i \in R$ (Li et al., 2006):

$$\min J(\omega, \xi_i) = \frac{1}{2} \omega^2 + \frac{1}{2} C \sum_{i=1}^n \bar{v}_i \xi_i^2 \quad (15)$$

$$y_i = \omega^T \phi(x_i) + b + \xi_i; i = 1, 2, \dots, n \quad (16)$$

where $\phi(): R^d \rightarrow R^d$: denotes operator mapping the input into a higher dimensional space; $\omega \in R^d$: is the weight vector in primal weight space; and $\xi_i \in R$ and $b \in R$: are the error variable and bias term, respectively.

The model of WLS-SVM can be formulated by the optimization problem (Eq. (12)) and the training set in the first weight space as follows:

$$y(x) = \omega^T \phi(x) + b \quad (17)$$

In general, the structure of $\phi(x)$ is unknown. So, indirect calculation of ω from Eq. (15) is impossible. Hence, the solutions of WLS-SVM regression will be achieved by constructing a Lagrangian:

$$\begin{aligned} L(\omega, b, e, x) = \\ J(\omega, e) - \sum_{i=1}^n \alpha_i \\ \left[\omega^T \phi(x_i) + b + \xi_i - y_i \right] \end{aligned} \quad (18)$$

where α_i : denotes the Lagrangian multipliers. The optimality is as follows:

$$\frac{\partial L}{\partial \omega} = 0, \frac{\partial L}{\partial b} = 0, \frac{\partial L}{\partial e_i} = 0, \dots, \frac{\partial L}{\partial \alpha_i} = 0 \quad (19)$$

Omitting ω and ξ result the following system:

$$\begin{bmatrix} \Omega + V_\gamma & I_n^T \\ I_n & 0 \end{bmatrix} \begin{bmatrix} a \\ b \end{bmatrix} = \begin{bmatrix} y \\ 0 \end{bmatrix} \quad (20)$$

where

$$V_\gamma = \text{diag} \left\{ \frac{1}{\gamma_1} \dots \frac{1}{\gamma_n} \right\}; \quad (21)$$

$$\Omega_{i,j} = \left\langle \phi(x_i), \phi(x_j) \right\rangle_H;$$

$$i, j = 1, 2, \dots, n$$

$$y = [y_1, \dots, y_n]^T;$$

$$I_n^T = [1, \dots, 1]; \quad (22)$$

$$\alpha = [\alpha_1, \dots, \alpha_n]$$

in which the weight factors \bar{v}_k are given by Widodo and Yang (2008):

$$\bar{v}_k = \begin{cases} 1 & \text{if } \left| \frac{\xi_i}{\hat{\delta}} \right| \leq c_1 \\ \frac{c_2 - \left| \frac{e_i}{\hat{\delta}} \right|}{c_2 - c_1} & \text{if } c_1 \leq \left| \frac{\xi_i}{\hat{\delta}} \right| \leq c_2 \\ 10^{-4} & \text{otherwise} \end{cases} \quad (23)$$

where $\hat{\delta}$: denotes the standard deviation for the error parameters $\xi_i = \frac{d_i}{D_{ij}^{-1}}$; the

constants c_1 and c_2 : are normally selected as $c_1 = 2.5$ and $c_2 = 3$. Here D_{ij}^{-1} : is the i th first diagonal element in D^{-1} , in Eq. (20). According to the Mercer's Theorem, a kernel $K(.,.)$ is:

$$\begin{aligned} K(x_i, \bar{x}_j) = \\ \left\langle \phi(x_i), \phi(\bar{x}_j) \right\rangle_H; \quad (24) \\ i, j = 1, 2, \dots, n \end{aligned}$$

Then, the WLS-SVM model is derived as:

$$y(x) = \sum_{i=1}^n \alpha_i K(x_i, x) + b \quad (25)$$

$K(x_i, \bar{x}_j)$ function is actually a function in the initial space expressed as the inner product of two vectors in the feature space. In order to equate the $K(x_i, \bar{x}_j)$ function with the inner product of two vectors in the feature space, a certain positive $K(x_i, \bar{x}_j)$ function must be symmetric, which holds true in the Mercer condition. The SVM is usually used with three Kernel RBF functions of basic Gaussian radius, polynomials, and the linear Kernel function. The Gaussian radial basis function (RBF) is typically employed as the kernel function in the WLS-SVM approach, which is expressed as:

$$K_{RBF}(x, \bar{x}) = \exp\left(-\frac{\|x - \bar{x}\|^2}{\sigma^2}\right) \quad (26)$$

where σ^2 : denotes a positive real constant, and it is commonly called the kernel width.

4.3. Adaptive Neural Fuzzy Inference System

This system is defined as a neuro-fuzzy that constructs a useful model for different modeling. The structure of ANFIS includes 5 layers (Figure 2):

Layer 1: input for the next layers.

Layer 2: an adaptive step, controlling parameter is calculated based on the membership functions C_j^i in Eq. (27). Two antecedent variables C_i and δ_i for each $\mu C_1^1(x_1)$ are:

$$\mu C_1^1(x_1) = \exp\left(-\frac{(c_i - x)^2}{2\delta_i^2}\right) \quad (27)$$

Layer 3: The calculation of preliminary weights in this layer were done by using

$$w_i = \mu C_1^1(x_1) * \mu C_2^2(x_2) * \dots * \mu C_m^m(x_m) \quad (28)$$

Layer 4: In this layer, the weights calculated from the previous layer are normalized. Eq. (29) shows the normalization of weights.

$$\bar{w}_i = \frac{w_i}{\text{sum}(w_i)} \quad (29)$$

Layer 5: The output of this layer is the total output of the system as shown in Eq. (30). The output value is constructed as sum of f_i and a de-fuzzification step is done to have the final value. ANFIS utilizes the

fuzzy steps as follows:

$$f_i = \bar{w}_i(\alpha_0 + \sum(\alpha_i x_i)) \quad (30)$$

If $x_1 = C_1^k, x_2 = C_2^k, \dots$, and $x_m = C_m^k$, then:

$$f_k = \alpha_0^k + \sum_{i=1}^m \alpha_i^k x_i \quad (31)$$

where x_i : denotes the controlling factors including the column height, compressive strength of concrete core without confinement and FRP modulus of elasticity, C_j^i : represents the linguistic label, $\mu C_j^i(x)$: implies the membership value for determining the dependency of factor (x) to C_{ji} , and α_i : denotes the parameter of linear function for measuring y (Pham et al., 2018).

4.4. Particle Swarm Optimization

Particle Swarm Optimization (PSO) is based on the idea of collective intelligence to find optimal answers in a search space. PSO is formed by a random group of individuals and then optimized by updating generations. In each generation, each person is optimized with two superior positions. The first amount of pbest is the best position that the person has ever reached. The overall best result of Gbest is the other best result that this individual pursues, which represents the optimum location in the entire search of the entire population (Zhou et al., 2011). RMSE is used as the index in this research. By lowering the RMSE, the accuracy of the model will increase.

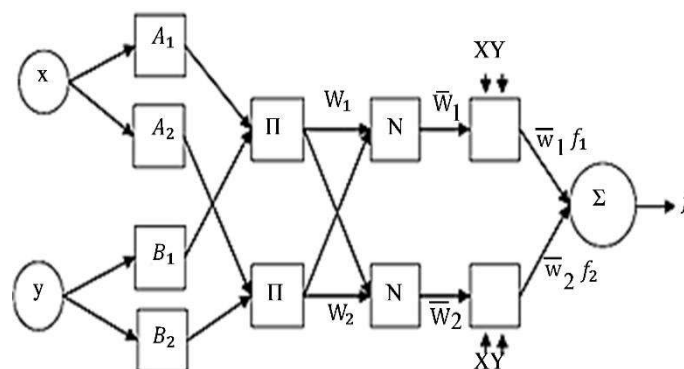


Fig. 2. The structure of the adaptive neural fuzzy inference system (ANFIS)

$$RMSE = \sqrt{\sum_{i=1}^n ((p_i - y_i) / n)} \quad (32)$$

where p_i : denotes the predicted value obtained by the model, y_i : represents the value of the shear strength, and n : implies the number of input data.

The next location will be constructed with the next velocity of a particle if the criteria at position x_i are not met. The formulas are as below:

$$v_i^{k+1} = \omega v_i + ac_1 r_1 (pbest_i - x_i) + ac_2 r_2 (Gbest_i - x_i) \quad (33)$$

$$x_i^{k+1} = x_i + v_i^{k+1} \quad (34)$$

where ω : is the Inertia weight, c_1 and c_2 : are two positive constants known as acceleration coefficients, r_1 and r_2 : are random numbers between 0 and 1, x_i^k : denotes the location of individual i in k , v_i^k : represents the velocity of individual i in k , x_i^{k+1} : implies the location of individual i in $k+1$, v_i^{k+1} : denotes the velocity of individual i in $k+1$, $Pbest$: represents the best location of individual i in the swarm, and $Gbest$: denotes the optimum location of the all individuals in the swarm. The method stops when the criteria are met. Table 3 represents the values of PSO meta-heuristic method. Given the combination of PSO method with ANFIS method for optimization of prior and posterior parameters, the following parameters are selected based on a trial and error process.

Table 3. Parameters related to the PSO method

Number of population	40
Maximum number of iterations	1000
Ideal weight	1
Ideal slope to weight ratio	0.99
Private learning coefficient	1
Public learning coefficient	2

4.5. ANFIS Trained by PSO

The ANFIS method uses the scores related to neural networks and fuzzy systems simultaneously. The main challenge in this method is data training. In ANFIS method, fuzzy anterior and posterior

parameters are adjusted using the gradient descent methods. The responses of the gradient-descent-based method may be stuck in local optimizations. Therefore, the use of meta-heuristic algorithms such as PSO algorithm with random search nature can be considered as alternative and useful approaches. The objective function of the evolutionary algorithms used is the Root Mean Square Error (RMSE). To solve the optimization problem using the PSO-ANFIS algorithms, the w_i weight obtained from the anterior fuzzy parameters and linear parameters are adjusted through meta-heuristic algorithms. Considering the combination of the PSO method with the ANFIS method to optimize the anterior and posterior parameters, the parameters of population size and maximum number of iterations in the PSO algorithm were selected at 40 and 1000, respectively based on a trial and error process. After loading the training data and creating the initial structure, the fuzzy inference system of the Sogeno type was used to train the system designed by PSO and, the training process was repeated 1000 times.

4.6. Performance Indicators

Performance of LS-SVM, WLS-SVM, ANFIS and PSO-ANFIS methods were compared using R^2 , MAPE, MAE and RMSE. The closer the coefficient R^2 are to 1, the closer the predicted values will be to the actual values. Eqs. (35) to (38) show the mathematical formula as the criteria for evaluating performance in the proposed methods in the present study:

$$RMSE = \sqrt{\left[\left(\frac{1}{n} \right) \times \sum_{i=1}^n [p_i - y_i]^2 \right]} \quad (35)$$

$$MAE = \left[\left(\frac{1}{n} \right) \times \sum_{i=1}^n [p_i - y_i] \right] \quad (36)$$

$$MAPE = \left[\left(\frac{1}{n} \right) \sum_{i=1}^n \left[\frac{p_i - y_i}{y_i} \right] \times 100 \right] \quad (37)$$

$$R^2 = \left[\frac{n \sum y_i p_i - (\sum y_i)(\sum p_i)}{\sqrt{((n(\sum y_i^2) - (\sum y_i)^2) \times (n(\sum p_i^2) - (\sum p_i)^2))}} \right]^2 \quad (38)$$

where p_i : is the predicted value and y_i : is the real value for n samples.

5. Discussion

There are simple ways to divid the data. In these methods, the performance of the model is not well demonstrated because of their dependency on which data is selected for training and which data for testing. This dependence sometimes makes the model more accurate and sometimes less accurate. Here, to predict the model, the data were divided into two training and validation classes. The k-fold cross validation method, has been used. To select the k value, it must be ensured that the number of data points in the training subset and the validation subset have a same distribution regime. In this study, 67% of the data were used as a proportion of training subsets and 33% for validation subsets. Using cross-validation k equal to $k = 3$, 59 randomly selected data were used as training and 36 data were used for validation. To predict the compression strength of reinforced concrete columns confined by FRP, the data were trained by four methods of LS-SVM, WLS-SVM, ANFIS and PSO-ANFIS. In the PSO-ANFIS method, a FIS (fuzzy inference system) model was created and PSO is then searches for the most appropriate front and back parameters in ANFIS. To achieve better performance in PSO-ANFIS method, the value of initial parameter of inertia weight is assumed to 1. The RMSE value in this method is also obtained for 1000 iterations. To achieve maximum performance using the LS-SVM and WLS-SVM methods, the most appropriate values for the setting parameter (γ_2) and the RBF core parameter (σ^2) need to be determined. In this study, the best value of monitoring

parameters was determined using trial and error process. Therefore, the setting parameter value (5.1) and the RBF core parameter value (3.09) were selected.

R^2 , MAPE, MAE and RMSE for 95 FRP-confined concrete columns trained by LS-SVM, WLS-SVM, ANFIS and PSO-ANFIS methods are presented in Table 4. According to the coefficients of MAPE, MAE and RMSE, it can be seen that LS-SVM, WLS-SVM, ANFIS and PSO-ANFIS algorithms have generated values close to 1 for the coefficients and values close to zero for the RMSE, MAPE and MAE coefficients. The results also show that the PSO-ANFIS algorithm with $R^2 = 0.984$ in the experimental stage and $R^2 = 0.967$ in the validation stage ($R^2 \geq 0.95$) predicts the parameter with much higher accuracy than the other algorithms. Comparison of the results presented in this table shows that the efficiency and accuracy of the proposed methods to predict the compression strength of reinforced concrete columns confined by FRP is remarkable. The results also show that the PSO-ANFIS method predicts the compression strength of reinforced concrete columns confined by the FRP parameters with much higher accuracy than the other developed methods. Table 5 presents the results of ANN, GMDH, Gene Expression Programming (GEP) and ACI Codes for predicting the compression strength of reinforced concrete columns confined by FRP. Comparison of the results presented in this table with the results obtained from LS-SVM, WLS-SVM, ANFIS and PSO-ANFIS methods shows that the efficiency and accuracy of the proposed methods in the present study to predict the compression strength of reinforced concrete columns confined by FRP is more than the values presented in Codes and other calculation methods.

Table 4. Error measurement in various methods studied in the present study

Methods	LS-SVM		WLS-SVM		PSO -ANFIS		ANFIS	
	Test	Train	Test	Train	Test	Train	Test	Train
Parameter								
MAPE	8.32	6.53	10.72	8.96	11.17	12.58	11.84	12.93
MAE	3.436	3.095	4.140	4.200	3.375	3.060	3.894	1.070
RMSE	6.664	4.163	4.780	4.770	4.610	4.120	4.801	2.078
R^2	0.962	0.980	0.975	0.980	0.967	0.984	0.979	0.995

Table 5. The results of ANN, GMDH, GEP methods and ACI regulations

Method	ANN	GMDH	GEP	ACI
MAPE	5.52	11.49	8.94	34.74
RMSE	5.45	9.93	7.08	33.70
R^2	0.995	0.981	0.991	0.51
Reference	(Naderpour et al., 2019)	(Naderpour et al., 2019)	(Naderpour et al., 2019)	(ACI 440.2R-17, 2002)

The graphs of the ratio of the laboratory data to the predicted data by the training LS-SVM, WLS-SVM, ANFIS and PSO-ANFIS methods are shown in Figures 3-6 respectively. The horizontal axis represents the laboratory data and the vertical axis represents the predicted data. The low scatter of data around the $X = Y$ line indicates a reduction in prediction error and better system performance. Figures 7 to 10 also show the overlap of LS-SVM, WLS-SVM, ANFIS and PSO-ANFIS results with the laboratory data. According to the results of the diagrams, the performance of the PSO-ANFIS method is better than the other methods. The results show that the compressive strength predicted by the PSO-

ANFIS method is well compatible with the compressive strength obtained from the laboratory results. Also, considering all input parameters, PSO-ANFIS method with $RMSE = 4.610$ and $R^2 = 0.967$ has the highest accuracy.

Figure 11 presents the prediction results for all methods used in the present study. The results indicate that four methods of LS-SVM, WLS-SVM, ANFIS and PSO-ANFIS, result a relatively high values of R^2 ($R^2 \geq 0.95$). This shows that these methods have very high accuracy. The compression strength predicted using these methods is also reliable due to the low MAPE coefficient.

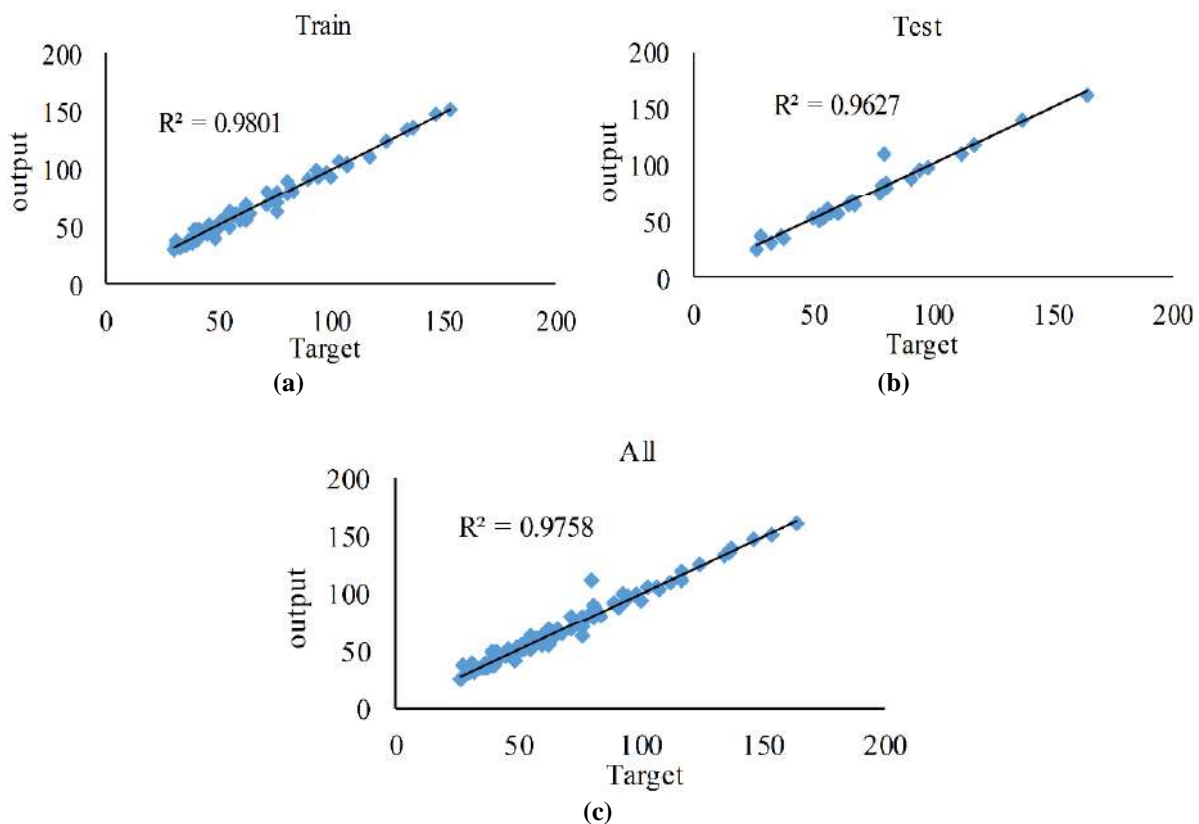


Fig. 3. Comparison of the compression strength predicted in the present study with the values of laboratory compression strength using LS-SVM method: a) Results obtained from the data training phase; b) Results obtained from the data test phase; and c) Results obtained from all laboratory data

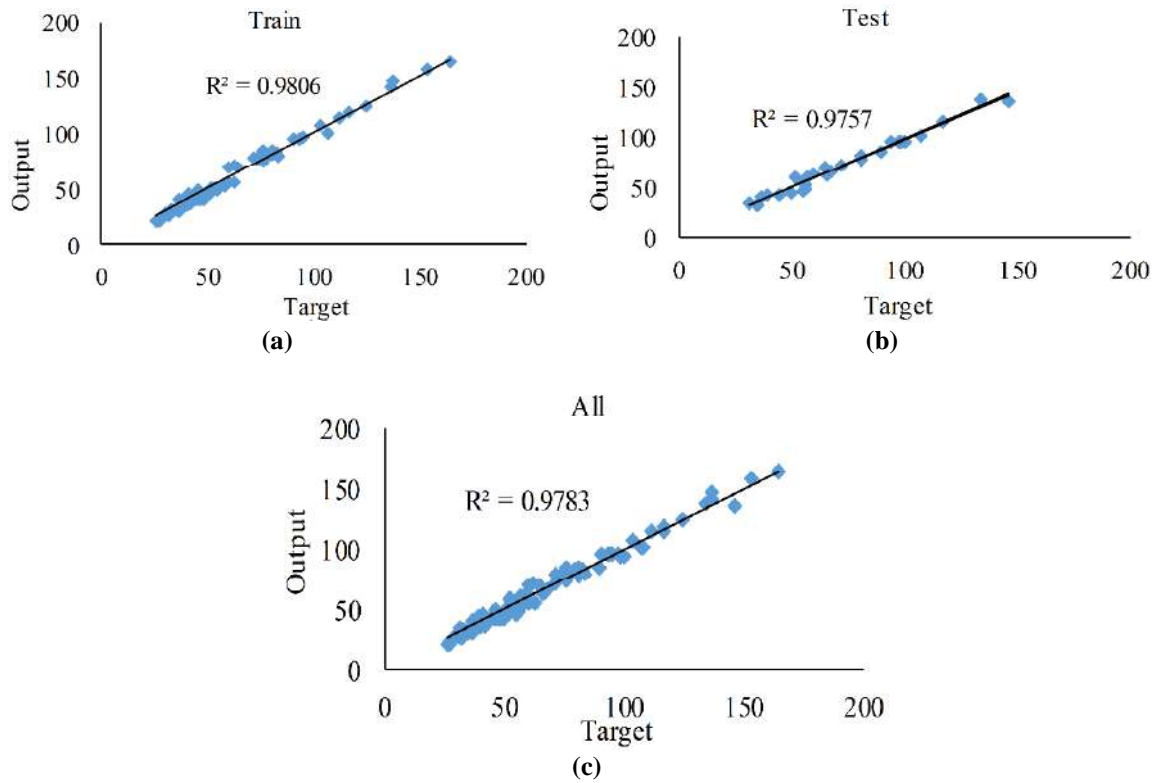


Fig. 4. Comparison of the compression strength predicted in the present study with the values of laboratory compression strength using WLS-SVM method: a) Results obtained from the data training phase; b) Results obtained from the data test phase; and c) Results obtained from all laboratory data

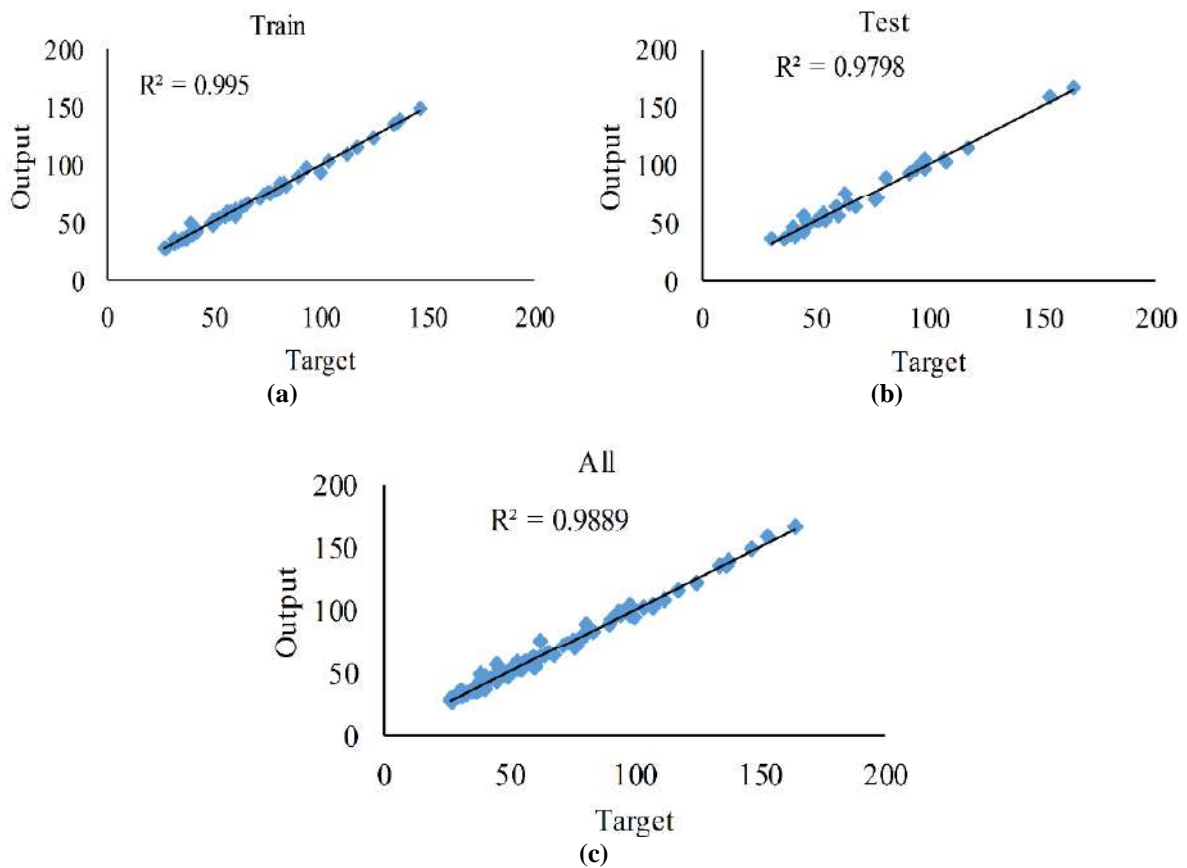


Fig. 5. Comparison of the compression strength predicted in the present study with the values of laboratory compression strength using ANFIS method: a) Results obtained from the data training phase; b) Results obtained from the data test phase; and c) Results obtained from all laboratory data

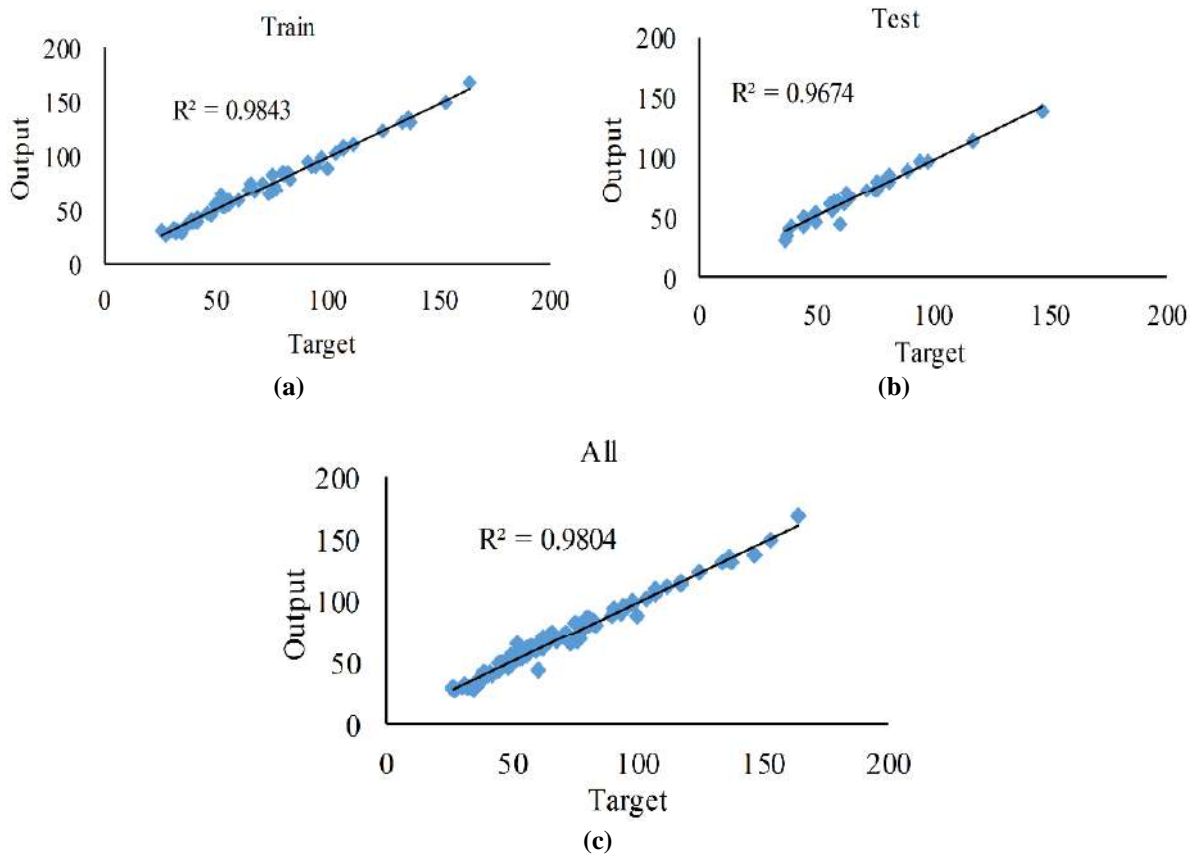


Fig. 6. Comparison of the compression strength predicted in the present study with the values of laboratory compression strength using PSO-ANFIS method: a) Results obtained from the data training phase; b) Results obtained from the data test phase; and c) Results obtained from all laboratory data

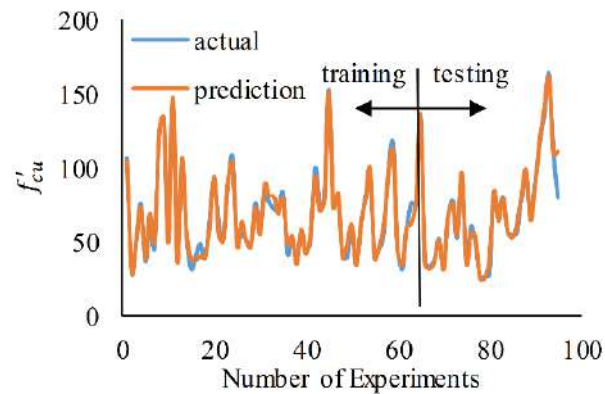


Fig. 7. Comparison of the laboratory results with those predicted by LS-SVM method

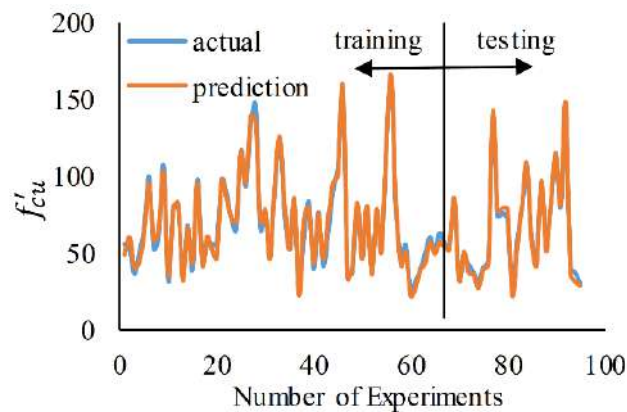


Fig. 8. Comparison of the laboratory results with those predicted by WLS-SVM method

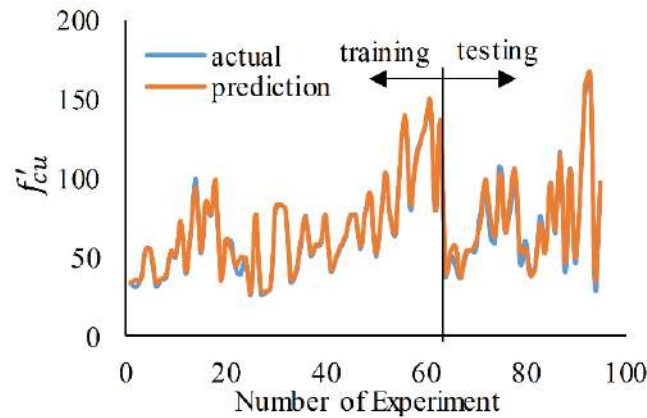


Fig. 9. Comparison of the laboratory results with those predicted by ANFIS method

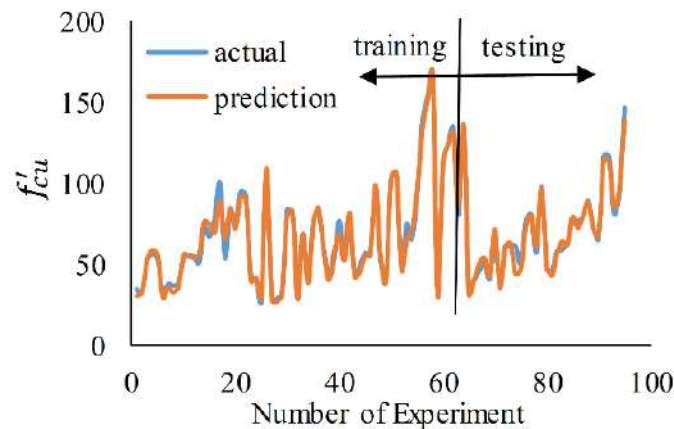


Fig.10. Comparison of the laboratory results with those predicted by PSO-ANFIS method

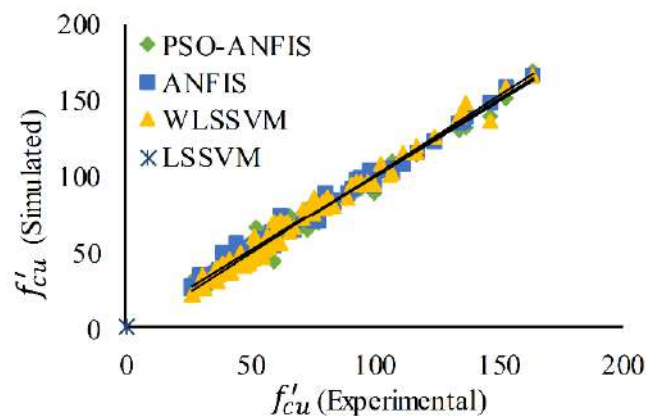


Fig.11. Comparison of the predicted values of compression strength of reinforced concrete columns confined by FRP based on the studied methods in terms of laboratory values

The error of programs code for LS-SVM, WLS-SVM, ANFIS and PSO-ANFIS methods in the training and testing subsets are shown in Figures 12-15 respectively. According to the diagrams, PSO-ANFIS methods have the highest accuracy and the lowest error in predicting the compression strength of reinforced concrete columns confined by FRP. Therefore, this algorithm will be acceptable for designing and

predicting the compression strength of reinforced concrete columns confined by FRP. In addition, despite the minor differences in the performance evaluation values in the training and testing stages, the statistical results show that the methods proposed in this study provide very accurate estimate of the compression strength of reinforced concrete columns confined by FRP.

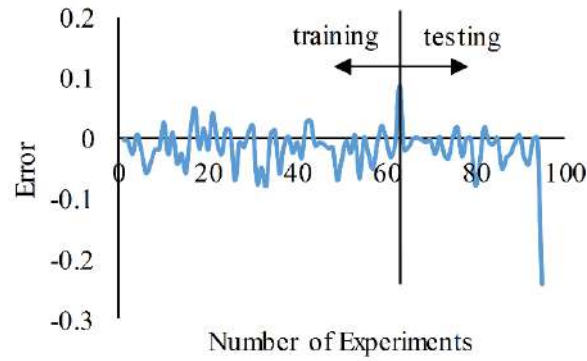


Fig.12. The error values obtained from the LS-SVM method for predicting compression strength of reinforced concrete columns confined by FRP in the training and testing data

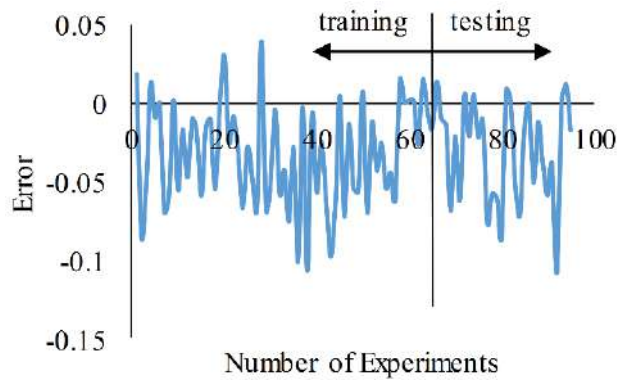


Fig.13. The error values obtained from the WLS-SVM method for predicting compression strength of reinforced concrete columns confined by FRP in the training and testing data

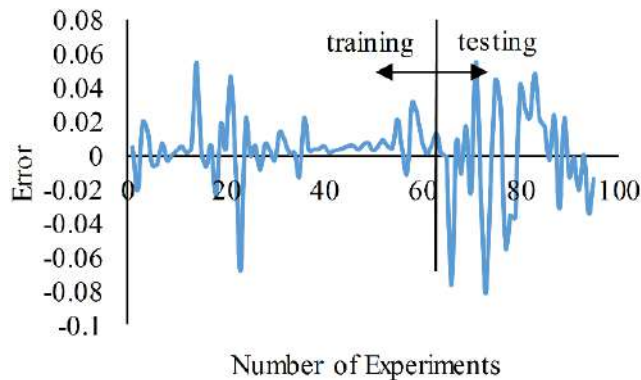


Fig.14. The error values obtained from the ANFIS method for predicting compression strength of reinforced concrete columns confined by FRP in the training and testing data

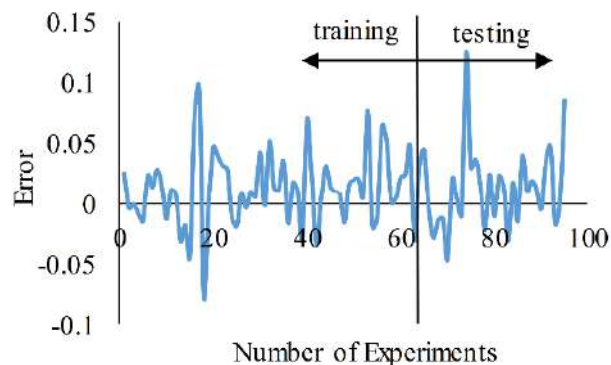


Fig.15. The error values obtained from the PSO-ANFIS method for predicting compression strength of reinforced concrete columns confined by FRP in the training and testing data

6. Conclusions

In this study, the compression strength of reinforced concrete columns confined by FRP was predicted using soft computational methods (LS-SVM, WLS-SVM, ANFIS and PSO-ANFIS). 95 laboratory data were selected for the development of the methods. For the first time, the effect of FRP and shear reinforcement on the strength of the column was also considered simultaneously by seven input parameters. RMSE, R^2 , MAPE and MAE coefficients were calculated for each of the methods and, the outputs of the studied methods were evaluated by other methods. Besides, the error range for each prediction was determined in all methods. Compared to existing models and methods, LS-SVM, WLS-SVM, ANFIS and PSO-ANFIS methods have very good results. The results show that in total the PSO-ANFIS methods with the root mean square error of 4.610 and the coefficient of determination of 0.967 has much accurate prediction than the LS-SVM, WLS-SVM, ANFIS, ANN, GMDH, GEP methods and ACI regulations. Finally, the paper concludes that soft computing is easily applicable to parallel architectures and data processing time with similar results being achieved.

7. References

- Abdelrahman, K. and El-Hacha, R. (2012). "Behavior of large-scale concrete columns wrapped with CFRP and SFRP sheets", *Journal of Composites for Construction*, 16, 430-439.
- ACI 440.2R-17. (2017). "Guide for the design and construction of externally bonded FRP systems for strengthening concrete structures", Reported by ACI committee 440, American Concrete Institute.
- AzimiPour, M., EskandariNaddaf, H. and Pakzad, A. (2020). "Linear and non-linear SVM prediction for fresh properties and compressive strength of high-volume fly ash self-compacting concrete", *Construction and Building Materials*, 230, 117021.
- Bengar, H.A. and Shahmansouri, A.A. (2020). "A new anchorage system for CFRP strips in externally strengthened RC continuous beams", *Journal of Building Engineering*, 30, 101230.
- Benzaid, R., Mesbah, H. and EddineChikh, N. (2010). "FRP-confined concrete cylinders: axial compression experiments and strength model", *Journal of Reinforced Plastics and Composites*, 29(16), 2469-2488.
- Cascardi, A., Micelli, F. and Aiello, M.A. (2017). "An artificial neural networks model for the prediction of the compressive strength of FRP-confined concrete circular columns", *Engineering Structures*, 140, 199-208.
- Chastre, C. and Silva, M.A.G. (2010). "Monotonic axial behavior and modelling of RC circular columns confined with CFRP", *Engineering Structures*, 32, 2268-2277.
- Chellapandian, M., SuriyaPrakash, S. and Sharma, A. (2017). "Strength and ductility of innovative hybrid NSM reinforced and FRP confined short RC columns under axial compression", *Composite Structure*, 176, 205-216.
- Choi, E., Cho, B.S. and Lee, S. (2015). "Seismic retrofit of circular RC columns through using tensioned GFRP wires winding", *Composites Part B Engineering*, 83, 216-225.
- Chou, J.S., Pham, T.P.T., Nguyen T.K., Pham A.D. and Ngo, N.T. (2019). "Shear strength prediction of reinforced concrete beams by baseline, ensemble, and hybrid machine learning models", *Soft Computing*, 24, 3393-3411.
- Demers, M. and Neale, K.W. (1999). "Confinement of reinforced concrete columns with fiber-reinforced composite sheets—an experimental study", *Canadian Journal of Civil Engineering*, 26, 226-241.
- Eid, R. and Paultre, P. (2017). "Plasticity-based model for circular concrete columns confined with fibre-composite sheets", *Engineering Structures*, 29(12), 3301-3311.
- Eid, R., Roy, N. and Paultre, P. (2009). "Normal and high-strength concrete circular elements wrapped with FRP composites", *Journal of Composites for Construction*, 13, 113-124.
- Galal, K., Arafa, A. and Ghobarah, A. (2005). "Retrofit of RC square short columns", *Engineering Structures*, 27(2), 801-813.
- Hadi, M.N.S., Hasan, H.A. and Sheikh, M.N. (2017). "Experimental investigation of circular high strength concrete columns reinforced with glass fiber-reinforced polymer bars and helices under different loading conditions", *Journal of Composites for Construction*, 21(4), 4017005-1-13.
- Hadi, M.N.S. (2010). "Behaviour of reinforced concrete columns wrapped with fibre reinforced polymer under eccentric loads", *Australian Journal of Structural Engineering*, 10(2), 169-178.
- Hadi, M.N.S. (2006). "Comparative study of eccentrically loaded FRP wrapped columns", *Composite Structures*, 74(2), 127-135.
- Haji, M., Naderpour, H. and Kheyroddin, A. (2018). "Experimental study on influence of proposed

- FRP-strengthening techniques on RC circular short columns considering different types of damage index”, *Composite Structures*, 209, 112-28.
- Issa, M.A., Alrousan, R.Z. and Issa, M.A. (2009). “Experimental and parametric study of circular short columns confined with CFRP composites”, *Journal of Composites for Construction*, 13(2), 135-147.
- Kamgar, R., Bagherinejad, M.H. and Heidarzadeh, H. (2020). “A new formulation for prediction of the shear capacity of FRP in strengthened reinforced concrete beams”, *Soft Computing*, 24, 6871-6887.
- Kar, S., Pandit, A.R. and Biswal, K.C. (2020). “Prediction of FRP shear contribution for wrapped shear deficient RC beams using adaptive neuro-fuzzy inference system (ANFIS)”, *Structures*, 23, 702-717.
- Kazemi Elaki, N., Shabakhty, N., Abbasi Kia, M. and Sanayee Moghaddam, S. (2016). “Structural reliability: an assessment using a new and efficient two- phase method based on artificial neural network and a harmony search algorithm”, *Civil Engineering Infrastructures Journal*, 49(1), 1-20.
- Khatibinia, M. and Mohammadizadeh, M.R. (2017). “Intelligent fuzzy inference system approach for modeling of debonding strength in FRP retrofitted masonry elements”, *Structural Engineering and Mechanics*, 56(5), 787-796.
- Lam, L. and Teng, J.G. (2003). “Design-oriented stress-strain model for FRP-confined concrete in rectangular columns”, *Journal of Reinforced Plastics and Composites*, 22(13), 1149-1186.
- Li, H.S., Lü, Z.Z. and Yue, Z.F. (2006). “Support vector machine for structural reliability analysis”, *Applied Mathematics and Mechanics*, 27(10), 1135-1143.
- Matthys, S., Toutanji, H., Audenaert, K. and Taerwe, L. (2005). “Axial load behavior of large-scale columns confined with fiber-reinforced polymer composites”, *ACI Structural Journal*, 102, 258-267.
- Moshiri, N., Hosseini, A. and Mostofinejad, D. (2015). “Strengthening of RC columns by longitudinal CFRP sheets: Effect of strengthening technique”, *Construction and Building Materials*, 79, 318-325.
- Mostofinejad, D. and Torabian, A. (2015). “Experimental study of circular RC columns strengthened with longitudinal CFRP composites under eccentric loading: comparative evaluation of EBR and EBROG methods”, *Journal of Composites for Construction*, 20(2), 4015055-1-15.
- Naderpour, H., Nagai, K., Fakharian, P. and Haji, M. (2019). “Innovative models for prediction of compressive strength of FRP-confined circular reinforced concrete columns using soft computing methods”, *Composite Structures*, 215, 69-84.
- Nair, A., Cai C.S. and Kong X. (2019). “Acoustic emission pattern recognition in CFRP retrofitted RC beams for failure mode identification”, *Composites Part B: Engineering*, 161, 691-701.
- Nematzadeh, M., Shahmansouri, A.A. and Fakoor, M. (2020). “Post-fire compressive strength of recycled PET aggregate concrete reinforced with steel fibers: Optimization and prediction via RSM and GEP”, *Construction and Building Materials*, 252, 119057.
- Park, Y.J. and Ang, A.H.S. (1985). “Mechanistic seismic damage model for reinforced concrete”, *Journal of Structural Engineering*, 111(4), 722-739.
- Pham, B.T., Hoang T.A., Nguyen, D.M. and Bui, D.T. (2018). “Prediction of shear strength of soft soil using machine learning methods”, *Catena*, 166, 181-191.
- Purba, B.K. and Mufti, A.A. (1999). “Investigation of the behavior of circular concrete columns reinforced with carbon fiber reinforced polymer (CFRP) jackets”, *Canadian Journal of Civil Engineering*, 26(5), 590-596.
- Ribeiro, F., Sena-Cruz, J., Branco, F.G. and Júlio, E. (2018). “Hybrid FRP jacketing for enhanced confinement of circular concrete columns in compression”, *Construction and Building Material*, 184, 681-704.
- Shahmansouri, A.A., Akbarzadeh Bengar, H. and Ghanbari, S. (2020). “Compressive strength prediction of eco-efficient GGBS-based geopolymer concrete using GEP method”, *Journal of Building Engineering*, 31, 101326.
- Shahmansouri, A.A., Akbarzadeh Bengar, H. and Jahani, E. (2019). “Predicting compressive strength and electrical resistivity of eco-friendly concrete containing natural zeolite via GEP algorithm”, *Construction and Building Materials*, 229, 116883.
- Silva, M.A.G. (2011). “Behavior of square and circular columns strengthened with aramid or carbon fibers”, *Construction and Building Materials*, 25(8), 3222-3228.
- Suykens, J.A.K., DeBrabanter, J., Lukas, L. and Vandewalle, J. (2002). “Weighted least squares support vector machines: Robustness and sparse approximation”, *Neurocomputing*, 48(1-4), 85-105.
- Suykens, J.A.K. and Vandewalle, J. (1999). “Least squares support vector machine classifiers”, *Neural Processing Letters*, 9(3), 293-300.
- Taban, M.H., Hajiazizi, M., and Ghobadian, R. (2021). “Prediction of Q-value by multi-variable regression and novel Genetic Algorithm based on the most influential parameters”, *Civil Engineering Infrastructures Journal*, 54(2), 267-280.
- Yasi, B. and Mohammadizadeh, M.R. (2018).

- “Identification of structural defects using computer algorithms”, *Civil Engineering Infrastructures Journal*, 51(1), 55-86.
- Yin, P., Huang, L., Yan, L. and Zhu, D. (2015). “Compressive behavior of concrete confined by CFRP and transverse spiral reinforcement. Part A: experimental study”, *Materials and Structures*, 49(3), 1001–1011.
- Zeng, J.J., Guo, Y.C., Gao, W.Y., Li, J.Z. and Xie, J.H. (2017). “Behavior of partially and fully FRP-confined circularized square columns under axial compression”, *Construction and Building Materials*, 152, 319-332.
- Zhou, D., Gao, X., Liu, G., Mei, C., Jiang, D. and Liu, Y. (2011). “Randomization in particle swarm optimization for global search ability”, *Expert Systems with Applications*, 38(12), 15356-15364.



This article is an open-access article distributed under the terms and conditions of the Creative Commons Attribution (CC-BY) license.



A Laboratory Study on the Potentiodynamic Polarization and Transport Properties of Binary Concrete with Silica Fume and Zeolite

Sobhani, J.^{1*}, Najimi, M.² and Pourkhorshidi, A.R.³

¹ Associate Professor, Department of Concrete Technology, Road, Housing and Urban Development Research Center (BHRC), Tehran, Iran.

² Ph.D., Department of Civil, Construction and Environmental Engineering, Iowa State University, Ames, Iowa, USA.

³ Ph.D. Candidate, Department of Concrete Technology, Road, Housing and Urban Development Research Center (BHRC), Tehran, Iran.

© University of Tehran 2021

Received: 16 Jun. 2020;

Revised: 07 Jun. 2021;

Accepted: 12 Jun. 2021

ABSTRACT: The current study aims to investigate influence of w/cm ratio, cementitious materials content and supplementary cementitious materials on the transport properties of concrete and chloride-induced corrosion rate of reinforcement. To do this, several mixes are designed with and without silica fume and natural zeolite as supplementary cementitious materials, w/cm of 0.4 and 0.5, and cementitious materials contents of 325 and 400 kg/m³. These mixes are subjected to evaluation of compressive strength, transport properties (i.e. absorption, water penetration depth and rapid chloride penetration test), and corrosion rate measurement through Potentiodynamic test and electrochemical measurements. The results of this study reveal that there is not strong correlation between corrosion rate of reinforcement and the measured strength and transport properties. The corrosion rate of reinforcement significantly decreased through reduction of water-to-cementitious materials ratio and use of supplementary cementitious materials; of which w/cm showed a more considerable influence. Increase in cement content, however, increased the transportation of water and chloride into the concrete and thus increased the corrosion rate of reinforcement.

Keywords: Concrete, Corrosion, Silica Fume, Transport Properties, Zeolite.

1. Introduction

Concrete is known to be an extensively utilized material due to its adaptability, appropriate durability and mechanical properties (Tang et al., 2015), however, this material degrade when confronted the environmental attacks. However, the most important failure of reinforced concrete structures is related to the chloride-induced

corrosion of reinforcements (Montemor et al., 2003; Hooton, 2019; Glass and Buenfeld, 2000; Manera et al. 2008; Cao et al., 2019; Rodrigues et al., 2021; Tangtakabi et al., 2021). Many defects due to reinforcement corrosion have been reported in concrete bridges, marine piers, and other strategic reinforced concrete structures exposed to chloride ions (Tarighat and Jalalifar, 2014; Cavaco et al.,

* Corresponding author E-mail: ja_sobhani@yahoo.com

2017; Navarro et al., 2018; ACI 222R, 2019).

Penetration of chloride ions due to the de-icing salts, marine environments, and chloride ions in concrete constituents such as aggregates or water are of the major causes of corrosion (Kirkpatrick et al., 2002; Lindquist et al., 2006; Chen et al., 2021; Qu, et al. 2021).

The corrosion of concrete structures and related repairs leads to huge costs. Enormous annual costs are spent on renovation, repairs, and traffic delays due to corrosion on reinforced concrete bridges in North America (Kirkpatrick et al., 2002; Lindquist et al., 2006; Liang and Wang, 2020).

Available statistics showed that 25 to 40 percent of concrete bridges in Norway, US and UK, corrode annually and needed for repair programs with costly budgets (Webster, 2000). In south costal line of Iran the most concrete structures suffer the corrosion problems.

A number of these structures have essentially become nonfunctional due to chloride-induced corrosion of reinforcements. As such, investigating corrosion of reinforcement in concrete, recognizing parameters affecting the corrosion rate, and finding solutions to improve corrosion resistance of reinforced concrete structures have not been more urgent (Sanchez et al., 2017; Oliveira and Cascudo, 2018).

While several factors influence properties of concrete and thus the protection that concrete provides for the reinforcement, it is well defined in the literature that w/cm ratio, cement content,

and supplementary cementitious materials (SCMs) like silica fume, fly ash, slag are the governing factors that can affect physical, mechanical and durability (Malhotra and Mehta, 1996; Gu et al., 2000; Madani et al. 2016; Samimi et al., 2017; Nguyen et al., 2020). SCMs can lead to reduction in chloride-ion penetration into concrete (Mangat and Molloy, 1991; Choia et al., 2006; Boğaa and Topçub, 2012; Ahmadi et al., 2014; Tang et al., 2015). For this reason, a superior corrosion resistance of the steel reinforcement in these concretes is expected (Glass and Buenfeld, 2000). The content of SCM is also important parameter which can improve the mechanical and durability properties of concrete (Choia et al., 2006; Boğaa and Topçub, 2012).

In pursuit of the above mentioned need for investigate the effective parameters on corrosion of reinforcement; this paper evaluates the influence of w/cm ratio, cementitious materials content and silica fume and natural zeolite on corrosion rate of reinforcement.

2. Experimental Detail

2.1. Materials

Type I Portland cement as a plain binder, silica fume and natural zeolite as SCM (secondary binders), fine and coarse aggregates, High Range Water Reducer (HRWR), and tap water. The properties of the used binders are presented in Tables 1-3. The used silica fume contained 87% silica with few percentages of calcium oxide, alumina, iron oxide and magnesium oxide. Natural zeolite confirms the requirement of ASTM C 618.

Table 1. Chemical composition of cementitious materials

Chemical analysis (%)	Portland cement-Type I	Silica fume	Natural zeolite
Calcium oxide (CaO)	63.00	2.24	1.68
Silica (SiO ₂)	21.95	87.26	67.79
Alumina (Al ₂ O ₃)	4.35	1.5	13.66
Iron oxide (Fe ₂ O ₃)	3.80	3.80	1.44
Magnesium oxide (MgO)	2.00	2.00	1.2
Sodium oxide (Na ₂ O)	0.30	--	2.04
Potassium oxide (K ₂ O)	0.77	--	1.42
Sulfur trioxide (SO ₃)	2.43	0.11	0.52

Table 2. Mechanical and physical properties of Portland cement

Compound/Property (Unit)	Value
Tricalcium silicate (C ₃ S) (%)	48.07
Dicalcium silicate (C ₂ S) (%)	26.67
Tricalcium aluminate (C ₃ A) (%)	2.43
2 day compressive strength (MPa)	10.80
3 day compressive strength (MPa)	18.75
7 day compressive strength (MPa)	21.15
28 day compressive strength (MPa)	34.30
Initial setting time (min)	181
Final setting time (min)	268
Specific surface (m ² /kg)	315
Specific gravity (g/cm ³)	3.15
Loss on ignition (%)	1.71
Insoluble residue (%)	0.68
Autoclave expansion (%)	0.40

Table 3. Chemical and physical properties of natural zeolite according to ASTM C618

Requirements		Class N, Natural pozzolan, ASTM C618	Natural zeolite (clinoptilolite)
Chemical requirements	SiO ₂ +Al ₂ O ₃ +Fe ₂ O ₃ (%)	min, 70.0	82.89
	Sulfur trioxide (SO ₃) (%)	max, 4.0	0.52
	Moisture content (%)	max, 3.0	2.9
	Loss on ignition (%)	max, 10.0	9.85
Physical requirements	Amount retained when wet-sieved on 45 μm sieve (%)	max, 34	28
	¹ Strength activity index, at 7 days (percent of control)	min, 75	120
	¹ Strength activity index, at 28 days (percent of control)	min, 75	127
	Water requirement (percent of control)	max, 115	114
² Pozzolanic activity (%)	Autoclave expansion or contraction (%)	max, 0.8	0.02
	8 days	-	45.8
	30 days	-	54.3

¹Note that, the strength activity index was determined based on ASTM C311 by replacing 20% of Portland cement with natural zeolite; ² Pozzolanic activity was measured through thermo-gravimetric analysis by combining 50% natural zeolite with 50% Ca(OH)₂ powder.

The higher Pozzolanic activity of silica fume can be related to its lower particle size (see Figure 1 for particle size distribution of cementitious materials) and higher content of reactive silica (shown in Table 3).

The properties of utilized aggregates is presented in Table 4. A HRWR polycarboxylate-based was also used to maintain a constant slump of 65 ± 15 mm for all the studied concrete mixes.

2.2. Mixture Proportions

Table 5 summarizes mixture proportions

of the selected concretes. As this study was aimed to assess the effects of influential parameters on the corrosion rate of reinforcement in mixtures, the designed concretes included concrete mixtures with w/cm of 0.4 and 0.5, cementitious materials content of 325 and 400 kg/m³, and two sources of supplementary cementitious materials, i.e. silica fume and natural zeolite. Table 5 is divided into two groups of mixes: 1) normal concrete mixes having normal cement as a sole binder, and 2) mixes containing Portland cement as the

primary binder and SCMs as the secondary binder; which labeled as binary mixes. Normal mix NC.5-325 was assigned as the reference mix containing 325 kg/m³ Portland cement and w/cm of 0.5. Normal concrete mixes NC.4-325, NC.5-400, and NC.4-400 were designed without use of SCMs to evaluate the influence of cementitious material content and w/cm on the corrosion rate. Binary mixes SC.5-325, SC.4-325, SC.5-400 and SC.4-400 were designed similar to normal mixes, but by replacing 7.5% with silica fume. Binary

mixes NZL.5-325 and NZH.5-325 contained 15 and 30% natural zeolite.

As mentioned earlier, different amounts of HRWR was used to keep the constant flow for all the selected mixes. In Table 5, reducing w/cm or replacing cement with SCMs increased the demand for HRWR. Increases in the cementitious materials content, however, decreased the used amount of HRWR which could be related to the higher amount of water in the mix when cementitious materials content increases for a constant w/cm.

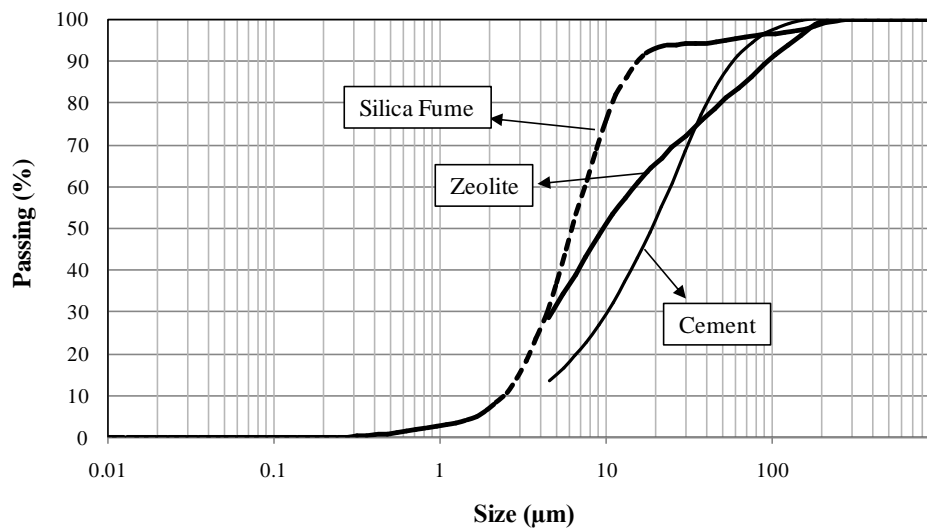


Fig. 1. Particle size distribution of cementitious materials

Table 4. Aggregate properties

Aggregate type	Specific gravity	Absorption (%)	Passing sieve #200 (75 μm) (%)
Fine aggregates (0 - 4.75 mm)	2.46	2.50	2.37
Coarse aggregates (4.75 - 19 mm)	2.56	2.17	--

Table 5. Mixture proportions of the selected concretes

Mix ID	Cement (kg/m ³)	Silica fume (kg/m ³)	Natural zeolite (kg/m ³)	w/cm	Water (kg/m ³)	Fine aggregate (kg/m ³)	Coarse aggregate (kg/m ³)	HRWR (% of cementitious materials content)
Normal mixes								
NC.5-325 (Reference)	325	0	0	0.50	162.5	885.4	901.2	0.261
NC.4-325	325	0	0	0.40	130	918.3	933.9	0.426
NC.5-400	400	0	0	0.5	200	953.3	786	0.071
NC.4-400	400	0	0	0.4	160	953.3	786	--
Binary mixes								
SC.5-325	300.6	24.4	0	0.50	162.5	885.4	901.2	0.502
SC.4-325	300.6	24.4	0	0.40	130	915.5	930.8	0.824
SC.5-400	370	30	0	0.5	200	953.3	786	0.357
SC.4-400	370	30	0	0.4	160	953.3	786	0.424
NZL.5-325	276.3	0	48.7	0.5	162.5	877	877	0.433
NZH.5-325	227.5	0	97.5	0.5	162.5	870	870	1.146

-- : No data recorded.

2.3. Corrosion Test Setup and Electrochemical Measurements

Specimens (Cylindrical) with size of 85 (diameter) \times 200 (height) mm were utilized for electrochemical investigations. Two reinforcing bars (with diameter of 10 mm) included in specimens as reinforcing bars (Figure 2). For test measurement, reinforced specimens were cast and stored in wet-curing for 28 days in saturated limewater. Then, specimens were subjected to cyclic-pondings comprising two-weeks of exposure to sodium chloride solution (5% NaCl by weight) followed by two weeks in dry condition. At different ages of pondings, Potentiodynamic test was conducted to measure the corrosion rate of rears in specimens.

The setup utilized in this research, is a simulation of a “cored reinforced concrete specimen” of concrete structure element which an inspector engineer, might be gained from a real structure. In the used setup, it can be seen a “near-to-real” simulation of such petrochemical system.

3. Experimental Results

3.1. Compressive Strength

Table 6 summarizes the compressive strength test results of the selected mixes at the age of 28 and 90 days (150 \times 300 mm cylindrical specimens). The compressive strength increased when w/cm decreased, cementitious materials content increased, or

a portion of PC was replaced with silica fume. The improvements due to increases in cementitious materials content was less significant compared to those observed by use of silica fume and reduction in w/cm. Use of natural zeolite, however, resulted in slight decreases in the compressive strength; particularly at the age of 28 days.

For mixtures without SCM, except NC.4-325, almost 85% of 90-day compressive strength was achieved in 28 days. For SC concrete, except SC.4-325, almost 95% of 90-day compressive strength was gained in 28 days. For NZH.5-325, 70% of 90-day compressive strength was developed at 28 days highlighting late pozzolanic reactivity of natural zeolite (Shekarchi et al., 2012). Low dosage natural zeolite worked like the regular concrete without SCM.

Decreases in w/cm from 0.5 to 0.4 led to 42.9 and 28.5% improvements in 28-day compressive strength of normal concrete having 325 and 400 kg/m³ of Portland cement, respectively. These enhancements were respectively 31.2 and 25.2 % at the age of 90 days. The improvements due to the reduction in w/cm were lower for silica fume contained concretes. When w/cm reduced from 0.5 to 0.4, the compressive strength of silica fume contained concrete improved averagely 22% and 10% for mixes having cementitious materials content of 325 and 400 kg/m³, respectively.

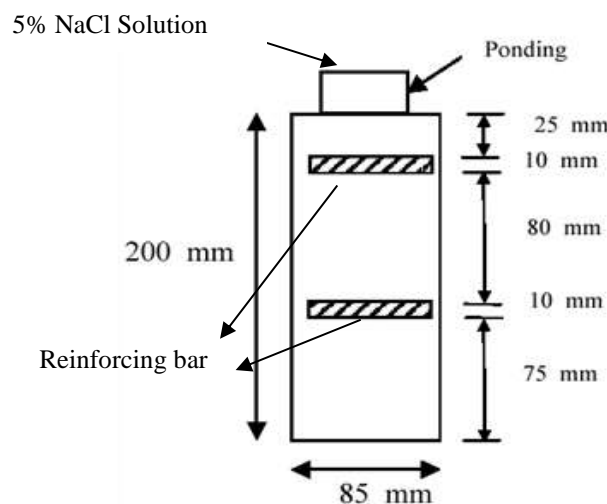


Fig. 2. Schematic of ponding test setup for reinforced concrete specimens

Table 6. Compressive strength and transport properties

Mix ID	Compressive strength (MPa)		Water penetration depth (mm)		24 h-Water absorption (%)		Chloride ion penetration (C)	
	28 days	90 days	28 days	90 days	28 days	90 days	28 days	90 days
Normal mixes								
NC.5-325 (Ref)	23.8	28.2	17.3	15.7	7.5	7.0	7863	6848
NC.4-325	34.0	37.0	15.8	13.1	4.5	4.9	2484	1624
NC.5-400	27.0	31.7	15.7	13.3	8.2	6.8	7120	7521
NC.4-400	34.7	39.7	13.3	12.5	6.6	6.7	7174	5494
Binary mixes								
SC.5-325	35.5	36.4	15.6	12.7	7.2	6.0	1757	1043
SC.4-325	40.1	47.8	12.7	11.3	4.2	4.7	1024	718
SC.5-400	42.7	44.8	11.6	11.0	6.7	6.7	1534	1541
SC.4-400	46.3	49.6	12.0	11.3	5.1	6.1	1093	1157
NZL.5-325	23.1	27.4	13.5	11.5	8.0	8.0	1914	958
NZH.5-325	18.1	26.2	9.5	10.5	7.8	7.6	572	408

The mentioned improvements were average of improvements in 28 and 90 days. An increase in cementitious materials contents from 325 to 400 kg/m³ resulted in averagely 13 and 22% increases in compressive strength of normal and silica fume contained concrete having w/cm of 0.5, respectively. These enhancements were averagely 5 and 10% for w/cm of 0.4, respectively.

Use of silica fume as a supplementary cementitious material led to significant improvements in the compressive strength of the selected concretes. On contrary, use of natural zeolite resulted in a slight decrease in compressive strength at the age of 28 days. Silica fume contained concretes produced averagely 54 and 26% higher 28-day compressive strength than those of normal concrete for w/cm of 0.5 and 0.4, respectively. In the case of natural zeolite contained concrete, the 28-days compressive strength of mixes containing 15 and 30% natural zeolite were 3 and 24% lower than that of reference concrete, respectively. Once curing age extended to 90 days, natural zeolite contained mixes produced similar strength to that of reference concrete. This behavior can be related to the late pozzolanic activity of natural zeolite at later ages. The 90-day compressive strength of silica fume contained concretes were 27 to 35% higher than that of normal concretes.

3.2. Transport Properties

Transport properties of the selected concretes were evaluated through measurements of water penetration depth as per BS EN 12390-8, water absorption according to BS 1881-122 and rapid chloride penetration based on ASTM C1202. Table 6 documents the results of transport properties. Generally speaking; reduction in w/cm and use of SCMs were effective in improving transport properties of the selected concretes. The observed improvements were more significant when w/cm was reduced than when a portion of cement was replaced by SCMs. Increases in cementitious materials content was only effective in improving water penetration depth of the selected concretes.

Water penetration depth was measured on 15 cm cubic specimens by applying water under pressure of 0.5 MPa for 3 days. Overall, the penetration depth was slightly decreased by reduction in w/cm, use of higher cementitious materials content and partial replacement of Portland cement with SCMs. Use of SCMs was, however, the most effective factor in improving (i.e. decreasing) water penetration depth into the concrete. The penetration depths of silica fume contained mixes were up to 26% (averagely 15.6%) lower than those of normal concrete mixes for similar w/cm and cementitious materials content. Binary mixes containing 15 and 30% natural zeolite presented averagely 24 and 39%

lower penetration depth than those of reference mix, respectively. For the cementitious materials content of 325 kg/m^3 , reduction in w/cm from 0.5 to 0.4 improved water penetration depth of normal and silica fume contained concrete by averagely 14%. In the case of normal concrete having cementitious materials content of 400 kg/m^3 , the reductions due to the decreases in w/cm were about 15 and 6% at the age of 28 and 90 days, respectively. For the similar cementitious materials content (i.e. 400 kg/m^3), this reduction in w/cm resulted in almost 3% increase in penetration depth of silica fume contained concretes. Increases in cementitious materials content also improved the water permeability of the selected concretes. The water penetration depth of the selected mixes improved by averagely 10% when cementitious materials content increased from 325 to 400 kg/m^3 .

Decreases in w/cm led to more considerable improvements in water absorption of the selected concretes. On average, water absorption of normal and silica fume contained concretes decreased by averagely 33.4 and 13.2%, respectively, when w/cm was reduced from 0.5 to 0.4. Increases in cementitious materials content, however, resulted in increase in water absorption; in particular, for concretes having w/cm of 0.4. Water absorption of concretes (normal and silica fume contained mixes) having w/cm of 0.4 was increased by averagely 34% with increases in cementitious materials content. For w/cm of 0.5, water absorption did not change by the increases in cementitious materials content. Application of SCMs did not show significant effect in water absorption of the selected concretes. Water absorption of silica fume contained concretes were averagely 10% lower than that of normal concretes. On the other hand, natural zeolite contained concretes produced averagely 8% higher water absorption than that of reference concrete.

Rapid Chloride Penetration Test (RCPT) was conducted on 10 cm diameter by 5 cm

height disks per ASTM C1202. The charge passed through concrete disks significantly reduced by use of SCMs. The passing charges of binary mixes containing silica fume was 56 to 85% (averagely 75%) lower than those of normal concrete. A similar reduction was observed by use of natural zeolite in percentages higher than silica fume. Mixes NZL.5-325 and NZH.5-325 had almost 80% lower RCPT value than that of reference mix. Use of higher cementitious materials content resulted in averagely 66% increases in RCPT results of the selected mixes. The increases were more magnified for mixes with w/cm of 0.4 than mixes with w/cm of 0.5, and for normal concretes than silica fume contained concretes. As RCPT is related to the movements of different ions; in particular hydroxyls (OH^-), the observed increases by use of higher cementitious materials content can be related to production of higher calcium hydroxide as a main production of Portland cement hydration. On the other hand, use of SCMs reduces RCPT passing charges through 1) consumption of hydroxyls; and 2) production of more C-S-H by reactions with calcium hydroxide leading to lower permeability. Decreases in w/cm resulted in 72 and 36% reduction in RCPT of normal and silica fume contained mixes having 325 kg/m^3 of Portland cement, respectively. Lower reductions of averagely 13 and 27% were observed when cementitious materials content of 400 kg/m^3 was used.

3.3. Corrosion Rate Measurements

Potentiodynamic polarization curves were obtained at a scan rate of 0.1667 mV/s using a four electrode arrangement shown in Figure 3. Solartron 1287 electrical interface and associated software CorrWare were utilized to control the test procedures and analyze the data (see Figure 3). A Hg/HgSO_4 in saturated K_2SO_4 solution (0.64 V/NHE) and platinum bar were used as reference and counter-electrodes, respectively (RE and SE in Figure 3). Reinforcing rebar as working electrode was

connected to WE terminal as depicted in Figure 3.

Using the results of potentiodynamic polarization test, corrosion rate of reinforcement embedded in the selected concrete mixes were estimated. Table 7 documents the corrosion rate and corrosion current density of reinforcement at various ages of testing. The one-year reinforcement' corrosion rate for the selected mixes is also presented in Figure 4. Generally, decreases in w/cm and use of SCMs reduced the corrosion rate of the reinforcement. These improvements were more significant for w/cm than for those related to the use of SCMs. Increase in cement content, however, resulted in increases in the corrosion rate of reinforcement.

Reductions in w/cm from 0.5 to 0.4 led to significant reduction in corrosion rate of reinforcement. For normal concretes, the reduction in w/cm resulted in averagely 75,

77 and 89% reduction in 180, 270, and 365-day corrosion rates, respectively. For the same ponding ages of 180, 270 and 365 days, the improvements due to reduction in w/cm were averagely 72, 75 and 92% for silica fume contained concretes, respectively.

Use of supplementary cementitious materials, in particular silica fume, was also useful in improving (i.e. reducing) the corrosion rates. The 180, 270, and 365-day corrosion rates of reinforcement embedded in silica fume contained concrete mixes were averagely 68, 38 and 30% lower than those embedded in normal concrete mixes, respectively. Replacing 15 and 30% of cement with natural zeolite led to 63 and 90% reduction in 180-day corrosion rate, respectively. This reduction was 64% at 270 day by use of 30% natural zeolite as SCMs, while 270-day corrosion rate of NZL.5-325 was higher than that of reference concrete.

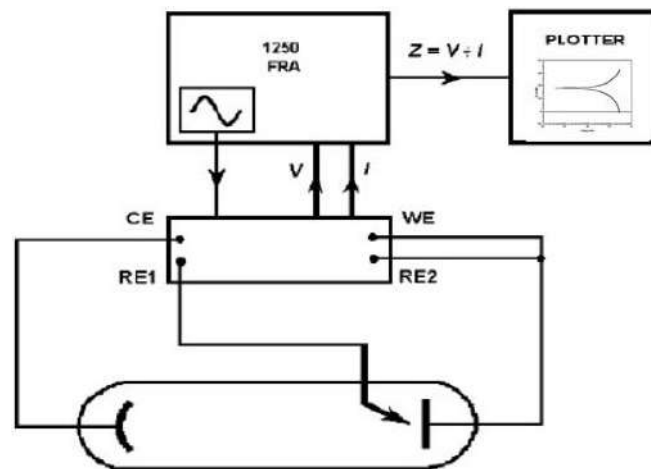


Fig. 3. Schematic of four electrode setup for electrochemical measurements

Table 7. Corrosion rate and current density based on potentiodynamic polarization test

Mix ID	Corrosion rate (mm/yr)			Corrosion current density (mA/cm ²)		
	180 days	270 days	365 days	180 days	270 days	365 days
Normal mixes						
NC.5-325 (Reference)	0.313	0.120	0.077	0.0270	0.0104	0.0066
NC.4-325	0.078	0.028	0.005	0.0067	0.0024	0.0004
NC.5-400	--	0.112	0.175	--	0.0097	0.0151
NC.4-400	0.169	--	0.028	0.0146	--	0.0024
Binary mixes						
SC.5-325	0.087	0.065	0.058	0.0075	0.0056	0.0050
SC.4-325	0.031	0.017	0.004	0.0027	0.0015	0.0003
SC.5-400	0.236	0.079	0.139	0.0204	0.0068	0.0120
SC.4-400	0.050	0.019	0.013	0.0043	0.0016	0.0011
NZL.5-325	0.114	0.182	--	0.0098	0.0157	--
NZH.5-325	0.032	0.043	--	0.0028	0.0037	--

Note: -- means no data recorded or failed measurement

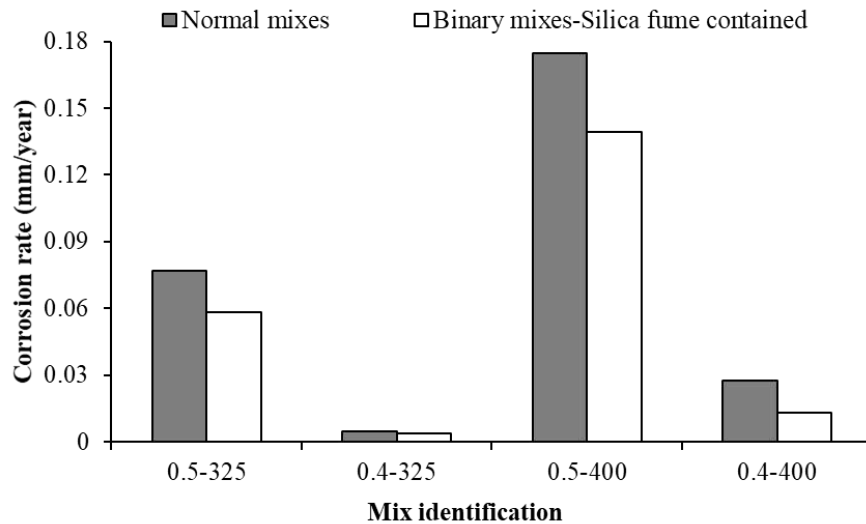


Fig. 4. One-year reinforcement' corrosion rate of the selected mixes measured by potentiodynamic polarization

Increases in cementitious materials content, however, increased the corrosion rate of reinforcement. On average, the reinforcement corrosion rate of normal and silica fume contained concrete mixes having cementitious materials content of 400 kg/m^3 were 2.8 and 2.1 times of those mixes having cementitious materials content of 325 kg/m^3 , respectively. The best combination was when w/cm reduced and a portion of Portland cement was replaced with silica fume. The corrosion rates of NC.5-325 and NC.5-400 (average of 180, 270 and 365 days) were almost as 14 and 10 times of those of SC.4-325 and SC.4-400, respectively.

It is worth mentioning that effect of age of ponding on the corrosion was not discussed due to the different condition of samples at the time of testing. The reason is that concretes were in different conditions of full or empty dike at different ages; i.e. 180 days (full dike), 270 and 365 days (empty dike). As such, the difference between the trends in different ages could be related to the above-mentioned fact.

Table 8 shows the correlation factor between corrosion rate and the measured strength and transport properties. As expected there is an inverse relationship between corrosion rate and compressive strength. Although it's not a strong relationship which means that compressive strength cannot be a proper indicator for the

evaluation of chloride-induced corrosion resistance of concrete. The corrosion rate of reinforcement showed direct relationship with the measured transport properties. The relationships, however, were not strong enough to be used as direct indices for prediction of corrosion rate of reinforcement in concrete. It can be particularly seen that the results of rapid chloride penetration test cannot be justified as an index for chloride-induced corrosion of reinforcement.

The direct relationship does not mean a strong correlation between rapid transport property tests and corrosion rate, but only showing that higher transport property led to higher penetration of chlorides and thus higher corrosion rate. From chemical point of view, the lower transport property is related to pozzolanic reactivity producing more C-S-H gel or silica fume acting as both pozzolans and nucleation sites which result in an improved pore system. Lower w/c also contributes physically to an improved pore system lowering the pore volume. An improved pore structure results in less chloride penetration and less chloride available at the level of reinforcement. It should be noted that while all these result in lower corrosion rate, the relationship is not strong and therefore, it is not easy to effectively predict the service life using transport property (Andrielli et al., 2018; Ramezani-pour et al., 2015).

Table 8. Correlation between corrosion rate and the measured strength and transport properties

	Compressive strength		Water penetration depth		Water absorption		Rapid chloride penetration test	
	28 days	90 days	28 days	90 days	28 days	90 days	28 days	90 days
Corrosion rate-180 days	-0.12	-0.22	0.46	0.65	0.43	0.34	0.74	0.78
Corrosion rate-270 days	-0.56	-0.64	0.33	0.32	0.76	0.73	0.48	0.42
Corrosion rate-365 days	-0.37	-0.43	0.15	0.17	0.80	0.66	0.38	0.52

4. Conclusions

The current study investigated influences of water-to-cementitious materials ratio, cementitious materials content and supplementary cementitious materials on the transport properties and corrosion rate of reinforcement in vibratory-placed concrete through testing reinforced concrete mixes having w/cm of 0.4 and 0.5, silica fume and natural zeolite as SCMs, and total cementitious materials content of 325 and 400 kg/m³. From the observations of this study, the following conclusions can be drawn:

- Overall, w/cm ratio and supplementary cementitious materials were more influential on the transport properties of the selected mixes compared to cementitious materials content. The studied transport properties (i.e. water absorption, water penetration depth and rapid chloride penetration) considerably improved by reduction of w/cm ratio and use of supplementary cementitious materials. Increases in cementitious materials content slightly reduced the water penetration depth of the selected concretes and increased water absorption and passing charges in rapid chloride penetration test.
- The corrosion rate of reinforcement significantly decreased through reduction of w/cm ratio and use of supplementary cementitious materials. These improvements were more significant when w/cm decreased than when SCMs were included. Increase in cement content increased the corrosion rate of reinforcement.
- The corrosion rate of reinforcement showed direct relationship with the measured transport properties. The relationships, however, were not strong

enough to be used as direct indices for prediction of corrosion rate of reinforcement in concrete.

5. Acknowledgment

The authors gratefully acknowledge the financial and laboratory supports from the Road, Housing and Urban Development Research Center (BHRC) of Iran.

6. References

- ACI (American Concrete Institute). (2019). *ACI 222R: Guide to protection of reinforcing steel in concrete against corrosion*, Farmington Hills (MI): American Concrete Institute, USA.
- Ahmadi, B., Sobhani, J., Shekarchi, M., Najimi, M. (2014). "Transport properties of ternary concrete mixtures containing natural zeolite with silica fume or fly ash", *Magazine of Concrete Research*, 66(3), 150-158.
- Boğaa, A.R. and Topçub, İ.B. (2012). "Influence of fly ash on corrosion resistance and chloride ion permeability of concrete", *Construction and Building Materials*, 31, 258-264.
- Cao, Y., Gehlen, C., Angst, U., Wang, L., Wang, Z. and Yao, Y. (2019). "Critical chloride content in reinforced concrete, An updated review considering Chinese experience", *Cement and Concrete Research*, 117, 58-68.
- Cavaco, E.S., Bastos, A. and Santos, F. (2017). "Effects of corrosion on the behaviour of precast concrete floor systems", *Construction and Building Materials*, 145, 411-418.
- Chen, S., Duffield, C. Miramini, S., Raja, B.N.K. and Zhang, L. (2021). "Life-cycle modelling of concrete cracking and reinforcement corrosion in concrete bridges: A case study", *Engineering Structures*, 237(15), 112143.
- Choia, Y.S., Kima, J.G. and Leeb, K.M. (2006). "Corrosion behavior of steel bar embedded in fly ash concrete", *Corrosion Science*, 48(7), 1733-1745.
- Glass, G.K. and Buenfeld, N.R. (2000). "Chloride-induced corrosion of steel in concrete", *Progress in Structural Engineering*, 2(4), 448-458.
- Gu, P., Beaudoin, J.J. and Zhang, M.H. and Malhotra, V.M. (2000). "Performance of reinforcing steel in concrete containing silica fume and blast-furnace slag ponded with sodium-

- chloride solution”, *ACI Materials Journal*, 97(3), 254-262.
- Hooton, R.D. (2019). “Future directions for design, specification, testing, and construction of durable concrete structures”, *Cement and Concrete Research*, 124, 105827.
- Kirkpatrick, T.J., Weyers, R.E., Sprinkel, M.M. and Anderson-Cook, C.M. (2002). “Impact of specification changes on chloride-induced corrosion service life of bridge decks”, *Cement and Concrete Research*, 32(8), 1189-1197.
- Liang, Y. and Wang, L. (2020). “Prediction of corrosion-induced cracking of concrete cover: A critical review for thick-walled cylinder models”, *Ocean Engineering*, 213(1), 107688.
- Lindquist, W.D., Darwin, D., Browning, J. and Miller, G.G. (2006). “Effect of cracking on chloride content in concrete bridge decks”, *ACI Materials Journal*, 103(6), 467-473.
- Madani, H., Ramezani-pour, A.A., Shahbazinia, M., Bokaeian, V. and Ahari, S.H. (2016). “The influence of ultrafine filler materials on mechanical and durability characteristics of concrete”, *Civil Engineering Infrastructures Journal*, 49(2), 251-262.
- Malhotra, V.M. and Mehta, P.K. (1996). *Pozzolanic and cementitious materials*, Taylor & Francis.
- Manera, M., Vennesland, O. and Bertolini, L. (2008). “Chloride threshold for rebar corrosion in concrete with addition of silica fume”, *Corrosion Science*, 50, 554-560.
- Mangat, P.S. and Molloy, B.T. (1991). “Influence PFA, slag and microsilica on chloride induced corrosion of reinforcement in concrete”, *Cement and Concrete Research*, 21, 819-834.
- Montemor, M.F., Simoes, A.M.P. and Ferreira, M.G.S. (2003). “Chloride-induced corrosion on reinforcing steel: form the fundamentals to the monitoring techniques”, *Cement Concrete Composites*, 25, 491-502.
- Navarro, I.J., Yepes, V., Martí, J.V. and González-Vidoso, F. (2018). “Life cycle impact assessment of corrosion preventive designs applied to prestressed concrete bridge decks”, *Journal of Cleaner Production*, 196(20), 698-713.
- Nguyen, C.V., Lambert, P. and Bui, V.N. (2020). “Effect of locally sourced pozzolan on corrosion resistance of steel in reinforced concrete beams”, *International Journal of Civil Engineering*, 18, 619-630.
- Oliveira, A.M. and Cascudo, O. (2018). “Effect of mineral additions incorporated in concrete on thermodynamic and kinetic parameters of chloride-induced reinforcement corrosion”, *Construction and Building Materials*, 192, 467-477.
- Qu, F., Li, W., Dong, W., Tam, V.W.Y. and Yu, T. (2021). “Durability deterioration of concrete under marine environment from material to structure: A critical review”, *Journal of Building Engineering*, 35 102074
- Ramezani-pour A.A., Rezaei H.R. and Savoj, H.R. (2015). “Influence of silica fume on chloride diffusion and corrosion resistance of concrete—a review”, *Asian Journal of Civil Engineering*, 16, 301-321.
- Rodrigues, R., Gaboreau, S., Gance, J., Ignatiadis, I. and Betelu, S. (2021). “Reinforced concrete structures: A review of corrosion mechanisms and advances in electrical methods for corrosion monitoring”, *Construction and Building Materials*, 269, 121240
- Samimi, K., Kamali-Bernard, S., Maghsoudi, A., Maghsoudi, M. and Siad, H. (2017). “Influence of pumice and zeolite on compressive strength, transport properties and resistance to chloride penetration of high strength self-compacting concretes”, *Construction and Building Materials*, 151, 292-311.
- Sanchez, J., Fulla, J. and Andrade, C. (2017). “Corrosion-induced brittle failure in reinforcing steel”, *Theoretical and Applied Fracture Mechanics*, 92, 229-232.
- Shekarchi, M, Ahmadi, B. and Najimi M. (2012) “Use of natural zeolite as Pozzolanic material in cement and concrete composites”, In: V.J. Inglezakis and A.A. Zorpas (eds.) *Handbook of Natural Zeolite*, Bentham Science, 30, 665-694.
- Tang, S.W., Yao, Y., Andrade, C. and Li, Z.J. (2015). “Recent durability studies on concrete structure”, *Cement and Concrete Research*, 78 (A), 143-154.
- Tangtakabi, A., Ramesht, M.H., Golsoorat Pahlaviani, A., Pourrostan, T. (2021). “Assessment of corrosion in offshore R.C. piers and use of microsilica to reduce corrosion induced oxidation (A case study of wharves 11 and 12 in Imam Khomeini Port-IRAN)”, *Civil Engineering Infrastructures Journal*, November 2021, (in press), DOI: 10.22059/CEIJ.2021.325670.1761.
- Tarighat, A. and Jalalifar, F. (2014). “Assessing the performance of corroding RC bridge decks: A critical review of corrosion propagation models”, *Civil Engineering Infrastructures Journal*, 47(2), 173-186.
- Webster, M.P. (2000). “Assessment of corrosion-damaged concrete structures”, PhD Thesis, The University of Birmingham, UK.
- Wu, F., Gong, J.H. and Zhang, Z. (2014). “Calculation of corrosion rate for reinforced concrete beams based on corrosive crack width”, *Journal of Zhejiang University SCIENCE A*, 15, 197-207.



This article is an open-access article distributed under the terms and conditions of the Creative Commons Attribution (CC-BY) license.



Development of the Fragility Curves for Conventional Reinforced Concrete Moment Resistant Frame Structures in Qods Town, Qom City, Iran

Dehghani, E.^{1*} and Soltanimohajer, M.²

¹ Associate Professor, Faculty of Civil Engineering, University of Qom, Qom, Iran.

² M.Sc. Student, Faculty of Civil Engineering, University of Qom, Qom, Iran.

© University of Tehran 2021

Received: 13 Jul. 2020;

Revised: 24 Jan. 2021;

Accepted: 30 Jan. 2021

ABSTRACT: In the Second World Conference on Disaster Risk Reduction (WCDRR) the concept of resilience has been presented as an Effective Strategy to improve post-earthquake conditions. One of the principles of resilience is “quick response”, which requires having relevant information to determine the level of vulnerability of the city. For this purpose, many studies have been done in recent years to investigate the seismic behavior of a variety of infrastructures in a city. The fragility curve is one of the most popular tools among researchers to investigate the probabilistic seismic behavior of structures. It expresses the degree of structural vulnerability by indicating the exceedance probability of damage versus the given level of ground shaking. In this study, 24 fragility curves are developed for four typical intermediate Reinforced Concrete Moment Resistant Frame structures in Qods town (located in Qom, Iran) with two number of stories (4 and 8) and two number of bays (1 and 2). They are derived through nonlinear incremental dynamic analysis in one and two horizontal directions under two sets of near-field and far-field ground motion records. The results indicate that the seismic response of structures is the same for uni-directional and bi-directional analyses. Also, it seems that the response of the structures with periods greater than 1 sec is in correlation with the mass-to-stiffness ratio. Change in the width and number of bays of the structure does not affect the probability of failure, as far as the width to the number of bays ratio remains constant. Furthermore, the probability of failure is higher when the structure is subjected to near-field earthquake ground motion records.

Keywords: Damage Evaluation, Fragility Curve, Incremental Dynamic Analysis, Reinforced Concrete Moment Resistant Frame, SAP2000.

1. Introduction

Most of Iran's densely populated areas, which are located in the Alpine-Himalayan belt of China and a pressure zone due to the convergence of the two plates of Saudi Arabia and Eurasia, are considered as active tectonic zones. The occurrence of major

earthquakes in the history of seismicity in these areas has made Iran the sixth most earthquake-prone country in the world (Taghizade et al., 2009).

The past experiences from these devastating earthquakes show that one of the important factors in the extent of the damage in these events is the lack of

* Corresponding author E-mail: dehghani@qom.ac.ir

sufficient information on the level of damage and how it is distributed throughout the city in the early hours, which delays the initial measures and interferes with crisis management.

Seismic risk assessment of different types of structures in a city provides the necessary information to estimate the damage and its distribution throughout the city. It can increase the resilience of the city by reducing the time of reaction to earthquakes, better management of outreach capacities, and reduction of damage. To do this, various methods for calculating seismic risk have been developed by the American Council on Applied Technology (ATC-13, 1985) (Rojahn, 1985), the Peer Earthquake Engineering Research Center (PEER) (Cornell and Krawinkler, 2000; Moehle and Deierlein, 2004), the US Central Crisis Management Agency-National Institute of Building Sciences (FEMA-NIBS) (Whitman and et al., 1996). Among the proposed methods, fragility models have always been of interest to researchers and are considered as one of the effective tools in seismic risk assessment that are calculated and presented in different ways.

In recent years, several studies have been conducted in this field in Iran. Ahmadi-Pazoki et al. (2015) evaluated the fragility curves of the 3 and 6-story steel braced-frame buildings with and without infill panels for three levels of damage including Immediate Occupancy (IO), Life Safety (LS), and Collapse Prevention (CP). The probable damages and the related costs were estimated by using engineering economics methods in cost-benefit analysis, and the relationship between costs and damages for buildings with infill panel was proposed. Results showed that selecting a more appropriate limit state is more cost-efficient and the results are not sensitive to the minimum absorption rate and the structure's useful life.

Abdollahzadeh et al. (2015) investigated the seismic risk of a special truss moment-frame structure located in Tehran by

developing fragility curves using the capacity spectrum method. The seismic hazard of the study area was described by using a reduced elastic response spectrum with a damping ratio of 5%. The results of this study showed that the special truss moment-frame with a Vierendeel middle panel suffered extensive damage due to buckling and early fracture of truss web members as well as special truss moment-frames with an X-diagonal middle members segment due to low seismic capacity.

Mohsenian et al. (2017) evaluated the seismic sensitivity of tunnel-form buildings with 5 and 10 stories to in-plan one-way mass eccentricity and determined the level of performance of the buildings under the design earthquake for various mass eccentricities.

Kouhestanian et al. (2019) developed the fragility curves of 3, 5, and 8-storey Reinforced Concrete Moment Resistant Frame structures with a soft and very soft-story under the main earthquake record and subsequent earthquakes, to investigate the effect of irregularity and aftershocks. The analysis results showed that the effect of irregularity and aftershocks on the seismic vulnerability of the 5 and 8-story structures was more pronounced than the 3-story structure.

Pahlavan et al. (2019) studied the seismic performance of low, medium, and high-rise reinforced concrete buildings located in the north of Iran. In their study, based on the results of previous field research, two structural deficiencies, including the reduced strength of concrete and insufficient overlap length of column's longitudinal bars were considered as common practical defects in the studied structures. The fragility curves of the models were derived through nonlinear incremental dynamic analysis under 20 far-field earthquake records. The models were also retrofitted with the conventional method of steel jacket of the columns and their seismic damage was determined for different functional levels. Comparison of the median values of seismic fragility of

models with structural weakness and retrofitted models showed that the median values of seismic fragility were significantly increased in the retrofitted models.

Mobinipour et al. (2020) investigated the influence of pulse-type of earthquake records on the fragility curves of the Steel Special Moment Resisting Frames (SMRFs). The results indicated that the median value of the collapse capacity due to near-fault ground motions was 76% that of the far-fault records for the ten-story example SMRF.

In this paper 24 fragility curves have been developed, with the aims of predicting the seismic performance of conventional concrete structures in Qods town of Qom city. They have been derived through nonlinear incremental dynamic analysis in one and two horizontal directions under two sets of near-field and far-field ground motion records. The geographical location of the case study region is shown in Figure 1.

2. Modeling

In this study, after conducting field investigations in Qods town, the Reinforced Concrete Moment Resistant Frame structure with intermediate ductility is chosen as the conventional residential

building and is categorized into four groups:

- 4-story structure with a width of 6 meters (C406);
- 4-story structure with a width of 12 meters (C412);
- 8-story structure with a width of 6 meters (C806);
- 8-story structure with a width of 12 meters (C812).

The geometric characteristics of the case study structures are shown in Figure 2.

Due to the common construction practice adopted in this area, these structures are modeled in three dimensions using frame elements. The structures are designed based on the provisions of the fourth edition of the Iranian 2800 Code (BHRC, 2016) and ACI 318-14 (2014) specifications. The beam and column sections are determined between 30 and 60 cm in proportion and the ratio of longitudinal reinforcement has been calculated as 1 to 3% for columns and 0.35 to 1.5% for beams. The nonlinear behavior of materials is modeled by using concentrated plastic hinges in accordance with ASCE 41-13 (2014) specifications and the geometric nonlinearity of the structure (P-Delta) is considered by reducing the elements of the structure's stiffness matrix. The first and second natural period of vibration of each structure is reported in Table 1.



Fig. 1. Geographical location of the case study region

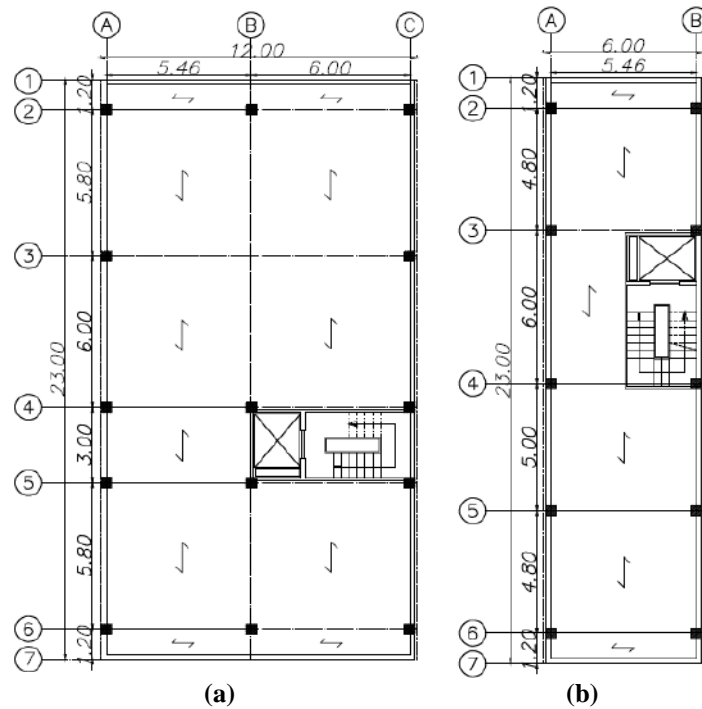


Fig. 2. Geometric characteristics of the case study structures: a) Four- and eight-story structures with a width of 12 m; and b) Four- and eight-story structures with a width of 6 m

Table 1. Natural period of vibration of building models

Building model	First mode period (sec)	Second mode period (sec)
C812	1.97	1.93
C806	1.94	1.9
C412	1.4	1.2
C406	1.2	1.19

The structures are subjected to 28 near-field and 22 far-field earthquake ground motion records adopted from FEMA p695 (2009). Two sets of analysis are performed; in the first set, the structures are subjected to the selected records in one direction (transverse), and in the second set, they are analyzed in two perpendicular directions simultaneously using incremental dynamic analysis.

3. Development of Fragility Curve

In order to develop the fragility curve, the structure drift ratio (Figure 3) and the Peak Ground Acceleration (PGA) have been selected as the parameters describing the seismic behavior of the structure (Damage Measure) and the intensity of the ground motion (Intensity Measure), respectively. The hunt and fill algorithm has been employed to determine the intensity levels. The damage states are selected according to

FEMA-356 (2006), IO, LS and CP. Structural performance levels and their corresponding damages for the concrete frame is reported in Table 2.

Table 2. Structural performance levels and damages for concrete frame (FEMA356, 2000)

Structural performance level	IO	LS	CP
Drift	1 %	2 %	4 %

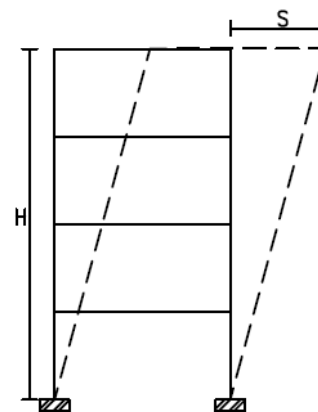


Fig. 3. Drift Ratio = δ/H , δ : is the roof relative displacement and H : is the height of the structure

The Lognormal Cumulative Distribution Function (CDF) is applied to the responses obtained from different records for a given seismic intensity to compute the probability of exceedance for each of the damage limit states as discrete. Finally, by using linear interpolation relationships, the fragility curve is obtained for each model. Eq. (1) shows the relationship between the fragility curve and the parameters used in this study.

$$\begin{aligned}
 P[D \geq Ds_i | IM = im] &= P[\text{Drift} \geq \text{Drift}(Ds_i) | PGA] \\
 &= 1 - P[\text{Drift} \leq \text{Drift}(Ds_i) | PGA] \\
 &= 1 - P \left[\Phi \left(\frac{\text{Ln}(\text{Drift}(Ds_i)) - \theta_d}{\beta_d} \right) \middle| PGA \right]
 \end{aligned}
 \tag{1}$$

where $P[A | B]$: is the conditional probability of A given B occurs, D : describes the uncertainty in damage state, IM : is the intensity measure, im : is a particular value of IM , Ds_i : is the damage state (IO, LS, CP), PGA : varies between 0.005g and 3g (0.005, 0.055, ...), $\Phi(s)$: is the standard normal cumulative distribution function, θ_d : is the mean natural logarithm of data, and β_d : is the standard deviation of the natural logarithm of data.

The software employed in this study is SAP2000, which has been augmented by the fragility curve code to perform incremental dynamic analysis.

4. Fragility Curve Code

In this study, the procedure of developing the fragility curve has been programmed in the MATLAB software. The “fragility curve code” algorithm is shown in Figure 4.

As can be seen in this figure, five parameters are received as input, including the initial step (S_0), the constant coefficient (S_x), the incremental coefficient (d_s), which are used to determine the intensity levels, and the height of the structure (H) and the node number (point name), which are used to extract the relative displacement of the user’s desired points. Then, the SAP2000 software is opened and the model is called.

The intensity levels are then determined using the hunt and fill algorithm and used to perform incremental dynamic analysis. The results of this part are saved in the response matrix and are used as the input of the fragility model in the next part. In the fragility model, the damage matrix is represented by the lognormal distribution and the user’s desired performance levels. Finally, the response curve and the fragility curve are drawn as the output of the second and third parts of the fragility code, respectively.

5. Results

In this study, 24 fragility curves are derived for four typical intermediate Reinforced Concrete Moment Resistant Frame structures. The analysis is carried out in one and two horizontal directions under two sets of near-field and far-field ground motion records. The structures are coded as follows for reference: C406, C412, C806, and C812 respectively denote the 4-story structure with a width of 6 m, 4-story structure with a width of 12 m, 8-story structure with a width of 6 m, and 8-story structure with a width of 12 m. The near-field and far-field records are presented with suffixes NF and FF, respectively, and the direction of the analysis is indicated by X, XY, and YX. In order to distinguish between the curves for different analyses, the aforementioned suffixes are added to the code name of the structures (Figure 5).

6. Results of Bi-Directional Analysis

In order to investigate the simultaneous effect of longitudinal and transverse components of earthquake records on structural vulnerability and also to identify the more vulnerable direction, longitudinal and transverse fragility curves obtained from the bi-directional analysis are compared with the transverse fragility curve obtained from uni-directional analysis as shown in Figure 6.

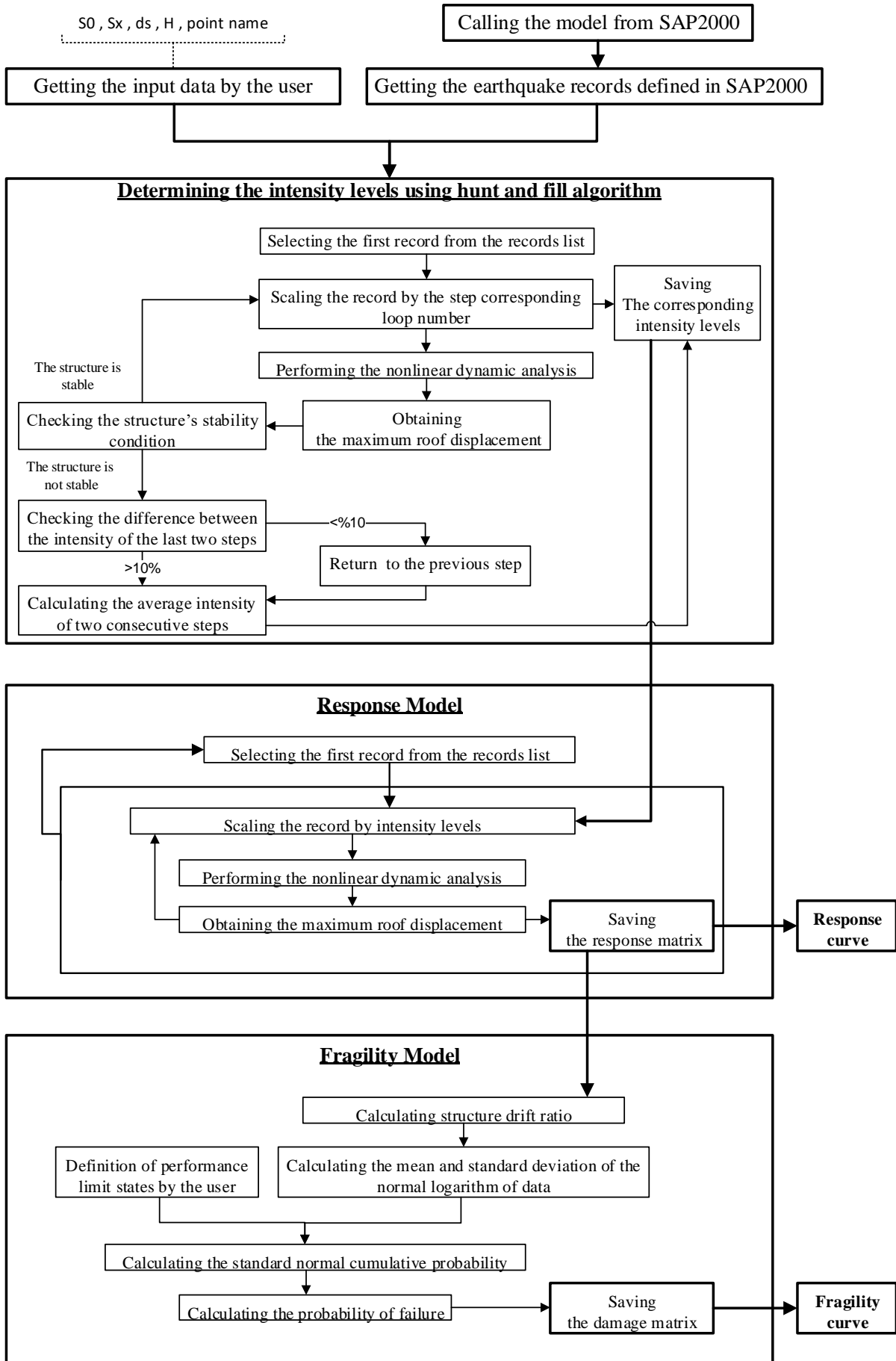


Fig. 4. Fragility curve code algorithm

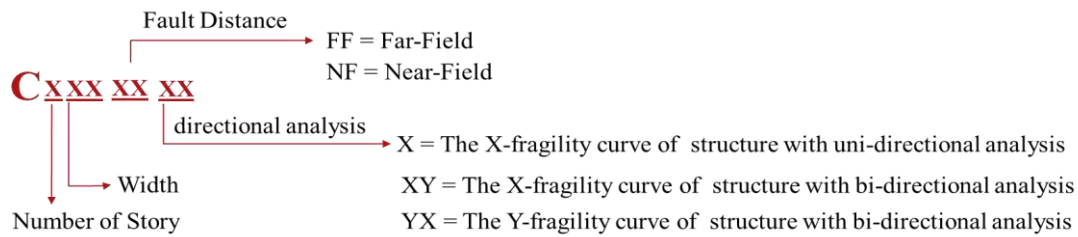


Fig. 5. Sample's Code

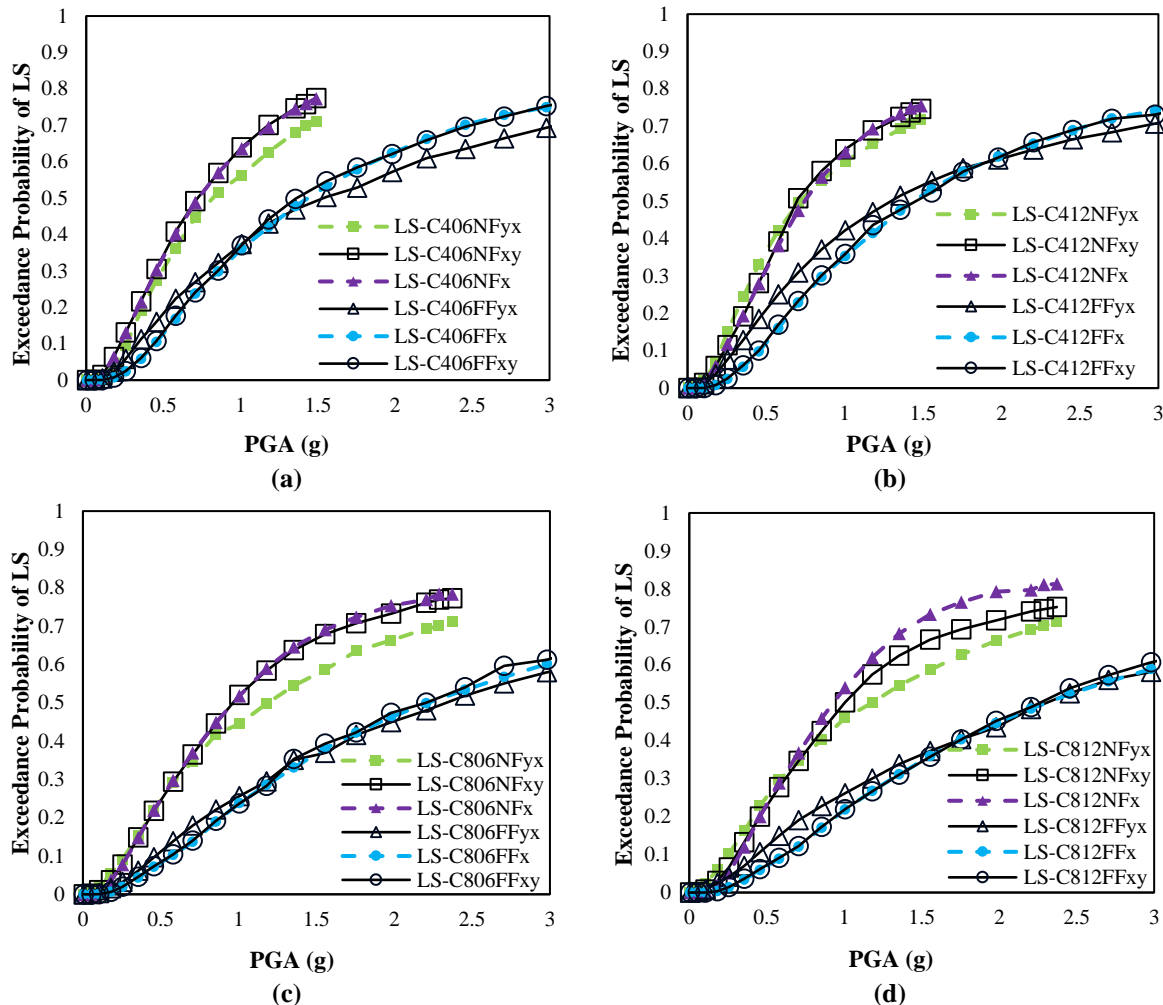


Fig. 6. Longitudinal and transverse fragility curves obtained from uni-directional and bi-directional analysis: a) C406; b) C412; c) C806; and d) C812

As can be observed in Figure 6, except for the fragility curve for model C812NF in which the difference between the results of the two analyses is less than 10%, it can be concluded that the results of the analyses for the case study structures, which comply to the regular structures as per 2800 standard code, are close to each other despite the 5% accidental torsion considered herein. Furthermore, the fragility curves obtained from the longitudinal and transverse direction analysis of the case study structures are very close to each other,

though their difference increases with increasing intensity. In general, it can be stated that the damage probability is higher in the transverse direction. Therefore, the following evaluations in the paper are performed based on the fragility curve of the transverse direction resulting from the uni-directional analysis of structures.

7. Results of Uni-Directional Analysis

In this section, to investigate the effect of the width and height of the structure on their

vulnerability and also to identify the more destructive earthquakes, the fragility curve of the transverse direction of the structures under near-field and far-field earthquake records for three damage limit states, including IO, LS, and CP have been compared with each other.

As can be seen in Figure 7, the probability of failure of structures with different widths and number of bays, in which the ratio of the width of the structure to the number of bays is equal, is the same; in structures with different heights, the probability of failure of shorter structures is higher. Also, the probability of failure of

structures subjected to near-field records is higher as compared to the far-field records.

In order to further examine the observations made in the above paragraph; the capacity curve of each structure is plotted using pushover analysis. The strength and stiffness of each structure are determined by using the equivalent bilinear curve whose slope of the first line and the area below it is equal to the initial slope and the area below their capacity curve, respectively. Note that, due to the unequal mass of the structures, the ratio of mass-to-strength and mass-to-stiffness are shown in Figure 8 for a better comparison.

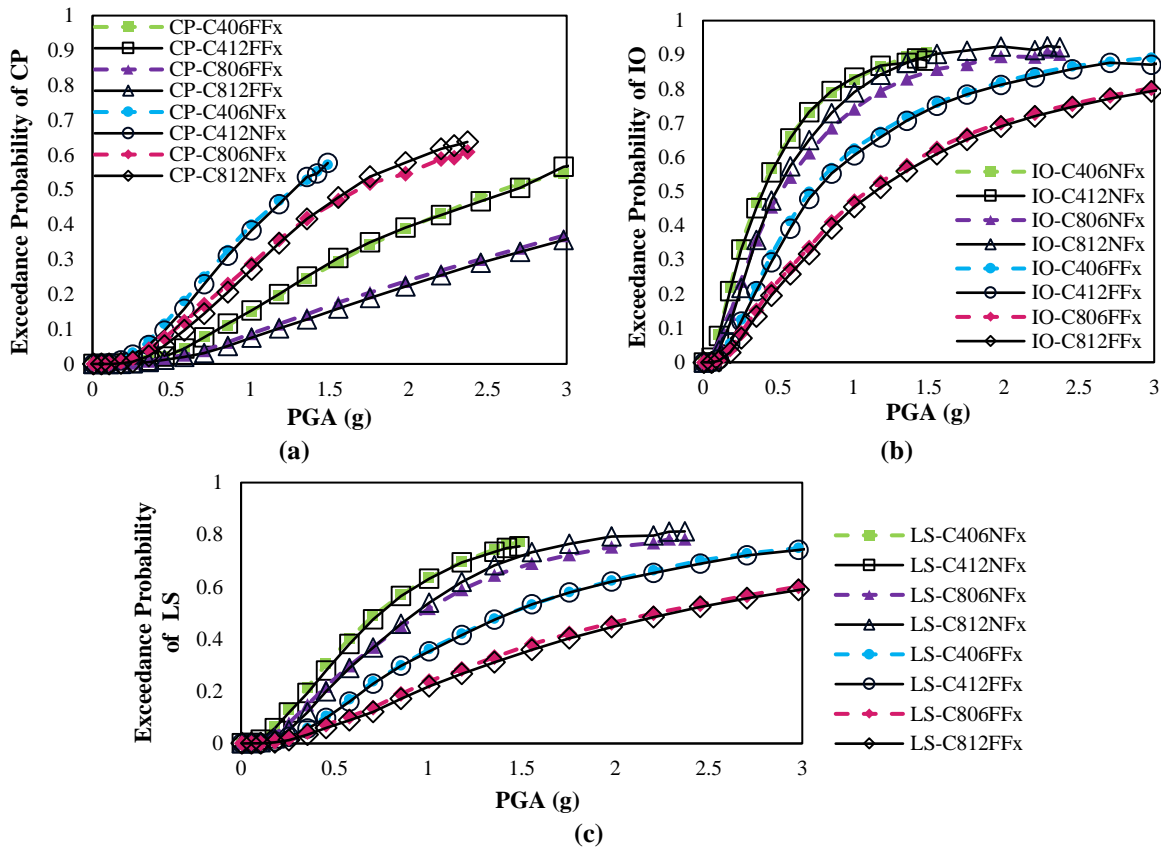


Fig. 7. Fragility curves in the transverse direction for the case study structures: a) exceedance probability for CP limit state; b) exceedance probability for IO limit state; and c) exceedance probability for LS limit state

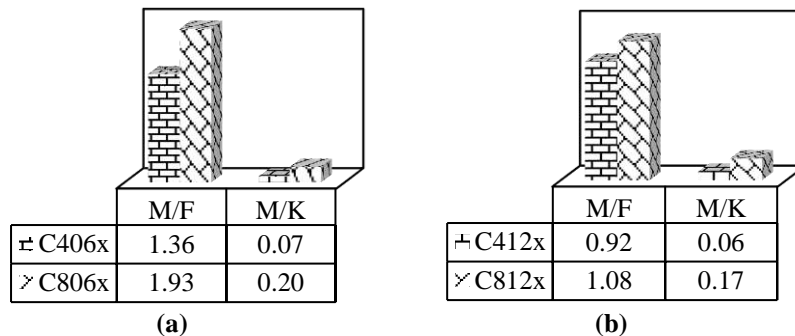


Fig. 8. Dynamic characteristics of the case study structures: a) C406 and C806; and b) C412 and C812

As can be observed in Figure 8, for structures of the same height and different widths, the mass-to-stiffness ratios are close to each other and the mass-to-strength ratio of the wider structures is smaller. Furthermore, in structures with the same width and different heights, the mass-to-stiffness and mass-to-strength of shorter structures are less.

By comparing the results of the fragility curve of the structures and their dynamic characteristics, it seems that the response of structures is determined based on the mass-to-stiffness ratio. Newmark et al. (1959) evaluated the seismic behavior of single-degree-of-freedom structures under nonlinear dynamic analysis and found out that for structures with periods greater than one second, the maximum displacement resulting from the linear and nonlinear analysis is equal. The probability of failure of shorter structures that have a lower mass-to-stiffness ratio can be justified by referring to the response spectrum of records used. The pseudo-velocity spectrum for near-field and far-field earthquake records are shown in Figure 9.

It is observed in Figure 9 that, approximately the range of period of

vibration 0 to 4 seconds is an acceleration-sensitive region, 4 to 9 seconds is a velocity-sensitive region and 9 to 15 seconds is displacement sensitive region. Since the period of vibration of the structures studied in this paper is between 1 to 2 seconds, the pseudo-accelerations spectrum has been used to interpret the above observations. The pseudo-accelerations spectrum for near-field and far-field earthquake records are shown in Figure 10.

Figure 10 shows that, the shorter structures with a period of vibration of one second are subjected to bigger spectral accelerations than the taller structures with a period of vibration of two seconds.

8. Performance Evaluation of Case Study Structures Subjected to Seismic Excitation

In order to evaluate the seismic risk of Reinforced Concrete Moment Resistant Frame structures located in Qods town, the probability of failure for different damage limit states for a PGA of 0.3g, which is the design base acceleration of Qom city as per 2800 standard code, is presented in Figure 11.

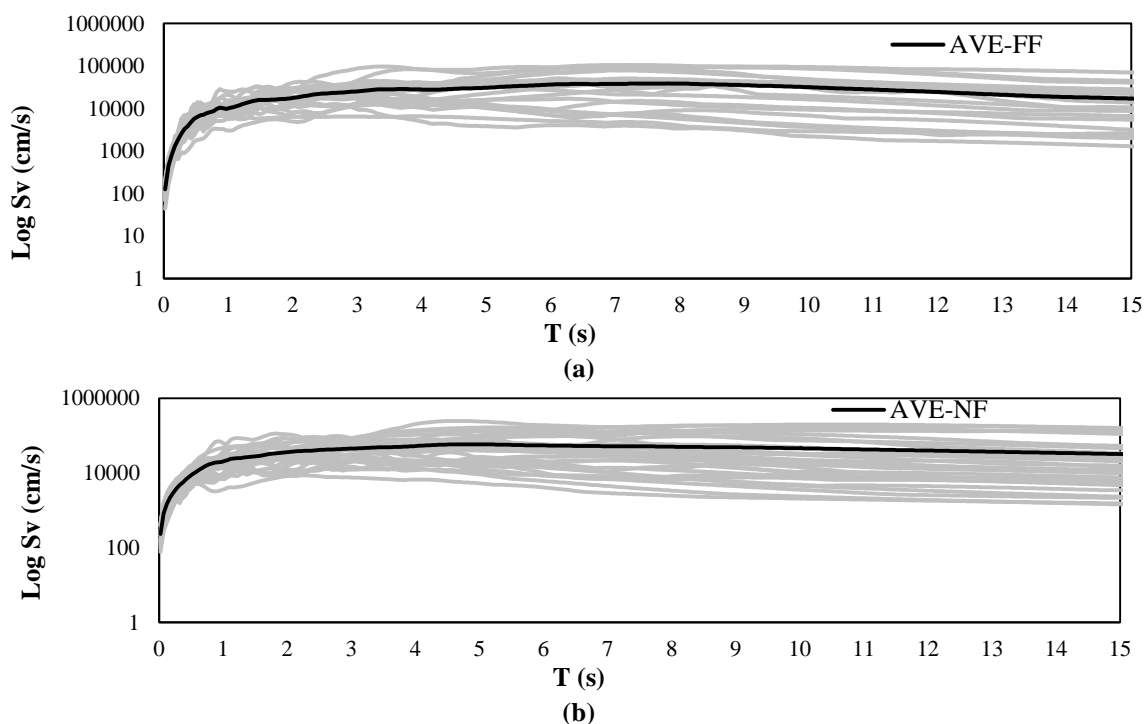


Fig. 9. Average pseudo-velocity spectrum for: a) near-field earthquake records; and b) far-field earthquake records

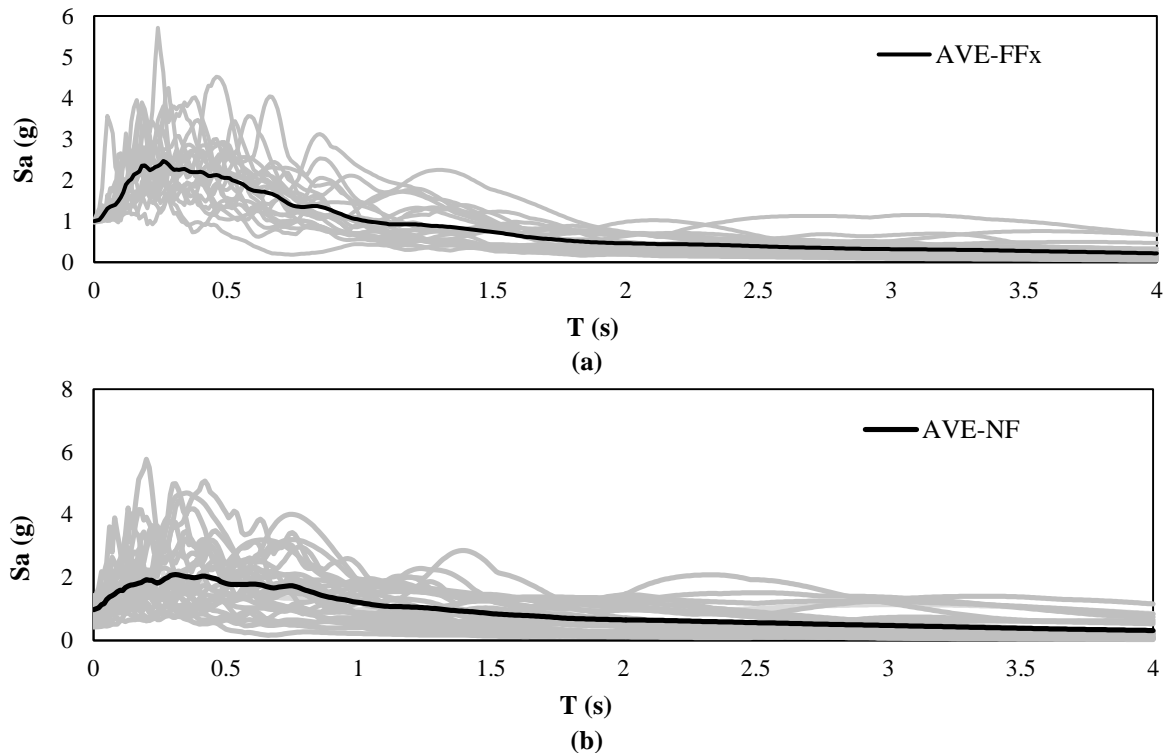


Fig. 10. Pseudo-accelerations spectrum for: a) far-field earthquake records; and b) near-field earthquake record

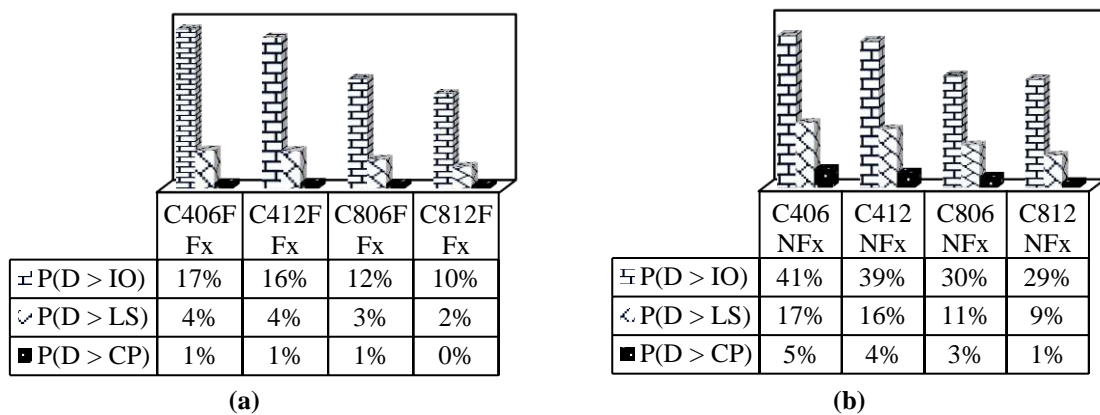


Fig. 11. Probability of failure for different limit states subjected to an acceleration of 0.3g: a) far-field and b) near-field

According to Figure 11, the probability of experiencing extensive damage to the structures for a seismic intensity of $PGA = 0.3g$ under near-field and far-field earthquakes such that the lives of the residents are endangered or the buildings require serious repairs, is about less than 5% and 20%, respectively.

9. Conclusions

In order to predict the seismic performance of conventional residential buildings of Qods town (located in Qom, Iran), 24 fragility curves were developed for four

typical intermediate Reinforced Concrete Moment Resistant Frame structures in this area: 4 and 8 story with 1 bay, 4 and 8 story with 2 bays. They were derived through nonlinear incremental dynamic analysis in one and two horizontal directions under two sets of near-field and far-field ground motion records.

Based on the analysis results the following conclusions are drawn:

- The probability of failure for LS limit state under near-field and far-field records with a PGA of $0.3g$ for conventional Reinforced Concrete Moment Resistant Frame structure

located in Qods town is respectively estimated less than 5% and 20%.

- The results indicate that the seismic response of structures, which are categorized as regular according to the provisions of the 2800 standard, is the same for uni-directional and bi-directional analyses. Although 5% accidental torsion taken into account.
- Since the response of the structures with periods greater than 1 sec is in correlation with the mass-to-stiffness ratio, the damage spectrum is applicable.
- The change in the width and number of bays of the structure does not affect the probability of failure, as far as the width to the number of bays ratio is kept constant. However, the change in the height of the structure affects the probability of failure, and the shorter structures are more susceptible to damage.
- Based on the seismic response of the structures in the present study, the probability of failure is higher when the structure is subjected to near-field earthquake ground motion records.

10. References

- Abdollahzadeh, G.R., Sajjini, M. and Asghari, A. (2015). "Seismic fragility Assessment of Special Truss Moment Frames (STMF) using the Capacity Spectrum Method", *Civil Engineering Infrastructures Journal*, 48(1), 1-8.
- ACI 318-14. (2014). *Building code requirements for structural concrete*, American Concrete Institute, Farmington Hills, MI.
- Ahmadi Pazoki, M., Shakib, H. and Mohammadi, P. (2015). "Cost-benefit analysis of construction and rehabilitation of steel braced frames with infill panels using seismic damage fragility curves", *Journal of Sharif Civil Engineering*, 31.2(1.2), 51-59.
- ASCE 41-13. (2014), *Seismic evaluation and retrofit of existing buildings*, American Society of Civil Engineers, Reston, VA.
- ATC-13. (1985). *Earthquake damage evaluation data for California*, Federal Emergency Management Agency (FEMA), 492 p.
- Cornell, C. and Krawinkler, H. (2000). "Progress and challenges in seismic performance assessment", *PEER Center News*, 3, 1-3.
- FEMA-356 (2000) "Prestandard and commentary for seismic rehabilitation of buildings", *Federal Emergency Management Agency*, 7(2), Washington DC.
- FEMA P695. (2009). *Recommended methodology for quantification of building system performance and response parameters*, Project ATC-63, Prepared by the Applied Technology Council, Redwood City.
- Building and Housing Research Center. (2016). *Iranian code of practice for seismic resistance design of buildings, Standard No. 2800, 3rd Edition*, Building and Housing Research Center, Tehran, Iran, (In Persian).
- Kouhestanian, H., Pahlavan, H., Shafaei, J. and Shamekhi Amiri, M. (2019). "Probabilistic seismic assessment of RC buildings considering soft and extreme soft story irregularities subjected to main shock-aftershock sequences", *Amir Kabir Journal of Civil Engineering*, 53(2), 457-478.
- Mohsenian, V., Rostamkalae, S., Moghadam, A.S. and Beheshti-Aval, S.B., (2017). "Evaluation of seismic sensitivity of tunnel form concrete buildings to mass eccentricity in the plan", *Journal of Sharif Civil Engineering*, 33.2(3.2), 3-16.
- Moehle, J. and Deierlein, G.G. (2004). "A framework methodology for performance-based earthquake engineering", *Proceedings of the 13th World Conference on Earthquake Engineering*, 679, 3812-3814.
- Mobinipour, A. and Pourzeynali, S. (2020). "Assessment of near-fault ground motion effects on the fragility curves of tall steel moment resisting frames", *Civil Engineering Infrastructures Journal*, 53(1), 71-88.
- Newmark, N.M. (1959). "A method of computation for structural dynamics", *Journal of Engineering Mechanics Division*, ASCE, July 67-94.
- Pahlavan, H., Naseri, A. and Einolahi, A. (2019). "Probabilistic seismic vulnerability assessment of RC frame structures retrofitted with steel jacketing", *Amir Kabir Journal of Civil Engineering*, 51(3), 585-598.
- Rojahn, C. and Sharpe, R.L. (1985). "Earthquake damage evaluation data for California", Applied Technology Council.
- Taghizade, F., Eskandari, M., Afsari, N. and Gheitanchi, M.R. (2009). "Studying seismotectonics and seismicity of Qom province", *Earth*, 3(3), 59-70.
- Whitman, R.V., Lagorio, H.J. and Schneider, P.J. (1996) "Fema- nibs earthquake loss estimation methodology", in *Natural Disaster Reduction*. pp. 113-114, ASCE.



This article is an open-access article distributed under the terms and conditions of the Creative Commons Attribution (CC-BY) license.



Simulation of Near-Fault Seismic Ground Motions of 03 November, 2002 Denali Earthquake Using Modified Semi-Empirical Approach

Rajaram, C.^{1*} and Pradeep Kumar, R.²

¹ Associate Professor, School of Civil Engineering, Rajeev Gandhi Memorial College of Engineering and Technology, Nandyal, India.

² Professor, Earthquake Engineering Research Centre, International Institute of Information Technology, Hyderabad, India.

© University of Tehran 2021

Received: 23 Aug. 2020;

Revised: 17 Aug. 2021;

Accepted: 30 Aug. 2021

ABSTRACT: An effective earthquake (Mw 7.9) struck Alaska on 3 November, 2002. It ruptured 340 km along three faults namely, the Susitna Glacier, Denali and Totschunda faults in central Alaska. The earthquake was recorded at 23 stations in Alaska and the Peak Ground Acceleration (PGA) of 0.32g was recorded at station PS10, which was located 3 km from the fault rupture. In this study, strike-slip Denali fault has been considered for studying the characteristics of ground motions through modified semi-empirical approach. The ground motion records of the 2002 Denali earthquake are generated through MATLAB code. The results revealed that modified semi-empirical approach is fairly good in agreement with observed ground motion records at all stations. A perfect match is observed between Fourier amplitude spectra of simulated and observed ground motions at PS09 and CARLO stations. A good match is observed between elastic response spectra of observed and simulated ground motions.

Keywords: Denali Earthquake, Fourier Amplitude Spectrum, Ground Motion Prediction Equation, Synthetic Accelerogram.

1. Introduction

A massive earthquake of magnitude M7.9 occurred on 3 November 2002 at a depth of 4.2 km in central Alaska (AEIC, 2003). The rupture started at 48 km of Susitna Glacier fault, propagated towards 226 km of Denali fault and terminated at 66 km of Totsunda fault (Lin et al., 2020). The Trans-Alaska pipeline pump station 10 located 3 km from surface rupture recorded a peak ground acceleration of 0.32g. It was the strongest event ever recorded in the interior of Alaska. Fortunately, no fatalities recorded

in the densely populated region. The Denali fault behavior is similar to that of the San Andreas fault system in California (Uenishi, 2017). The rupture history of Denali earthquake was analyzed using teleseismic P-wave data to understand the rupture initiation and the behavior of Denali fault (Ozacar et al., 2004; Yousef and Jonathan 2020). Past studies showed that this earthquake was initiated by an unknown thrust fault propagating towards east (Kikuchi and Yamanaka, 2002; Lin et al., 2020). Echelon features were also observed on the surface during rupture along the

* Corresponding author E-mail: rajaram.chenna@research.iiit.ac.in

Denali fault.

2. Description of Denali Earthquake

2.1. Tectonic Setting and Fault Motion

The 2002 Denali earthquake happened due to interaction between Pacific plate and North American plate. This thrust motion was the cause of the 1964 Alaska earthquake (M9.2), which was the largest inland seismic event in central Alaska (Lin et al., 2020). The mainshock originated about 20 km towards east of the foreshock. The strike and dip angles of Susitna Glacier fault were 262° and 48° , respectively. The strike angle of Denali fault was 102° with vertical dip. The scrap height of Susitna Glacier fault measured was about 4.0 m. The average and peak slip of Denali fault were 2.14 and 9.94 m, respectively (Dreger, 2003). The average slip of Totschunda fault was 1.7 m. Figure 1 shows the location of the Denali fault and the epicenter of the 3 November 2002 Denali earthquake. The geophysical parameters of the earthquake are shown in Table 1.

2.2. Seismicity of the Denali Fault

A foreshock of M6.7 occurred on 23 October 2002 in Nenana Mountain range before a main shock. Around 15,000 aftershocks were occurred during first two months after the main shock (AEIC, 2003). The first earthquake documented was the one on Sanak and Shumagin Islands, south of the Alaskan Peninsula, in July 1788. Alaska experienced few major-to-great earthquakes from 1899 to 1969. Among them, 1946 Aleutian Islands (M8.6), and 1964 Alaskan earthquake (M9.2) caused extensive property damage and topographic changes (USGS, 1964). The earthquake on the Denali fault prior to the 2002 was the magnitude 7.2 that occurred in July 1912 (Rachkovski et al., 2003). Since no seismographs and no reports were available in Alaska at that time, the location of the 1912 shock is uncertain. Figure 1 shows past seismicity of Alaskan region since 1898. The list of past major earthquakes experienced by Alaska since 1899 is shown in Table 2.

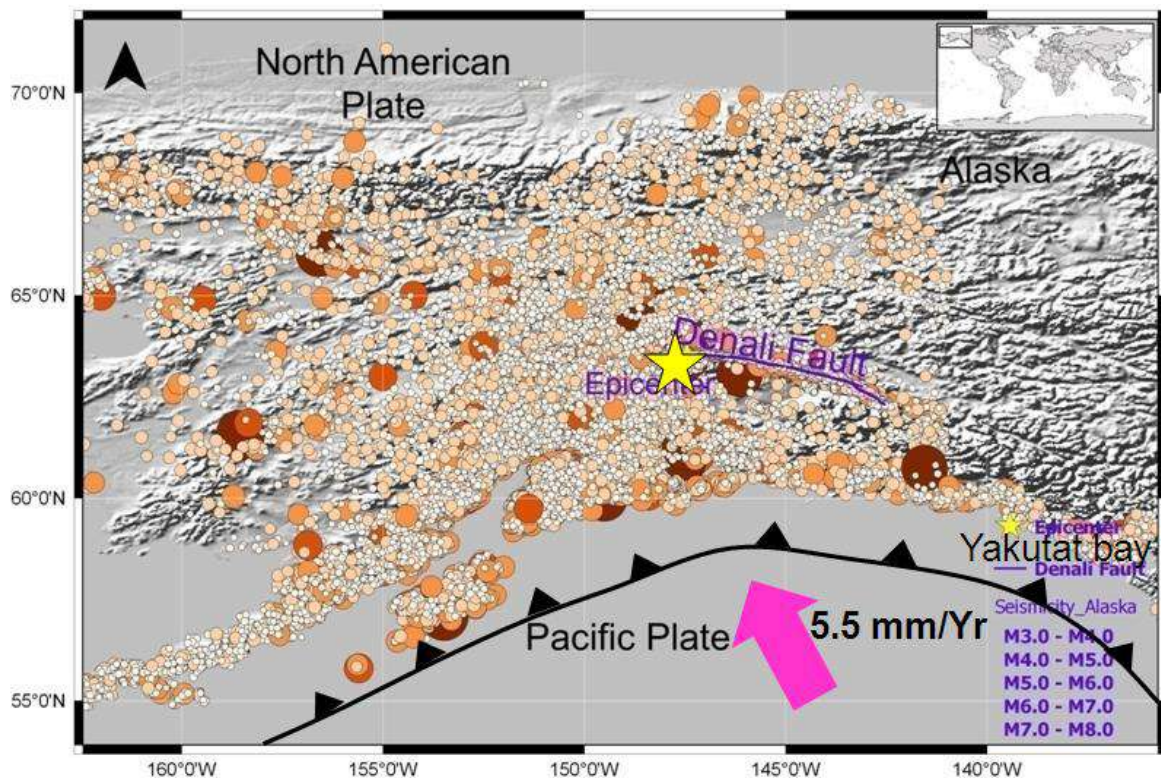


Fig. 1. Location of Denali fault, epicenter (denoted with star) of 3 November 2002 Denali earthquake. Past seismicity of Alaska in the region of Denali since 1898 (Data Source: USGS, 2013; AEIC, 2013)

Table 1. Geophysical parameters of 3 November 2002, Denali earthquake

Parameters	Values
Magnitude	7.9
Type of fault	Strike-slip fault
Name of fault	Denali fault
Seismic moment (Nm)	8.45×10^{20}
Strike angle	102° (Dreger, 2003)
Dip angle	90° (Dreger, 2003)
Shear wave velocity, β (km/s)	3.55 (Dreger, 2003)
Rupture velocity, V_r (km/s)	2.84
Average and peak slip (m)	2.14 and 9.94 m
Slip rise time (s)	2-4
Seismic moment, M_0 (Nm)	8.45×10^{20} (Dreger, 2003)
Shear modulus (N/m ²)	3.52×10^{10}
Material density (kg/m ³)	2790

Table 2. Major to great earthquakes experienced by Alaska in past since 1899 (Source: USGS, 2013)

S No.	Date	Magnitude	Location
1	10 September 1899	8.6	Yakutat bay
2	09 October 1900	7.7	Kodiak island
3	22 July 1937	7.3	Southeast of Fairbanks
4	15 October 1947	7.3	Southeast of Fairbanks
5	07 April 1958	7.3	Central Alaska
6	28 March 1964	9.2	Great Alaska
7	04 February 1965	8.7	Rat island
8	03 October 2002	7.9	Denali
9	23 June 2014	7.9	Aleutian islands

3. Literature Review

The wave propagation theory was used to develop artificial ground motions using composite source method and the method yields good results for 1991 Uttarkashi earthquake (Anderson, 2015). However, the main drawback of the method is it requires geophysical parameters such as fault plane solutions, stress drop etc. The availability of these parameters is difficult for a site of interest. Empirical Green's function method suites to develop ground motion records, if small event accelerograms exist in the study area. This method is validated with a M8.5 scenario earthquake and yields good results (Krishnavajjhala, 2021). The stochastic simulation method fails to simulate near-field ground motions of large earthquakes.

The current study considers semi-empirical method to simulate ground motion records for the 2002 Denali earthquake. A step-by-step procedure of the method is described in the following section. This method yields good results for ground motions of several earthquakes such

as 1999 Chi-Chi earthquake (Rajaram, 2016), 1991 Uttarkashi earthquake, 2009 Bhutan earthquake (Sandeep et al., 2017), 2013 Doda earthquake (Rajaram and Pradeep, 2016) and 2013 Pakistan earthquake (Rajaram and Pradeep, 2020). The main objective of the study is to find out the efficacy of the method for Alaska region. For this purpose, the 2002 Denali earthquake of magnitude 7.9 have been chosen to generate accelerograms. In this analysis, the Ground Motion Prediction Equation (GMPE), geophysical parameters are derived with the Alaskan data during 1971-2014.

3.1. Observed Ground Motions

Around 42 seismic stations digitally recorded the Denali earthquake operated by various organizations (AEIC, UoAF, USGS, ATWC and Alyeska). More than 50% of seismic stations are located in Anchorage metropolitan region. The sampling frequency for R109 and CARLO seismic stations is 100 Hz and for other stations, it is 200 Hz (Tadahiro et al., 2016).

The locations of ground motion records are taken from Pacific Earthquake Engineering Research are shown in Figure 2. The current study addresses Denali fault alone due to complexity of the fault. Near-field ground motions records at stations PS10, PS09, CARLO and R109 are considered in this study and its ground motion records are shown in Figure 3. The parameters such as, location of seismic stations relative to the

fault and epicenter, horizontal and vertical fault slip and spectral decay frequency are shown in Table 3. The PGA values of Fault Normal (FN) and Fault Parallel (FP) components are shown in Table 4. The Fourier amplitude spectra and acceleration response spectra at all stations are shown in Figures 4 and 5. Each seismic station ground motion characteristics are described below.

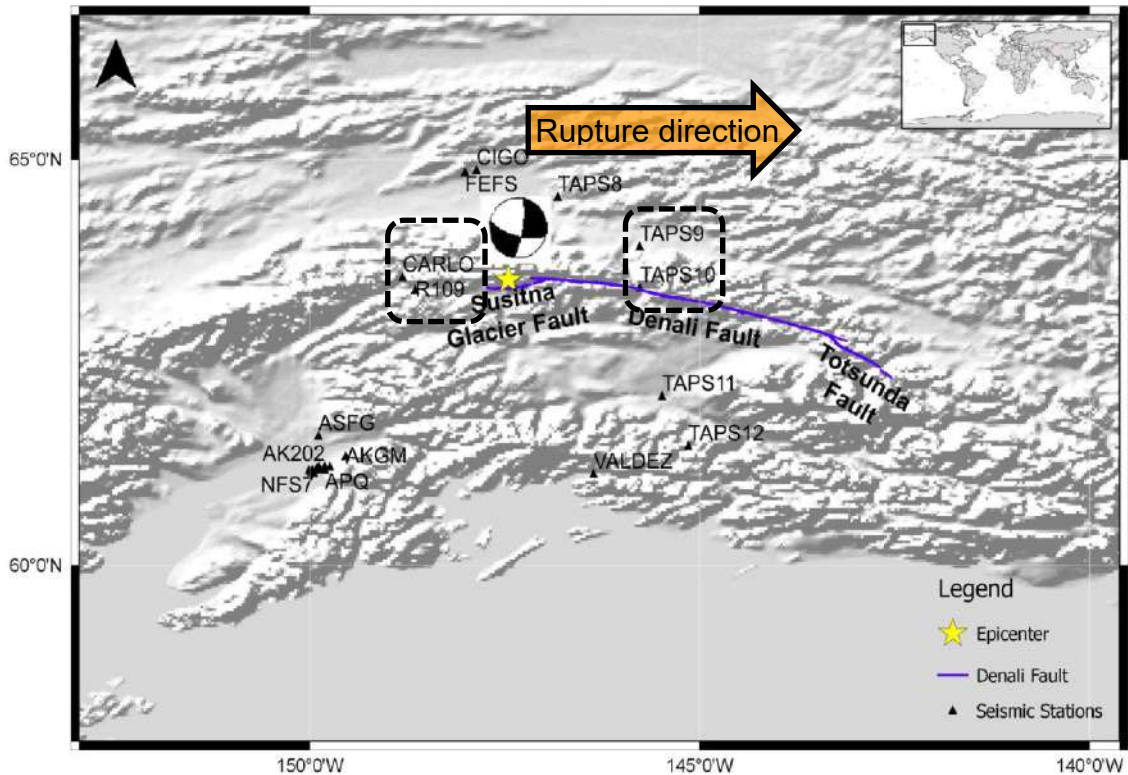
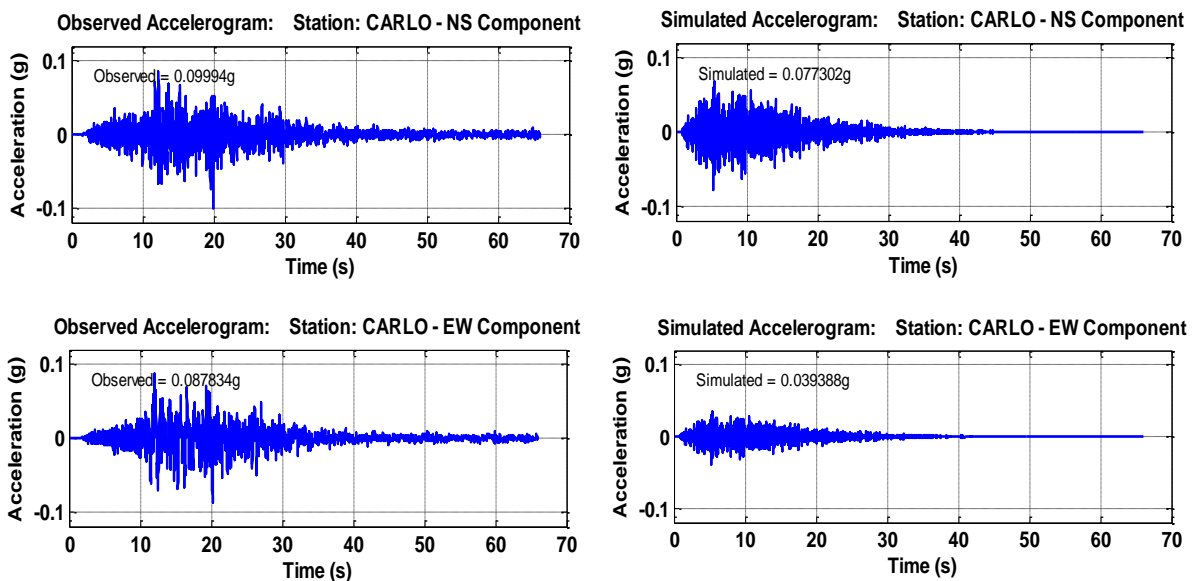


Fig. 2. Locations of the strong ground motion stations that recorded during 2002 Denali earthquake (Data Source: USGS, 2013; AEIC, 2013)



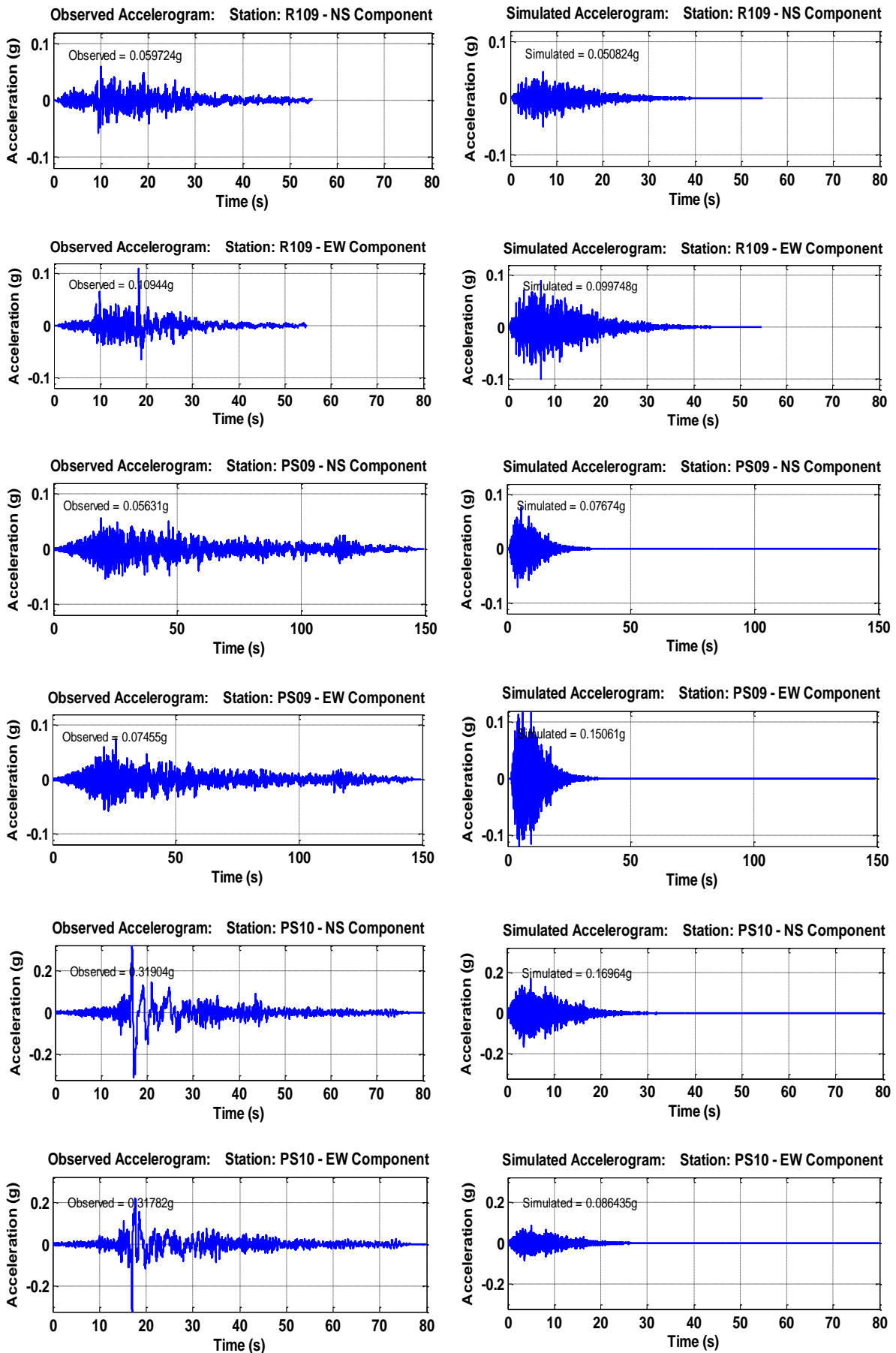


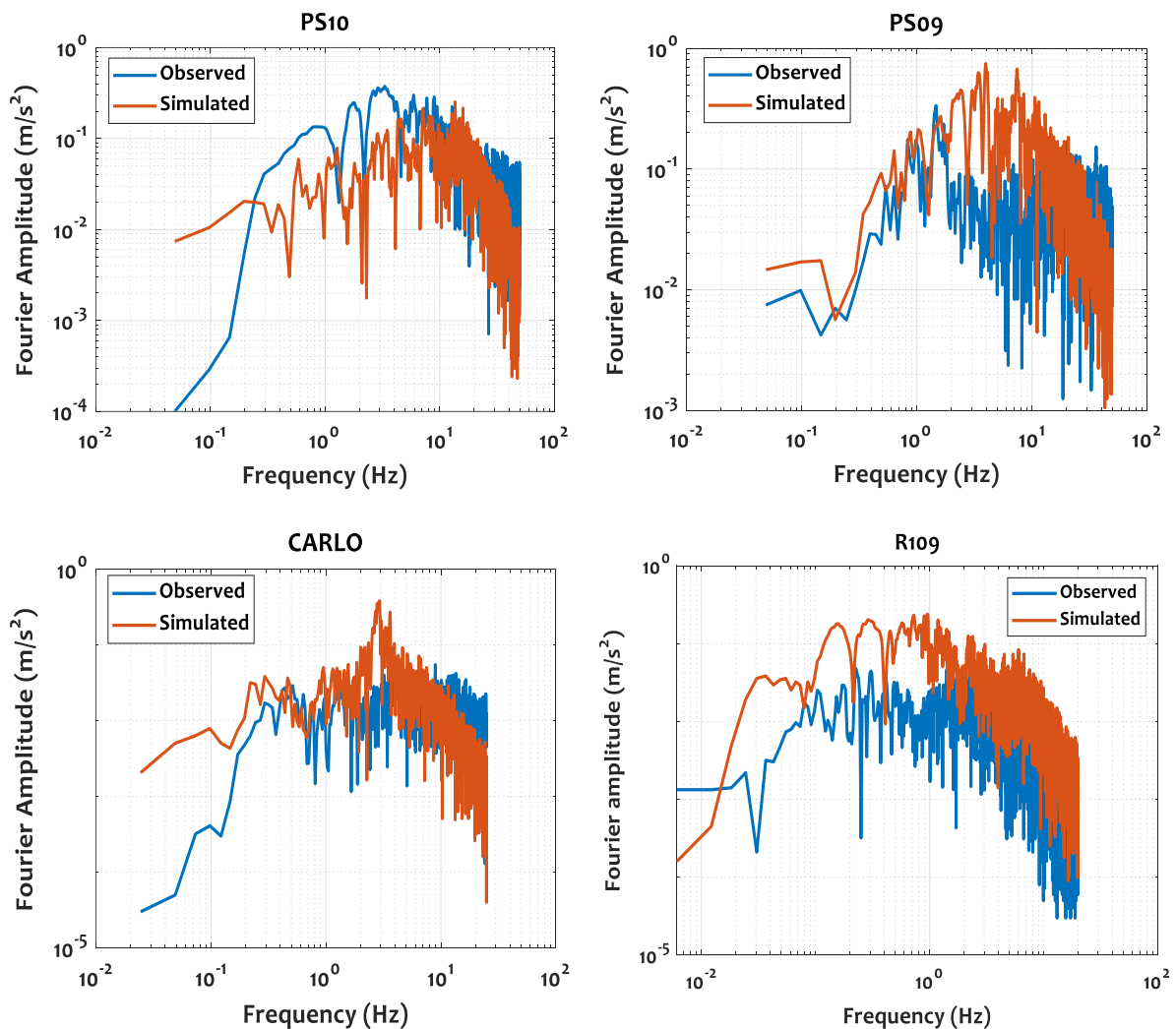
Fig. 3. Ground motion records obtained through instruments and simulation at CARLO, R109, PS09, and PS10 stations of the 2002 Denali earthquake (Data Source: SMVDC, 2013)

Table 3. Location of seismic stations relative to the fault and epicenter, horizontal and vertical fault slip and frequency decay of 3 November 2002, Denali earthquake

Station	Latitude ($^{\circ}$ N)	Longitude ($^{\circ}$ W)	Epicentral distance (km)	Distance from fault (km)	Horizontal fault slip (m)	Vertical fault slip (m)	Spectral decay frequency (Hz)
PS10	63.423	145.765	85.0	3.0	5.6	1.6	1.0
PS09	63.931	145.768	94.0	56.0	6.0	1.48	5.0
CARLO	63.551	148.809	68.0	59.0	3.9	1.06	5.0
R109	63.395	148.646	63.0	49.0	2.28	0.49	2.0

Table 4. Comparison of between observed, and simulated ground motions of 03 November 2002, Denali earthquake

Station	Observed PGA (g)		Simulated PGA (g)	
	FN	FP	FN	FP
PS10	0.319	0.317	0.17	0.086
PS09	0.056	0.074	0.076	0.15
CARLO	0.099	0.08	0.077	0.04
R109	0.06	0.109	0.05	0.10

**Fig. 4.** Fourier amplitude spectra obtained through observed and simulated ground motions at PS10, PS09, CARLO and R109 stations during 2002 Denali earthquake

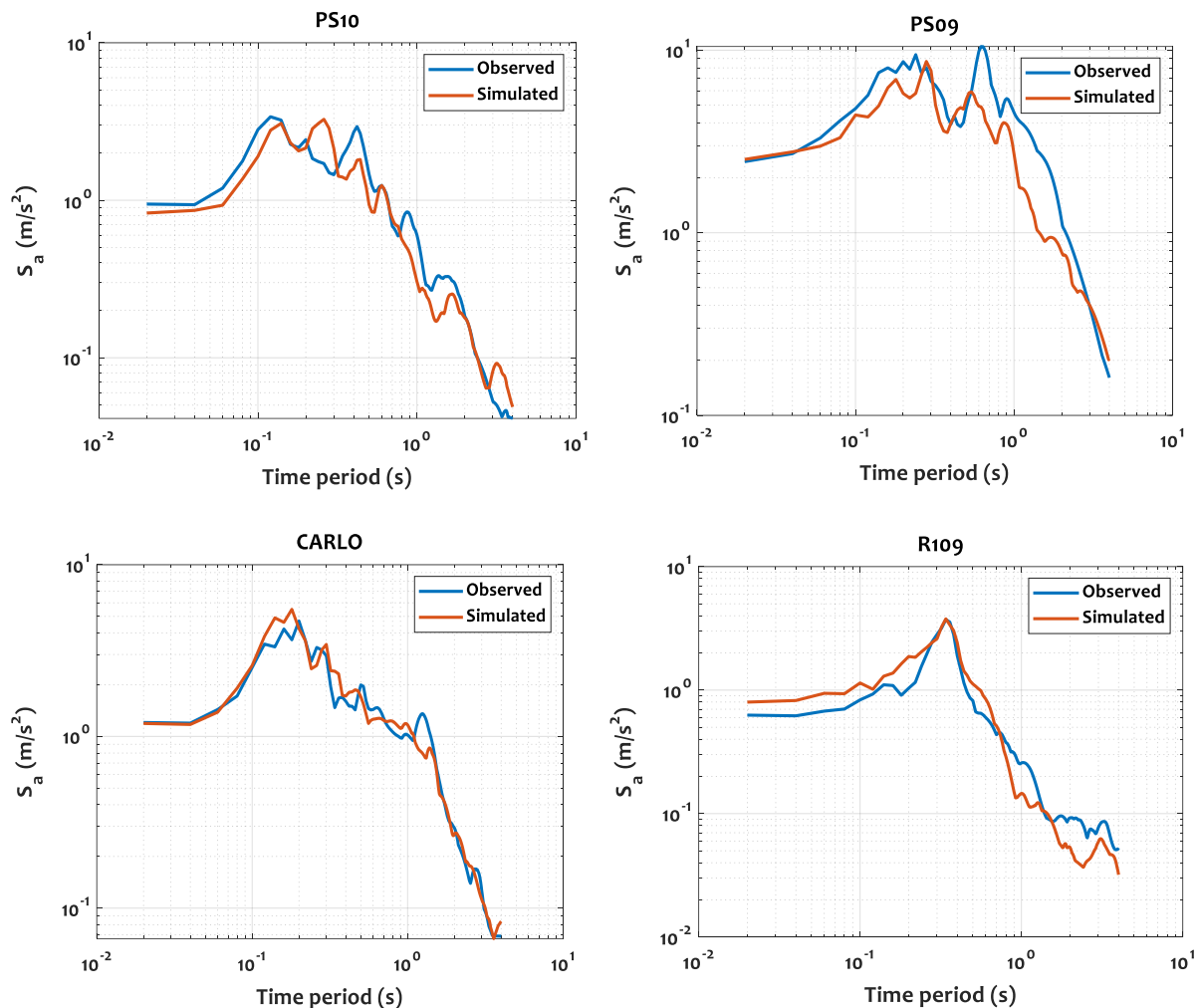


Fig. 5. Comparison of elastic acceleration response spectra between observed and simulated ground motions during 2002 Denali earthquake

Station PS10: Trans-Alaskan pipeline station 10 is located 3 km from the fault rupture of Denali fault and 85 km from the epicenter of the earthquake. The fault slipped 4-6 m horizontally and 0.5 m vertically at PS10 (Andrea and Chao, 2016; Wang et al., 2016). More than 0.3g PGA was recorded along both horizontal directions. It is observed that PGA, PGV and PGD of FN components are 1-30% higher than FP components. The corner frequency of Fourier amplitude is at 0.09 Hz and the decay starts at 1 Hz. High spectral acceleration on response spectrum is observed at a time period of 0.14 s.

Station PS09: Trans-Alaska pipeline station 09 is located 56 km from the fault rupture of Denali fault and 94 km from the epicenter of the earthquake. The fault slipped 4-6 m horizontally at PS09. Less

than 0.1g PGA was observed along both horizontal directions. The corner frequency of Fourier amplitude is at 0.1 Hz and the decay starts at 1 Hz. High spectral acceleration on response spectrum is observed at a time period of 0.6 s.

Station CARLO: It is a temporary station located on the Denali highway, which is 59 km from the fault rupture of Denali fault and 68 km from the epicenter of the earthquake. The fault slipped 1 m horizontally at CARLO (Wang et al., 2016). Less than 0.1g PGA was observed along both horizontal directions. The corner frequency of Fourier amplitude is at 0.1 Hz and the decay starts at 1 Hz. High spectral acceleration on response spectrum is observed at a time period of 0.2 s.

Station R109: It is also a temporary station located on the Parks highway, which

is 49 km from the fault rupture of Denali fault and 63 km from the epicenter of the earthquake. The fault slipped 1 m horizontally at R109 (Wang et al., 2016). More than 0.05g PGA was observed along both horizontal directions. The corner frequency of Fourier amplitude is at 0.1 Hz and the decay starts at 1 Hz. High spectral acceleration on response spectrum is observed at a time period of 0.35 s.

4. Generation of Ground Motion Prediction Equation (GMPE) and Q Parameter

4.1. GMPE

The general functional form of GMPE is expressed in Eq. (1).

$$f(Y) = a + f_1(M) + f_2(R) + f_3(S) + \sigma \quad (1)$$

where Y : is predicted PGA, $f_1(M)$: is a function of magnitude of earthquake, $f_2(R)$: is a function of epicentral distance, $f_3(S)$: is a function of site categories like rock and soil sites, and σ : is a value of relating uncertainties in the predicted $f(Y)$. A detailed procedure for developing GMPE is given by Rajaram (2016).

The functional form for modeling the ground motion attenuation can be represented using Eq. (2).

$$\log_{10}(Y) = a + bM + c \log_{10} \sqrt{R^2 + h^2} + eS + \sigma \quad (2)$$

where σ : is the standard deviation of the logarithm of Y , M : is the magnitude, R : is the Epicentral distance, h : is a function of M , S : is site categories (1 for soil site and 0 for rock site) and a , b , and e : are regression

analysis coefficients.

The dataset consists of 57 seismic station records in the Alaska for studying the GMPE relationship. The Alaskan earthquake information and ground motion records are taken from SMVDC (2013) (see Table 5). Since most of the seismic stations are located on rock site, the term $f_3(S)$ is taken as zero. The distribution of dataset used in this analysis is from the earthquakes with a magnitude range of 5-7.9 and an Epicentral distance range of 35-190 km. The distribution of magnitude and number of seismic stations with respect to epicentral distance is shown in Figure 6. The dataset consists of two orthogonal horizontal components of PGA values, the resultant value has been chosen for the purpose of analysis.

The coefficient ' c ' in Eq. (2), which is a negative value, means the attenuation rate with respect to Epicentral distance. In other words, it is a weighted average of c 's, each of which is obtained from a data set of one earthquake at all Epicentral distances. The coefficient ' c ' must be greater than 1.0 for the short period amplitude attenuation relation, since this term includes the geometrical spreading of body wave and inelastic attenuation. Hence, the analysis considered the weighted average of c 's for a fixed at all Epicentral distances. Similarly, the coefficient b means the amplitude increase rate with respect to magnitude at a fixed distance. In other words, it is a weighted average of b 's, each of which is obtained from a dataset at a particular distance range for all earthquakes. In this analysis, the weighted average of b and c are taken at all Epicentral distances and at all earthquakes, respectively.

Table 5. The Alaskan earthquake information and dataset (Data source: SMVDC, 2013)

Earthquake	Date	Mw	No. of stations
Southeastern Alaska	04 Jun 2014	5.7	3
Southern Alaska	22 Jun 2009	5.5	8
Nelchina	25 Aug 2004	5.3	3
Rampart	02 Apr 2003	5.0	1
Denali	03 Nov 2002	7.9	30
Nenana mountain	23 Oct 2002	6.7	5
SE Alaska	28 Feb 1979	7.4	3
Anchorage	01 Jan 1975	5.9	4

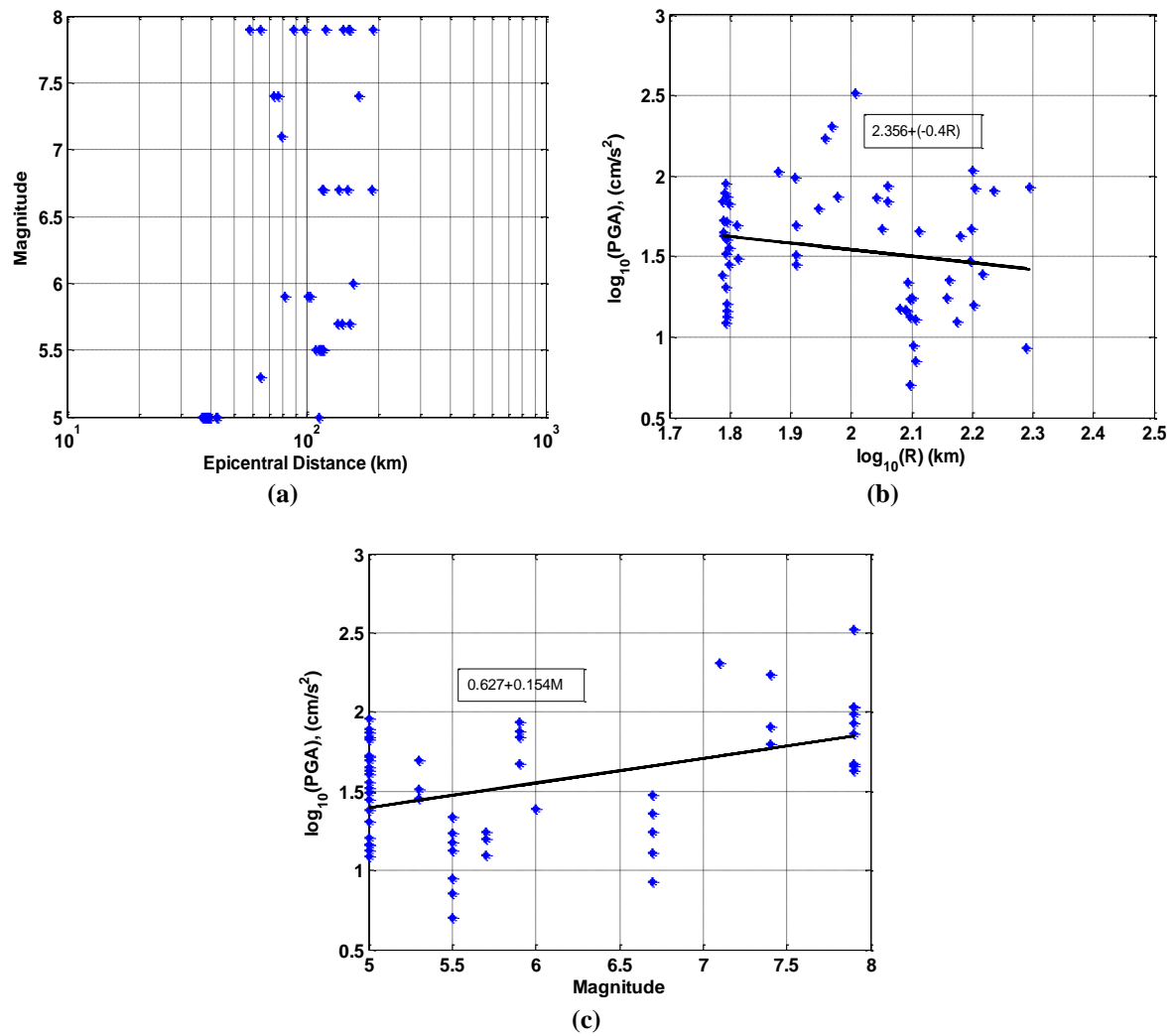


Fig. 6. Generation of GMPE: a) Distribution of magnitude and number of seismic stations with respect to Epicentral distance; b) Distribution of horizontal PGA to Epicentral distance; and c) Distribution of horizontal PGA to magnitude

The residual values represent the ratio of logarithmic of observed to predicted PGAs as shown in Eq. (3).

$$\text{Residual} = \log_{10} \left(\frac{Y_{\text{observed}}}{Y_{\text{predicted}}} \right) \quad (3)$$

where Y_{observed} is the observed value from ground motion record (e.g. PGA), while $Y_{\text{predicted}}$ represents the value predicted by the GMPE. The regression coefficients are calculated using regression analysis. The GMPE obtained from the analysis is shown in Eq. (4), which resembles Hasegawa’s GMPE, proposed for Canadian region in 1981 (Hasegawa et al., 1981). The GMPE in Eq. (4) considers a seismic catalog from 1971 to 2014, whereas Hasegawa

considered from 1971 to 1981.

$$\log_{10}(Y) = 2.356 + 0.15M - 2.207 \log_{10} \sqrt{R^2 + h^2} + 0.243 \dots (5.0 \leq M \leq 8.0) \quad (4)$$

4.2. Frequency Dependent Q Parameter

There are several techniques to investigate site effects due to local site conditions. In general, H/V spectral ratio method is used to calculate the site effects. In general, Q is represented as $Q = Q_0 f^n$, (Hajiazizi et al., 2021) where Q_0 : is the Q value at 1 Hz and n varies from 0 to 1.

The procedure for estimating the Q factor is as follows:

- Collection of ground motion records for a region of interest. Convert all ground motion records into frequency domain.

- Computing the ratio of horizontal to vertical amplitude spectra and also compute average amplitude spectrum.
- Compute the Q parameter against frequency using Eq. (5).

$$\log_{10} A(R, f) - \log C - \log GS - \log F(f) \\ = \log S(f) - 1.36 \frac{fR}{\beta Q(f)} \quad (5)$$

where C : is a constant and GS : is geometrical spreading term. $F(f)$: is derived through H/V spectral ratio method shown in Figure 7. Hence at each frequency, the values of $Q(f)$ and $S(f)$ are obtained by fitting the above equation to the observed Fourier amplitude spectra shown in Figure 8.

- Estimation of Q parameter value for a region of interest through regression analysis (power law).

For the purpose of analysis, 57 ground motion records have been considered along three translational directions to plot H/V spectral ratio. The ground motion records are transformed into frequency domain using Fast Fourier Transform (FFT). The H/V spectrum is obtained as the ratio of vector summation of two horizontal component spectra along FN and FP components and vertical component

spectral amplitude V at each frequency. The average H/V spectrum is obtained by arithmetic average of individual H/V spectra over all time windows. A plot is drawn between the H/V spectral ratio on the ordinates and the frequency on the abscissa. From the analysis, it is observed that the average amplification factor increases as the frequency increases till 0.15 Hz. Then it starts decreasing from 10 Hz. No significant amplification of H/V ratio is observed, as most of the ground motions are recorded on rock site. Q value is estimated from Eq. (5). It is found that the frequency dependent Q parameter for Alaska region is $Q(f) = 23.89f^{1.02}$. The parameters for generating synthetic accelerogram are derived for Alaskan region. The methodology and generation of synthetic accelerogram at stations through modified semi-empirical approach are as follows.

5. Generation of Ground Motions using Semi-Empirical Approach

The semi-empirical method was first developed by Midorikawa (1993). Later, the method was modified by Sandeep et al. (2015). The method is based on ω^2 model (Boore, 1983). A step-by-step procedure of the method is described below.

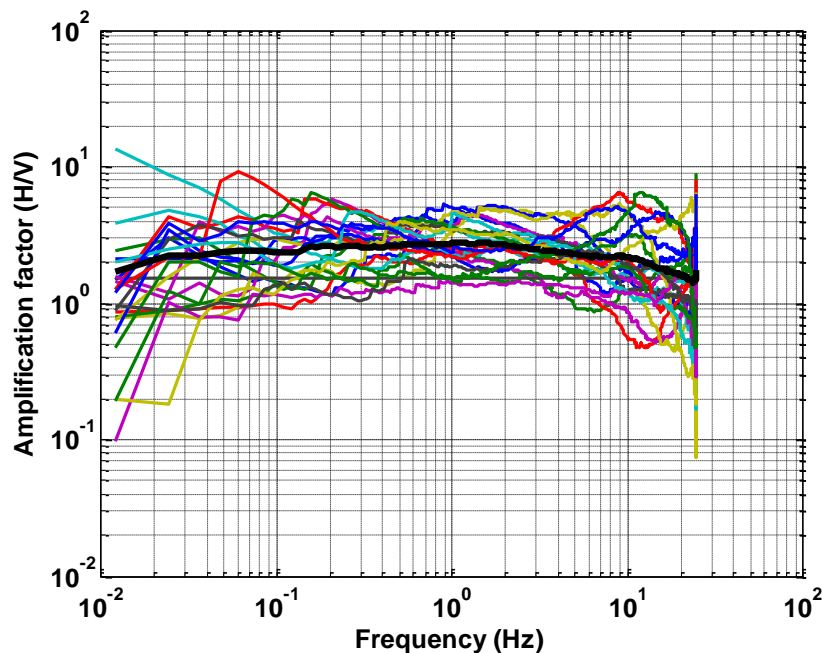


Fig. 7. Amplification of H/V for Alaska region

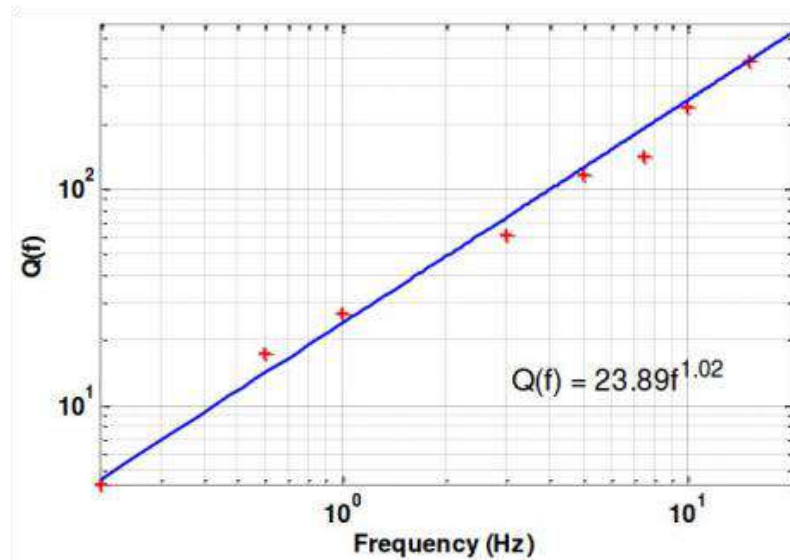


Fig. 8. Determination of Q parameter value for Alaska region

Step-1: Divide the fault plane into number of sub faults (N) based on scaling relationship between Richter magnitude of large (M) and small (m) earthquakes and Eq. (6) is as follows (Sato, 1989):

$$N = 10^{0.5(M-m)}. \quad (6)$$

Step-2: The white Gaussian noise is initially normalized and then converted to zero mean and variance. The time series of white Gaussian noise is converted into Fourier spectrum through Fourier transform and maintained maximum amplitude as unity.

Step-3: The amplitude spectrum is passed through theoretical filters proposed by Boore (1983) as shown in Eq. (7).

$$A(f) = CS(f)D_s(f)F_R(f, R). \quad (7)$$

where C : is a constant including seismic moment (M_0). The filter $S(f)$: represents the source acceleration spectrum (Javier et al., 2016), filter $D_s(f)$: represents near site attenuation of high frequencies, and filter $F_R(f, R)$: represents effect of anelastic attenuation.

Step-4: The filtered amplitude spectrum $A(f)$ is again converted into time series $A(t)$ and ensures the time series must be normalized. A correction function $F(t)$ is introduced to minimize the difference

between slip duration of the target and small earthquake considered (Krishnavajjhala, 2021). The correction function is calculated using Eq. (8).

$$F(t) = \delta(t) + [(N-1)/T_R(1-e^{-1})].e^{(-t/T_R)}. \quad (8)$$

where $\delta(t)$: represents delta function, and T_R : is the rise time of the target earthquake.

Step-5: Construction of acceleration envelope waveform $e_{ij}(t)$, modified by Sandeep et al. (2015) and Lal et al. (2018), is shown in Eq. (9).

$$e_{ij}(t) = \left[a_{ij} \frac{t}{T_d} e^{\left(1 - \frac{t}{T_d}\right)} \right]; \quad E(t) = \sqrt{\sum_{i=1}^N \sum_{j=1}^N e_{ij}^2(t - t_{ij})}. \quad (9)$$

where a_{ij} : is the peak ground acceleration at each sub-fault obtain from ground motion prediction equations. T_d : represents duration parameter, t_{ij} : is the arrival time at observation point (Rajaram, 2016)

Step-6: The acceleration time history record at each sub-fault $A_{ij}(t)$ is calculated by multiplication of the envelope waveform e_{ij} with filtered white noise acceleration time history $A(t)$, and correction function $F(t)$. Eq. (10) is shown below:

$$A_{ij}(t) = e_{ij}(t).A(t).F(t) \tag{10}$$

Step-7: The summation of acceleration time history records at each sub-fault gives final acceleration record $AC(t)$. Further, it is resolved into two horizontal components along EW and NS directions.

The schematic diagram of modified semi-empirical approach is shown in Figure 9. The summary of modified semi-empirical approach for simulation of NS and EW component of earthquake ground motion is illustrated in Figure 10.

6. Results and Discussion

The modified semi-empirical method is implemented to generate synthetic accelerograms of the 03 November 2002 Denali earthquake. A MATLAB code earlier written, has been modified with correction function to obtain synthetic accelerograms at each station (Rajaram and Pradeep, 2016; MATLAB, 2018). A comparison study of PGA, duration, frequency, response spectra has been done between observed and simulated ground

motions. The Fourier amplitude spectra and acceleration response spectra at all stations are shown in Figures 4 and 5. A comparison between PGA and duration of simulated and observed ground motions are shown in Figures 11 and 12. The synthetic accelerograms at selected stations are explained below:

Station PS10: The simulated accelerograms have lesser PGAs than observed accelerograms. The simulated PGA values are lesser than observed PGA values. A good match is observed between duration of simulated and observed ground motions. But, the Fourier amplitude spectrum overestimates the observed ground motion spectrum. A good match is observed between response spectra of observed and simulated ground motion.

Station PS09: The simulated accelerograms have higher PGAs than observed accelerograms. A good match is observed between duration of simulated and observed ground motions. The Fourier amplitude spectrum matches with observed ground motion spectrum. A good match is observed between response spectra of observed and simulated ground motion.

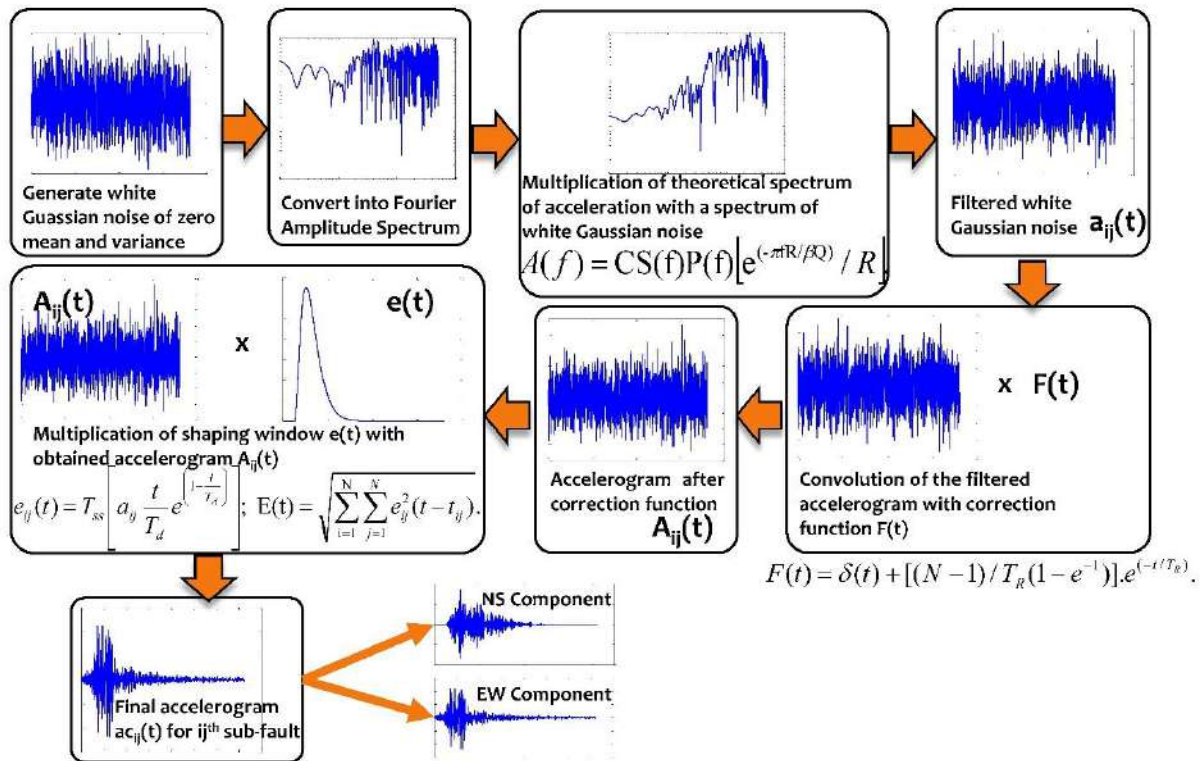


Fig. 9. Schematic diagram of modified semi-empirical approach

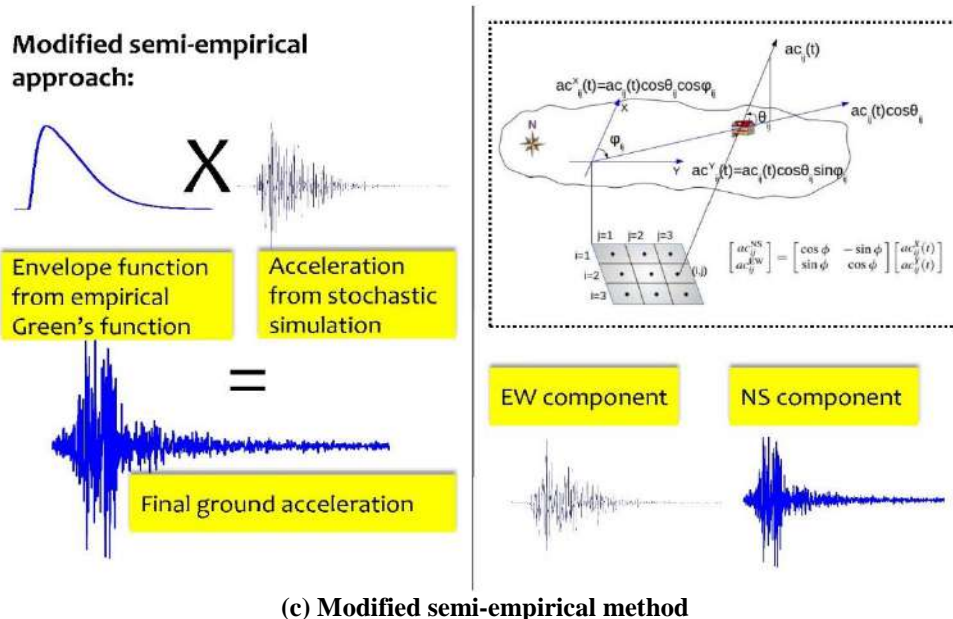
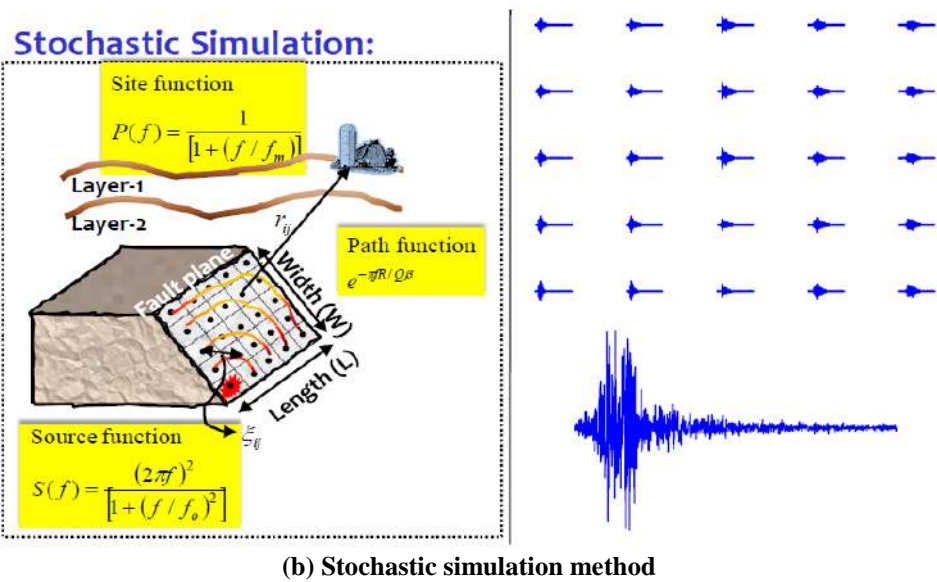
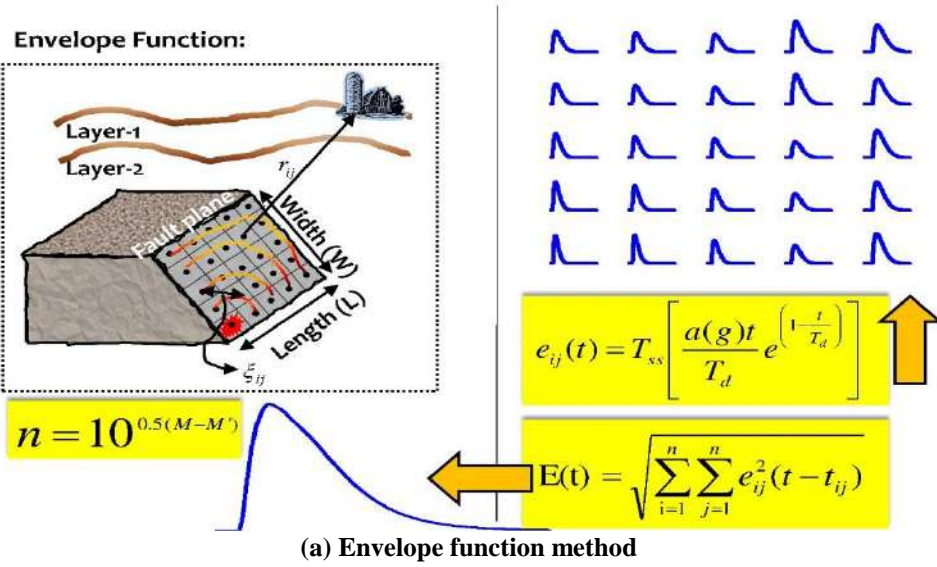


Fig. 10. Schematic diagram of: a) Envelope function method; b) Stochastic simulation method; and c) Modified semi-empirical method (combination of above methods)

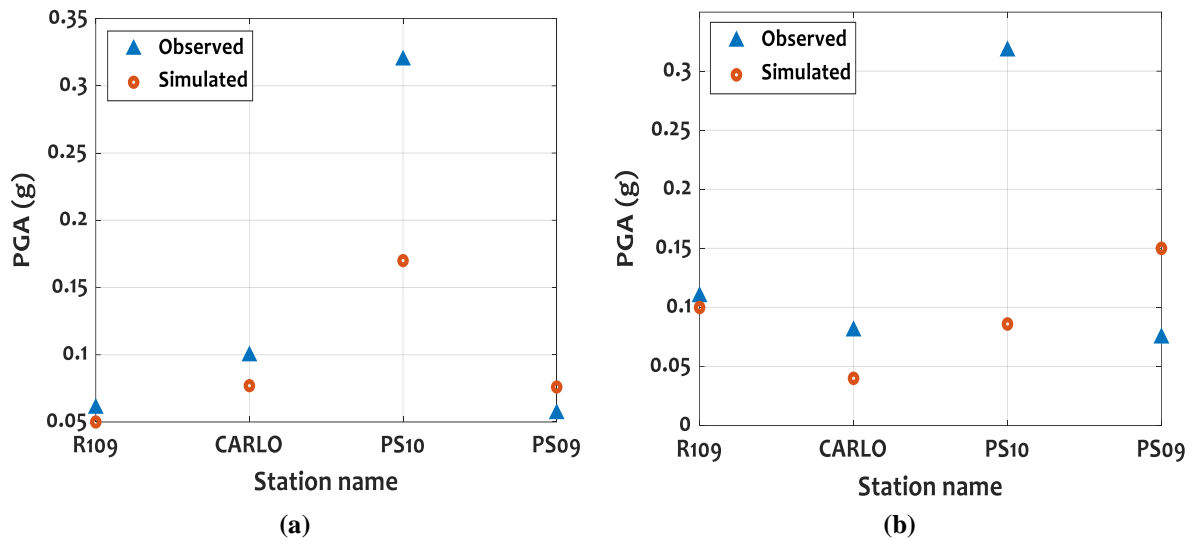


Fig. 11. Comparison of PGAs between observed and simulated ground motions during 2002 Denali earthquake: a) FP; and b) FN

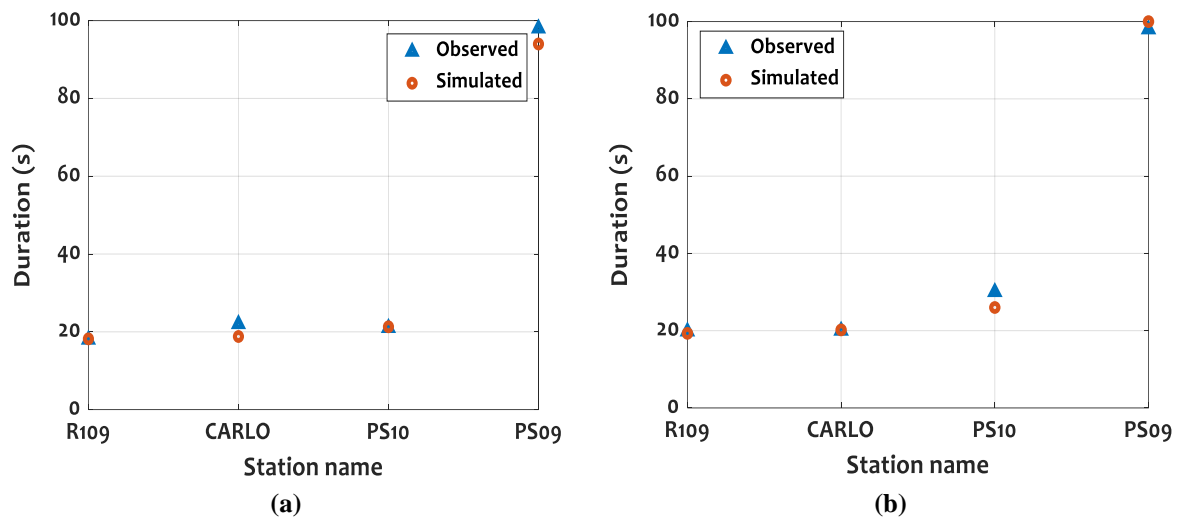


Fig. 12. Comparison of duration parameter between observed and simulated ground motions during 2002 Denali earthquake: a) FP; and b) FN

Station CARLO: The simulated accelerograms have lesser PGAs than observed accelerograms. A good match is observed between duration of simulated and observed ground motions. The Fourier amplitude spectrum matches with observed ground motion spectrum. A good match is observed between response spectra of observed and simulated ground motion.

Station R109: The simulated accelerograms have lesser PGAs than observed accelerograms. A good match is observed between duration of simulated and observed ground motions. The Fourier amplitude spectrum underestimates with observed ground motion spectrum. A good

match is observed between response spectra of observed and simulated ground motion.

From the results, it is observed that the variation between observed and simulated ground motions is due to lack of seismicity, and ground motion record data. Envelope waveform function plays a vital role in semi-empirical simulation which is dependent on GMPE. The PGA and duration of simulated ground motion give satisfactorily results with observed ground motions. Also, a good match is observed between response spectra and Fourier amplitude spectra between observed and simulated ground motions.

7. Conclusions

In this study, a strike-slip Denali fault was considered for studying the characteristics of ground motions through modified semi-empirical approach. A MATLAB code was modified with correction function to generate ground motion records of 2002 Denali earthquake. For this purpose, four seismic stations PS10, PS09, CARLO and R109 were selected that recorded the 2002 Denali earthquake. The acceleration records were compared with observed acceleration records at the stations. From the above results, it is concluded that the results obtained from the proposed approach are good with observed ground motion records at all stations. The PGA values obtained from the proposed approach are nearer to the observed PGA values at CARLO and R109 stations. A perfect match is observed between Fourier amplitude spectra of the simulated and observed ground motions at PS09 and CARLO stations. The response spectra obtained from simulated ground motion matches with observed ground motions at all stations.

8. References

- AEIC (Alaska Earthquake Information Center). (2019). <http://earthquake.alaska.edu/>
- Anderson, J.G. (2015), "The composite source model for broadband simulations of strong ground motions", *Seismological Research Letters*, 86(1), 68-74.
- Andrea, B. and Chao, L. (2016). "Near-field radiated wave field may help to understand the style of the super-shear transition of dynamic ruptures", *Physics of the Earth and Planetary Interiors*, 261, 133-140.
- Boore, D.M. (1983). "Stochastic simulation of high frequency ground motion based on seismological models of radiated spectra", *Bulletin of Seismological Society of America*, 73, 1865-1894.
- Consortium of Organizations for Strong-Motion Observation Systems (COSMOS). (2013), <http://strongmotioncenter.org/vdc/scripts/earthquakes.plx>, dated: 20 August 2013.
- Dreger, D. (2003). "Finite source modeling of great earthquakes", Annual Report, Berkeley Seismological Laboratory, University of California, Berkeley, United States of America.
- Hajiazizi, M., Taban, M.H. and Ghobadian, R. (2021). "Prediction of Q-value by multi-variable regression and novel Genetic Algorithm based on the most influential parameters", *Civil Engineering Infrastructures Journal*, 54(2), 267-280.
- Hasegawa, H.S., Basham, P.W. and Berry, M.J. (1981). "Attenuation relations for strong seismic ground motion in Canada", *Bulletin of Seismological Society of America*, 71, 1943-1962.
- Javier, L., Miguel, A.S., Miguel, A.J., Yanet, A. and Marcos, C. (2016). "Local earthquakes of the Mexico Basin in Mexico City: κ , Q , source spectra and stress drop", *Bulletin of the Seismological Society of America*, 106(4), 1423-1437.
- Kikuchi, M. and Yamanaka, Y. (2002). "Source rupture processes of the central Alaska earthquake of Nov. 3, 2002, inferred from tele-seismic body waves", EIC Seismological Note 129, Earthquake Research Institute (ERI), University of Tokyo, Tokyo.
- Krishnavajhala, S. (2021). "Simulation of strong ground motion in the National Capital Region, India, from a future 8.5 magnitude earthquake using two-step empirical Green's function method", *Bulletin of Seismological Society of America*, 111(4), 1-18.
- Lal, S., Joshi, A., Sandeep., Monu, T., Parveen, K., Chun-Hsiang, K., Che-Min, L., Kuo-Liang, W. and Sharma, M.L. (2018). "Modeling of the strong ground motion of 25th April 2015 Nepal earthquake using modified semi-empirical technique", *Acta Geophysica*, 66, 461-477.
- Lin, Z., Liu, Z.J., Weldon, R.J., Tian, J., Ding, C. and Du, Y. (2020). "Modeling repeated co-seismic slip to identify and characterize individual earthquakes from geomorphic offsets on strike-slip faults", *Earth and Planetary Science Letters*, 545, 1-14.
- MATLAB (2018). *The MathWorks, Inc.*, Natick, Massachusetts, United States of America.
- Midorikawa, S. (1993). "Semi-empirical estimation of peak ground acceleration from large earthquakes", *Tectonophysics*, 218, 287-295.
- Mobinipour, S.A. and Pourzeynali, S. (2020). "Assessment of near-fault ground motion effects on the fragility curves of tall steel moment resisting frames", *Civil Engineering Infrastructures Journal*, 53(1), 71-88.
- Ozacar, A.A. and Beck, S.L. (2004). "The 2002 Denali fault and 2001 Kunlun fault earthquakes: Complex rupture processes of two large strike-slip events", *Bulletin of Seismological Society of America*, 94, S278-S292.
- Rajaram, C. and Pradeep R.K. (2020). "Preliminary estimation of ground motion of September 24, 2013, Pakistan earthquake using modified semi-empirical approach", *Journal of Seismology and*

Earthquake Engineering, 22, 1-12.

- Rajaram, C. (2016). "Numerical modeling of near fault seismic ground motions for strike-slip and dip-slip faults", Ph.D. Thesis, International Institute of Information Technology, Hyderabad, India.
- Rajaram, C. and Pradeep R.K. (2016). "Simulation of near-field ground motion characteristics of May 01, 2013, Doda earthquake using modified semi-empirical approach", *Natural Hazards*, 82, 1411-1430.
- Ratchkovski, N.A., Hansen, R.A., Stachnik, J.C., Cox, T., Fox, O., Rao, L., Clark, E., Lafevers, M., Estes, S., MacCormack, J.B. and Williams, T. (2003). "Aftershock sequence of the Mw 7.9 Denali fault, Alaska, earthquake of 3 November 2002 from regional seismic network data", *Seismological Research Letters*, 74, 743-752.
- Sandeep, A., Joshi, A., Kamal, P., Kumar, A. and Kumar, P.D. (2015). "Modeling of strong motion generation areas of the Niigata, Japan, earthquake of 2007 using modified semi empirical technique", *Natural Hazards*, 77, 933-957.
- Sandeep, A., Joshi, A., Lal, S., Kumar, P. and Sah, S.K. (2017). "Simulation of strong ground motion of the 2009 Bhutan earthquake using modified semi-empirical technique", *Pure and Applied Geophysics*, 174(12), 4343-4356.
- Sato, R. (1989). *Handbook of fault parameters of Japanese earthquakes*, Kajima, Tokyo (in Japanese).
- Strong Motion Virtual Data Centre (SMVDC). (2015), <http://strongmotioncenter.org/vdc/scripts/earthquakes.plx>, dated: 20 August 2015.
- Tadahiro, K., Olga, J.K., Robert, B.D. and Walter, J.S. (2016). "Semi-automated procedure for windowing time series and computing Fourier amplitude spectra for the NGA-West2 database", PEER Report No. 2016/02, Pacific Earthquake Engineering Research Center, University of California, Berkeley, CA.
- Uenishi, K. (2017). "Rupture, waves and earthquakes", *Proceedings of the Japan Academy Series B: Physical and Biological Sciences*, 93(1), 28-49.
- United States Geological Survey (USGS). (2019). <https://www.usgs.gov/> dated: 24 April 2019.
- Wang, D., Mori, J. and Koketsu, K. (2016). "Fast rupture propagation for large strike-slip earthquakes", *Earth and Planetary Science Letters*, 440, 115-126.
- Yousef, B. and Jonathan, P.S. (2020). "Data resources for NGA-subduction project", PEER Report No. 2020/02, Pacific Earthquake Engineering Research Center, University of California, Berkeley, CA.



This article is an open-access article distributed under the terms and conditions of the Creative Commons Attribution (CC-BY) license.



Influences of Polyvinyl Alcohol Fiber Addition on the Specimen Size Effect and Energy Absorption of Self-Consolidating Concrete

Abbasi Nattaj Omrani, I.¹, Ardeshir-Behrestaghi, A.^{2*} and Saeedian, A.¹

¹ M.Sc., Department of Civil Engineering, Mazandaran University of Science and Technology, Babol, Iran.

² Assistant Professor, Department of Civil Engineering, Mazandaran University of Science and Technology, Babol, Iran.

© University of Tehran 2021

Received: 19 Sep. 2020;

Revised: 23 Jan. 2021;

Accepted: 30 Jan. 2021

ABSTRACT: Polyvinyl alcohol is one of the most efficient synthetic fibers in concrete technology; however, the size effect was rarely evaluated in Polyvinyl alcohol fiber-reinforced concretes. In this research, six types of SCC mixtures containing two dosages of PVA fibers were designed in two strength levels and different sizes of cylindrical specimens were cast. The fresh properties, 28-day compressive strength, and pre-peak energy per unit volume of PVA-FRSCC were evaluated through laboratory tests. Several theoretical models, including Size Effect Law, Modified Size Effect Law, Multi-fractal Scaling Law, and Sim et al. model, were also refined to study the size effect in the designed mixtures under uniaxial compressive failure. Based on the obtained results, the inclusion of Polyvinyl alcohol fibers had significant effect on the performance of the designed concretes. The incorporation of PVA fibers reduced the specimen size effect and improved the ductility and pre-peak energy absorption of plain SCC.

Keywords: Compressive Strength, Energy Absorption, Polyvinyl Alcohol Fiber, Self-Consolidating Concrete, Size Effect.

1. Introduction

Poor tensile strength and inadequate resistance to cracking are the main defects of conventional concrete. These weaknesses are caused by the propagation of micro cracks under the gradual variation of environment and applied loads (Juarez et al., 2015). Internal micro cracks are formed at the mortar-aggregate interface and initiate the brittle behavior of concrete structures (Jebli et al., 2018). It has been shown that the inclusion of randomly distributed fibers can reduce the above

mentioned problems and improve the mechanical characteristics of concrete by bridging the micro cracks (Li et al., 2018; Chang et al., 2020; Sobhani and Pourkhorshidi, 2021). Ramezani and Esfahani (2018) showed that the addition of the optimum amount of steel fibers, alongside with Polypropylene fibers, can enhance the durability and scaling resistance of concretes subjected to cold weather environments.

Polyvinyl alcohol (PVA) is a hydrophilic synthetic fiber that forms a strong connection with the hydrated Portland

* Corresponding author E-mail: ardashir_b_eng@yahoo.com

cement and obtains a noticeable tensile strength, ranging from 880 to 1600 MPa (Si et al., 2020; Ling et al., 2020). Several research studies have focused on the incorporation of PVA fibers in Engineered Cementitious Composites (ECC) (Arain et al., 2019; Zhang and Zhang, 2018; Wang et al., 2020), and structural concretes (Wang et al., 2017; Nuruddin et al., 2015; Xie et al., 2018). According to the mentioned studies, PVA fibers applied noteworthy improvements on the mechanical performance and ductility of concrete. Despite improving these aspects, the addition of synthetic fibers decreases the homogeneity and fluidity of concrete, and causes obstacles in the consolidation process of fresh concrete (Cao et al., 2017).

On the other hand, the durability and mechanical distinction of Fiber-Reinforced Concrete (FRC) can be hampered by improper compaction, which also interrupts the uniform dispersion of fibers. Thus, it is necessary for FRC to obtain a sufficient viscosity and eliminate the demand for mechanical vibration in its consolidation process. Self-Consolidating Concrete (SCC) has managed to push the boundaries and solve the mentioned problems. Unlike conventional concrete, SCC is a highly-workable concrete that compacts itself without utilizing mechanical vibration and flows through the cramped spaces between congested reinforcements in complex formworks (Si et al., 2018).

The synergy between SCC and FRC, called Fiber-Reinforced Self-Consolidating Concrete (FRSCC), merges the rheological stability of SCC with the mechanical advantages of FRC, and eliminate the need for external vibration. In this type of concrete, fiber volume fraction connects the fresh and hardened properties of the material. Therefore, obtaining the optimum fiber volume fraction is one of the most important parameters of FRSCC mixtures (Ferrara et al., 2012).

The dissimilarity between the compressive strength of laboratory size specimens and larger structural elements is

another fundamental challenge. Heterogeneous quasi-brittle materials like concrete, are affected by the size effect phenomenon due to the energy released in the Fracture Process Zone (FPZ), which unlike the Linear Elastic Fracture Mechanics (LEFM), is large and full of cracks. The non-linear behavior of concrete in this large inelastic zone indicates that its nominal compressive strength is influenced by both shape and size of the specimen (Bazant and Oh, 1983).

According to the size effect phenomenon, smaller samples achieve higher strength compared with larger specimens. Based on the fracture mechanics, Bazant (1984) presented a theoretical model, called Size Effect Law (SEL), for specimens with equivalent shapes and crack lengths as follows:

$$f_c(D) = \frac{B f_{cs}}{\sqrt{1 + \frac{D}{D_0}}} \quad (1)$$

where $f_c(D)$: is the compressive strength of specimen, f_{cs} : is the compressive strength of standard cylindrical (150 × 300 mm) or cubic (150 × 150 × 150 mm) specimen, D : is the specimen diameter, and B and D_0 : are to be accomplished via regression analysis as the experimental coefficients.

By adding a size-independent parameter to the Bazant model, Kim and Eo (1990) developed the SEL and proposed the Modified Size Effect Law (MSEL) based on the non-linear fracture mechanics. They indicated that versus the Bazant model, large structural members without initial cracks can withstand stress; therefore, specimens with equivalent shapes and varying initial cracks were examined. MSEL is:

$$f_c(D) = \frac{B f_{cs}}{\sqrt{1 + \frac{D}{D_0}}} + C f_{cs} \quad (2)$$

where B , C , and D_0 : are to be accomplished via regression analysis as the experimental coefficients.

Based on the fractal nature of concrete microstructure, Carpinteri and Chiaia (1997) presented a theoretical model, called Multifractal Scaling Law (MFSL). They indicated that the impacts of material disarray on the mechanical characteristics of concrete diminished, as the specimen diameter increased. They proposed the MFSL model as follows:

$$f_c(D) = f_{c_{\infty}} \sqrt{1 + \frac{L_{ch}}{D}} \quad (3)$$

where $f_{c_{\infty}}$ and L_{ch} : are to be accomplished via regression analysis as the experimental coefficients.

Sim et al. (2013) considered more operative elements like the aspect ratio and unit weight of concrete, and presented a new theoretical model. They reported that the size effect vanished, as the unit weight of concrete increased. Their model is:

$$f_c(D) = \frac{A \sqrt{n_1^{X_4}}}{\sqrt{1 + B D \left(\frac{\rho_c}{\rho_0}\right)^{-X_2}}} f_{cs} + C f_{cs} \quad (4)$$

where ρ_0 : is the unit weight of normal weight concrete, equals to 2300 kg/m^3 , and A , B , C , X_2 , and X_4 : are to be accomplished via regression analysis as the experimental coefficients.

Some of these models were originally designed to assess the size effect in tensile failure; however, the ultimate failure of specimens under uniaxial compression is also caused by the propagation of macro-cracks, implying Mode I failure. Thus, through considering the compressive strength of standard specimens, the mentioned models can be applied for the compressive failure of concretes without initial notch (Asadollahi et al., 2016).

The purpose of this research is to conduct an experimental and numerical investigation to evaluate the impacts of PVA fiber addition on the fresh properties, 28-day compressive strength, specimen size effect, and pre-peak behavior of self-consolidating concrete.

The permeability characteristics and

mechanical behavior of concretes, containing alternative aggregates and fibers, have been studied before in the pre-peak region of stress-strain curves (Prathipati et al., 2020; Cui et al., 2012). In this study, the effect of PVA fibers on the pre-peak performance of SCC is assessed under compression. Also, the empirical coefficients of several size effect models, including SEL, MSEL, MFSL, and Sim et al. (2013) model, were obtained via regression analysis for PVA-FRSCC mixtures.

2. Materials and Methods

2.1. Cement and Aggregates

The utilized fine particles are type II Portland cement, conforming to ASTM C150 (ASTM, 2002), natural river sand with bulk specific gravity and water absorption of 2.63 and 1.95%, respectively, and limestone powder, as the filler material (Madani et al., 2016). The used coarse aggregate was also provided from a local river, having a bulk specific gravity of 2.67, water absorption of 1.3%, and the maximum size of 12.5 mm, conforming to ASTM C33 (ASTM, 2003). Figures 1 and 2 illustrate the gradation of the fine and coarse aggregates, respectively.

2.2. Fiber and Chemical Admixtures

In order to attain a fluid SCC, high-performance poly-carboxylate superplasticizer was used in all mixtures. The utilized water was clean tap water. As one of the main factors of FRSCC mixtures, fiber volume fractions were carefully designed after conducting several experiments. Polyvinyl alcohol fiber with a length of 6 mm and volume fractions of 0.05% and 0.08% was used in the designed mixtures. The utilized fibers were manufactured at Anhui Wanwei group Co. No surface pre-treatment was conducted on the fibers, to maintain the fiber/mortar bonding quality. The mechanical properties of polyvinyl alcohol fiber are given in Table 1 (Hossain et al., 2013). Figure 3 shows the image of the fiber.

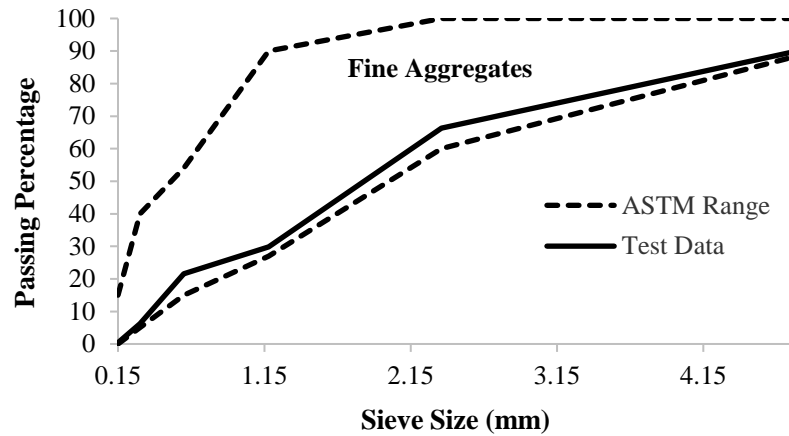


Fig. 1. Gradation of the utilized fine aggregates

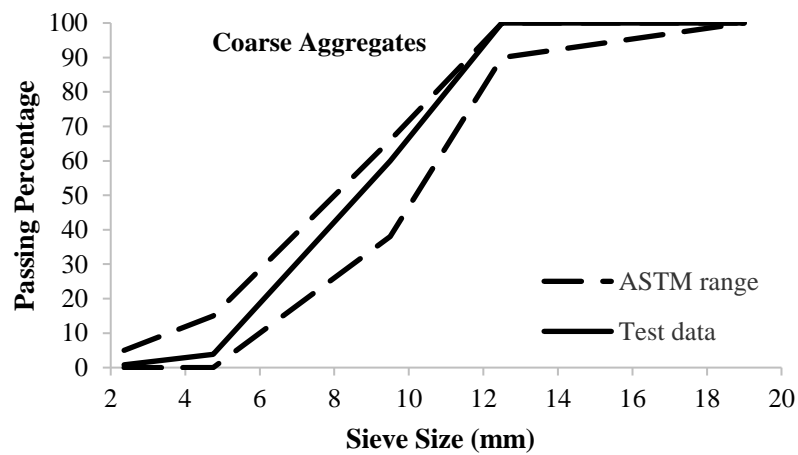


Fig. 2. Gradation of the utilized coarse aggregates



Fig. 3. Polyvinyl alcohol fiber with a length of 6 mm

Table 1. Properties of PVA fibers (Hossain et al., 2013)

Property	PVA fiber
Density (kg/m^3)	1300
Young's modulus (GPa)	32
Length (mm)	6
Diameter (mm)	0.04
Tensile strength (MPa)	1400
Elongation capacity (%)	7

2.3. Mixture Procedure

An experimental process was carried out to design the optimal mix proportions. Six types of FRSCC mixtures containing two different dosages of PVA fibers were created in two strength classes, including LSCC, LSCC-PVA-0.05, LSCC-PVA-0.08, MSCC, MSCC-PVA-0.05, and MSCC-PVA-0.08, where LSCC and MSCC stand for low strength SCC and medium strength SCC, respectively. The exact mix proportions are provided in Table 2.

Although higher dosages of PVA fibers were used in other cementitious composites, the incorporation of these hydrophilic fibers in self-consolidating concretes must be limited due to the specific requirements of SCC at the fresh state. It was reported that the inclusion of 0.15% and 0.2% of PVA fibers can cause serious decrease in the workability and fluidity of self-consolidating concrete (Hossain et al., 2012). The mentioned report has been proven through the experimental phase of this research. At first, 0.15% and 0.2% of PVA fibers were included into the matrix; however, noticeable decrease in the flowability of concrete was observed, and the fresh properties of these mixtures did not reach the self-consolidating criteria. Also, this obstacle could not be solved through increasing the amount of superplasticizer or heightening the W/C ratio, because increasing the amount of these elements can compromise the homogeneity of the system. After trying several fiber dosages, the optimum volumes of PVA fibers were achieved in this study.

In addition, the incorporation of these low volumes of PVA fibers can still imply noticeable effect on the hardened behavior of SCC. For example, it was reported that the addition of 0.125% of PVA fibers increased the 28-day splitting tensile and flexural strength of SCC by 44.4% and 26.4%, respectively (Hossain et al., 2013).

The W/C ratios of the plain mixtures and fiber-reinforced mixtures were kept similar; however, higher amounts of cement and water were utilized in fiber-reinforced

mixtures in an analogous way, to provide the suitable hydration process of cementitious particles. It was observed that low water and cement content can cause serious segregation in fiber-reinforced mixtures. This phenomenon is due to the hydrophilic properties of PVA fibers. Thus, the optimum amounts of water and cementitious particles were included in PVA fiber-reinforced mixtures to prevent segregation and control the presence of PVA fibers inside the matrix.

Ninety cylindrical (Cy) specimens with three different diameters of 75, 100, and 150 mm, and an aspect ratio (height/diameter) of 2, were cast. A laboratory concrete mixer was used to prepare the FRSCC mixtures. First, the natural river sand and coarse aggregates were mixed for 10 seconds. Then, the combination of cement and limestone powder was added into the mixture, and after mixing for 30 seconds, 65% of the total volume of plain water was dispersed throughout the mixture, and mixing continued for another 30 seconds. Afterwards, the residual water containing the whole superplasticizer was included and stirring was continued for 1 minute. After stopping for 10 seconds, PVA fibers were distributed gradually into the mixture and blended for 2 minutes to achieve a homogeneous fiber-reinforced SCC.

2.4. Curing Process and Preparation for Testing

Once the mixing operation was over, fresh concrete tests were carried out to examine the fresh stability of SCC before and after the addition of PVA fibers. The mentioned tests were slump flow time and diameter, V-funnel flow time, and L-box, conforming to EFNARC (2005) and ACI 237R (ACI, 2007). The obtained results of these tests can assess the fluidity, segregation resistance, filling ability, and passing ability of fresh concrete in restricted and unconfined conditions (EFNARC, 2005).

Table 2. Mix proportions of PVA-FRSCC mixtures (kg/m³)

Mixing schemes	Water	Cement	W/C	Fine agg.	Coarse agg.	Limestone powder	Super plasticizer	Fibers
LSCC	192	400	0.48	850	667	215	6.5	---
LSCC-PVA-0.05	240	500	0.48	850	667	215	8.125	0.65
LSCC-PVA-0.08	240	500	0.48	850	667	215	8.125	1.04
MSCC	178.6	470	0.38	800	667	215	12	---
MSCC-PVA-0.05	226.6	596.3	0.38	800	667	215	15.2	0.65
MSCC-PVA-0.08	226.6	596.3	0.38	800	667	215	15.2	1.04

After conducting the fresh concrete tests, cylindrical specimens were cast without any external vibration. The samples were demolded after 24 hrs of casting and cured in a water pool until the required duration of the compressive strength test, conforming to ASTM C192 (ASTM, 2006a). After 28 days of curing, neoprene pads were used to cap the specimens, according to ASTM C1231 (ASTM, 2006b), and the compressive strength test was operated by using a 200-KN pressure jack, conforming to ASTM C39 (ASTM, 2006c). In these tests, the axial load was applied at the rate of 3 kN/s. Figure 4 shows the symbolic failure mode of cylindrical specimens.

3. Results and Discussions

3.1. Fresh Properties

Fresh properties of the PVA-FRSCC mixtures are given in Table 3. According to the Slump flow time (T_{500} time) test results, the incorporation of 0.05% and 0.08% of PVA fibers increased the recorded time for low strength SCC by 27.14% and 65%,

respectively, and increased the recorded time for medium strength SCC by 5.67% and 21.27%, respectively. According to the results of the Slump flow diameter test, the inclusion of 0.05% and 0.08% of PVA fibers lessened the fluidity of low strength SCC by 4.42% and 21.4%, respectively, and lowered the fluidity of medium strength SCC by 6.87% and 19.37%, respectively. LSCC-PVA-0.08 had the lowest fluidity among the mixtures, reaching a diameter of about 532 mm, while the least approved value of spread for SCC is supposed to be 550 mm (EFNARC, 2005).

The results of the V-funnel flow time test showed that all mixtures met the requirements of SCC (6 s to 12 s), and obtained a sufficient segregation resistance (EFNARC, 2005). According to the test results, the addition of 0.05% and 0.08% of PVA fibers decreased the filling ability of low strength SCC by 5.7% and 12.58%, respectively, and lessened the filling ability of medium strength SCC by 1.97% and 9.7%, respectively.

**Fig. 4.** Typical crack pattern of failed cylindrical specimens

Table 3. Fresh properties of PVA-FRSCC mixtures

Mixing schemes	Slump flow		V-funnel (s)	L-box (H_2/H_1)
	T_{500} (s)	D-final (mm)		
LSCC	1.4	677	8.42	0.8
LSCC-PVA-0.05	1.78	647	8.9	0.76
LSCC-PVA-0.08	2.31	532	9.48	0.68
MSCC	4.23	716	10.61	0.85
MSCC-PVA-0.05	4.47	667	10.82	0.83
MSCC-PVA-0.08	5.13	577	11.64	0.78

Based on the L-box test results, the inclusion of 0.05% and 0.08% of PVA fibers decreased the passing ability of low strength SCC by 5% and 15%, respectively, and lowered the passing ability of medium strength SCC by 2.35% and 8.23%, respectively. Except for LSCC, MSCC, and MSCC-PVA-0.05, other mixtures did not achieve the approved L-box index for SCC, which is 0.8 (EFNARC, 2005).

As expected, the hydrophilic nature of PVA fiber causes a reduction in the workability and fluidity of fresh SCC. Moreover, increasing the PVA fiber volume fraction heightens the slump reduction in both low strength and medium strength mixtures. This impact was more significant in low strength mixtures.

3.2. Compressive Strength

The 28-day compressive strength test results for cylindrical specimens are given in Table 4. Increasing the diameter of cylindrical specimens from 75 to 150 mm, lowered the average compressive strength of LSCC, LSCC-PVA-0.05 and LSCC-PVA-0.08 by 19.54%, 17.6% and 12.84%, respectively, and decreased the average compressive strength of MSCC, MSCC-PVA-0.05 and MSCC-PVA-0.08 by 12.56%, 12.65% and 8.55%, respectively. The compressive strength of three samples were studied for each specimen size, and the standard deviation of these data sets are included in Table 4.

Figure 5 illustrates the reduction of compressive strength, as the size of cylindrical specimen increases. As can be observed from Figure 5, the inclusion of PVA fibers lowered the rate of strength reduction and lessened the size effect in cylinders. This effect was more pronounced

in specimens containing 0.08% of PVA fibers. Based on the test results, the inclusion of 0.05% and 0.08% of PVA fibers decreased the rate of the strength reduction of low strength cylinders by 17.19% and 49.07%, respectively, and lowered the rate of the strength reduction of medium strength cylinders by 8.53% and 42.02%, respectively. Consequently, increasing the PVA fiber volume fraction heightens the diminution of the size effect in cylinders. The addition of PVA fibers improves the ductility of the brittle self-consolidating concrete by counteracting the spread of internal micro cracks and creating a well-made connection with the cementitious mortar. Thus, PVA fiber-reinforced SCC can exhibit a better resistance against the size effect.

Table 5 summarizes the equations of strength reduction. Increasing the PVA fiber volume fraction lessened the gradient of these equations, which indicates a reduction in the dependency of the concrete's strength on the specimen size.

As expected from Hossain et al. (2013) results, the compressive strength of cylindrical specimen was decreased by increasing the PVA fiber content. Unlike Khaloo et al. (2014) results, it can be seen from Table 4 that increasing the PVA fiber volume fraction caused a greater rate of strength reduction in medium strength specimens, compared with low strength specimens. It can be assumed that the low amount of water in medium strength specimen allows the hydrophilic PVA fiber to develop higher internal voids that causes a considerable strength reduction.

3.3. Theoretical Analysis of Size Effect

The empirical coefficients of four size

effect models (see Eqs. (1-4)), were achieved through regression analysis, and the mentioned size effect models were refined for the designed concretes. Tables 6 to 9 summarize the results for SEL, MFSL, MSEL and Sim et al. model, respectively. In addition, the correlation coefficients (R^2)

were obtained by utilizing non-linear model fit in Mathematica. As can be observed from these tables, the high values of R^2 demonstrate the efficiency of the refined models in evaluating the size effect of the designed mixtures.

Table 4. Results of the 28-day compressive strength test

Mixing schemes	Size (mm)		Compressive strength (MPa)				Average
	Diameter	Height	Test 1	Test 2	Test 3	Standard deviation	
LSCC	75	150	22.8	28.1	29	2.73	26.6
	100	200	26.1	23.3	25.1	1.58	24.8
	150	300	23.6	19.9	20.8	1.57	21.4
LSCC-PVA-0.05	75	150	29.2	19.9	26	3.85	25
	100	200	23.9	22.4	21	1.18	22.4
	150	300	23.8	18.9	19.1	2.26	20.6
LSCC-PVA-0.08	75	150	22.1	23	20.4	1.07	21.8
	100	200	21.1	18.7	19.4	1	19.7
	150	300	22.1	18.1	17	2.19	19
MSCC	75	150	35.5	34.4	37.6	1.32	35.8
	100	200	36.8	30.8	32.1	2.57	33.2
	150	300	34.6	30.4	29.1	2.34	31.3
MSCC-PVA-0.05	75	150	32.5	31	31.4	0.63	31.6
	100	200	29.6	29.6	30.4	0.37	29.8
	150	300	23.6	28.7	30.5	2.92	27.6
MSCC-PVA-0.08	75	150	30.1	31.9	29.2	1.12	30.4
	100	200	31.3	27.3	27.9	1.76	28.8
	150	300	32	25.1	26.3	3	27.8

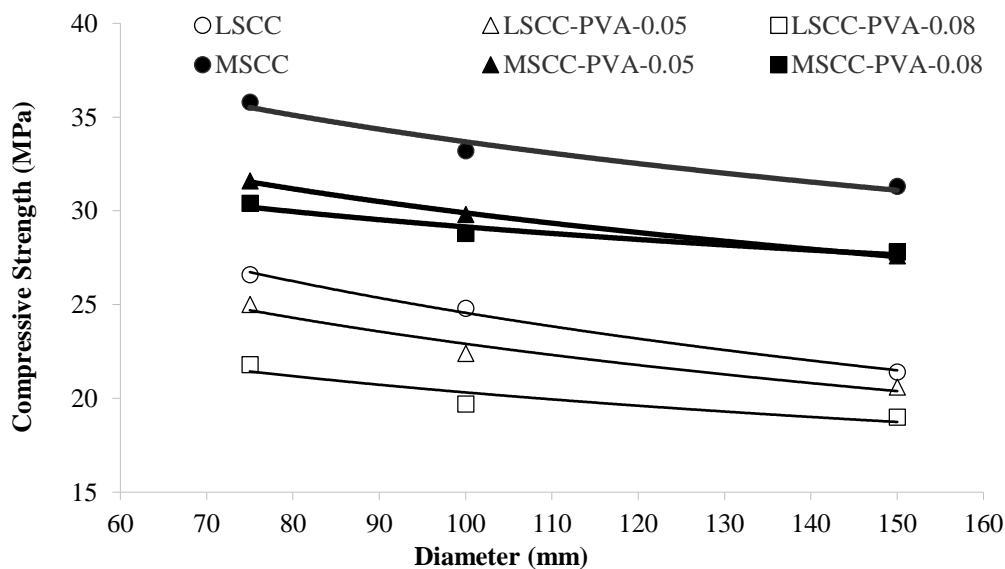


Fig. 5. Compressive strength reduction of low strength and medium strength cylindrical specimens with different diameters

Table 5. Logarithmic equations of strength reduction for different mixes

Mixing schemes	Logarithmic equations
LSCC	$y = -7.56 \ln(x) + 59.379$
LSCC-PVA-0.05	$y = -6.22 \ln(x) + 51.567$
LSCC-PVA-0.08	$y = -3.88 \ln(x) + 38.223$
MSCC	$y = -6.37 \ln(x) + 63.035$
MSCC-PVA-0.05	$y = -5.74 \ln(x) + 56.364$
MSCC-PVA-0.08	$y = -3.66 \ln(x) + 46.031$

Table 6. SEL relation coefficients for different mixes with the use of nonlinear regression analysis

Mixing schemes	Coefficients		
	B	D_0	R^2
LSCC	1.84	63.47	0.99
LSCC-PVA-0.05	1.66	81.25	0.98
LSCC-PVA-0.08	1.35	171.62	0.99
MSCC	1.35	173.97	0.99
MSCC-PVA-0.05	1.37	164.91	0.99
MSCC-PVA-0.08	1.2	319.47	0.99

Table 7. MFSL relation coefficients for different mixes with the use of nonlinear regression analysis

Mixing schemes	Coefficients		
	$f_{c\infty}$	L_{ch}	R^2
LSCC	14.6	179.01	0.99
LSCC-PVA-0.05	14.79	136.66	0.98
LSCC-PVA-0.08	15.62	67.79	0.99
MSCC	26.03	65.85	0.99
MSCC-PVA-0.05	22.91	68.53	0.99
MSCC-PVA-0.08	24.84	36.52	0.99

Table 8. MSEL relation coefficients for different mixes with the use of nonlinear regression analysis

Mixing schemes	Coefficients			
	B	C	D_0	R^2
LSCC	6.68	-5.16	858.5	0.99
LSCC-PVA-0.05	30.64	0.47	0.042	0.98
LSCC-PVA-0.08	24.6	0.64	0.029	0.99
MSCC	17.75	0.65	0.055	0.99
MSCC-PVA-0.05	1.28	0.57	18.47	0.99
MSCC-PVA-0.08	11.66	0.77	0.055	0.99

Table 9. Chemical and physical properties of natural zeolite according to ASTM C618

Mixing schemes	Coefficients					
	A	B	C	X_2	X_4	R^2
LSCC	1.17	0.11	0.02	145.8	1.31	0.99
LSCC-PVA-0.05	4.92	2.57	0.47	-107.91	13.86	0.98
LSCC-PVA-0.08	6.71	4.9	0.64	-263.55	29.78	0.99
MSCC	569.62	46.87	1.06	-14048.9	-1208.76	0.99
MSCC-PVA-0.05	0.95	0.24	0.57	16.43	0.85	0.99
MSCC-PVA-0.08	6.2	9.56	0.77	-107.07	15.08	0.99

Figures 6a and 6b assess the effects of PVA fiber addition on the SEL results of low strength and medium strength cylinders. The mentioned figures indicate that medium strength cylindrical specimens exhibit a greater inclination toward the strength criterion and obtain higher values of transitional size (D_0), compared with low strength cylindrical specimens, conforming to Dehestani et al. (2014) results. Furthermore, the inclusion of PVA fibers lessened the size effect by switching the

SEL results toward the strength criterion. This trend was more significant in mixtures containing 0.08% of fiber content.

Table 10 compares the obtained SEL results with the reported results of Saedian et al. (2017), in order to differentiate between the impacts of PVA fibers and Polypropylene fibers. Based on the data of Table 10, the addition of 0.08% of PVA fibers increased the transitional size of low strength cylinders by 170.39%. Whereas, the incorporation of 0.25% of

Polypropylene fibers, with the length of 6 mm, increased the same aspect in low strength cylinders by 5.22%, in Saeedian et al. (2017) research. Consequently, PVA fibers seem to be more efficient in switching the SEL results of cylindrical specimens toward the strength criterion, compared with Polypropylene fibers.

Figures 7a and 7b display the diagrams of MFSL for cylindrical specimens. Medium strength cylindrical specimens obtained lower values of internal characteristic length (L_{ch}) and had a greater tendency toward the Euclidian regime, compared with low strength cylindrical

specimens. Thus, low strength cylinders show a more brittle behavior. In addition, it can be observed from Figures 7a and 7b that the incorporation of PVA fibers lessened the impacts of specimen size and shifted the MFSL results toward the plastic criterion in both low strength and medium strength cylinders. Also, as expected from the multifractal scaling law, enlarging the specimen size decreased the effects of material disorder in cylinders; meaning that the MFSL results tended to move away from the fractal regime, as the cylinder diameter increased.

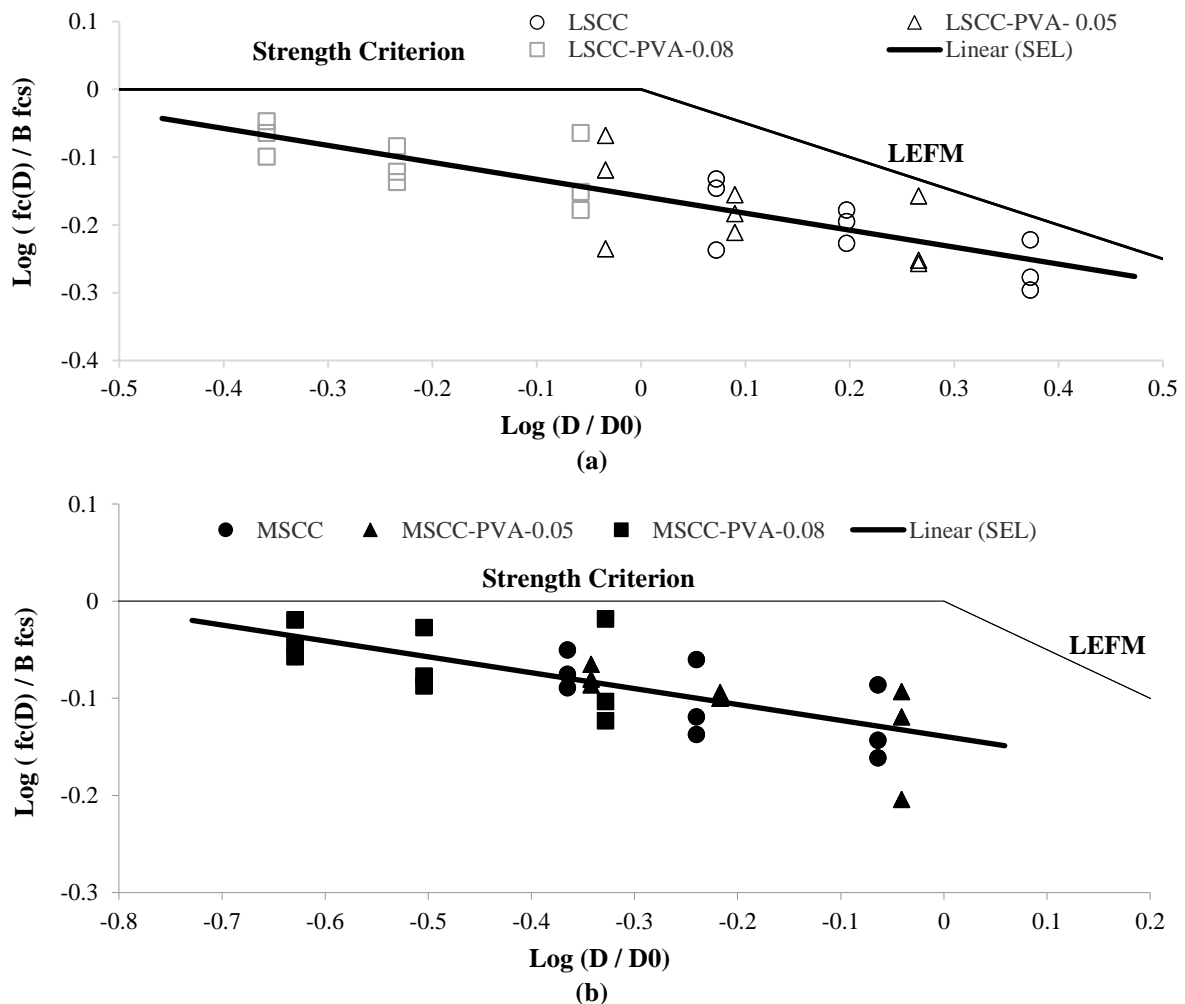


Fig. 6. a) Results of size effect law (SEL) for low strength cylinders; and b) Results of size effect law (SEL) for medium strength cylinders

Table 10. Comparison of transitional size coefficient (D_0) in the present study and Saeedian et al. (2017) research

Reference	Fiber type (Length)	Fiber volume fraction	D_0 of SEL	
			Plain LSCC	Fiber reinforced LSCC
Saeedian et al. (2017)	Polypropylene fiber (6 mm)	0.25%	118.72	124.92
The present study	Polyvinyl alcohol fiber (6 mm)	0.08%	63.47	171.62

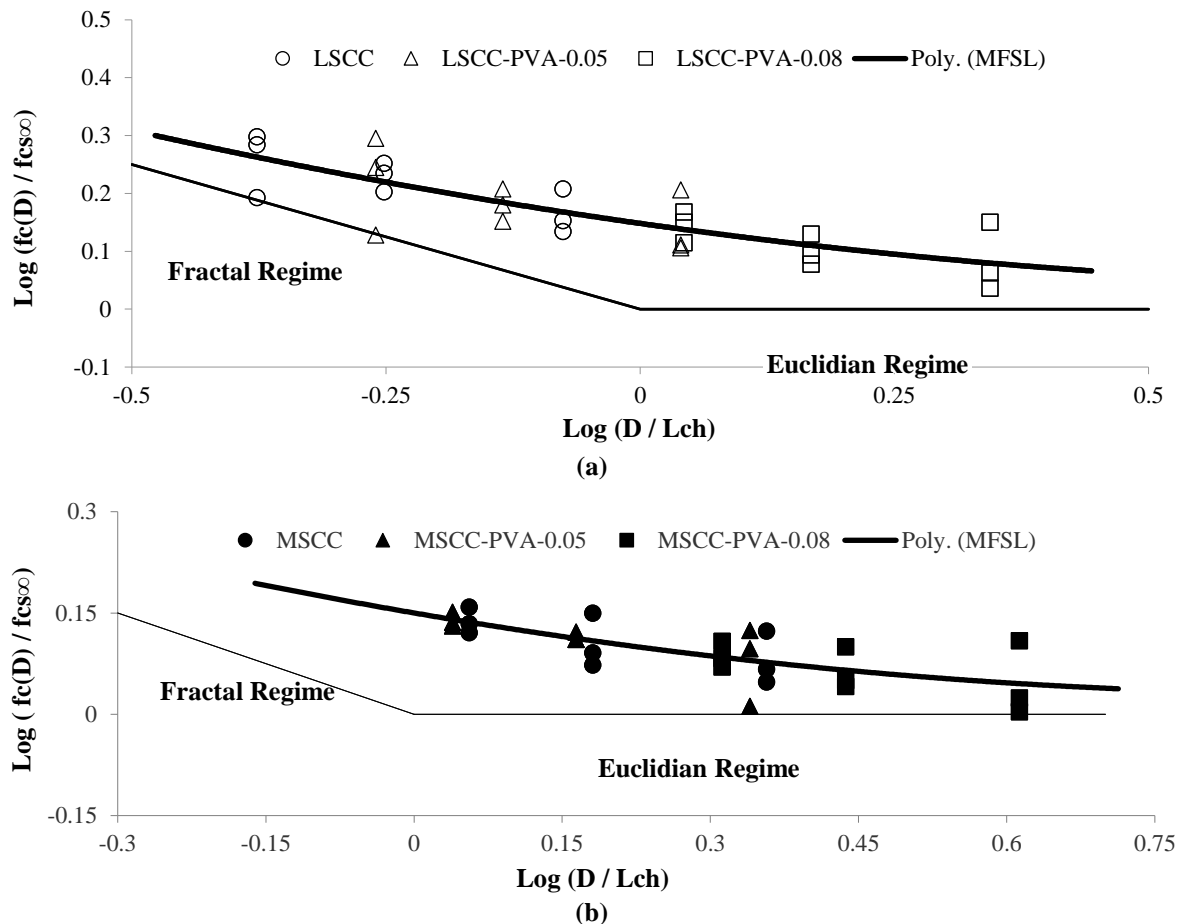


Fig. 7. a) Results of multifractal scaling law (MFSL) for low strength cylinders; and b) Results of multifractal scaling law (MFSL) for medium strength cylinders

Table 11 compares the obtained MFSL results with the reported results of Akbari et al. (2019). As can be observed from this table, the inclusion of 0.3% of steel fibers with a length of 33 mm in Akbari et al. (2019), lessened the internal characteristic length of cylindrical specimens by 49.37%. While, the addition of 0.08% of PVA fibers in the present study decreased the internal characteristic length of medium strength cylinders by 44.54%.

In order to evaluate the credibility of the refined size effect equations, scatter plots of predicted compressive strength versus measured compressive strength are displayed in Figures 8a to 8f. As can be seen from these figures, the predictions of the refined size effect models show an analogous tendency compared to the measured data for all mixtures. Thus, the obtained empirical coefficients of the size effect models, presented in Eqs. (1-4), can analyze the size effect and predict the

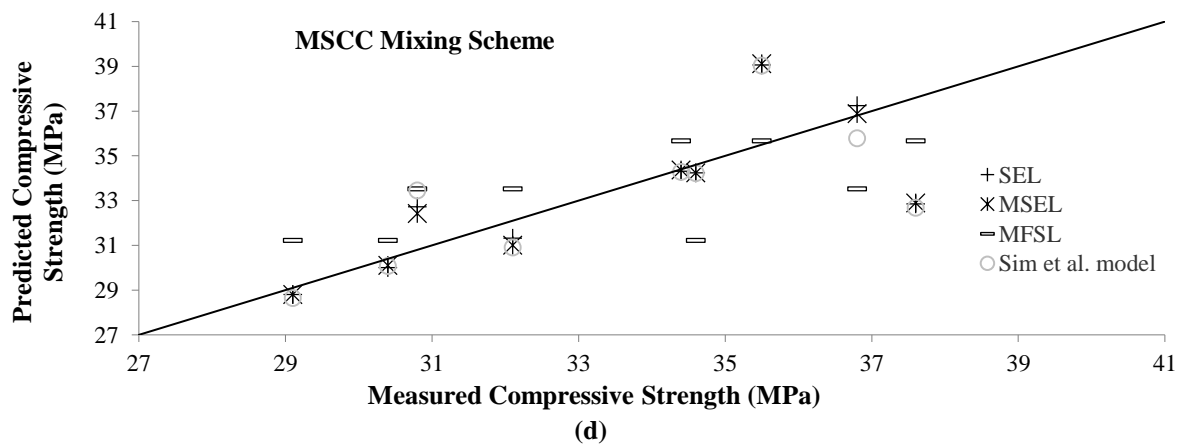
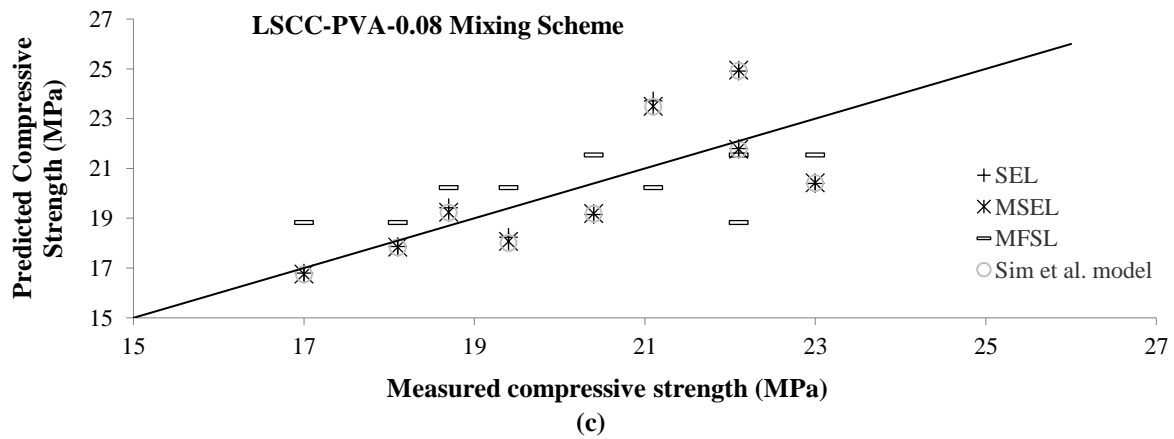
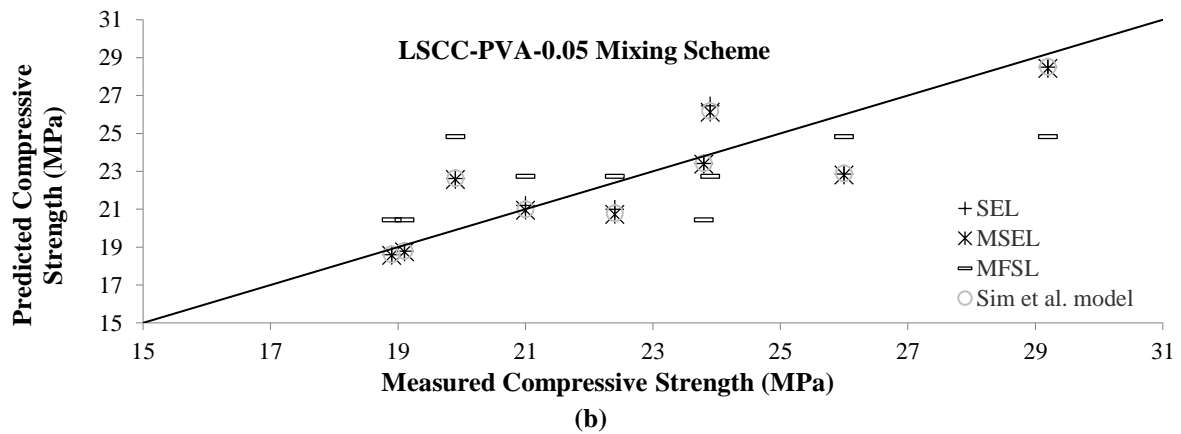
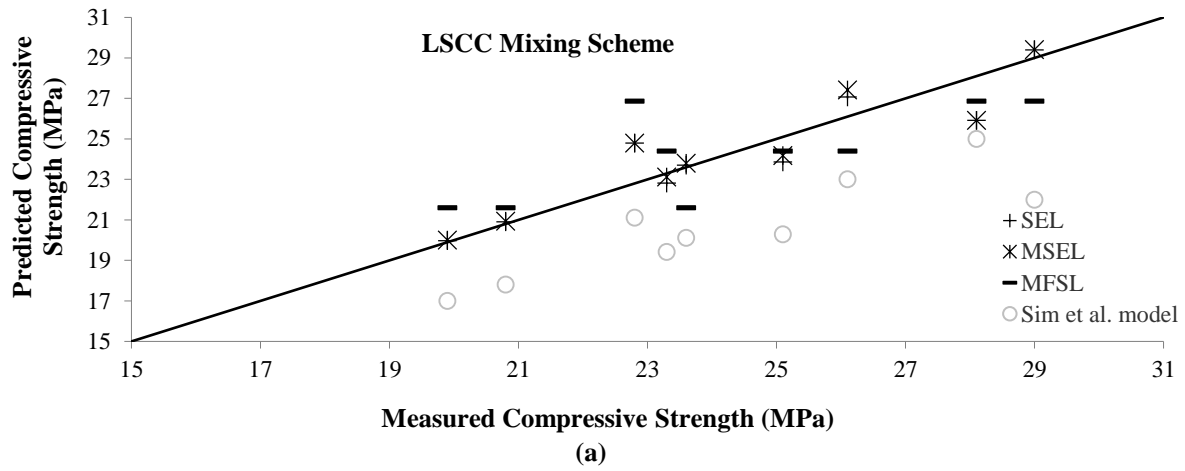
strength for PVA fiber-reinforced self-consolidating concretes.

3.4. Pre-Peak Stress-Strain Curves

Figures 9a and 9b display the pre-peak stress-strain curves of low strength and medium strength standard cylinders under compression, respectively. It has already been reported that the localization of compressive failure and initiation of internal micro cracks gradually begins in the pre-peak portion of stress-strain curve. Through measuring this area, the pre-peak energy per unit volume of concrete can be assessed, which represents the dissipation of energy due to the formation of micro cracks up to peak stress (Jansen and Shah, 1997). The mentioned area was calculated

via $E = \int_0^{\varepsilon} \sigma d\varepsilon$ relation, where E , σ and ε :

represent pre-peak energy absorption, stress and strain, respectively.



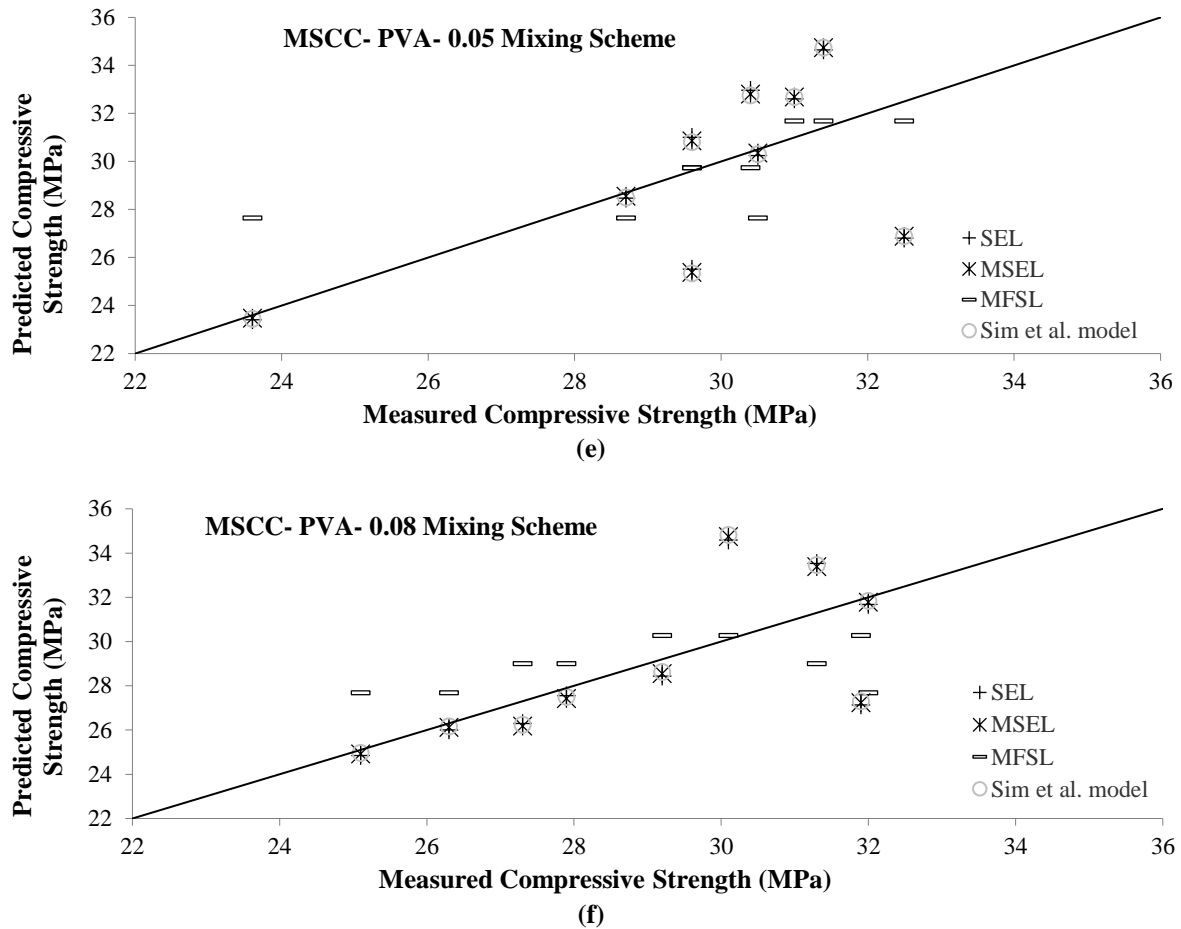


Fig. 8. a) Comparison between the predicted and measured compressive strength results for LSCC mixing scheme; b) Comparison between the predicted and measured compressive strength results for LSCC-PVA-0.05 mixing scheme; c) Comparison between the predicted and measured compressive strength results for LSCC-PVA-0.08 mixing scheme; d) Comparison between the predicted and measured compressive strength results for MSCC mixing scheme; e) Comparison between the predicted and measured compressive strength results for MSCC-PVA-0.05 mixing scheme; and f) Comparison between the predicted and measured compressive strength results for MSCC-PVA-0.08 mixing scheme

Table 11. Comparison of internal characteristic length coefficient (L_{ch}) in the present study and Akbari et al. (2019) research

Reference	Fiber type (Length)	Fiber volume fraction	L_{ch} of MFSL	
			Plain MSCC	Fiber reinforced MSCC
Akbari et al. (2019)	Steel fiber (33mm)	0.3%	86.16	43.62
The present study	Polyvinyl alcohol fiber (6mm)	0.08%	65.85	36.52

As can be seen from Figures 9a and 9b, increasing the PVA fiber content expanded this area for low strength and medium strength cylinders, which indicates an increment in the energy absorption and ductility of concrete in the pre-peak stress-strain portion. The shapes of the fiber-reinforced and plain specimen's curves are mostly linear; however, the stretched strain of fiber-reinforced specimens indicate a higher curvature for fiber-reinforced cylinders at peak stress. Also, the inclusion of PVA fibers increased the strain of

specimens at peak stress, under compressive failure. This trend was more significant in cylinders incorporating 0.08% of PVA fibers. Table 12 reports the impacts of PVA fiber addition on the pre-peak stress-strain characteristics of SCC. Based on the obtained results, the addition of 0.05% and 0.08% of PVA fibers increased the pre-peak energy per unit volume of low strength cylinders by 51.7% and 61.3%, respectively, and heightened the mentioned aspect of medium strength cylinders by 23.3% and 42.5%, respectively.

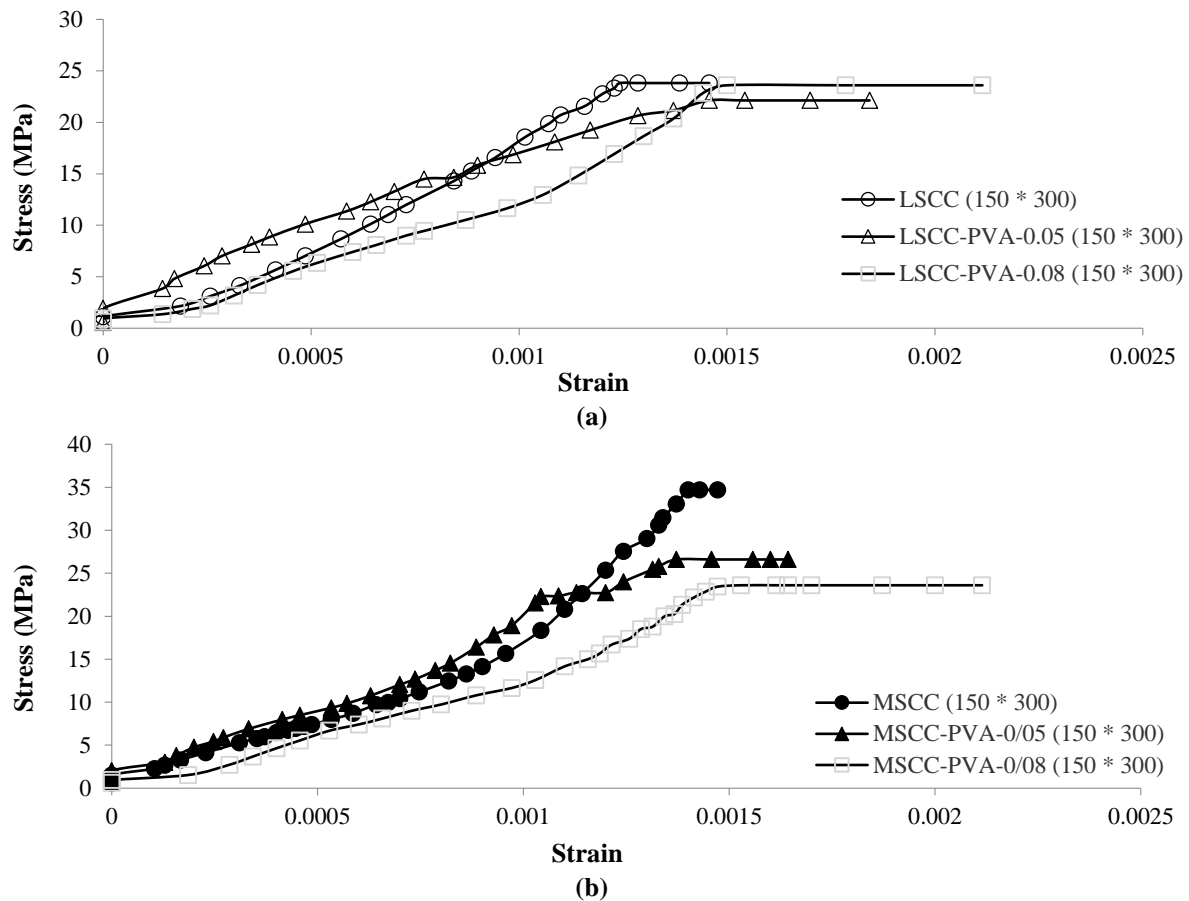


Fig. 9. a) Pre-peak stress-strain curve of low strength cylinders with the diameter of 150 mm containing different dosages of PVA fibers; and b) Pre-peak stress-strain curve of medium strength cylinders with the diameter of 150 mm containing different dosages of PVA fibers

Table 12. Pre-peak energy absorption per unit volume for standard cylinders

Mixing schemes	E (N.mm/mm ³)
LSCC	0.01814
LSCC-PVA-0.05	0.02752
LSCC-PVA-0.08	0.02927
MSCC	0.02058
MSCC-PVA-0.05	0.02539
MSCC-PVA-0.08	0.02933

4. Conclusions

Four theoretical models, including SEL, MSEL, MFSL, and Sim et al. model, were refined to evaluate the size effect in PVA fiber-reinforced SCC mixtures under compression. These conclusions have been drawn:

- All cylindrical specimens exhibited a more ductile behavior after the inclusion of PVA fibers. The addition of 0.08% of PVA fibers lowered the rate of strength reduction in low strength and medium strength cylinders by 49.07% and 42.02%, respectively, as the specimen

diameter increased. Furthermore, the hydrophilic properties of PVA fibers lessened the compressive strength of all samples. This effect was more noteworthy in medium strength specimens containing a lower amount of internal water.

- Increasing the PVA fiber content shifted the SEL results toward the strength criterion and reduced the size effect in cylinders. The addition of 0.08% of PVA fibers heightened the transitional size of low strength cylinders and medium strength cylinders by 170.39% and 83.63%, respectively.

- The MFSL results indicated a more brittle behavior in smaller samples. The incorporation of 0.08% of PVA fiber content lowered the internal characteristic length of low strength cylinders and medium strength cylinders by 62.13% and 44.54%, respectively. PVA fiber-reinforced cylindrical specimens with a W/C ratio of 0.38 attained the least values of internal characteristic length and revealed the best performance against the size effect.
- The pre-peak energy per unit volume of low strength and medium strength standard cylinders were calculated through evaluating the area under the stress-strain curves up to peak stress. According to the obtained results, the inclusion of PVA fibers enhanced the ductility of both low strength and medium strength specimens in the pre-peak portion of stress-strain curve, and increased the strain at peak stress.

5. Acknowledgements

This work was supported by the Civil Engineering Department of Mazandaran University of Science and Technology.

6. References

- ACI (American Concrete Institute). (2007). *Self-consolidating concrete*, ACI 237R-07, Farmington Hills, MI.
- Akbari, M., Khalilpour, S. and Dehestani, M. (2019). "Analysis of material size and shape effects for steel fiber reinforcement self-consolidating concrete", *Engineering Fracture Mechanics*, 206, 46-63.
- Araim, M.F., Wang, M., Chen, J. and Zhang, H. (2019). "Study on PVA fiber surface modification for strain-hardening cementitious composites (PVA-SHCC)", *Construction and Building Materials*, 197, 107-116.
- Asadollahi, S., Saeedian, A., Dehestani, M. and Zahedi, F. (2016). "Improved compressive fracture models for self-consolidating concrete (SCC)", *Construction and Building Materials*, 123, 473-80.
- ASTM. (2002). *Standard specification for Portland cement*, ASTM C150, West Conshohocken, PA.
- ASTM. (2003). *Standard specification for concrete aggregates*, ASTM C33/C33M-16, West Conshohocken, PA.
- ASTM. (2006a). *Standard practice for making and curing concrete test specimens in the laboratory*, ASTM C192/C192M-02, West Conshohocken, PA.
- ASTM. (2006b). *Standard practice for use of unbonded caps in determination of compressive strength of hardened cylindrical concrete specimens*, ASTM C1231/C1231M-15, West Conshohocken, PA.
- ASTM. (2006c). *Standard test method for compressive strength of cylindrical concrete specimens*, ASTM C39/C39M-16b, West Conshohocken, PA.
- Bažant, Z.P. and Oh, B.H. (1983). "Crack band theory for fracture of concrete", *Matériaux et Construction*, 16(3), 155-177.
- Bažant, Z.P. (1984). "Size effect in blunt fracture: concrete, rock, metal", *Journal of engineering mechanics*, 110(4), 518-535.
- Cao, Q., Cheng, Y., Cao, M. and Gao, Q. (2017). "Workability, strength and shrinkage of fiber reinforced expansive self-consolidating concrete", *Construction and Building Materials*, 131, 178-185.
- Carpinteri, A. and Chiaia, B. (1997). "Multifractal scaling laws in the breaking behavior of disordered materials", *Chaos Solitons Fractals*, 8(2), 135-150.
- Chang, J., Cui, K. and Zhang, Y. (2020). "Effect of hybrid steel fibers on the mechanical performances and microstructure of sulphoaluminate cement-based reactive powder concrete", *Construction and Building Materials*, 261, 120502.
- Cui, H.Z., Lo, T.Y., Memon, S.A., Xing, F. and Shi, X. (2012). "Experimental investigation and development of analytical model for pre-peak stress-strain curve of structural lightweight aggregate concrete", *Construction and Building Materials*, 36, 845-859.
- Dehestani, M., Nikbin, I.M. and Asadollahi, S. (2014). "Effects of specimen shape and size on the compressive strength of self-consolidating concrete (SCC)", *Construction and Building Materials*, 66, 685-691.
- EFNARC (European Federation of National Associations Representing for Concrete). (2005). *Specification and guidelines for self-compacting concrete*, Surrey, U.K.
- Ferrara, L., Bamonte, P., Caverzan, A., Musa, A. and Sanal, I. (2012). "A comprehensive methodology to test the performance of steel fiber reinforced self-compacting concrete (SFR-SCC)", *Construction and Building Materials*, 37, 406-424.
- Hossain, K.M.A., Lachemi, M., Sammour, M. and Sonebi, M. (2013). "Strength and fracture energy characteristics of self-consolidating concrete incorporating polyvinyl alcohol, steel and hybrid

- fibers", *Construction and Building Materials*, 45, 20-29.
- Hossain, K.M.A., Lachemi, M., Sammour, M. and Sonebi, M. (2012). "Influence of Polyvinyl alcohol, steel, and hybrid fibers on fresh and rheological properties of self-consolidating concrete", *Journal of Materials in Civil Engineering*, 24, 1211-1220.
- Jansen, D.C. and Shah, S.P. (1997). "Effect of length on compressive strain softening of concrete", *Journal of Engineering Mechanics*, 123(1), 25-35.
- Jebli, M., Jamin, F., Malachanne, E., Garcia-Diaz, E. and El-Youssoufi, M.F. (2018). "Experimental characterization of mechanical properties of the cement-aggregate interface in concrete", *Construction and Building Materials*, 161, 16-25.
- Juarez, C.A., Fajardo, G., Monroy, S., Duran-Herrera, A., Valdez, P. and Magniont, C. (2015). "Comparative study between natural and PVA fibers to reduce plastic shrinkage cracking in cement-based composite", *Construction and Building Materials*, 91, 164-170.
- Khaloo, A., Raisi, E.M., Hosseini, P. and Tahsiri, H. (2014). "Mechanical performance of self-compacting concrete reinforced with steel fibers", *Construction and Building Materials*, 51, 179-186.
- Kim, J.K. and Eo, S.H. (1990). "Size effect in concrete specimens with dissimilar initial cracks", *Magazine of Concrete Research*, 42(153), 233-238.
- Li, B., Chi, Y., Xu, L., Shi, Y. and Li, C. (2018). "Experimental investigation on the flexural behavior of steel-polypropylene hybrid fiber reinforced concrete", *Construction and Building Materials*, 191, 80-94.
- Ling, Y.F., Zhang, P., Wang, J. and Shi, Y. (2020). "Effect of sand size on mechanical performance of cement-based composite containing PVA fibers and nano-SiO₂", *Materials*, 13(2), 325.
- Madani, H., Ramezani-pour, A.A., Shahbazinia, M., Bokaeian, V. and Ahari, S. (2016). "The influence of ultrafine filler materials on mechanical and durability characteristics of concrete", *Civil Engineering Infrastructures Journal*, 49(2), 251-262.
- Nuruddin, M.F., Ullah Khan, S., Shafiq, N. and Ayub, T. (2015). "Strength prediction models for PVA fiber-reinforced high-strength concrete", *Journal of Materials in Civil Engineering*, 27(12), 04015034.
- Prathipati, S.R.R.T., Rao, C.B.K. and Murthy, N.R.D. (2020). "Mechanical behavior of hybrid fiber reinforced high strength concrete with graded fibers", *International Journal of Engineering*, 33(8), 1465-1471.
- Ramezani, A.R. and Esfahani, M.R. (2018). "Evaluation of hybrid fiber reinforced concrete exposed to severe environmental conditions", *Civil Engineering Infrastructures Journal*, 51(1), 119-130.
- Saedian, A., Dehestani, M., Asadollahi, S. and Vaseghi Amiri, J. (2017). "Effect of specimen size on the compressive behavior of self-consolidating concrete containing polypropylene fibers", *Journal of Materials in Civil Engineering*, 29(11), 04017208.
- Si, R., Wang, J., Guo, S., Dai, Q. and Han, S. (2018). "Evaluation of laboratory performance of self-consolidating concrete with recycled tire rubber", *Journal of Cleaner Production*, 180, 823-831.
- Si, W., Cao, M. and Li, L. (2020). "Establishment of fiber factor for rheological and mechanical performance of polyvinyl alcohol (PVA) fiber reinforced mortar", *Construction and Building Materials*, 265, 120347.
- Sim, J.I., Yang, K.H., Kim, H.Y. and Choi, B.J. (2013). "Size and shape effects on compressive strength of lightweight concrete", *Construction and Building Materials*, 38, 854-864.
- Sobhani, J., Pourkhorshidi, A. (2021). "The effects of cold-drawn crimped-end steel fibers on the mechanical and durability of concrete overlay", *Civil Engineering Infrastructures Journal*, 54(2), 319-330.
- Wang, L., Zhou, S.H., Shi, Y., Tang, S.W. and Chen, E. (2017). "Effect of silica fume and PVA fiber on the abrasion resistance and volume stability of concrete", *Composite Part B: Engineering*, 130, 28-37.
- Wang, Q., Lai, M.H., Zhang, J., Wang, Z. and Ho, J.C.M. (2020). "Greener engineered cementitious composite (ECC), The use of pozzolanic fillers and oiled PVA fibers", *Construction and Building Materials*, 247, 118211.
- Xie, T., Mohamed Ali, M.S., Visintin, P. and Oehlers, D.J. (2018). "Partial interaction model of flexural behavior of PVA fiber-reinforced concrete beams with GFRP bars", *Journal of Composites for Construction*, 22(5), 04018043.
- Zhang, Z. and Zhang, Q. (2018). "Matrix tailoring of Engineered Cementitious Composites (ECC) with non-oil-coated, low tensile strength PVA fiber", *Construction and Building Materials*, 161, 420-431.



This article is an open-access article distributed under the terms and conditions of the Creative Commons Attribution (CC-BY) license.



Reduction Factors for Laterally Loaded Pile Groups Accounting for Pile Cross Sections and Soil Properties

Talebi, A.¹ and Derakhshani, A.^{2*}

¹ M.Sc. Student, Department of Civil Engineering, Faculty of Engineering, Shahed University, Tehran, Iran.

² Associate Professor, Department of Civil Engineering, Faculty of Engineering, Shahed University, Tehran, Iran.

© University of Tehran 2021

Received: 29 Sep. 2020;

Revised: 03 Apr. 2021;

Accepted: 17 Apr. 2021

ABSTRACT: P-y analysis approach is among the most widely used methods implemented for simulating the pile behavior under lateral loading. To obtain the p-y curve of a pile group, that of a single pile should be modified by a group reduction factor which is conventionally determined by the pile spacing to diameter ratio and the pile row number in the group. The pile section types and soil characteristics i.e. internal friction angle are among other important factors affecting the group reduction factor. However, the influence of these parameters has not been investigated in previous researches, thoroughly. In this study, continuum models of eight pile groups with different conditions regarding pile section types and soil properties were built and analyzed. It was found that the group reduction factor of the pile group with square tube section is less than that of the group of piles with pipe sections, due to group effects. On the other hand, for the pile groups of both section types, the greater internal friction angle, increases the shadowing and edge effects which results in lower group reduction factor. Moreover, the group reduction factors calculated based on numerical modeling results were compared with the recommendations of AASHTO and FEMA guidelines. It was also shown that the continuum model results conform with the results of experimental studies.

Keywords: Group Reduction Factor, Internal Friction Angle, Pile Group, P-y Curve, Section Properties, Soil-Pile Interaction.

1. Introduction

In addition to axial force, piles should be designed to withstand lateral load. The lateral forces may be applied to the piles used in the structures such as walls retaining the soil pressure, port structures influenced by the mooring forces, offshore structures that are under the influence of waves and marine currents, high-rise structures which

are affected by the wind and different types of structures founded on piles in earthquake-prone zones. The piles experience lateral deformation under lateral loading and interact with the surrounding soil. Therefore, the analysis of piles under lateral load is complicated and the lateral load effects on the pile behavior should be analyzed by appropriate methods (Asaadi et al., 2017; Hajitaheriha et al., 2021).

* Corresponding author E-mail: adera@shahed.ac.ir

In general, piles are rarely used individually, so the study of pile group behavior is of utmost importance in geotechnical engineering. On the other hand, the lateral bearing capacity of a single pile differs from that of the same pile in a pile group. Each pile under lateral force, creates a shear zone in the front soil, and by overlapping these areas created by the nearby piles, the shear area is enlarged. If the spacing between the adjacent piles in a row or in different rows decreases, there will be more interference. The pile-soil-pile interaction is mainly due to the effect of adjacent piles in a row of piles on each other (edge effect) as well as the mutual effects of piles in two adjacent rows (shadowing effect). These two group effects are shown in Figure 1.

To consider the non-linear behavior of the soil-pile interaction, p-y curves are typically utilized, where, p is the soil resistance and, y is the horizontal

displacement. It should be noted that in this method, the pile group effects are taken into account by applying a correction coefficient called P-multiplier (P_m) for each row of the pile group (Figure 2). Because of the decrease in the pile bearing capacity due to group effects, this corrective factor is less than or equal to one.

The p-y curves are empirical curves that model the non-linear behavior of the soil. These curves are derived from the piles behavior under horizontal load in real conditions. Using these curves is very common for simulating the soil behavior in professional practice. Depending on the type of soil at each depth, the corresponding p-y curve is determined. Then, these curves describe the behavior of non-linear springs to be used along the piles for analysis. There are programs specifically developed for analyzing piles under horizontal loads using p-y curves (Das, 2015).

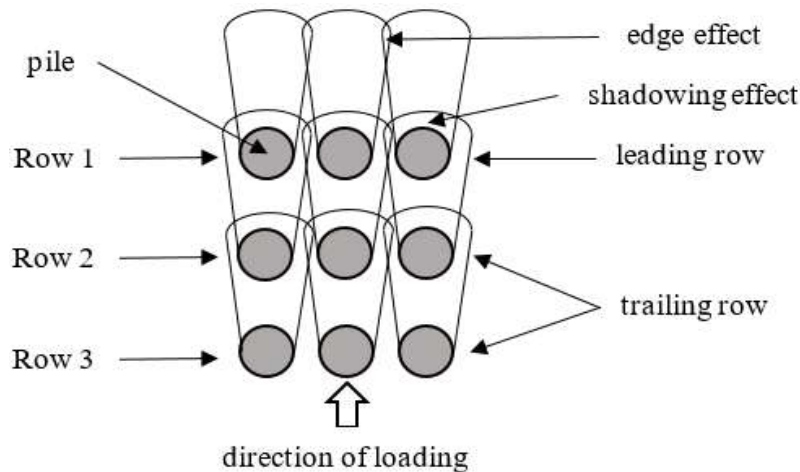


Fig. 1. Rows of pile group and overlapping zones (Fayyazi et al., 2012b)

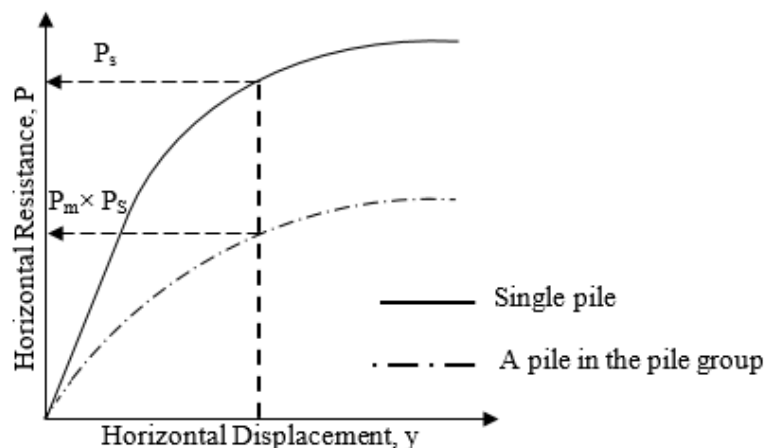


Fig. 2. P-multiplier definition (Fayyazi et al., 2014)

The maximum value of corrective coefficient i.e. P_m in a pile group, is for the first row which is called the leading row (Figure 1), and the lower values of P_m are corresponding to the next rows called trailing rows. Hence, as pile rows get closer to the lateral load, the P-multiplier becomes smaller (Brown et al., 1988).

P-multipliers can be obtained by performing a full-scale test. In the same way, many studies have been conducted in clay and sand (Ruesta and Townsend, 1997; Rollins et al., 1998; Brown et al., 2001; Rollins and Sparks, 2002; Rollins et al., 2003; Snyder, 2004; Rollins et al., 2005; Walsh, 2005; Rollins et al., 2006). But, physical modelling with full scale is difficult and costly. Hence, centrifuge experiments have also been used to calculate P_m as conducted by McVay et al. (1995, 1998) and Taghavi and Muraleetharan (2016). Another method for calculation of P_m , is to model the pile groups on the basis of continuum mechanics (Law and Lam, 2001; Fayyazi et al., 2012a,b, 2014; Tehrani et al., 2016; Asadi et al., 2017). In this way, it is possible to solve a variety of problems involving different types of piles and soils. The artificial intelligence-based methods have been also utilized to solve geotechnical engineering problems (Saeedi Azizkandi and Fagher, 2014; Kohestani et al., 2017; Avval and Derakhshani, 2019; Khorrami and Derakhshani, 2019; Jafariavval and Derakhshani, 2020; Khorrami et al., 2020) amongst which the P-multipliers were estimated by the Genetic Programming and Model Tree approaches (Khoshroo and Derakhshani, 2020; Talebi and Derakhshani, 2019).

As per cyclic nature of seismic loads, the leading and trailing rows are interchanged by changing direction of lateral load. In order to account for this load reversal, one can consider the average P_m value of different rows. This average corrective coefficient is referred to as the “group reduction factor”. Due to the above-mentioned problems associated with

experimental studies, available laboratory data are limited, so that it is difficult to study about group reduction factors. To solve this problem, data from numerical modelling under various conditions can be used to compute the P-multipliers and consequently the group reduction factors.

In this study, the group reduction factor is calculated for groups of piles with different sections in various soils using a three-dimensional continuum modeling approach. The ability of the Finite Element Method (FEM) for numerical modeling of the pile group behavior was first investigated by modelling a full-scale experiment and comparing the predictions and observations. Then, the model is used to evaluate various groups of piles with either pipe or square tube sections in the soils of different internal friction angle values. Next, the effects of variations of these key parameters on the group reduction factor are assessed. Finally, the group reduction factors computed based on numerical results of this study, are compared with those recommended in codes of practice and experimental data.

2. Validation of the Continuum Model

To verify the performance of the continuum model, an existing well-documented laboratory research was considered. Christensen (2006) tested a full-scale 3×3 pile group under lateral load in a multilayered soil. In this experiment, the piles were 324 mm in diameter with a thickness of 9.5 mm and a length of 12.8 m. The position of piles in pile group and the loading direction are depicted in Figure 3. Properties of the soil profile in the test site are given in Table 1.

Christensen (2006) calculated the row reduction factors of the pile group. By simulating the behavior of the tested pile group using p-y curves, he computed the P_m values of 1, 0.7 and 0.65, for the leading row as well as the second and third (trailing) rows. The group reduction factor which is equal to the average reduction factors of the

rows, was 0.783 for this experiment.

Christensen test was used to validate the continuum model built using FEM in the Abaqus3D (Hibbitt et al., 2016; Rezaei et al., 2016). In Figure 4, the model geometry is presented in which the pile positions in the soil as well as the FE mesh are visible. Solid elements were used to model piles and soil in the continuum model. The Mohr-Coulomb constitutive model was used in the continuum model. Additionally, according to the sensitivity analysis, for the soil model dimension being sufficiently large and boundary does not affect quality of modeling results, the 5D and 10D intervals

are respectively considered from outer piles in the perpendicular direction to the lateral load and in the lateral load direction (Fayyazi et al., 2014).

To verify the accuracy of the numerical modeling, the results of the Christensen test were compared with the corresponding results from the continuum model. To this end, two important curves of total group load-deflection curve and bending moment distribution along the pile are exhibited in Figures 5 and 6, respectively. As can be seen, the values obtained from numerical modeling and those measured in the test are in good agreement.

Table 1. Characteristics of different soil layers in the study of Christensen (2006)

Depth (m)	Unit weight (kN/m ³)	Shear modulus (kN/m ²)	Poisson's ratio	Friction angle (degrees)	Dilation angle (degrees)	Undrained shear strength (kN/m ²)
0-2.1	16.7	29600	0.3	40	0	0
2.1-2.4	16.8	15800	0.3	40	0	0
2.4-2.7	19.1	7000	0.3	0	0	41
2.7-3.7	19.1	7000	0.3	0	0	50
3.7-4.6	19.1	8100	0.3	0	0	40
4.6-6.3	18.1	17800	0.3	38	0	0
6.3-8	19.1	6500	0.3	0	0	57
8-12.8	16.7	22600	0.3	33	0	0

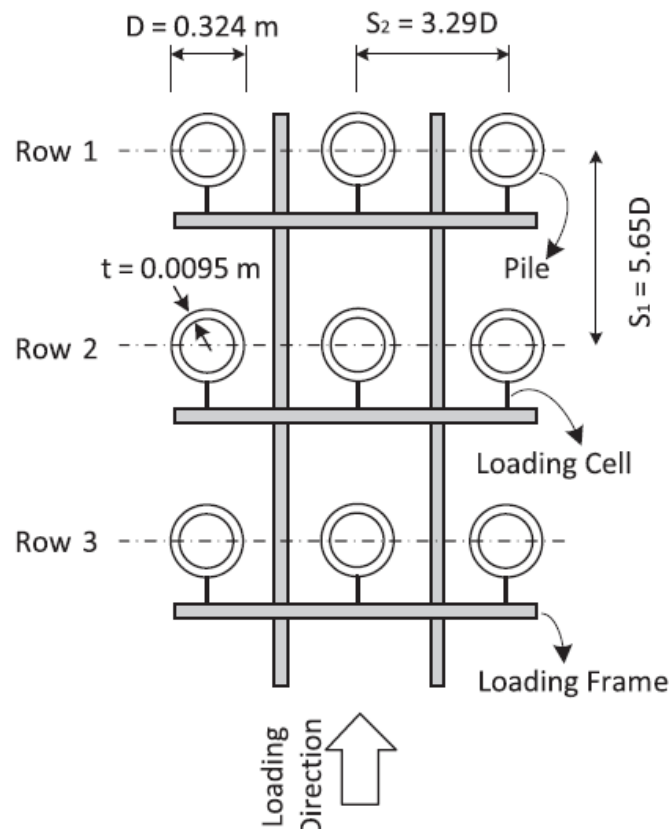


Fig. 3. Plan of the pile group test conducted by Christensen (2006)

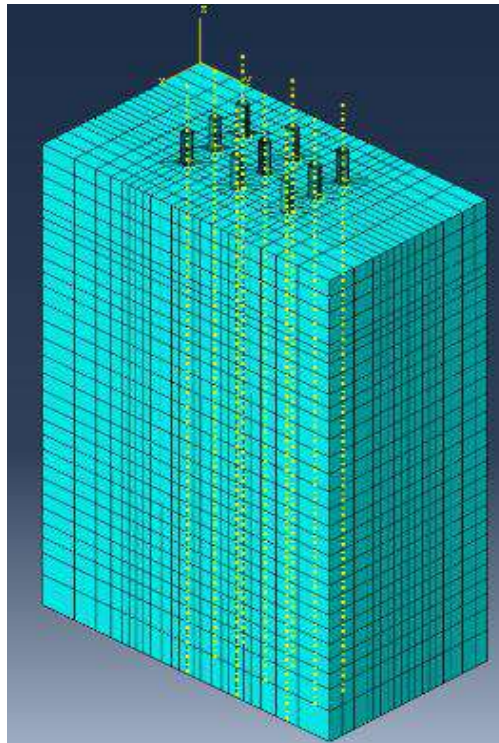


Fig. 4. Model geometry

In summary, comparison of the pile group response from continuum model with Christensen test, indicate that the 3D numerical modeling can efficiently simulate the pile group behavior under lateral loading.

3. Numerical Modeling

To study pile section effects on group reduction factor, two sections were considered. The first one is a circular hollow section with the diameter of 30 cm, which is briefly referred to as “Pipe”. The second section called “Square Tube”, is a hollow square with its EI (flexural rigidity) equal to that of the pipe section and a height of 25.14 cm. These sections are demonstrated in Figure 7. In both cases, the thickness of section is 1 cm and the pile length is 10 meters. The pile groups were modeled in dry and cohesionless soils of different internal friction angles using the Mohr-Coulomb constitutive law. Table 2 lists different values of parameters used for building different models to study the effects of pile sections on the group reduction factor in granular soils with various properties.

To evaluate the influence of granular soil internal friction angle on the group reduction factor, when utilizing different sections, the friction angle values were chosen to be 25, 30, 35 and 40 degrees.

As shown in Figure 8, the dimensions of the model were selected in accordance with the sensitivity analysis described in the verification section. As can be seen, a 3×3 pile group was modeled with the ratio of pile center to center spacing to the pile diameter of 3 (i.e. $S/D = 3$). Piles were made of St37 steel and the soil behavior was analyzed with the Mohr-Coulomb constitutive model.

3.1. Preliminary Results of Pile Group Analysis

In this section, a brief review is given about the group pile lateral load and bending moment via presentation of the analysis results of a sample group pile. Figure 9 presents the p-y curves of the single pile and the corresponding pile the middle of the group. The curves are the plotted for the pipe and the square tube pile sections while the maximum lateral deflection was considered to be 5 cm.

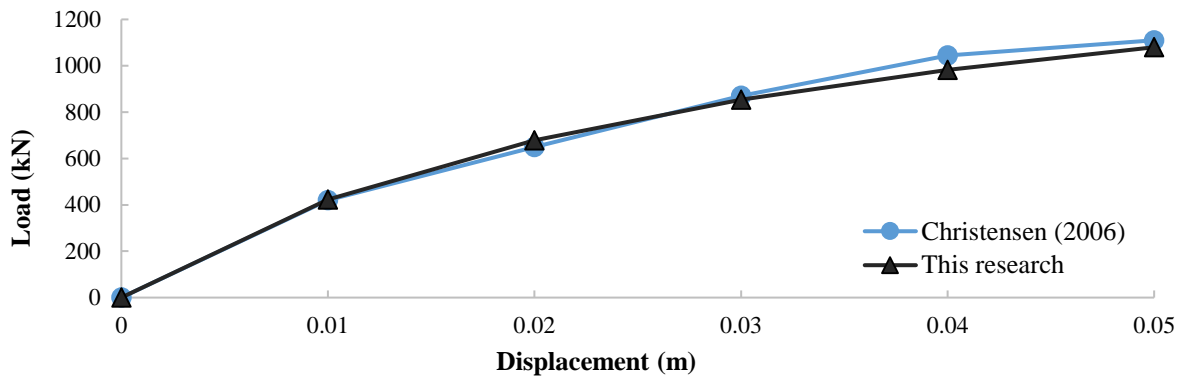


Fig. 5. Computed versus observed total group load-displacement curve

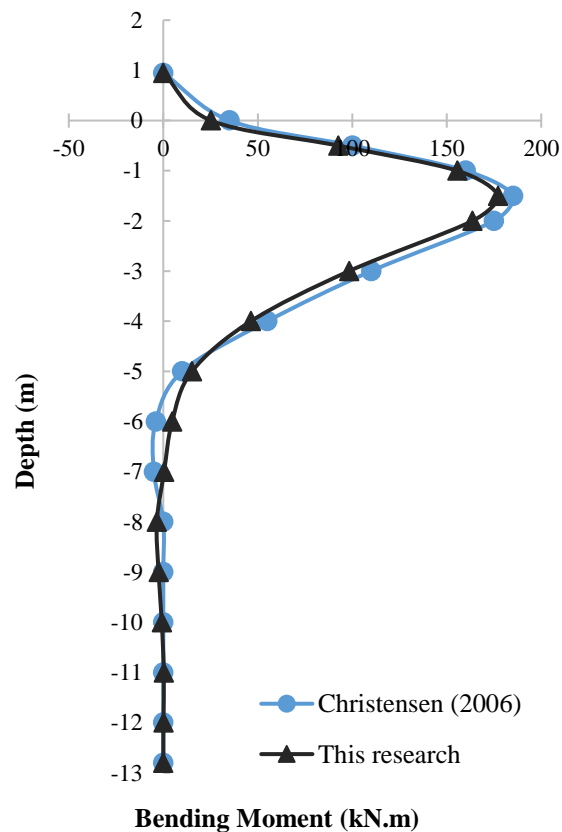


Fig. 6. Computed versus observed total group bending moment profile



Fig. 7. Types of pile sections: a) Pipe; and b) Square tube

Table 2. Variations of model parameters to study the group reduction factor

Section of the piles in the group	Pile arrangement	S/D	ϕ (°)
Pipe	3 × 3	3	25
			30
			35
			40
Square tube	3 × 3	3	25
			30
			35
			40

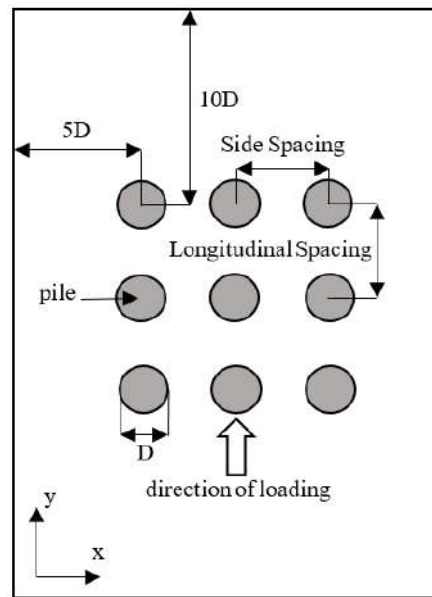


Fig. 8. Continuum model plan

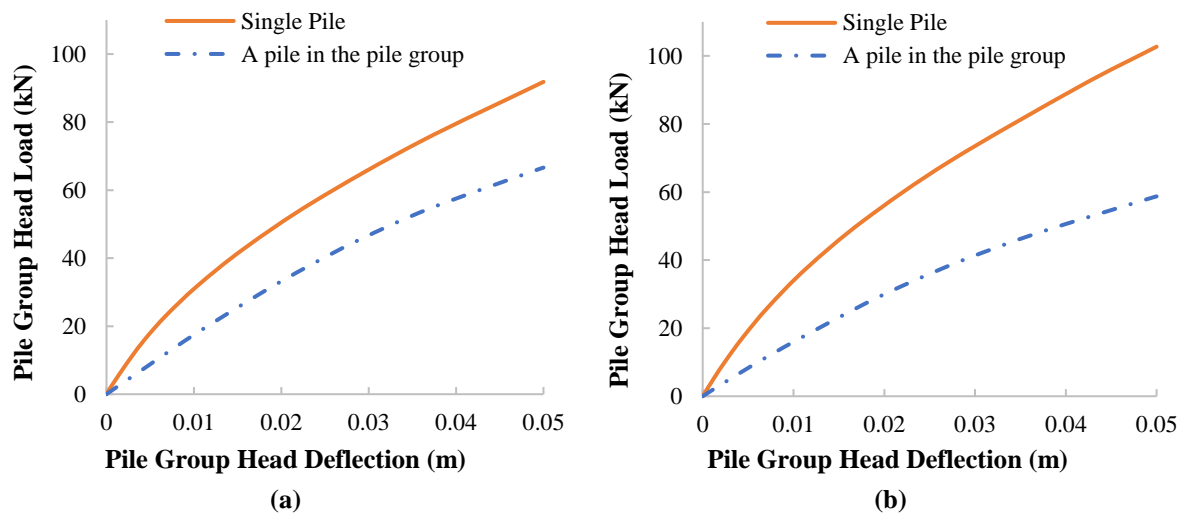


Fig. 9. Load vs. deflection of pile group head for: a) Pipe; and b) Square tube sections ($\phi = 25^\circ$)

As seen in this figure, when the internal friction angle of soil is constant, by changing the section type, the group behavior varies. When the pile section changes from pipe to square tube, the difference between the lateral force of the single pile and that of the middle pile in the group increases. In Figure 10, the distribution of lateral force is demonstrated along the pile. As shown, the lateral load carried by the single pile compared to the pile in the middle of the group is greater in case of the square tube section in contrast to pipe section.

To study the group effects in various conditions of pile section and soil types, the pile group lateral resistance can be plotted

against the pile group head deflection with the help of numerical modeling outputs. For instance, the curves of Figure 11 are presented for different pile sections in a soil with friction angle of 25° .

Pile group behavior in the soils of different friction angles is similar to that of the piles located in the soil with friction angle of 25° as depicted in Figure 11. Figure 12 illustrates the lateral force of the pile group head with pipe and square tube sections, at maximum deflection, for different internal friction angles of the soil. As can be seen, the lateral load of the pile group with pipe section is greater in comparison with the case of square tube section.

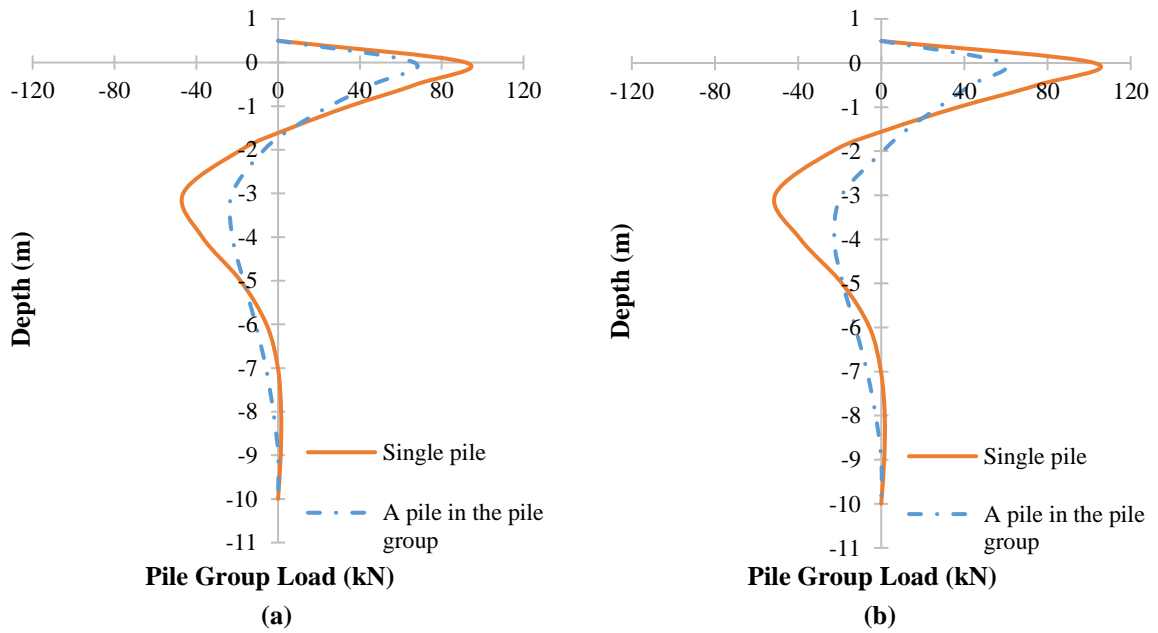


Fig. 10. Lateral load variations of the pile groups with depth for different sections ($\phi = 25^\circ$): a) Pipe; and b) Square tube

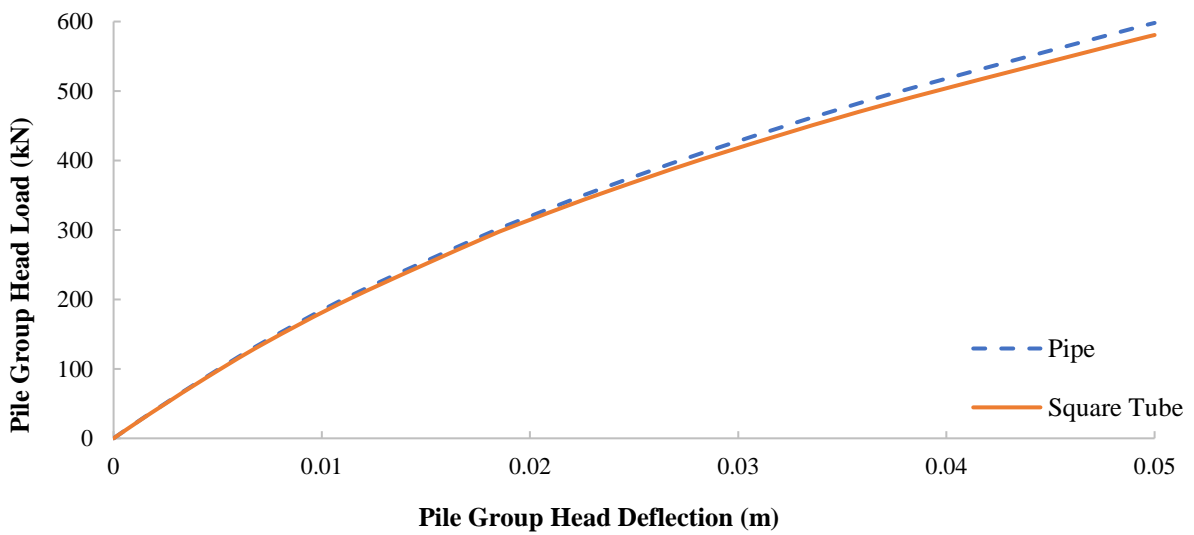


Fig. 11. Lateral load versus deflection of pile groups with different sections ($\phi = 25^\circ$)

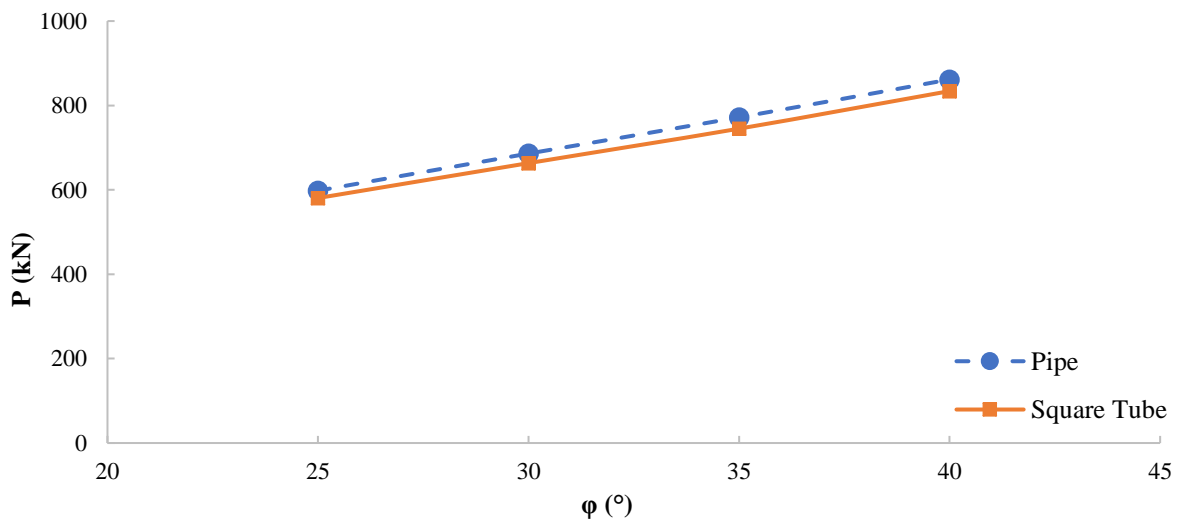


Fig. 12. Pile group head load vs. soil friction angle for different pile sections

3.2. Effects of Pile Section Type on the Group Reduction Factor

In this section, the results from different models built based on Table 2 is evaluated. To investigate the effects of pile sections on the group reduction factor in soils with different friction angles, the continuum modeling was carried out and group reduction factors were obtained and given in Figure 13.

When the internal friction angle increases, the group reduction factor decreases for all pile sections. In fact, by increasing the soil friction angle, the soil shear strength and therefore its bearing capacity increases. According to the results of all pile sections, when the soil has more resistance, with a friction angle of 40° , the lowest group reduction factor is attained, and when the soil is weaker, with a friction angle of 25° , a greater group reduction factor is obtained.

By comparing the results of different pile sections, it is found that the Square Tube section has less group reduction factor than Pipe section. The use of square tube section

piles could extend the area affected by the piles in the soil and as a result, the shadowing effect and edge effect increase, so the group reduction factor decreases.

4. Continuum Model Results vs. Design Guidelines and Experimental Studies

4.1. Comparison with Available Recommendations for Practice

Two important methods for estimating the P-multipliers of the group piles are proposed by AASHTO (2012) and FEMA (2012) regulations. Both of these references provide simple suggestions based on the results of a number of laboratory studies to predict the P_m for the rows of pile groups. To obtain the group reduction factor, one can calculate the average of the P_m values of different pile rows.

The values of proposed P-multipliers by the AASHTO are presented in Table 3. The weak point of this recommendation is that the effect of pile section type and the soil type in which the pile group constructed, are not taken into account.

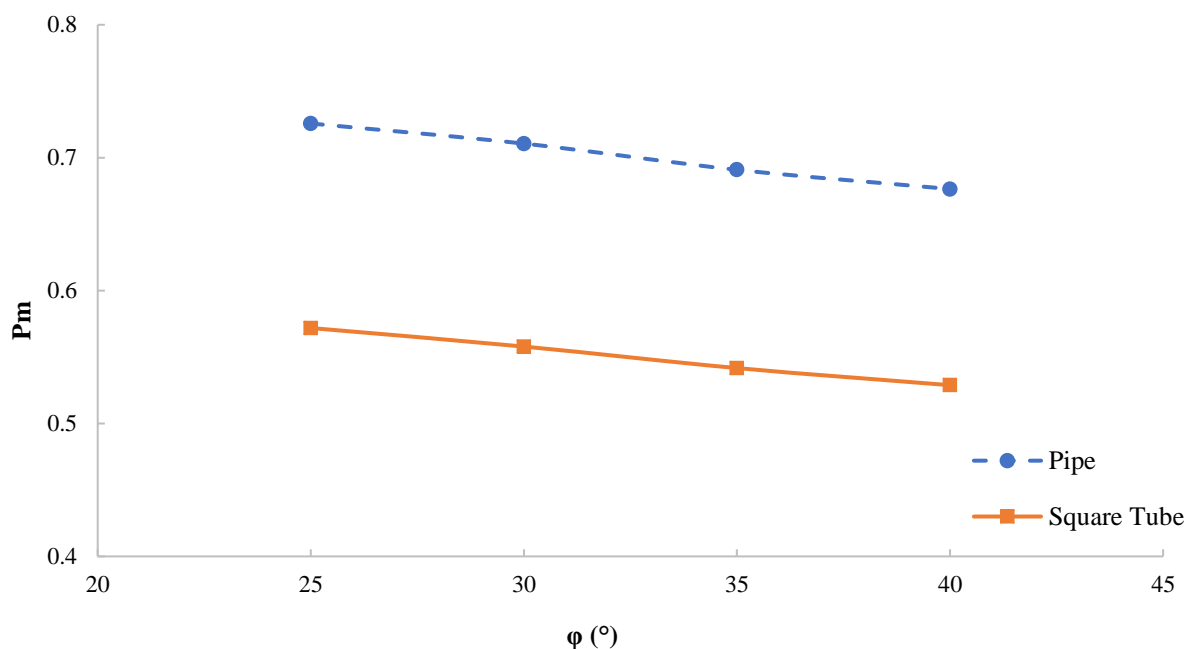


Fig. 13. Group reduction factor for different pile sections versus soil friction angle

Table 3. Proposed P-multipliers by AASHTO guidelines

Pile spacing in the direction of loading	P_m		
	Row 1	Row 2	Row 3
3D	0.8	0.4	0.3
5D	1	0.85	0.7

The FEMA regulations provide the relationships presented in Table 4 to calculate the P-multipliers. Similar to AASHTO, this regulation only considers the effects of row number and ratio of pile spacing to pile diameter in the pile group for determining the P-multipliers and it does not pay attention to the other parameters involved.

The results of numerical modeling are compared with predictions of the existing regulations in Figure 14. In this figure, the group reduction factors for piles of different sections with S/D of 3, are plotted versus soil internal friction angle.

Considering the curve of pile group with pipe section, the reduction factors obtained from continuum models are higher than the estimations by the ASSHTO and FEMA guidelines, so, they suggest conservative values. However, the curve of pile group with square tube section shows more conservative values in contrast to FEMA recommendation, and less conservative estimates compared to the AASHTO values.

In fact, these regulations provide a constant value for several different sections and soil types. The estimates of the regulations were close to the values obtained from numerical analysis for pile group with square tube section. In case of

pile group with pipe section, when the internal friction angle is greater, the reduction factors obtained from numerical modeling are closer to the regulations' recommendations. In general, it is found that the regulations are more conservative concerning weaker soils. However, in stronger soils, estimations of the guidelines are closer to the predicted values through numerical modeling.

4.2. Comparison with Pervious Experimental Data

Comparison of the continuum model results with the experimental data is demonstrated in Figure 15. The experimental data points provided in this figure are obtained from the centrifuge tests conducted by McVay et al. (1995) and the full-scale tests performed by Brown et al. (1988) and Morrison and Reese (1988). These experimental studies were selected in a way that their condition is similar to that of the continuum models as much as possible, however, some features of the physical and numerical models could be slightly different. As shown in Figure 15, the group reduction factors obtained from the experiments are close to the data points calculated based on the continuum model results.

Table 4. Proposed P-multipliers by FEMA guidelines

First (leading) row piles	$P_m = 0.26\ln(S/D) + 0.5 \leq 1$
Second row piles	$P_m = 0.52\ln(S/D) \leq 1$
Third or higher row piles	$P_m = 0.6\ln(S/D) - 0.25 \leq 1$

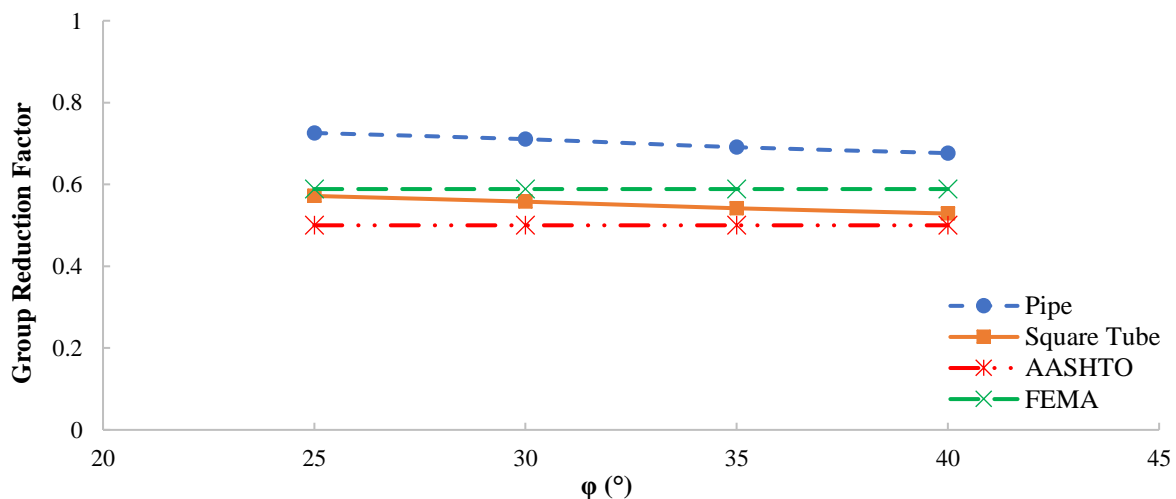


Fig. 14. Comparison of continuum model results with recommendations of guidelines

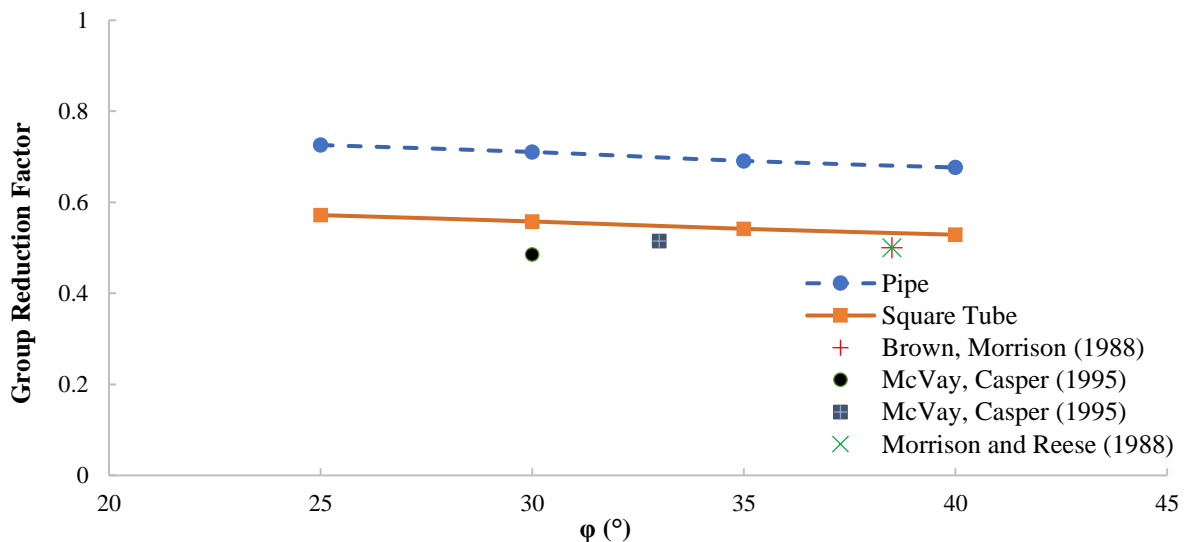


Fig. 15. Comparison of continuum model results with experimental data

5. Conclusions

The use of p-y curves is one of the conventional approaches for evaluating the pile behavior under lateral loads. Considering the group effects, when using this method to analyze the pile group under lateral load, the p-y curves should be modified. This modification is done by applying a constant coefficient smaller than one (i.e. P-multiplier) to the whole p-y curve. For cyclic and seismic loadings where the direction of loading changes repeatedly, the average of P-multipliers of the pile rows, called the group reduction factor, is used for pile group analysis.

Various factors affect the value of reduction factor, however, design guidelines recommend its value just on the basis of pile row number and spacing to diameter ratio of the piles. In this study, the influence of pile section and soil friction angle on the group reduction factor were investigated. To this end, continuum models of a 3×3 pile group with spacing to diameter ratio of 3 with different sections were built in soils of different friction angle. By using the p-y model, the group reduction factor was calculated for each continuum model. According to the results of this study, the following conclusions are drawn:

- Group reduction factor for square tube piles is less than the pipe piles in different soils. This means that the group

effect is greater in case of square tube section. As a result, using the pipe piles in a group is more efficient than the square tube piles.

- By increasing the soil shear strength due to the increase of friction angle, soil among piles transfers the effects of piles on each other better. In other words, the overlapping areas affected by the piles are increased, so, the pile-soil-pile interactions increase. Subsequently, greater group effects lead to lower group reduction factor.
- The modeling results were compared with the results of AASHTO and FEMA guidelines. Since these regulations only consider the effects of row number and the ratio of spacing to diameter of piles, they suggest the same amount of reduction factors for all the pile sections and soil properties. By comparing the group reduction factors based on recommendations of these guidelines, it can be inferred that these regulations offer conservative values for pipe section. On the other hand, the group reduction factors of the pile groups with square tube section are close to the values recommended by the guidelines. In addition, it was shown that the group reduction factors obtained from the numerical modeling are close to those computed based on measurements through the physical modelling.

It is worth noting that this study is limited to the group piles located in the sandy soils and further research should be conducted to account for those constructed in the clay. Moreover, this study is restricted to specific steel pile profiles and pile group configuration, hence, other types of pile sections and group arrangements might be investigated in future research programs. Accordingly, the results of the current study may not be generalized to all different groups of piles without the mentioned considerations.

6. References

- AASHTO (American Association of State Highway and Transportation Officials). (2012). *AASHTO LRFD bridge design specifications*, Washington, D.C.,
- Asaadi, A., Sharifipour, M. and Ghorbani, K. (2017). "Numerical simulation of piles subjected to lateral spreading and comparison with shaking table results", *Civil Engineering Infrastructures Journal*, 50(2), 277-292.
- Avval, Y.J. and Derakhshani, A. (2019). "New formulas for predicting liquefaction-induced lateral spreading: model tree approach", *Bulletin of Engineering Geology and the Environment*, 78(5), 3649-3661.
- Brown, D.A., Morrison, C. and Reese, L.C. (1988). "Lateral load behavior of pile group in sand", *Journal of Geotechnical Engineering*, 114(11), 1261-1276.
- Brown, D.A., O'Neill, M., Hoit, M., McVay, M., El Naggar, M. and Chakraborty, S. (2001). *Static and dynamic lateral loading of pile groups*, National Academy Press.
- Christensen, D.S. (2006). "Full scale static lateral load test of a 9 pile group in sand", M.Sc. Thesis, Brigham Young University.
- Das, B.M. (2015). *Principles of foundation engineering*, Cengage learning, Cengage Learning, Boston, USA.
- Fayyazi, M.S., Taiebat, M., Finn, W. and Ventura, C. (2012a). "Evaluation of group factor method for analysis of pile groups" *Fifteenth World Conference on Earthquake Engineering*, Lisbon, Portugal.
- Fayyazi, M.S., Taiebat, M., Finn, W.L. and Ventura, C.E. (2012b). "Evaluation of P-multiplier method for performance-based design of pile groups", *Second International Conference on Performance-Based Design in Earthquake Geotechnical Engineering*, Taormina, Italy.
- Fayyazi, M.S., Taiebat, M. and Finn, W.L. (2014). "Group reduction factors for analysis of laterally loaded pile groups", *Canadian Geotechnical Journal*, 51(7), 758-769.
- FEMA (Federal Emergency Management Agency). (2012). *Foundation analysis and design*. FEMA P-751, In NEHRP Recommended Provisions: Design Examples, Washington, D.C., National Institute of Building Sciences, Building Seismic Safety Council.
- Hajitaheriha, M.M., Jafari, F., Hassanlourad, M. and Hasani Motlagh, A. (2021). "Investigating the reliability of negative skin friction on composite piles", *Civil Engineering Infrastructures Journal*, 54(1), 23-42.
- Hibbit, H.D., Karlsson, B.I. and Sorensen, E.P. (2016). *ABAQUS 2016 user's manuals*, Hibbit, Karlsson & Sorensen Inc., Pawtucket, Rhode Island, USA.
- Jafariavval, Y. and Derakhshani, A. (2020). "New formulae for capacity energy-based assessment of liquefaction triggering", *Marine Georesources and Geotechnology*, 38(2), 214-222.
- Khorrami, R. and Derakhshani, A. (2019). "Estimation of ultimate bearing capacity of shallow foundations resting on cohesionless soils using a new hybrid M5-GP model", *Geomechanics and Engineering*, 19(2), 127-139.
- Khorrami, R., Derakhshani, A. and Moayedi, H. (2020). "New explicit formulation for ultimate bearing capacity of shallow foundations on granular soil using M5 Model Tree", *Measurement*, 163, 108032.
- Khoshrroo, R. and Derakhshani, A. (2020). "New formulation of reduction factors for pile groups under lateral loading through Model Tree technique", *Ships and Offshore Structures*, 15(10), 1120-1128.
- Kohestani, V.R., Vosoghi, M., Hassanlourad, M. and Fallahnia, M. (2017). "Bearing capacity of shallow foundations on cohesionless soils: A random forest based approach", *Civil Engineering Infrastructures Journal*, 50(1), 35-49.
- Law, H.K. and Lam, I.P. (2001). "Application of periodic boundary for large pile group", *Journal of Geotechnical and Geoenvironmental Engineering*, 127(10), 889-892.
- McVay, M., Casper, R. and Shang, T.-I. (1995). "Lateral response of three-row groups in loose to dense sands at 3D and 5D pile spacing", *Journal of Geotechnical Engineering*, 121(5), 436-441.
- McVay, M., Zhang, L., Molnit, T. and Lai, P. (1998). "Centrifuge testing of large laterally loaded pile groups in sands", *Journal of Geotechnical and Geoenvironmental Engineering*, 124(10), 1016-1026.
- Morrison, C.S. and Reese, L.C. (1988). "A lateral-load test of a full-scale pile group in sand", Texas University at Austin Geotechnical Engineering Center.

- Rezaei, M., Hamidi, A. and Farshi Homayoun Rooz, A. (2016). "Investigation of peak particle velocity variations during impact pile driving process", *Civil Engineering Infrastructures Journal*, 49(1), 59-69.
- Rollins, K.M., Lane, J.D. and Gerber, T.M. (2005). "Measured and computed lateral response of a pile group in sand", *Journal of Geotechnical and Geoenvironmental Engineering*, 131(1), 103-114.
- Rollins, K.M., Olsen, K.G., Jensen, D.H., Garrett, B.H., Olsen, R.J. and Egbert, J.J. (2006). "Pile spacing effects on lateral pile group behavior: Analysis", *Journal of Geotechnical and Geoenvironmental Engineering*, 132(10), 1272-1283.
- Rollins, K.M., Olsen, R., Egbert, J., Olsen, D., Jensen, K. and Garrett, B. (2003). "Response, analysis, and design of pile groups subjected to static and dynamic lateral loads", Utah Department of Transportation Research and Development Division, Report No. UT-03.03.
- Rollins, K.M., Peterson, K.T. and Weaver, T.J. (1998). "Lateral load behavior of full-scale pile group in clay", *Journal of Geotechnical and Geoenvironmental Engineering*, 124(6), 468-478.
- Rollins, K.M. and Sparks, A. (2002). "Lateral resistance of full-scale pile cap with gravel backfill", *Journal of Geotechnical and Geoenvironmental Engineering*, 128(9), 711-723.
- Ruesta, P.F. and Townsend, F.C. (1997). "Evaluation of laterally loaded pile group at Roosevelt Bridge", *Journal of Geotechnical and Geoenvironmental Engineering*, 123(12), 1153-1161.
- Saeedi Azizkandi, A. and Fakher, A. (2014). "A simple algorithm for analyzing a piled raft by considering stress distribution", *Civil Engineering Infrastructures Journal*, 47(2), 215-227.
- Snyder, J.L. (2004). "Full-scale lateral-load tests of a 3×5 pile group in soft clays and silts", M.Sc. Thesis, Brigham Young University.
- Taghavi, A. and Muraleetharan, K.K. (2016). "Analysis of laterally loaded pile groups in improved soft clay", *International Journal of Geomechanics*, 17(4), 04016098.
- Talebi, A. and Derakhshani, A. (2019). "Estimation of P-multipliers for laterally loaded pile groups in clay and sand", *Ships and Offshore Structures*, 14(3), 229-237.
- Tehrani, F., Prezzi, M. and Salgado, R. (2016). "A multidirectional semi-analytical method for analysis of laterally loaded pile groups in multi-layered elastic strata", *International Journal for Numerical and Analytical Methods in Geomechanics*, 40(12), 1730-1757.
- Walsh, J.M. (2005). "Full-scale lateral load test of a

3×5 pile group in sand", M.Sc. Thesis, Brigham Young University.



This article is an open-access article distributed under the terms and conditions of the Creative Commons Attribution (CC-BY) license.



Developing a Hybrid ANN-Jaya Procedure for Backcalculation of Flexible Pavements Moduli

Ghanizadeh, A.R.^{1*}, Heidarabadizadeh, N.² and Khalifeh, V.³

¹ Associate Professor, Department of Civil Engineering, Sirjan University of Technology, Sirjan, Iran.

² Research Assistant, Department of Civil Engineering, Sirjan University of Technology, Sirjan, Iran.

³ Assistant Professor, Department of Civil Engineering, Sirjan University of Technology, Sirjan, Iran.

© University of Tehran 2021

Received: 05 Oct. 2020;

Revised: 19 Jul. 2021;

Accepted: 19 Jul. 2021

ABSTRACT: This research aim is to develop a procedure for backcalculation of flexible pavements moduli based on the hybridization of the Artificial Neural Network (ANN) and the Jaya optimization algorithm. The ANN was applied to predict the pavement deflection basin, and the Jaya was employed for moduli backcalculation. The comparison of hybrid ANN-Jaya procedure with some backcalculation software indicates the high ability of the developed method to perform backcalculation of flexible pavements moduli. The comparison of the computational speed and accuracy of hybrid ANN-Jaya with ANN-PSO and ANN-GA indicates the superior performance of ANN-Jaya compared to other methods.

Keywords: Artificial Neural Network (ANN), Backcalculation, Falling Weight Deflectometer (FWD), Flexible Pavements, Jaya Optimization Algorithm.

1. Introduction

In the pavement engineering, the Falling Weight Deflectometer (FWD) device, is commonly applied to estimate the pavement stiffness modulus and the structural properties of the layers in a non-destructive manner (Saltan and Terzi, 2008; Gopalakrishnan and Papadopoulos, 2011; Li et al., 2018). The structural analysis of pavements has a key role in estimating the pavements life and determination of the optimal maintenance activities. As a part of FWD results interpretation process, the accurate measuring the pavement moduli

provides a reliable basis for the road management department to formulate pavement maintenance plans and rationally arrange funds., Utilizing the several sensors called geophones in the FWD test procedure, the deflection basin (deformations) of the pavement surface in response to the applied dynamic load pulse was measured at different radial distances from the center of rubber plate (the loading center). The dynamic load pulse simulates the moving wheel load and is produced by dropping a heavyweight on the pavement through a circular rubber plate. Moreover, the measured deflections can be employed

* Corresponding author E-mail: ghanizadeh@sirjantech.ac.ir

to evaluate the pavement life and estimate the pavement layers stiffness through backcalculation analysis.

The backcalculation of pavement layers moduli consists of comparing the deflections measured by the FWD and the calculated ones through an iterative process (using a pavement response model). Usually, in most backcalculation software, the multilayered elastic theory was employed for forward analysis of pavement structure. In this process, the modulus of each layer is initialized, and the pavement surface deflections will be calculated by forward analysis. In the subsequent iterations, the moduli of different layers are adjusted, and then the computed deviations are compared with the measured ones, until the difference is within the acceptable range. Over the years, different methods of intelligence computing and deep learning was emerged and developed to solve complicated problems (Vasant et al., 2019). Several static, dynamic and artificial intelligence methods have been implemented to the flexible pavement moduli backcalculation including dataset search, least squares, and soft computing such as genetic algorithm, neural network and, fuzzy logic system (Saric and Pozder, 2017; Guzzarlapudi et al., 2017; Abdalnibe, 2019; Zhang et al., 2021). In recent years, advanced computational intelligence methods have been proposed with higher computational speed and accuracy.

Saltan et al. (2002) used a backcalculation process to predict the thickness of layers affecting the pavement service life. They used the Artificial Neural Network (ANN) to eliminate the time-consuming calculations based on linear elastic theory and Finite Element. They obtained a value of $R^2 = 0.94$ and $R^2 = 0.88$ based on the training and testing data, respectively (Saltan et al., 2002).

Gopalakrishna and Thompson (2004) used the ANN to predict the moduli of the three-layer pavement based on FWD measurements. They modeled the asphalt

layer as linear and base and subgrade as nonlinear layers. The Coefficient of Determination (R^2) for predicting the asphalt and subgrade moduli was obtained 0.98 and 0.97, respectively (Gopalakrishnan and Thompson, 2004). Ceylan et al. (2005) used the ANN for the pavement structural analysis and determined the deflection basin of full-depth asphalt pavements. They were able to estimate the asphalt layer modulus based on the FWD measurements and increase the speed of backcalculation process (Ceylan et al., 2005). Rakesh et al. (2006) used the ANN method to calculate the surface deflections of four pavement systems, including pavement with 2, 3, 4 and 5 layers, and compared the results with actual data. The value of R^2 for these systems was 0.997, 0.996, 0.997, and 0.997, respectively. Saltan and Terzi (2008) modeled the deflection basin of the flexible pavement using ANN with a cross-validation technique by applying a backcalculation process (Saltan and Terzi, 2008).

Gopalakrishnan (2010) proposed a new intelligent system for back-calculating the stress-dependent modulus of the layers using pavement deflection data. For this purpose, the integration of three methods, including Finite Element, ANN, and Particle Swarm Optimization (PSO) as a hybrid backcalculation tool, was used to develop a robust system for predicting the nonlinear modulus of granular base and subgrade layers. The values of R^2 obtained from the calculated modulus, and the actual data for the asphalt and subgrade layer were 0.996 and 0.984, respectively. In this research, the developed model has validated with BACKFAA and WESDEF software in the six different airport pavement sections (Gopalakrishnan, 2010).

Saltan et al. (2013) used the ANN approach to evaluate the structural properties of a typical flexible pavement, including the layers thickness, the Poisson's ratio, and the resilient modulus (Saltan et al., 2013). Ocal (2014) presented an

artificial intelligence algorithm to backcalculate the asphalt pavements moduli based on FWD results. For this purpose, a novel hybrid Gravitational Search Algorithm (GSA)-ANN method was proposed (Öcal, 2014). The Ant Colony Optimization algorithm was applied by Scimemi et al. (2016) to back-calculate the airport pavement moduli based on the surface deflection data. They evaluated back-calculated moduli in comparison with the field data utilizing the BACKGA software, and found that the maximum error is equal to 0.66%. Li and Wang (2019) used ANN and Genetic Algorithm (GA) to back-calculate the flexible pavement layers moduli.

You et al. (2020) utilized two ANN based back-calculation models to evaluate the interlayer conditions and predicting the layers moduli of four types of pavements. Moreover, the ANSYS software was applied to build the corresponding database. The results of two proposed ANN models compared to the results of two multiple regression models have shown that, there are no significant differences between them.

Fu et al. (2020) estimated the dynamic surface deflections of asphalt pavement subjected to the FWD and evaluate the static backcalculation of layer moduli using the MODULUS and EVERCALC software. They found that the static backcalculation process caused considerable errors due to regardless of the dynamic effects of FWD loading.

Wang et al. (2020) evaluated the traditional backcalculation method based on the finite element and the multilayer elastic theory compared to a new one without backcalculation based on the ANN to predict pavement surface deflections using Heavy Weight Deflectometer (HWD). They showed that the traditional approach overestimated tensile strain in a thin asphalt layer and concluded that the accuracy of the ANN was better than others.

The represented background for application of Computational Intelligence (CI) methods to back-calculate the

pavement layer properties, reveals that a comprehensive comparison of results obtained by these methods with actual field data as well as existing backcalculation software has not been performed. The limitations of the dataset for the development of ANN and the lack of developed software to implement the developed CI method are two other shortcomings. Also, the Jaya algorithm has not been used to perform backcalculation of flexible pavements moduli. Unlike other population-based optimization algorithm, lack of specific control parameters is the most important advantage of Jaya algorithm. Furthermore, better performance and faster convergence capability are two other reasons that this algorithm is employed in this research work.

In this paper, a hybrid optimization model (ANN-Jaya) is proposed for performing backcalculation of flexible pavements moduli, and an applied software is developed to implement it. Furthermore, the performance of the developed model is evaluated based on the field data as well as different backcalculation software, including ISSEM4, MODCOMP, MODULUS, WESDEF, and BACKFAA. Besides, the ability of the Jaya algorithm in terms of robustness, convergence rate and run time is compared with other optimization methods including the GA and the PSO algorithm.

2. Falling Weight Deflectometer (FWD)

The Falling Weight Deflectometer (FWD) is a testing device that was firstly introduced in France to estimate the structural capacity and physical properties of pavements (Ullidtz, 1987). In this device, an impact load is applied on a loading plate, and then the surface deflection can be measured at different radial distances using several geophones. In the LTPP program, the geophones distance from the loading center was assumed to be 0, 203, 305, 457, 610, 915, and 1525 mm (Von et al., 2002). The impact load can be

altered by changing the falling weight height. The load pulse is applied through a series of springs in a short time to the pavement surface (about 28 milliseconds). The falling load of the FWD device is not enough to evaluate the airport pavements that have a higher thickness and load capacity. In such a situation, the Heavy Falling Weight Deflectometer (HFWD) can simulate a Boeing 747-wheel load with a maximum dynamic pressure of 250 kN and loading time between 20 and 25 milliseconds. The schematic image of the FWD device is demonstrated in Figure 1. Some of the variables which affect the shape and dimension of the deflection basin include the Poisson's ratio, the thickness, the layers modulus, the load applied by the FWD, and the subgrade depth (Bendana et al., 1994). Having these values and deflections in different radial distances, the modulus of different layers can be obtained through backcalculation process.

3. Artificial Neural Network (ANN)

An artificial neural network (ANN) adapted from the behavior of the neurons of the brain nervous mechanism. The ANN consists of the artificial neurons which be

connected (Gurney, 2005). Each connection has a specific weight that increases or decreases the strength of the transmitted signal at a link. The ANN can determine nonlinear relationships between input and output variables. Since solving complex problems with traditional methods is very difficult, ANN is widely being used in various Civil Engineering fields. The feed-forward neural network is one of the most applicable types of ANN for modeling of engineering problems. It consists of several the processing units (the neuron, cell, or node) placed in the layers that connected the inputs to the output set. A multilayer feed-forward neural network includes input, hidden, and output layers which are composed of connected neurons.

For developing a multilayer feed-forward neural network, a learning rule should be used. One of the most popular tools for learning is the error back-propagation algorithm. The general architecture of this algorithm is shown in Figure 2. In this figure L is the number of neurons in the hidden layer and x_{p1} to x_{pN} are the input and y_{p1} to y_{pM} are the output variables. The elements as well as the computational process for a typical artificial neuron is shown in Figure 3.

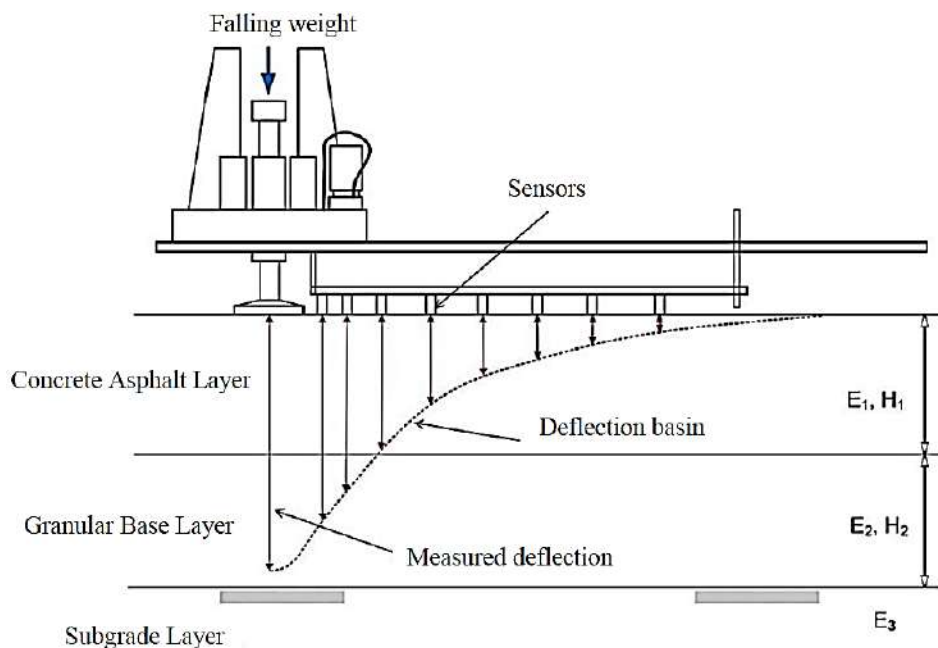


Fig. 1. Schematic image of the FWD and measuring the deflection basin for a flexible pavement

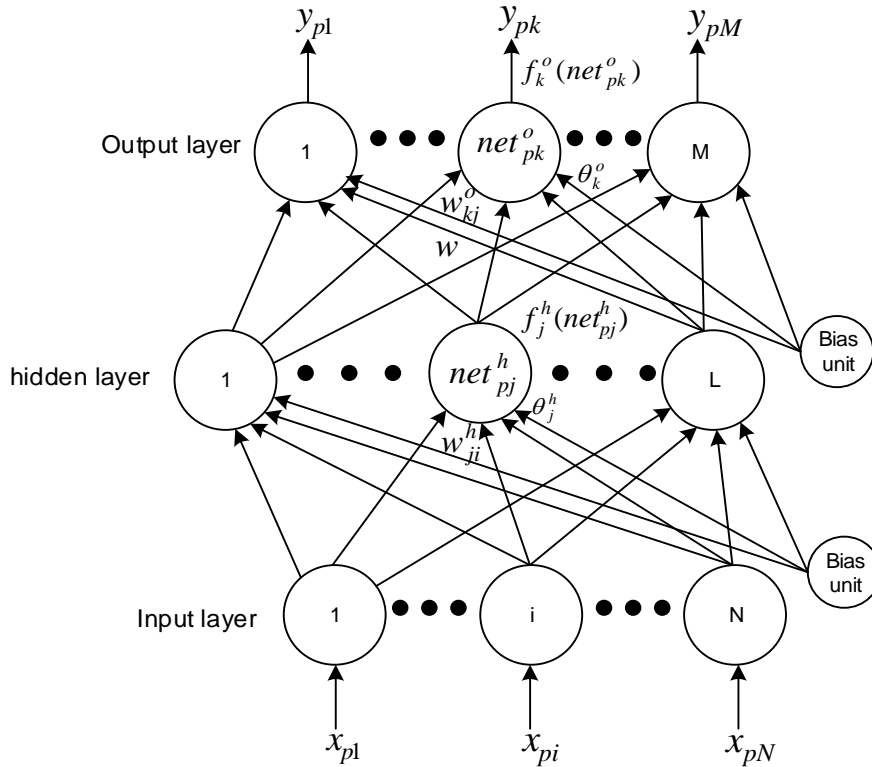


Fig. 2. Architecture of feed-forward neural network structure

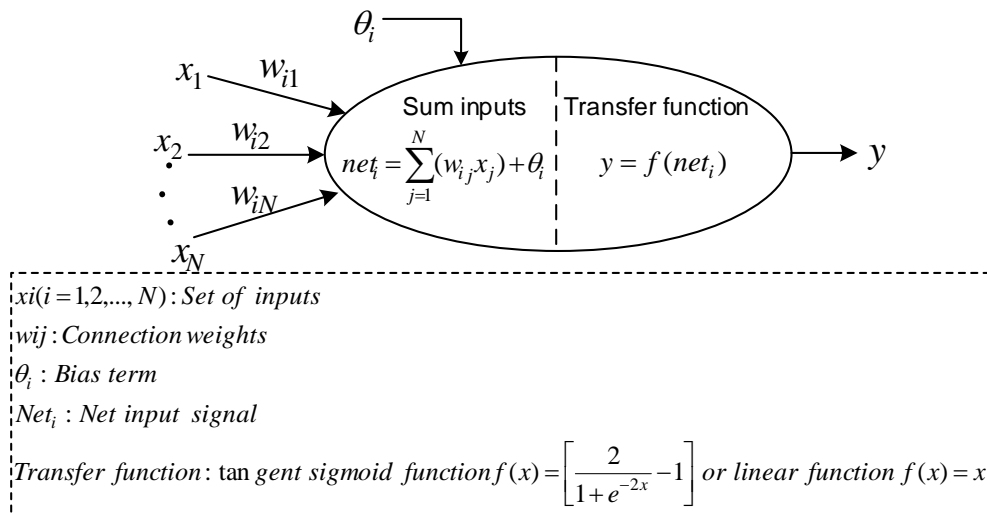


Fig. 3. Structure of a typical artificial neuron

where y_i is the output signal. Other variables are described in the figure. To propagate the activation, the input signals are assessed using their connection weights and enters into the activation function as input. The input signal of the neuron is obtained using Eq. (1):

$$net_i = \sum_{j=1}^N (w_{ij}X_j) - \theta_i \quad (1)$$

The output signal can also be computed utilizing the Eq. (2):

$$y_i = f(net_i) \quad (2)$$

in which f is the transfer function (activation function) and can be classified as a linear, sigmoid, and tangent sigmoid function. The tangent sigmoid transfer function can be acted as real neurons. The value of the output signal (y_i) for tangent

sigmoid activation function varies between 0 and 1. The tangent sigmoid function can be calculated by Eq. (3):

$$f(x) = \frac{2}{(1 + e^{-2x})} - 1 \quad (3)$$

Using the input and output data set, the recursive algorithm modifies the weights and biases for successive iterations. The recursive learning rule is based on minimizing the difference between the calculated and desired output values (error). The learning process is randomly started by assigning connection weights, and then the values of weights and biases are updated according to the error value in the successive iterations. The error back-propagation E^k : is determined utilizing the Eq. (4) at the end of each stage:

$$E^k = \frac{1}{2} \sum_i [t_i^k - y_i^k] \quad (4)$$

where t_i^k : is the real output for the i^{th} neuron and the k^{th} data in the training set. After completing the activation phase, the connection weights are adjusted and the backpropagation phase will begin. In this case, the output of the activation path is converted to the return path toward inputs, and the new connection weight of the neurons i and j are updated using Eq. (5):

$$w_{ij}(it + 1) = w_{ij}(it) + \eta \sum_k \delta_i^k X_j^k + \alpha [w_{ij}(it) - w_{ij}(it - 1)] \quad (5)$$

where α : is the momentum factor that affects the weight in consecutive iterations to prevent the algorithm from falling down in the local optima and oscillation. The bias values are also updated as follows:

$$\theta_i(it + 1) = \theta_i(it) + \eta \sum_k \delta_i^k + \alpha [\theta_i(it) - \theta_i(it - 1)] \quad (6)$$

This process is repeated for each of the training data, while the difference between the calculated and the desired outputs is minimized (Pekcan et al., 2008). Thereafter, two criteria including coefficient of determination (R^2 and Root Mean Square Error (RMSE) were employed to evaluate the neural network performance using the following equations.

$$RMSE = \sqrt{\frac{1}{N} \sum_{i=1}^N (d_i - y_i)^2} \quad (7)$$

$$R^2 = \frac{(N \sum_{i=1}^N (d_i y_i) - \sum_{i=1}^N d_i \sum_{i=1}^N y_i)}{(N \sum_{i=1}^N d_i^2 - (\sum_{i=1}^N d_i)^2) (N \sum_{i=1}^N y_i^2 - (\sum_{i=1}^N y_i)^2)} \quad (8)$$

where d_i : is the actual value, and y_i : is the predicted value for the i^{th} data from the neural network and N : is the number of data points.

4. Jaya Algorithm

Metaheuristic algorithms have been utilized to many complicated Civil Engineering problems (Kaveh and Dadras, 2017; Hajiazizi et al., 2021; Samadi et al., 2021; Sonmez et al., 2017; Ghanizadeh and Heidarabadizadeh, 2018; Ghanizadeh et al., 2020).

Most of the metaheuristic algorithms such as the Particle Swarm Optimization (PSO) (Eberhart and Kennedy, 1995), the Genetic Algorithm (GA) (Holland, 1975), the Teaching Learning-Based Optimization (TLBO) (Rao et al., 2011), and the Firefly Algorithm (FFA) (Yang, 2009) have several internal tuning parameters, and the tuning stage is necessary to determine these parameters. The internal tuning parameters are usually set for a specific problem, and there is no guarantee that these values will lead to a globally optimal solution in case of other issues.

Rao (2016) proposed a simple Jaya (a Sanskrit word meaning victory) algorithm that does not have any internal tuning parameter. The initial solutions of the Jaya,

P candidates, are randomly generated. Then, the variables of the solution are stochastically updated.

Suppose 'j' is the design variable, 'k' is the candidate solutions, and 'i' is the iteration number. The value of the jth variable for the kth candidate in the ith iteration is called $X_{j,k,i}$ and calculated from Eq. (9).

$$X'_{j,k,i} = X_{j,k,i} + r_{1,j,i} (X_{j,best,i} - |X_{j,k,i}|) - r_{2,j,i} (X_{j,worst,i} - |X_{j,k,i}|) \quad (9)$$

where $X_{j,best,i}$ and $X_{j,worst,i}$ are the values of "j" for the best and worst solution, respectively. Also $r_{1,j,i}$ and $r_{2,j,i}$ are the two random numbers in the range of 0 to 1. The term " $r_{1,j,i} (X_{j,best,i} - |X_{j,k,i}|)$ ": shows the tendency to the optimal solution and the term " $-r_{2,j,i} (X_{j,worst,i} - |X_{j,k,i}|)$ ": defines the avoidance to the worst solution. The updated value of $X_{j,k,i}$ ($X'_{j,k,i}$) is accepted only when the corresponding value of objective function is improved. All the acceptable values are maintained as the inputs of the next iteration.

The Jaya algorithm updates the costs of the solutions so that the cost of their

objective function converges to the optimal solution. After updating the solutions, with comparing the updated and corresponding old values, only one of them is selected for the next iteration, which will be the better value of objective function.

It should be noted that, the optimal solution is found in every iteration, and the worst one will be removed, simultaneously. Thereby, this algorithm provides both useful intensification and diversification of the search process in an appropriate way.

In this way, the algorithm always tries to get closer to the optimal solutions and to avoid diverging from the optimal solutions. The general procedure for the Jaya algorithm is presented in Figure 4 (Rao, 2016).

As can be seen, the Jaya algorithm need to the usual control variables (population size and number of generations), while, the other optimization algorithms such as PSO, GA, FA, FFA, etc. require the tuning of respective algorithm-specific parameters. The proper implementation of this procedure has positive effects on the performance of the algorithms, otherwise, either the calculations will increase or it will get stuck at the local optimal solution.

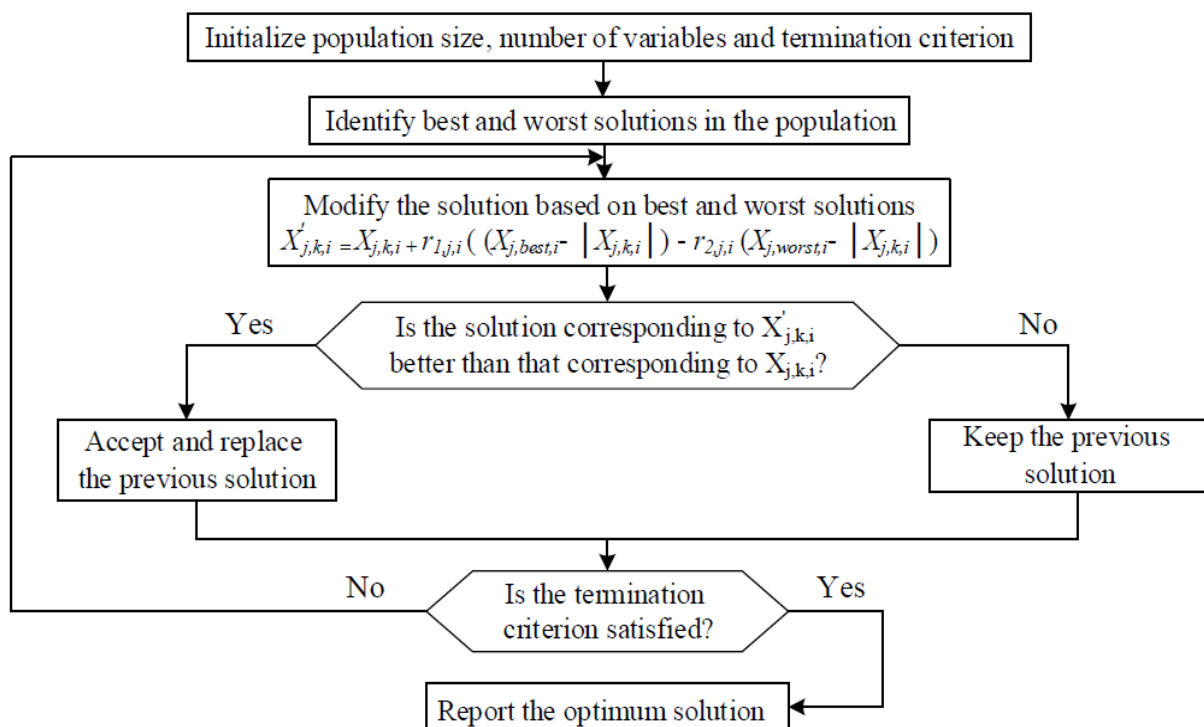


Fig. 4. The Jaya algorithm Flowchart (Rao, 2016)

5. Developing Feed-Forward Neural Network

5.1. Artificial Dataset

In this study, 10000 different flexible pavement sections, consisting of asphalt concrete, granular base, and subgrade soil, were analyzed to create a comprehensive dataset for training and testing artificial neural networks. The deflection of the pavement section surface was calculated in seven different radial distances (0, 203, 305, 457, 610, 915, and 1525 mm). The load was applied as a circular contact area with uniform vertical stress of 552 kPa and a contact radius of 152 mm. Table 1 shows the statistical characteristics of the analyzed pavement sections. The Poisson's ratio of the subgrade soil, granular base, and asphalt concrete were assumed to be 0.40, 0.35, and 0.35, respectively, which is commonly used in the literature (Maher and Bennert, 2008).

Previous studies have also shown slight changes in the pavement response due to changes in the Poisson ratio (Huang, 2004). The NonPAS program has been applied, which provide the possibility of linear and nonlinear analysis of pavements subjected to 10 circular contact loads using multilayered elastic theory. The NonPAS verification process showed that the NonPAS results compared to other applications such as KENLAYER and JULEA are very consistent (Ghanizadeh and Ziaie, 2015). The Statistical characteristics of the deflections obtained for different radial distances are shown in Table 2.

5.2. Optimal Architecture

The training and testing procedure was conducted using a developed program in MATLAB which is developed by MathWorks. In each run of the program, the

MATLAB toolbox assigns random values to the initial neural network weights and biases. Despite the consistency of the neurons and architecture of each layer, the random assignment of weights and biases strongly affects the ANN performance. To address this issue, another MATLAB-based program was developed to obtain the optimal number of neurons in the hidden layer of ANN. The number of neurons was considered to be between 5 and 100. With regards to the random values of weights, and the architecture with the least error was considered as the optimum architecture. In this study, the training, validating, and testing procedure were applied based on the 65% (6500 data points), 10% (1000 data points) and 25% (2500 data points) of the data, respectively. Moreover, the transfer function of the hidden and output layers was assumed as the tangent sigmoid and the linear, respectively.

The results showed that increasing the number of neurons up to 90 improves the performance of artificial neural networks. Therefore, the neural network with a hidden layer and with an architecture of 7-90-5 has sufficient accuracy for predicting the pavement surface deflections at different radial distances. The architecture of the selected neural network is shown in Figure 5.

5.3. Evaluation of ANN Performance

The ANN performance for prediction of surface deflections at different radial distances for the training and testing sets is shown in Figures 6 and 7, respectively. As can be seen, the coefficient of determination in all cases is more than 0.9999, which indicates the high accuracy of the developed model in predicting the surface deflections of flexible pavements.

Table 1. Statistical characteristics of the inputs used for dataset development

Statistical parameter	H ₁ (mm)	H ₂ (mm)	E ₁ (MPa)	E ₂ (MPa)	E ₃ (MPa)
Maximum	309	500	10000	2000	400
Minimum	50	100	500	100	20
Median	300	181	4319	728	100
Mean	178.38	282.55	4703	847	148
Standard deviation	79.42	119	2682	560	112

Table 2. Statistical characteristics of the outputs used for dataset development

Statistical parameter	D ₁	D ₂	D ₃	D ₄	D ₅	D ₆	D ₇
Maximum	3.0721	2.0286	1.494	1.0439	0.8883	0.6476	0.3793
Minimum	0.0567	0.0454	0.0414	0.0371	0.0334	0.0275	0.0169
Median	0.2657	0.2137	0.1893	0.1667	0.1481	0.1182	0.0743
Mean	0.3673	0.2982	0.2601	0.2224	0.1931	0.1502	0.0993
Standard deviation	0.3081	0.2466	0.2153	0.1827	0.1588	0.1254	0.0859

Deflection in mm.

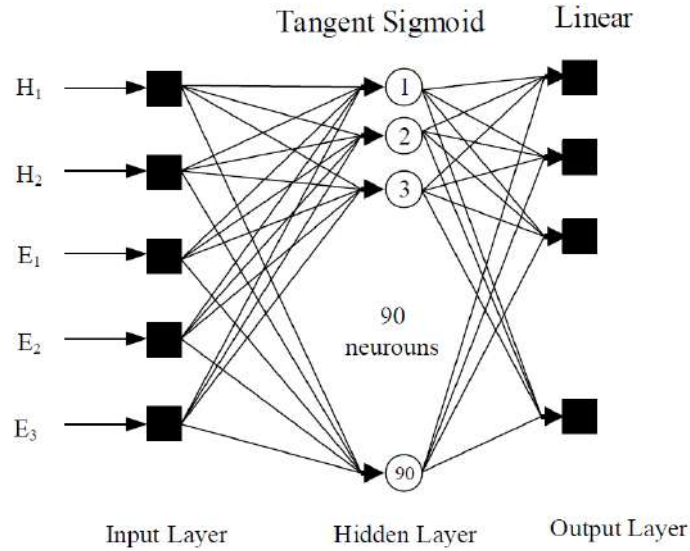
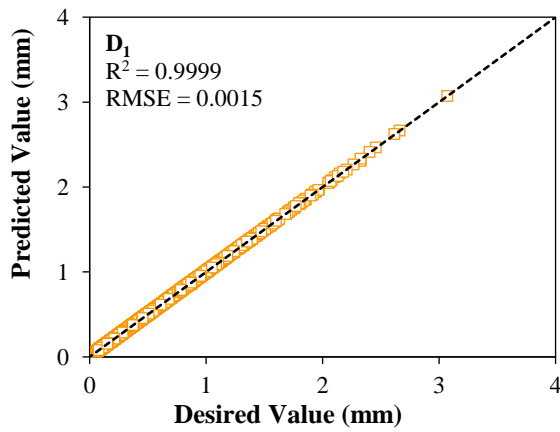
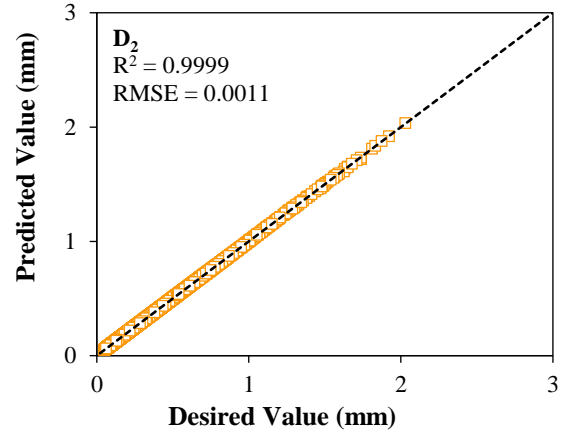


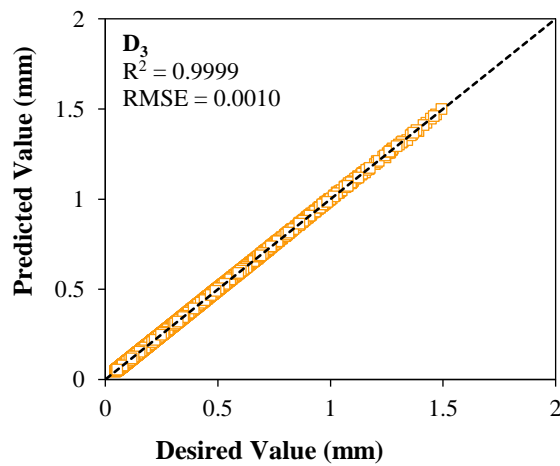
Fig. 5. Optimal ANN architecture



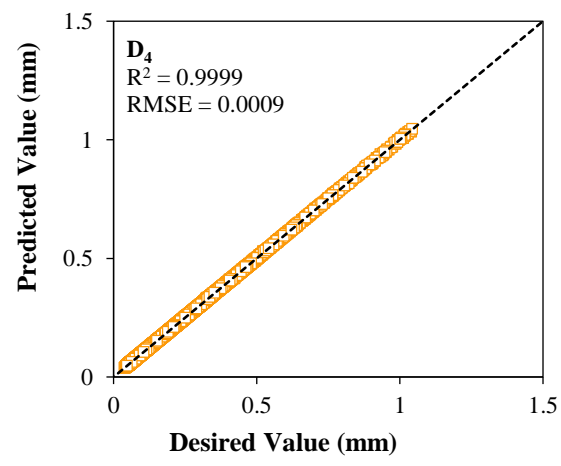
(a)



(b)



(c)



(d)

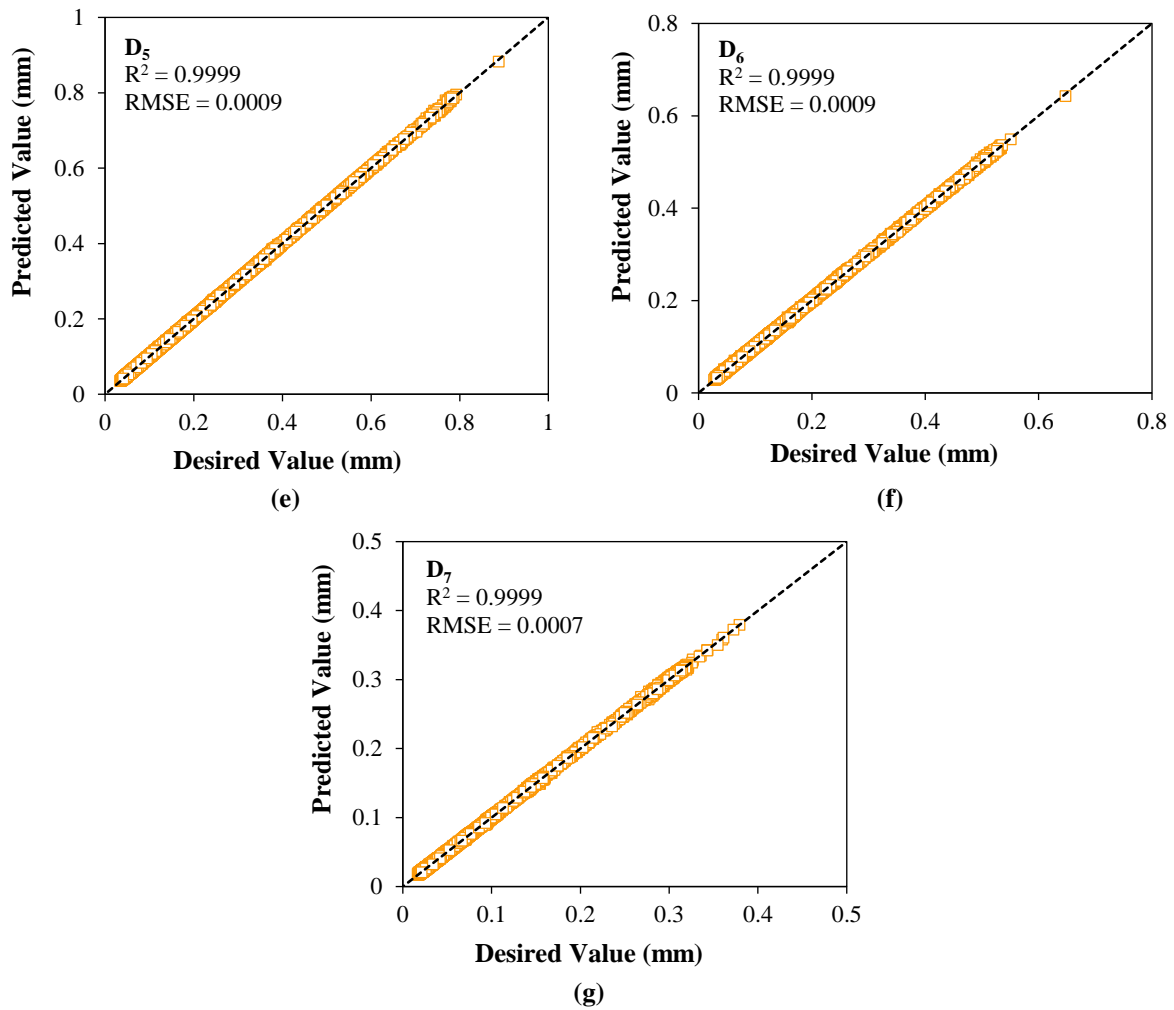
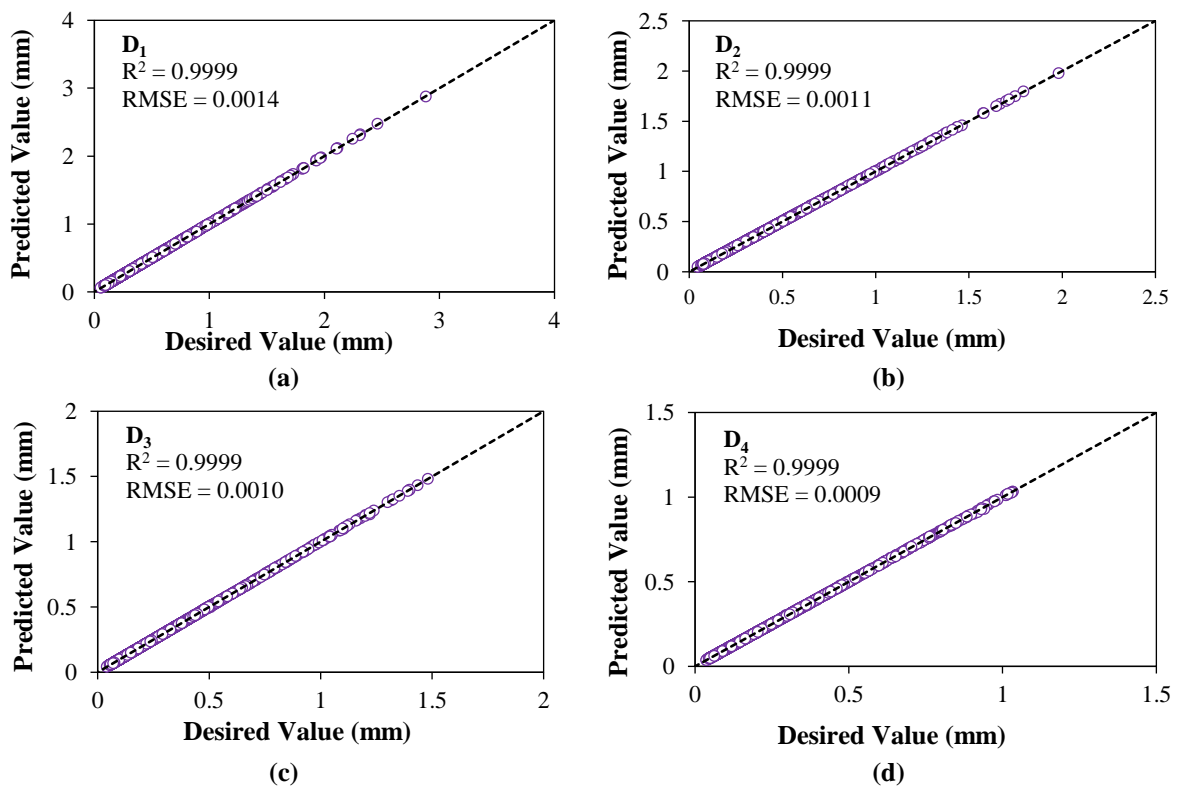


Fig. 6. ANN performance to predict the pavement surface deflections at different radial distances based on the training set



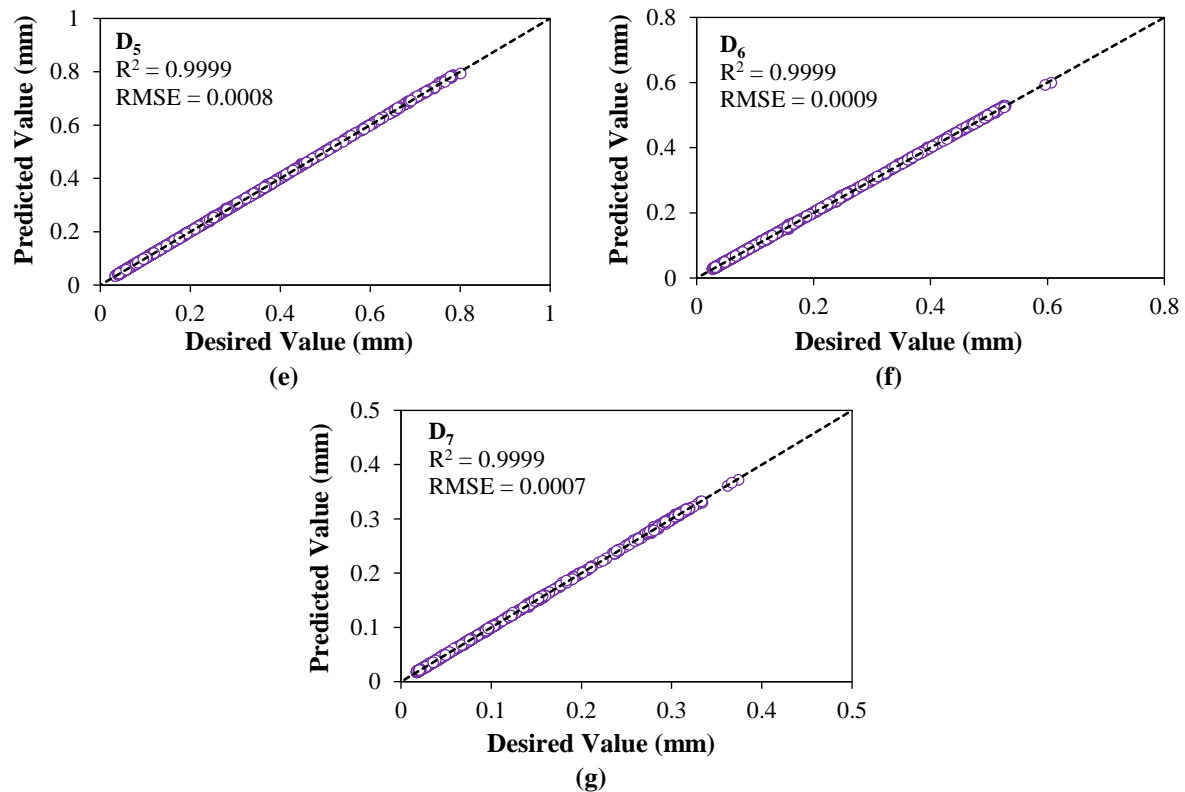


Fig. 7. ANN performance to predict the pavement surface deflections at different radial distances based on the testing set

6. Hybrid ANN-Jaya

6.1. Backcalculation Procedure Using Hybrid ANN-Jaya

In this paper, a procedure based on the hybridization of ANN (forward calculations) and Jaya (determining the modulus of layers) has been proposed for the moduli backcalculation of flexible pavements. The schematic diagram of this procedure is represented in Figure 8. The calculation of deflections is conducted using the ANN, and the Jaya applied to determine the optimum values of the neural network inputs so that the deflections calculated through the ANN are as close as possible to the FWD measured deflections. In other words, the difference between both measured and calculated deflection values should be minimized. Therefore, the objective function can be expressed according to Eq. (10).

$$f = \sum_{i=1}^n |D_i^m - D_i^c| \quad (10)$$

where D_i^m and D_i^c are the deflections measured by the FWD and calculated by ANN for i^{th} geophone, respectively, and n is the number of geophones ($n = 7$).

6.2. Implementation of Hybrid ANN-Jaya

To implement the hybrid ANN-Jaya, the JayaBack (a MATLAB-based program) which provides the possibility of fast and reliable backcalculation of the pavement layers moduli was developed. This program gets the inputs including the asphalt thickness and granular base layers (cm), the granular base and subgrade soil moduli (MPa), upper and lower range of the asphalt, deflection values at seven radial distances (mm), contact pressure of FWD device (MPa), the maximum number of iterations and the number of moduli generated per iteration and then determine the asphalt, granular base and subgrade soil moduli (MPa) using the algorithm represented in Figure 8. The graphical user interface (GUI) of JayaBack is shown in Figure 9.

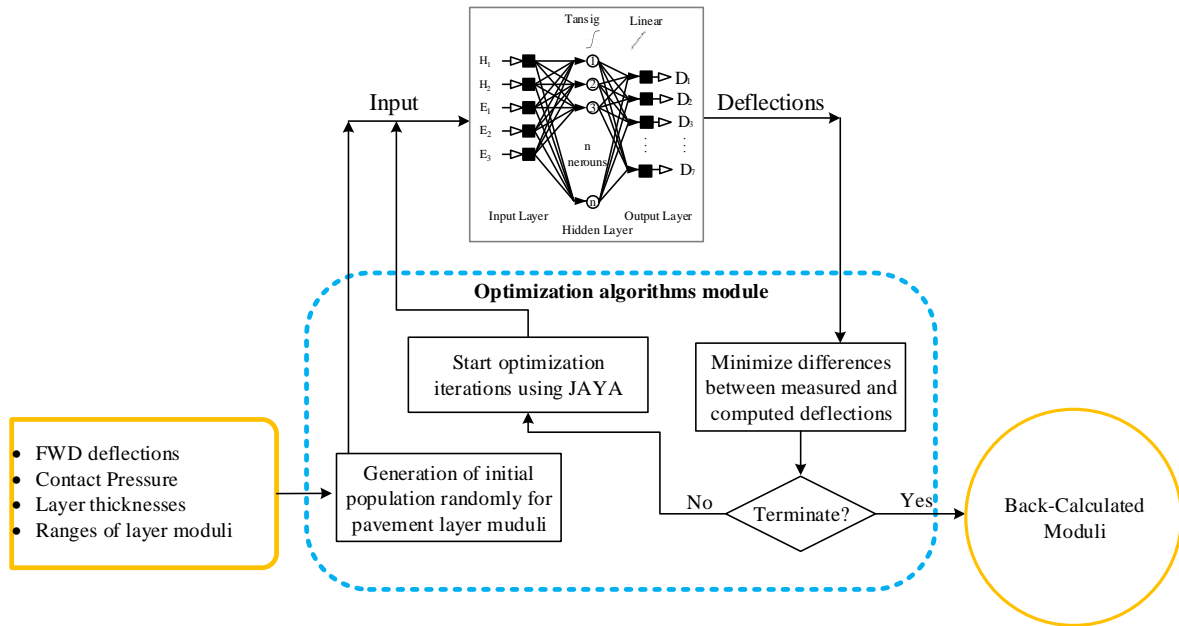


Fig. 8. Implementation of a hybrid ANN-Jaya approach for pavement layer backcalculation

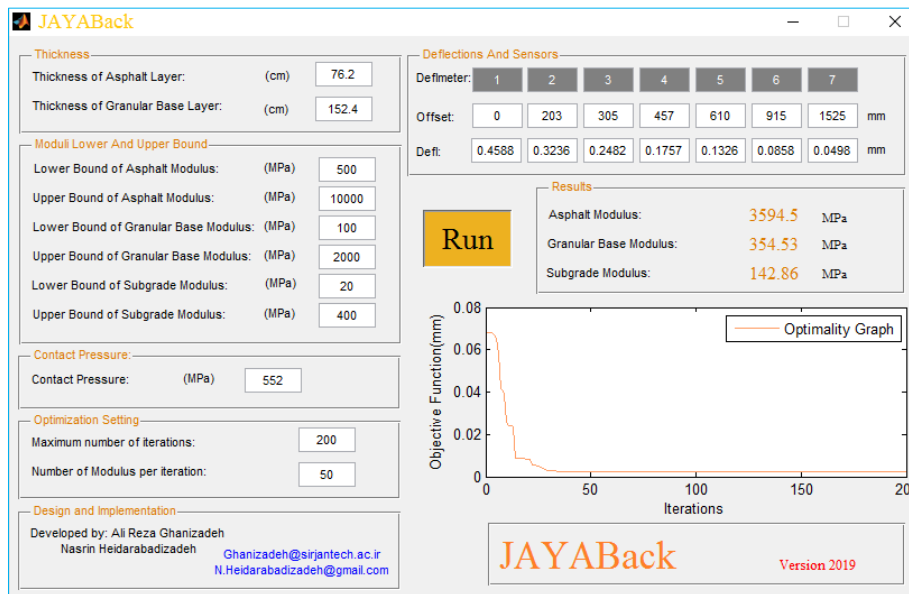


Fig. 9. The JayaBack program GUI

6.3. Validation of the ANN-Jaya Method

6.3.1. JayaBack Validation Using Field Data

To access the performance of the hybrid

ANN-Jaya method, the deflection values measured by FWD measured for six different pavement sections were used (Table 3). These values have been adapted from the SHRP-P-651 report (SHRP, 1991).

Table 3. Surface deflection values measured by the FWD (SHRP, 1991)

Section	Layer thickness (mm)		Radial distances (mm)						
	AC	Base	0	203	305	457	610	915	1525
1	106.5	127	0.2936	0.2290	0.1845	0.1361	0.1012	0.0615	0.0342
2	106.5	127	0.2839	0.2193	0.1779	0.0133	0.1005	0.0609	0.0316
3	106.5	127	0.2664	0.2079	0.1697	0.1284	0.0975	0.0597	0.0315
4	106.5	127	0.2573	0.2003	0.1645	0.1256	0.0960	0.0592	0.0318
5	76.2	152	0.4588	0.3236	0.2482	0.1757	0.1326	0.0858	0.0498
6	152.4	304.8	0.4198	0.3417	0.3026	0.2580	0.2218	0.1701	0.1078

To validate and evaluate the accuracy of the proposed procedure, the FWD measured deflections, the contact pressure and the thickness of Asphalt Concrete (AC) and granular base were given to the MODCOMP, ISSEM4, MODULUS, BACKFA, WESDEF, and JayaBack programs and the moduli for asphalt, granular base, and subgrade soil was backcalculated.

ISSEM4 program which has been developed by Dynatest Company, is based on the layered elastic theory (ELSYM 5) and employs an iterative procedure to match the measured deflections with the theoretical deflections calculated at the pavement surface (Bush and Baladi, 1989). MODCOMP was developed for the U.S. Army Cold Regions Research and Engineering Laboratory by Irwin and Szebenyi (1983). It uses the layered elastic theory for the forward computation of surface deflections and an iterative process for backcalculation of moduli. The program first calculates the modulus of the deeper layers, and then calculates the modulus of the upper layers. It can estimate the moduli for a pavement system having 2 to 15 layers and assumes that the lowest layer is as infinite half-space. It can also handle 6 different loads, each with 10 deflections. MODCOMP considers material behavior as linear elastic or nonlinear elastic for to estimate layers modulus (Irwin, 1983; William, 1999).

MODULUS program which has been developed at the Texas Transportation Institute, uses WESLEA's forward analysis program to create the deflection database, and employed the Pattern Search Algorithm for inverse calculation (Alexander et al., 1989; Richardson and Lusher, 2015; Van et al., 1989). The WESDEF uses the WESLEA program as forward analysis tool and to backcalculate the layers moduli that results in the best fit between a computed and a measured deflection basin (Hassan, 2003). The BAKFAA, was developed by Federal Aviation Administration (FAA) and uses the LEAF, a layered elastic theory

program, for forward analysis (Brill and Hughes, 2007; Gopalakrishnan, 2012).

The value of the moduli calculated by the JayaBack program and other programs are represented in Figure 10. Table 4 shows the percentage of the difference between the predicted modulus of the JayaBack and other programs.

As can be seen in Table 4, maximum difference between the predicted modulus of the JayaBack and the other programs for the asphalt layer, base, and subgrade was found to be 22.5, 33.7, and 19.9 percent, respectively. To evaluate the accuracy of the JayaBack, the backcalculated moduli by the ISSEM4, MODCOMP, MODULUS, WESDEF, BACKFA, and JayaBack program were given to the KENLAYER program, and the surface deflections in case of each pavement section was computed. Then, the deflection basin resulted from the KENLAYER program based on the backcalculated moduli of each program was compared to the deflection basin measured by the FWD device.

The values of R^2 and RMSE obtained from the comparison of the deflection basin measured by the FWD device and calculated by the KENLAYER program based on the backcalculated moduli using different software are given in Table 5. according to this table, the JayaBack deflection results, in comparison with the other programs, have more compatibility with the FWD results. Therefore, it can be concluded that the backcalculated modules obtained from the JayaBack are reliable. Figure 11 shows the deflection basins calculated based on the moduli backcalculated using the JayaBack and ones measured by the FWD device for six different sections.

6.3.2. Hybrid ANN-Jaya Method in Comparison with other Optimization Methods

To investigate the ability of the Jaya with the GA and PSO, the hybrid ANN-GA and ANN-PSO were developed, and their results were compared with ANN-Jaya. The

speed and accuracy of these three methods were investigated for the different

pavement sections mentioned in the previous article.

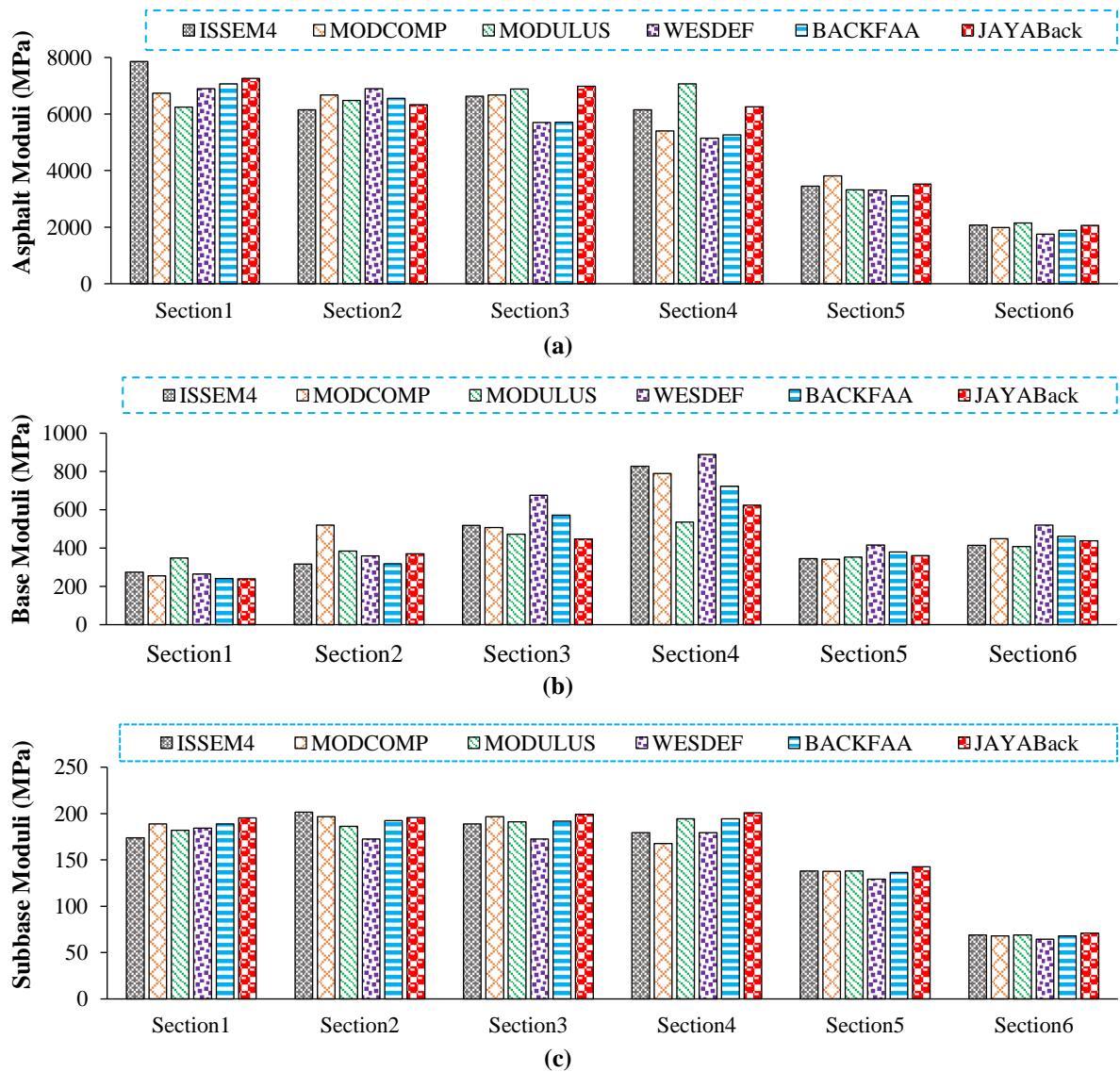


Fig. 10. Backcalculated moduli by JayaBack and other programs

Table 4. Difference between the moduli backcalculated by the JayaBack and other programs

		ISSEM4	MODCOMP	MODULUS	WESDEF	BACKFAA
Section 1	E ₁	7.7	7.7	16.2	5.2	2.7
	E ₂	12.7	6.1	31.1	9.3	0.7
	E ₃	12.4	3.4	7.3	6.1	3.4
Section 2	E ₁	2.9	5.2	2.4	8.2	3.4
	E ₂	17.1	28.6	3.5	3.4	16.6
	E ₃	2.8	0.4	5.1	13.5	1.7
Section 3	E ₁	5.3	4.6	1.3	22.5	22.1
	E ₂	13.5	11.6	5.3	33.7	21.7
	E ₃	5.5	1.4	4.4	15.6	4.0
Section 4	E ₁	1.8	15.8	11.5	21.4	18.9
	E ₂	24.5	20.8	16.4	29.8	13.8
	E ₃	12.0	19.9	3.3	12.0	3.3
Section 5	E ₁	3.1	4.6	3.1	10.1	4.3
	E ₂	6.0	2.5	7.6	15.7	5.1
	E ₃	0.4	3.4	3.9	17.3	8.9
Section 6	E ₁	3.3	3.5	3.3	10.4	4.4
	E ₂	4.5	5.5	2.2	13.5	5.0
	E ₃	2.3	7.5	6.2	6.5	13.4

Table 5. Evaluation of deflection basin, measured by the FWD, and calculated by the KENLAYER

		ISSEM4	MODCOMP	MODULUS	WESEDEF	BACKFAA	JayaBack
Section 1	R ²	0.99928	0.99983	0.99942	0.99977	0.99985	0.99986
	RMSE	0.01093	0.00499	0.00526	0.00689	0.00488	0.00103
Section 2	R ²	0.99681	0.99572	0.99608	0.99929	0.99916	0.99946
	RMSE	0.00709	0.00776	0.04308	0.02281	0.00536	0.00208
Section 3	R ²	0.99862	0.99932	0.99536	0.99623	0.99956	0.99958
	RMSE	0.00532	0.00202	0.04159	0.01442	0.00440	0.00176
Section 4	R ²	0.99954	0.99976	0.99357	0.99985	0.99961	0.99967
	RMSE	0.00945	0.02045	0.04342	0.01027	0.00407	0.00173
Section 5	R ²	1.00000	0.99992	1.00000	0.99935	0.99998	1.00000
	RMSE	0.00695	0.00552	0.00670	0.01224	0.00628	0.00175
Section 6	R ²	0.99999	0.99996	0.99999	0.99964	0.99999	0.99997
	RMSE	0.00862	0.00746	0.00843	0.01311	0.00694	0.00089

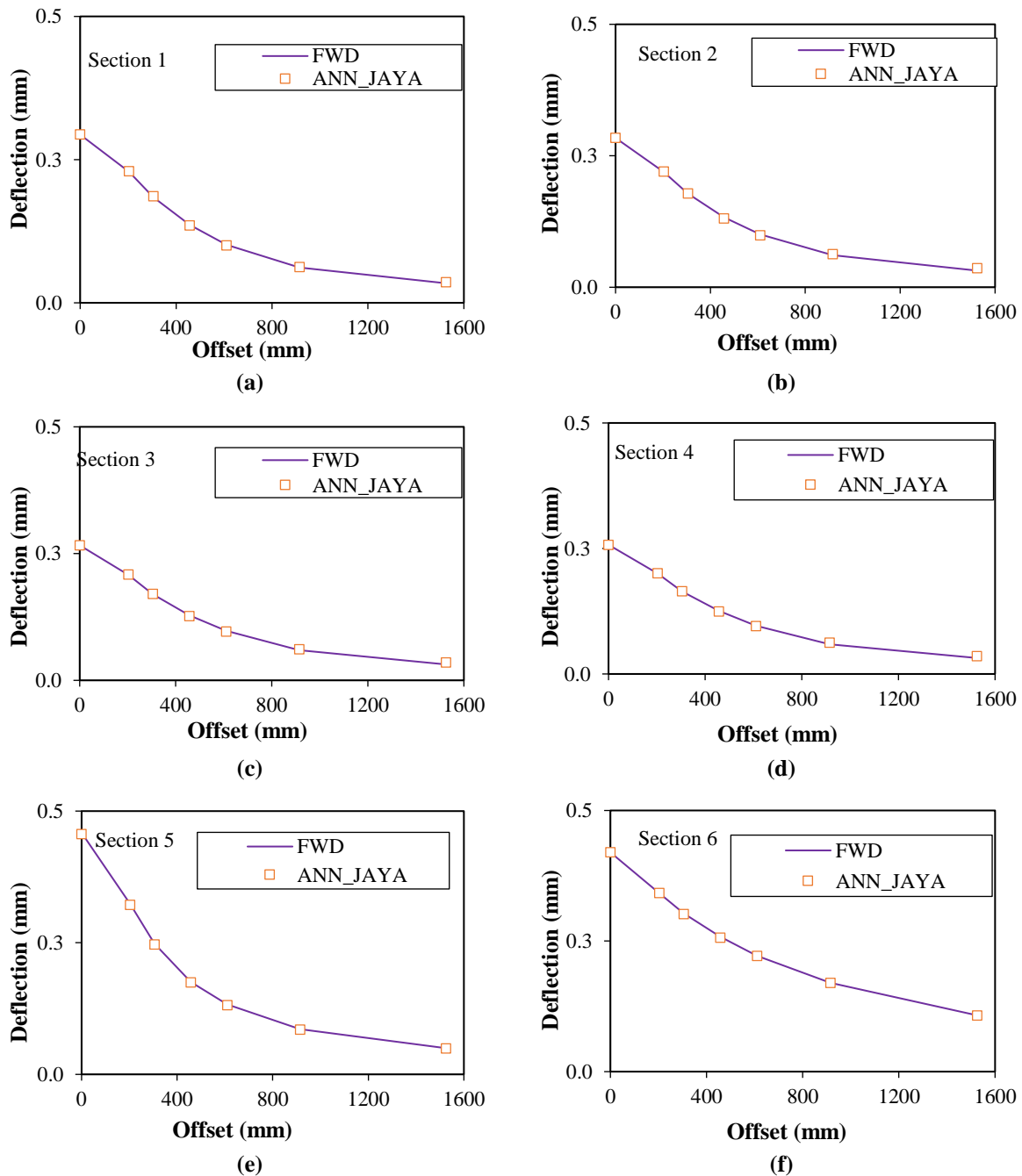


Fig. 11. Deflection basins calculated based on the JayaBack backcalculated moduli and ones measured by the FWD device; a) Section 1; b) Section 2; c) Section 3; d) Section 4; e) Section 5; and f) Section 6

Before the backcalculation, the tuning parameters of the optimization algorithms should be determined. The Jaya algorithm needs no tuning parameter. The PSO algorithm has two tuning parameters of c_1 and c_2 , which vary between 1 and 2. The Genetic Algorithm consists of two parameters, including the intersection probability and the probability of mutation, and the range of variations of these two parameters was considered to be [0.7-1] and [0.1-0.4], respectively (Yang, 2010). The optimal values were determined while the objective function was evaluated based on 50 particles and 1000 iterations. The optimal value of the c_1 and c_2 in the PSO algorithm was equal to 2. Moreover, the best value for crossover and mutation probability parameters were found to be 0.9

and 0.4, respectively.

The optimal values of the objective function can be seen for ANN-Jaya, ANN-PSO, and ANN-GA methods for six different pavement sections in Table 6. It is clear from this table that the optimal value of the objective function for the ANN-Jaya and ANN-PSO is approximately equal, although the ANN-Jaya has achieved a more accurate value. It can be also seen that the ANN-GA method has been trapped into the local optima, and in most cases, it is not able to find global optima. Figure 12 shows the convergence diagram of each method for six pavement sections. According to the figure, the convergence rate of the Jaya algorithm to the global optima is faster than the PSO and notably greater than the GA algorithm.

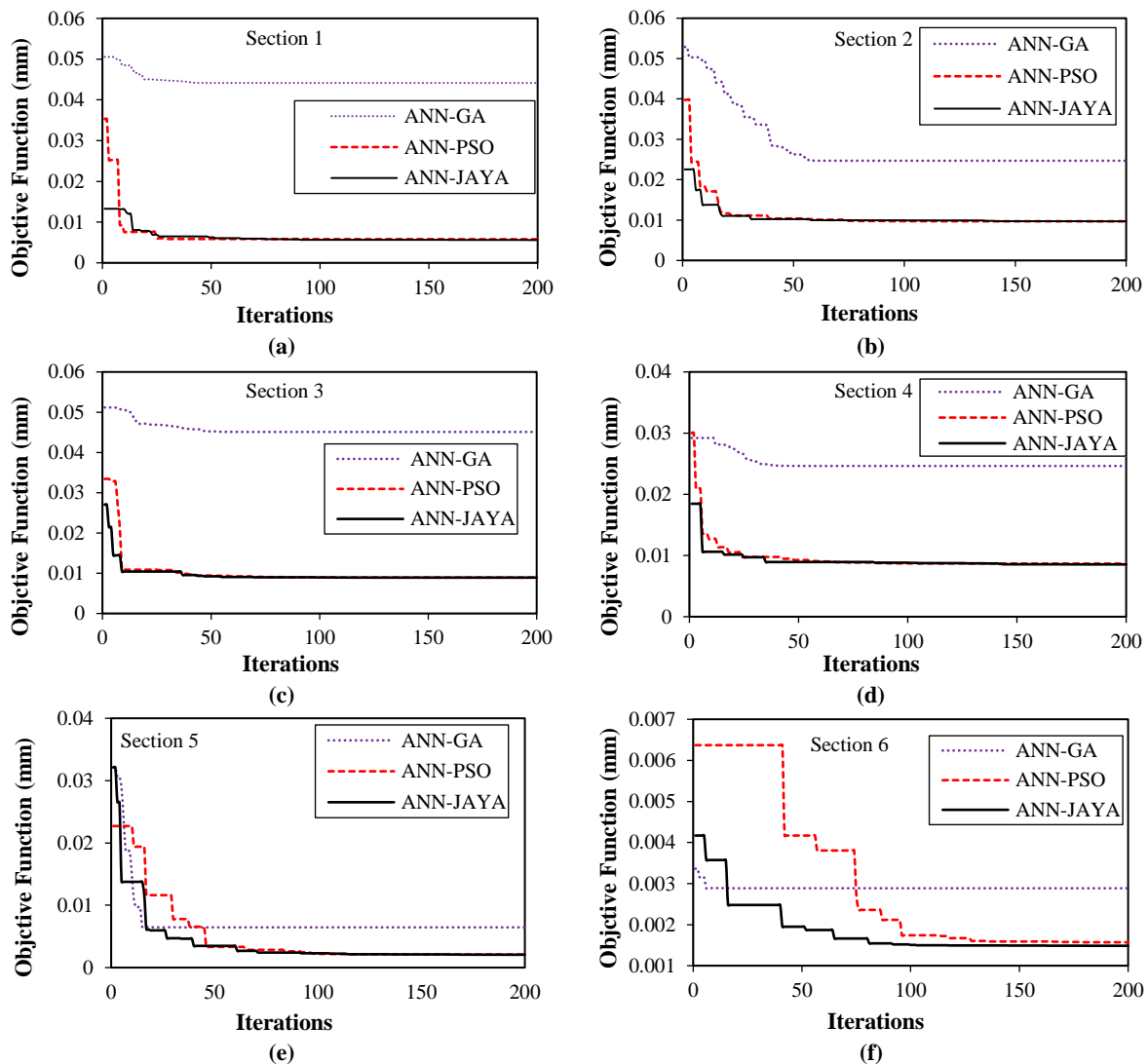


Fig. 12. The convergence diagram of ANN-GA, ANN-PSO and ANN-Jaya for different pavement sections; a) Section 1; b) Section 2; c) Section 3; d) Section 4; e) Section 5; and f) Section 6

Table 6. Optimal values of the objective function derived from backcalculation using different methods

Section	ANN-GA	ANN-PSO	ANN-Jaya
1	0.044151	0.005788	0.005586
2	0.024705	0.009703	0.009701
3	0.045097	0.008931	0.008909
4	0.024637	0.008672	0.008546
5	0.006453	0.002098	0.002068
6	0.002886	0.001571	0.001486

6.4. Experimental Results

The proposed method was implemented in the MATLAB program. All computations were solved on an Intel Core i5-3210 M CPU 2.5 GHz with 4 GB of RAM. The developed program gets the input parameters including the asphalt and granular base layers thicknesses (cm), the granular base and subgrade soil moduli (MPa), asphalt content, the contact pressure of FWD device (MPa), the deflection values at seven radial distances (mm), the number of moduli generated per iteration and the maximum number of iterations. The software determines the asphalt, granular base and subgrade soil moduli (MPa) as the output.

In order to compare the robustness, stability, reliability and convergence of different optimization algorithms including the Jaya, PSO, and GA, each field data was run as much as 10 times by means of each optimization algorithms. To evaluate the robustness, stability, reliability and convergence of the developed model, each field data was run as much as 10 times. At

each implementation, five hundred iterations are run and, fifty modulus is considered at each iteration, and the objective function is RMSE value of predicted values of deflections with desired deflections. The thickness of asphalt concrete and granular base layers for each pavement section along with the measured deflections are given in Table 3. The lower and upper band of the resilient modulus were also considered for asphalt concrete layer, granular base layer, and subgrade soil layer as 500 to 10,000 MPa, 100 to 2000 MPa and 20 to 400 MPa, respectively.

Tables 7-9 indicate the statistical parameters of the optimal objective function value, the last optimization iteration, and the run time for the Jaya, PSO, and GA algorithms, respectively. In this study, the maximum number of iterations as well as the minimum RMSE have been used as the stopping criteria. As can be seen, the Jaya algorithm indicates the high robustness and superior convergence in comparison with the GA and PSO algorithms.

Table 7. The statistical parameters to evaluate of the Jaya algorithm

		Section 1	Section 2	Section 3	Section 4	Section 5	Section 6
Optimal objective function value (mm)	Min	0.001237	0.001886	0.001731	0.001714	0.000652	0.000980
	Max	0.001989	0.001980	0.001978	0.001990	0.001872	0.001990
	Average	0.001653	0.001940	0.001879	0.001852	0.001519	0.001637
	Sta.	0.000248	0.000029	0.000079	0.000089	0.000337	0.000230
	Dev						
Total time (sec)	Min	0.61	0.87	0.72	0.70	0.67	0.85
	Max	0.97	1.21	1.10	0.84	0.96	1.03
	Average	0.79	1.01	0.85	0.78	0.80	0.91
	Sta.	0.10	0.10	0.09	0.05	0.09	0.06
	Dev						
The latest iterations of optimality	Min	3	28	9	7	2	23
	Max	33	56	38	23	31	38
	Average	17.4	37.1	19.8	18.4	19	28.1
	Sta.	8.80	8.37	7.21	2.87	6.65	4.91
	Dev						

Table 8. The statistical parameters to evaluate of the PSO algorithm

		Section 1	Section 2	Section 3	Section 4	Section 5	Section 6
Optimal objective function	Min	0.001461	0.001900	0.001782	0.001796	0.001125	0.001152
	Max	0.001996	0.001994	0.001987	0.001996	0.001925	0.001991
value (mm)	Average	0.001702	0.001953	0.001904	0.001916	0.001570	0.001648
	Sta. Dev	0.000165	0.000029	0.000062	0.000054	0.000279	0.000338
Total time (sec)	Min	0.66	5.36	1.54	1.02	0.17	5.17
	Max	7.05	9.56	9.04	7.19	11.11	10.18
	Average	3.22	6.91	5.39	3.11	4.59	7.79
	Sta. Dev	1.72	1.29	2.09	1.60	3.34	1.61
The latest iterations of optimality	Min	5	34	13	14	8	28
	Max	41	52	48	45	67	54
	Average	19.7	41.5	29	19.8	28.4	41.5
	Sta. Dev	10.20	5.48	10.86	9.85	20.02	8.33

Table 9. The statistical parameters to evaluate of the GA algorithm

		Section 1	Section 2	Section 3	Section 4	Section 5	Section 6
Optimal objective function	Min	0.003789	0.002363	0.002248	0.002320	0.001765	0.001634
	Max	0.015410	0.010474	0.013726	0.008998	0.021849	0.001874
value (mm)	Average	0.008279	0.005942	0.005759	0.004917	0.010778	0.001715
	Sta. Dev	0.003149	0.002791	0.003260	0.001803	0.007063	0.000087
Total time (sec)	Min	370.77	367.24	368.21	369.57	284.44	0.46
	Max	416.56	374.35	399.72	420.18	417.61	4.98
	Average	383.99	369.40	375.94	410.13	396.06	2.13
	Sta. Dev	15.13	2.67	10.97	15.46	39.98	1.24
The latest iterations of optimality	Min	500	500	500	500	500	2
	Max	500	500	500	500	500	17
	Average	500	500	500	500	500	8.2
	Sta. Dev	0	0	0	0	0	4.24

7. Conclusions

The goal of this study was development of a moduli backcalculation method for the flexible pavements using the hybridization of the ANN and Jaya. The ANN was employed as the forward model to predict the pavement deflection basin, and the Jaya was applied to find the modulus of the layers based on the minimizing the difference between measured and calculated deflections. The results of this research can be concluded as follows:

- The developed ANN can predict the pavement deflections with high accuracy such that the coefficient of determination (R^2) in all cases is more than 0.9999.
- Comparison of results obtained by the hybrid ANN-Jaya method with other programs such as ISSEM4, MODCOMP, WESDEF, MODULUS and BACKFAA showed that the hybrid ANN-Jaya method can predict the pavement layers moduli with high accuracy.
- The deflection basins computed by the KENLAYER program based on the backcalculated moduli resulted from different programs as well as ANN-Jaya

procedure were compared to the deflection basin measured by the FWD device and results confirm that the ANN-Jaya procedure can be used as a reliable method for backcalculation of flexible pavements.

- Comparison of ANN-Jaya results with ANN-GA and ANN-PSO showed that the ANN-Jaya has a higher capability to find the optimum solutions in terms of convergence speed and finding global optima. It was also observed that, the ANN-GA was not able to find the global optima in most cases.
- The developed method was implemented in a computer program called JayaBack to facilitate the use of this method for moduli backcalculation of flexible pavements and further researches.
- The method (ANN-Jaya) and software (JayaBack) developed in this research can be used more accurately than the previous methods to predict the resilient modulus based on the FWD test results.

8. References

- Alexander, D.R., Kohn, S.D. and Grogan, W.P. (1989). "Nondestructive testing techniques and

- evaluation procedures for airfield pavements”, In *Nondestructive Testing of Pavements and Backcalculation of Moduli*, ASTM International, West Conshohocken, 502-524.
- Aubdulnibe, F.F. (2019). “An application of Artificial Neural Networks (ANNs) to the backcalculation of flexible pavement moduli”, *Journal of Physics: Conference Series*, 1362(1), 012146.
- Bendana, L., Yang, W. and Lu, J. (1994). “Interpreting data from the falling weight deflectometer”, Engineering Research and Development Bureau, New York State Department of Transportation, Research Report, 160.
- Brill, D.R. and Hughes, W.J. (2007). “New FAA pavement design software”, *International Airport Review*, 11(2), 17-20.
- Bush, A.J. and Baladi, G.Y. (1989). *Nondestructive testing of pavements and backcalculation of moduli*, ASTM International, West Conshohocke.
- Ceylan, H., Guclu, A., Tutumluer, E. and Thompson, M. R. (2005). “Backcalculation of full-depth asphalt pavement layer moduli considering nonlinear stress-dependent subgrade behavior”, *International Journal of Pavement Engineering*, 6(3), 171-182.
- Eberhart, R. and Kennedy, J. (1995). “A new optimizer using particle swarm theory”, *Proceedings of the 6th International Symposium on Micro Machine and Human Science*, Nagoya.
- Fu, G., Xue, C., Zhao, Y., Cao, D. and Alae, M. (2020). “Accuracy evaluation of statically backcalculated layer properties of asphalt pavements from falling weight deflectometer data”, *Canadian Journal of Civil Engineering*, 47(3), 317-325.
- Ghanizadeh, A.R. and Ziaie, A. (2015). “NonPAS: A program for nonlinear analysis of flexible pavements”, *International Journal of Integrated Engineering*, 7(1), 21-28.
- Ghanizadeh, A.R., Heidarabadzadeh, N. and Mahmoodabadi, M.J. (2020). “Effect of objective function on the optimization of highway vertical alignment by means of metaheuristic algorithms”, *Civil Engineering Infrastructures Journal*, 53(1), 115-136.
- Ghanizadeh, A.R. and Heidarabadzadeh, N. (2018). “Optimization of vertical alignment of highways in terms of earthwork cost using colliding bodies optimization algorithm”, *International Journal of Optimization in Civil Engineering*, 8, 657-674.
- Gopalakrishnan, K. (2010). “Neural network-swarm intelligence hybrid nonlinear optimization algorithm for pavement moduli backcalculation”, *Journal of Transportation Engineering*, 136(6), 528-536.
- Gopalakrishnan, K. (2012). “Instantaneous pavement condition evaluation using non-destructive neuro-evolutionary approach”, *Structure and Infrastructure Engineering*, 8(9), 857-872.
- Gopalakrishnan, K. and Papadopoulos, H. (2011). “Reliable pavement backcalculation with confidence estimation”, *Scientia Iranica*, 18(6), 1214-1221.
- Gopalakrishnan, K. and Thompson, M.R. (2004). “Backcalculation of airport flexible pavement non-linear moduli using Artificial Neural Networks”, *Proceedings of the FLAIRS Conference*, Florida.
- Gurney, K. (2005). *An introduction to neural networks*, CRC Press, London.
- Guzzarlapudi, S.D., Kumar Adigopula, V. and Kumar, R. (2017). “Comparative study of flexible pavement layers moduli backcalculation using approximate and static approach”, *Materials Today: Proceedings*, 4(9), 9812-9816.
- Hajiazizi, M., Taban, M.H. and Ghobadian, R. (2021). “Prediction of Q-value by multi-variable regression and novel Genetic Algorithm based on the most influential parameters”, *Civil Engineering Infrastructures Journal*, 54(2), 267-280.
- Hassan, H. and Mousa, R. (2003). “Evaluation of nondestructive testing data using AASHTO and WESDEF backcalculation approaches”, *Journal of Engineering and Applied Science*, 50(1), 75-93.
- Holland, J. (1975). *Adaptation in natural and artificial systems*, Michigan Press, Ann Arbor.
- Huang, Y.H. (2004). *Pavement analysis and design*, Pearson Education, New Jersey.
- Irwin, L. (1983). *User's guide to Modcomp2, Version 3.2*, Local Roads Program, Cornell University, Ithaca, NY.
- Kaveh, A. and Dadras, A. (2017). “A guided tabu search for profile optimization of Finite Element models”, *International Journal of Optimization in Civil Engineering*, 7(4), 527-537.
- Li, M. and Wang, H. (2019). “Development of ANN-GA program for backcalculation of pavement moduli under FWD testing with viscoelastic and nonlinear parameters”, *International Journal of Pavement Engineering*, 20(4), 490-498.
- Li, Y., Ma, D., Zhu, M., Zeng, Z. and Wang, Y. (2018). “Identification of significant factors in fatal-injury highway crashes using Genetic Algorithm and Neural Network”, *Accident Analysis and Prevention*, 111, 354-363.
- Maher, A. and Bennert, T.A. (2008). “Evaluation of Poisson's ratio for use in the mechanistic empirical pavement design guide (MEPDG)”, Transportation Resaerch Board, No. FHWA-NJ-2008-004.
- Öcal, A. (2014). “Backcalculation of pavement layer properties using artificial neural network based gravitational search algorithm”, Ph.D. Thesis,

- Middle East Technical University, Ankara, Turkey.
- Pekcan, O., Tutumluer, E. and Thompson, M. (2008). "Artificial Neural Network based backcalculation of conventional flexible pavements on lime stabilized soils", *Proceedings of the 12th International Conference of International Association for Computer Methods And Advances in Geomechanics (IACMAG)*, Goa, India.
- Rakesh, N., Jain, A., Reddy, M.A. and Reddy, K.S. (2006). "Artificial Neural Networks-Genetic Algorithm based model for backcalculation of pavement layer moduli", *International Journal of Pavement Engineering*, 7(3), 221-230.
- Rao, R. (2016). "Jaya: A simple and new optimization algorithm for solving constrained and unconstrained optimization problems". *International Journal of Industrial Engineering Computations*, 7(1), 19-34.
- Rao, R.V., Savsani, V.J. and Vakharia, D. (2011). "Teaching-learning-based optimization: A novel method for constrained mechanical design optimization problems", *Computer-Aided Design*, 43(3), 303-315.
- Richardson, D.N. and Lusher, M. (2015). "MoDOT pavement preservation research program volume III, development of pavement family and treatment performance models", Division of Construction and Materials, Final Report Prepared for Missouri Department of Transportation.
- Saltan, M. and Terzi, S. (2008). "Modeling deflection basin using artificial neural networks with cross-validation technique in backcalculating flexible pavement layer moduli", *Advances in Engineering Software*, 39(7), 588-592.
- Saltan, M., Tigdemir, M. and Karasahin, M. (2002). "Artificial Neural Network application for flexible pavement thickness modeling", *Turkish Journal of Engineering and Environmental Sciences*, 26(3), 243-248.
- Saltan, M., Uz, V.E. and Aktas, B. (2013). "Artificial Neural Networks-based backcalculation of the structural properties of a typical flexible pavement", *Neural Computing and Applications*, 23(6), 1703-1710.
- Samadi, D., Taghaddos, H., Nili, M.H. and Noghabaei, M. (2021). "Development of a bridge maintenance system using bridge information modeling", *Civil Engineering Infrastructures Journal*, 54(2), 351-364.
- Saric, A. and Pozder, M. (2017). "Artificial Neural Networks application in the backcalculation process of flexible pavement layers elasticity modulus", In: *International Symposium on Innovative and Interdisciplinary Applications of Advanced Technologies*, 549-559, Springer, Cham.
- Scimemi, G.F., Turetta, T. and Celauro, C. (2016). "Backcalculation of airport pavement moduli and thickness using the Lévy Ant Colony Optimization algorithm", *Construction and Building Materials*, 119, 288-295.
- Sonmez, M., Akgüngör, A.P. and Bektaş, S. (2017). "Estimating transportation energy demand in Turkey using the Artificial Bee Colony Algorithm", *Energy*, 122, 301-310.
- Strategic Highway Research Program (SHRP). (1991). "SHRP layer moduli backcalculation procedure software selection", SHRP Technical Report, Washington D.C.
- Ullidtz, P. (1987). *Pavement analysis, developments in Civil Engineering*, Elsevier, Netherlands.
- Van Cauwelaert, F.J., Alexander, D.R., White, T.D. and Barker, W.R. (1989). "Multilayer elastic program for backcalculating layer moduli in pavement evaluation", *1st International Symposium on Nondestructive Testing of Pavements and Backcalculation of Moduli*, Baltimore, Maryland, USA.
- Vasant, P., Zelinka, I. and Weber, G. (2019). *Intelligent computing and optimization*, Springer, Turkey.
- Von Quintus, H.L. and Simpson, A.L. (2002). *Back-calculation of layer parameters for LTPP test sections, Volume II: Layered elastic analysis for flexible and rigid pavements*, FHWA-RD-01-113, United States.
- Wang, H., Xie, P., Ji, R. and Gagnon, J. (2020). "Prediction of airfield pavement responses from surface deflections: Comparison between the traditional backcalculation approach and the ANN model", *Road Materials and Pavement Design*, 22(9), 1930-1945.
- William, G.W. (1999). "Backcalculation of pavement layers moduli using 3D nonlinear explicit finite element analysis", Ph.D. Thesis, West Virginia University Libraries.
- Yang, X.-S. (2009). *Firefly algorithms for multimodal optimization*, Springer, Cambridge.
- Yang, X.-S. (2010). *Nature-inspired metaheuristic algorithms*, Luniver press, UK.
- You, L., Yan, K. and Liu, N. (2020). "Assessing Artificial Neural Network performance for predicting interlayer conditions and layer modulus of multi-layered flexible pavement", *Frontiers of Structural and Civil Engineering*, 14(2), 487-500.
- Zhang, X., Otto, F. and Oeser, M. (2021). "Pavement moduli back-calculation using Artificial Neural Network and Genetic Algorithms", *Construction and Building Materials*, 287, 123026.



This article is an open-access article distributed under the terms and conditions of the Creative Commons Attribution (CC-BY) license.



The Effect of Hydrophobic Amorphous Carbon Powder on the Compressive Strength, Water Absorption and Rheological Attributes of Cement Mortar

Haji Hossein, A.R.¹, Bigdeli, H.R.¹, Mokhtari, F.¹, Jahantab, S.¹ and Habibnejad Korayem, A.^{2*}

¹ B.Sc. Student, School of Civil Engineering, Iran University of Science and Technology, Tehran, Iran.

² Associate Professor, School of Civil Engineering, Iran University of Science and Technology, Tehran, Iran.

© University of Tehran 2021

Received: 15 Oct. 2020;

Revised: 16 May 2021;

Accepted: 28 Jun. 2021

ABSTRACT: In this paper, the feasibility of employing amorphous carbon powder as a viable degradation inhibitor for cement mortars made with siliceous aggregates was investigated. Amorphous carbon powder is a by-product of the paraffin industry and was replaced by 0, 4, 6 and 8% of aggregate. Mechanical strength, rheology and water absorption were analyzed considering three common physical factors of concrete namely strength, workability and durability. Mechanical properties of mixtures were obtained using flexural and compressive strengths and rheological attributes were collected through flow table test. Results revealed that adding amorphous carbon powder to the bulk cement mortar could enhance the strength and durability of cement mortar. Replacing 8 wt.% of siliceous aggregate dust filler by amorphous carbon powder caused an increment about twofold in the 28-day compressive strength and reduction of the flow table results by about 20% compared to those of the control mixture. Moreover, hydrophobicity and impermeability properties of amorphous carbon -modified cement mortars, resulted in reduced moisture susceptibility.

Keywords: Amorphous Carbon, Cement Composites, Durability, Permeability.

1. Introduction

The durability of cement-based composites such as concrete and cement mortar has emerged as an area of focus in recent years (Li et al., 2019). Statistics indicate that rehabilitation of Reinforced Concrete (RC) structures has placed a significant financial burden on authorities' resources. As reported by the Federal Highway Administration (FHWA), \$300 million is

required for either rehabilitation or replacement of US national dilapidated bridges until 2020 (FHWA, 2019). In many cases of which, the RC deck's remediation takes precedence over other treatments (Samadi et al., 2021). Prior to year 2000, it was also estimated that remedial treatments undertaken as a result of chloride-induced corrosion would cost \$5 billion, according to FHWA (Glass and Buenfeld, 2000). Destructive marine environments are

* Corresponding author E-mail: ahkorayem@iust.ac.ir

proved to be efficacious on the durability of concrete due to their vast sulfate and chloride content (Homan et al., 2016; Isteita and Xi, 2017).

Chloride penetration is one of the major potential hazards for the RC structures. Cement matrix provides an appropriate environment for the embedded reinforcements (Ormellese et al., 2006; Glass and Buenfeld, 2000). This is due to an alkaline pH over 12.5 in which the corrosion process ceases to accelerate and causes no more dilapidation (Ormellese et al., 2006; Berke and Hicks, 2004). However, an internal source of unwelcome contamination in mixing progress would derange the passive film around the reinforcements (Berke and Hicks, 2004; Glass and Buenfeld, 2000). On the other hand, the chloride ions rendered by de-icing and marine salt mainly consisting of calcium chloride may contaminate the concrete as an external source (Glass and Buenfeld, 2000; Bamforth et al., 1997). Whether the source of contamination is internal or external, the worst-case scenario is exceeding the Chloride Threshold Level (CTL). CTL is the content of chloride at steel depth in which, the passive film around the steel breaks down and eventually, the corrosion process initiates and gradually worsens (Ann and Song, 2007). Many structures located near water along with off-shore structures (such as parking garage floors, bridge decks and floating docks) have to struggle with these problems (Isteita and Xi, 2017; Homan et al., 2016). New standards have constructors to care about the internal source of chloride ions (Hooton, 2019; Glass and Buenfeld, 2000). Moreover, new technologies such as additive manufacturing give more control on concrete production and have substantially reduced the risk of internal contamination (Li, 2018; Kooshafar and Madani, 2017). Considering the advances in the concrete production, chloride diffusion from external sources must be contained. As a result, several solutions are put forward to cope with this problem. Allen et

al. (1993) suggested resin repair mortars such as epoxy resins as an inhibitor especially in members with a concrete cover less than 12 mm. These mortars have widely been used as coatings. However, statistics show that periodic maintenance of 4 to 15 years is necessary as the coating debonds over time. Tatematsu and Sasaki (2003) used a salt adsorbent to separate and deactivate chloride ions in concrete. Kumar et al. (2018) studied the effect of ground granulated blast furnace slag together with calcium nitrate as an inhibitor.

Another crucial hazard for cement mortars is sulfate attack, which is defined as the physical and chemical reactions between hardened cement paste and sulfate ions. Sulfate attack also may be of an internal or external source. Two main products of the sulfate attack are calcium sulfate and ettringite (Collepari, 2003). Ettringite production is followed by enlargement which exerts pressure on the mortar and causes dilapidation (Ghasemalizadeh and Toufigh, 2020). The latter is also responsible for more permeability. Various methods have been used to prevent or treat the sulfate attack out of which using Ordinary Portland Cement (OPC) types II and V and pozzolanic cement is well-practiced particularly in sulfate dominated environments (Steiger, 2005). Tricalcium aluminate (C_3A) as an early-age strengthening agent reacts with the sulfate ions. Type II and IV of OPC have limited components of C_3A to 8 and 5%, respectively, thus reducing the reaction rate and helping to prevent the sulfate attack. Torii and Kawamura (1994) suggested that the replacement of OPC by fly ash and silica fume effectively enhances the resistance of the mortar to the sulfuric acid and sulfate solution attack. Lee (2009) stated that the use of recycled fine aggregates up to a maximum 50% replacement is effective under severe magnesium sulfate environment, irrespective of the type of recycled fine aggregates.

Water is one of the prerequisites for chloride and sulfate attack (Mobasher,

2006). Homan et al. (2016) illustrated that the moisture content of an RC plays a relatively crucial role in increasing the migration rate of chloride ions, owing to the additional seepage pressure provided by water. Subsequently, the reduction in the amount of absorbed water seems viable to increase the durability against chloride and sulfate attack. For example, the reduction in concrete absorption by addition of nanolime is proven to enhance durability of concrete (Coppola et al., 2018; Taglieri et al., 2017).

De Weerd et al. (2015) stated that although addition of waste glass powder can increase the risk of uncontrolled expansion due to alkali silica reaction, it works as an inhibitor when used as fine aggregate (≤ 1 mm) and in high percentages around 20% to 30%. Another alternative is hydrophobic treatment as an effective technique to minimize moisture transport into concrete. Hydrophobic treatment positive effect on durability and service life has been documented (Mora et al., 2019; Qu and Yu, 2018). As a result, many researchers have striven to prevent water absorption by various means. Zhou et al. (2020a,b) devised a new polymer with a hydrophilic head that absorbs cement hydration products and a hydrophobic chain that can act like a gate, stopping the transportation of ion-carrying liquids such as water. Introduction of 0.9 wt% of inhibitor was shown to have reduced water absorption to 30% of the reference value.

Asipita et al. (2014) deployed green *Bambusa arundinacea* leaves as a natural low-risk inhibitor and observed approximately 70% reduction in the water absorption after 2 hours. They used only 2 wt% of inhibitor and compared its performance with calcium nitrite and ethanolamine. The *Bambusa arundinacea* outperformed both inhibitors. Research conducted by Wong et al. (2015) rendered the effectiveness of paper sludge ash when used in the form of powder as cement replacement and coating. Tittarelli and Moriconi (2011) applied an aqueous emulsion of an alkyl-triethoxy-silan as a

hydrophobic agent. The experiments proved that bulk treatment is more effective during the concrete lifespan and using hydrophobic material as surface treatment is only efficacious during the initial dry-wet cycles.

Mora et al. (2019) developed hydrophobic silica particles which were effective even by low-percent incorporation. The effect of sodium acetate, fluoropolymer, silicone resin and silane when used as a surface hydrophobic inhibitor was assessed and results demonstrated that there is a positive correlation between surface cohesion and hydrophobicity (Liu and Hansen, 2016). Al-Kheetan et al. (2019) investigated whether concrete moisture content affects the performance of sodium acetate, fluoropolymer, silicone resin and silane as surface inhibitors. The results showed that silane is best for dry concrete mixtures while sodium acetate works best when the concrete is saturated.

Amorphous Carbon (AC) powder that is a processed by-product of the paraffin industry, is certified to have hydrophobic attributes (Ziari et al., 2017a,b). Where the AC powder to be disposed of as landfills, it would contaminate the soil and water. On the other hand, the utilization of waste as a construction material is a suitable means of disposal (Habibnejad Korayem et al., 2018; Ziari et al., 2017a,b). Besides, replacing aggregate by AC can help to reduce natural resource depletion (Madani et al., 2016). If applied, AC will be one of few recycled inhibitors that have low financial and environmental cost and can be easily added to bulk concrete. This is an advantage compared to surface inhibitors. Habibnejad Korayem et al. (2018) have investigated the effectiveness of AC in rutting and fatigue performance of asphalt mixtures. This research demonstrated that AC has sufficiently enhanced the moisture resistance properties of the asphalt mixture. Consequently, and due to the similarities between asphalt cement and cement mortar, AC powder to be investigated for

enhancement in concrete's mechanical and durability attributes. In the current study, AC is used as a partial replacement of aggregates to achieve a more durable mortar. The mechanical and rheological characteristics of concrete with and without AC were compared. To measure the influence of AC powder on durability, specimens were exposed to water absorption test. To detect the mechanical and rheological features, flexural strength, compressive strength and flow table were performed. The results indicate a significant increase in compressive strength and better performance of AC-modified concrete in moist ambiance. Conclusively, AC powder is an appropriate inhibitor due to its cost, environmentally friendly features and easy use. The data from this research can be used by stakeholders and policymakers to impose appropriate measures in selection and preparation of concrete materials in future constructions.

2. Materials

The specific gravity and water absorption for the utilized silica aggregate were 2.73 and 0.5%, respectively. The aggregate was graded in compliance with BS 196-1 (2005) and portrayed in Figure 1.

OPC Type II from Tehran Cement Plant was used as the binder. The X-Ray Fluorescence (XRF) results were used to identify the chemical compositions of OPC

which is depicted in Table 1. The AC powder which was used as a partial replacement of aggregates is a solid waste of the paraffin industry. Also, Table 2 indicates the physical and chemical properties of AC powder.

Figure 2 shows the visual and Scanning Electron Microscopy (SEM) images of the AC powder passed sieve #200. The surface roughness of AC is vividly seen in Figures 2b-2d at micro and nanoscale.

Experimentally, it was proved that using Polycarboxylate Ether (PCE) superplasticizer is best for AC dispersion (Shahbazi et al., 2020). As a result, PCE was utilized at 0.1% of cement mass for all mix designs.

3. Methods

Mixing was done as outlined in BS 196-1 (2005) with some exceptional changes. Hobart mixer equipped with a 5-liter bowl was used for mixing mortar. Mixing started with 30 seconds of dry mixing of sand, cement and AC powder to help the uniform dispersion of AC with other solid components. This stage was followed by adding the water and PCE superplasticizer in the next 30 seconds at a relatively constant rate. Then, 1 minute of medium speed mixing was followed by 75 seconds of rest. The final stage was mixing for a minute at a medium speed.

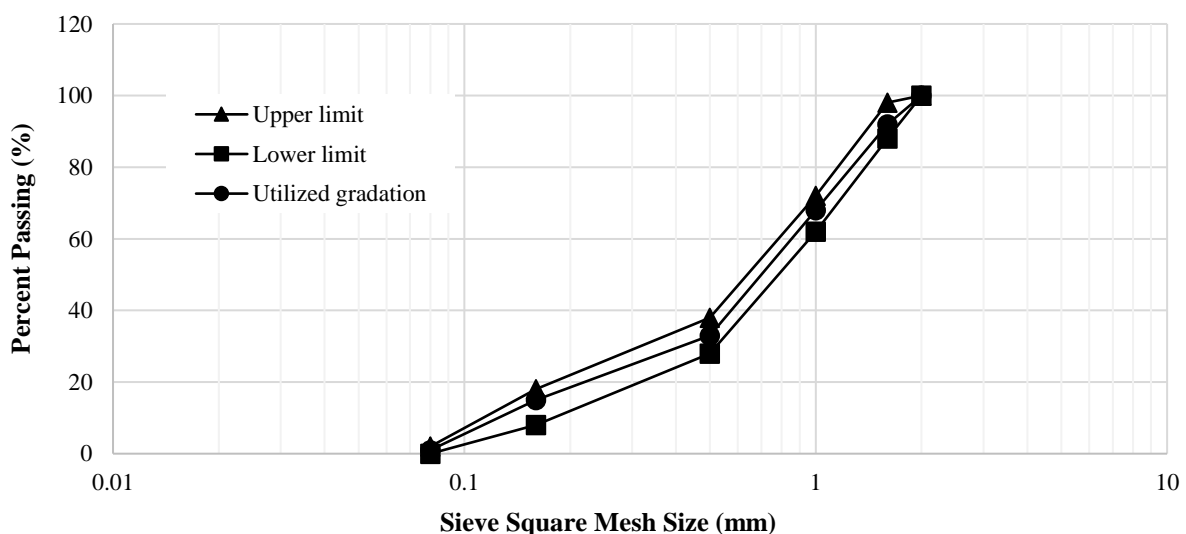
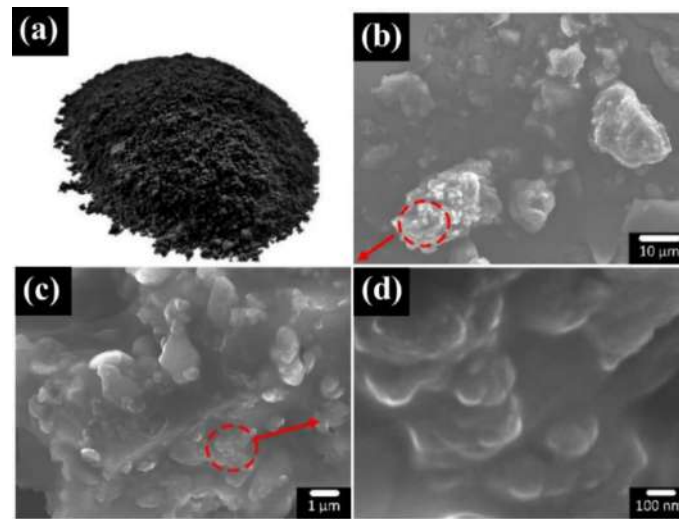


Fig. 1. Silica aggregate gradation based on BS 196-1 (2005)

Table 1. The XRF results for the utilized OPC

Chemical compositions (wt%)					
SiO ₂	Al ₂ O ₃	Fe ₂ O ₃	MgO	CaO	SO ₃
20.74	4.90	3.50	1.20	62.95	3.00

**Fig. 2.** a) The AC powder; and b-d) The SEM image in micro and nano scales**Table 2.** The physical and chemical properties of AC powder

Property or component	AC
Specific gravity	0.92
Particle size (μm)	10 - 70
Specific surface area (m ² /gr)	4.76
C (%)	74.38
O (%)	17.92
S (%)	7.24

3.1. Mix Design

The standard mix design for cement mortar was used as stated in BS 196-1 (2005). According to the British Standard, water-cement and aggregate-cement ratios were 0.5 and 3, respectively. PCE superplasticizer was added to the mix by 0.1% of cement mass. AC powder was replaced with 4, 6 and 8 percent of aggregate. Mix design with no AC content was used as a reference. Mix design for all percentages of replaced AC powder are reflected in Table 3.

3.2. Rheology

To evaluate the workability, mini-slump

and flow table tests were carried out according to ASTM C230 (2020). The tests were conducted immediately after mix procedure was complete.

3.3. Mechanical Tests

3.3.1. Flexural Strength

Flexural strength was measured by testing six 40 × 40 × 160 mm cubes, moulded for each mix design. Mechanical tests were carried out by a Universal Testing Machine (UTM) based on BS 196-1 (2005). After demolding, specimens were cured in saturated limewater in the room temperature (23 ± 2°C) for 7 and 28 days.

Table 3. Mix design of specimens

Mixture	Proportions in Kg/m ³				
	Cement	Aggregate	Water	AC	superplasticizer
AC 0%	406	1219	203	0	0.41
AC 4%	406	1171	203	48	0.41
AC 6%	406	1123	203	96	0.41
AC 8%	406	1075	203	144	0.41

3.3.2. Compressive Strength

To detect the compressive strength of mixtures, portions of flexural prisms were used. Each portion was 40 mm in depth and width and approximately 80 mm in length in accordance with ASTM C349 (2018).

3.4. Water Absorption

Investigating the water absorption of samples containing AC powder is one of the integral parts of this study to measure the competency of AC powder in limiting water ingress into concrete. Water absorption rate and volumetric water absorption tests were conducted based on ASTM C1585 (2014) and ASTM C642 (2013), respectively.

In the capillary water absorption rate test, the standard specimens, which are 100 mm diameter discs with a height of 50 mm, were cured for 28 days prior to testing and oven-dried for 24 h at 105 °C and then weighted. It is highly advised to ensure that water is only allowed to penetrate from the specified surface and the flow to be one-directional. To achieve this, waterproof plastic tapes were attached to the surroundings of the samples and a plastic sheet was used on top of it to hinder evaporation. The test started by placing the samples on rods, acting as supports, and immersed in water such that the whole bottom surface and 2 ± 1 mm of the height of them were in contact with water. The mass gain of the specimens was measured at certain time intervals after blotting to remove excess water within 15 s of removal from the pan and then immediately replaced on the support device.

The absorption, as shown in Eq. (1) is defined as the mass of absorbed water per unit area of the surface in contact with water divided by the density of water.

$$I = \frac{m_t}{a \times d} \quad (1)$$

where I : is the absorption, m_t : is the change in the specimen weight at the time t , a : is the exposed area of the specimen and d : is the density of the water.

In addition to the sorptivity test, the volumetric water absorption test was carried out in which the results can indicate the full capacity of the specimen to contain water. Samples were fully immersed in water after being completely dried out. The first weight measurement took place after 48 h of immersion and the test continued by 24 h intervals until the weight alteration was less than 0.5% which implies that the sample is saturated. Mass change percentage with respect to the initial dried mass of the specimen was then reported.

3.5. Microstructural Analysis

Fracture surface of cement mortars with and without AC powder were subjected to Energy Dispersive X-ray spectroscopy (EDX) as a means to identify the chemical composition and any cement-carbon reaction in the interfacial transition zone (ITZ).

4. Results and Discussion

4.1. Flow

The results from the flow table test indicate that the anticipated deterioration in workability can be concerning. However, by the means of the superplasticizer, modification is well possible. The flow feature of the carbon-containing mortars is less than that of the reference mixture yet, considerably acceptable. Both mini-slump and flow table results are rendered in Figure 3. The shape of data indicates a linear relationship between mini-slump results and AC powder content. However, when 8% AC is incorporated in the cement mortar, the flow is so low that special treatments such as addition of superplasticizer are needed. Other types of mixing procedures such as ultrasonication is highly recommended in such situations. Moreover, higher percentages of superplasticizer may not be the best practice due to the fresh plasticity index of the cement matrix and its deteriorating effect on the setting time.

4.2. Mechanical Strength

The results of mechanical strength are obtained in 7 and 28 days after moulding. Figure 4 portrays the compressive and flexural strengths. Overall, by replacing 8 percent of aggregate with the AC powder, the compressive strength after 28 days increased nearly 100% of the reference mix design with no AC content. Besides, the flexural strength is either remained the same or barely increased by different AC content. The increase in flexural strength is predominantly due to an increase in the compressive strength and ductility is not expected to change significantly by adding the AC powder. The means and standard deviations for all AC concentration levels are provided in Table 4.

The notable enhancement in the compressive strength can be a function of higher surface area and roughness of AC compared to those of silica aggregate. Therefore, cement can have a better bonding with the AC and as a result, the compressive strength elevates. The AC

powder is also capable of entrapping the water drops (Shahbazi et al., 2020) and cause a decreased practical w/c ratio and consequently, working in favour of strengthening.

4.3. Investigation of Hydrophobicity

One famous way to illustrate the level of hydrophobicity of a surface is to measure the contact angle of a water droplet on that surface (Arabzadeh et al., 2016; Chieng et al., 2018). The greater the internal contact angle is, the more hydrophobic the surface would be. As it can be seen in Figure 5, the water droplet on the control sample was absorbed and spread out far and eventually rested at 31 degrees. While, in the ACP incorporated samples the droplet retained its spherical shape with a contact angle 124, 142, 150 degrees for 4, 6, 8% ACP specimens respectively. The contact angle was measured by image processing technique using ImageJ software (Schneider et al., 2012).

Table 4. The mean and standard deviation of mechanical strengths

Mixture	Compressive strength (MPa)		Flexural strength (MPa)	
	7-day cured	28-day cured	7-day cured	28-day cured
ACP 0%	19.3 (1.6)*	24.4 (2.9)	5.4 (0.2)	7.9 (0.2)
ACP 4%	14.6 (1.5)	41.8 (1.6)	5.5 (0.2)	8.6 (0.2)
ACP 6%	17.7 (2.2)	46.5 (2.1)	5.5 (0.3)	8.9 (0.1)
ACP 8%	19.1 (1.9)	50.9 (2.2)	4.8 (0.2)	8.9 (0.2)

*Standard deviations are presented in brackets.

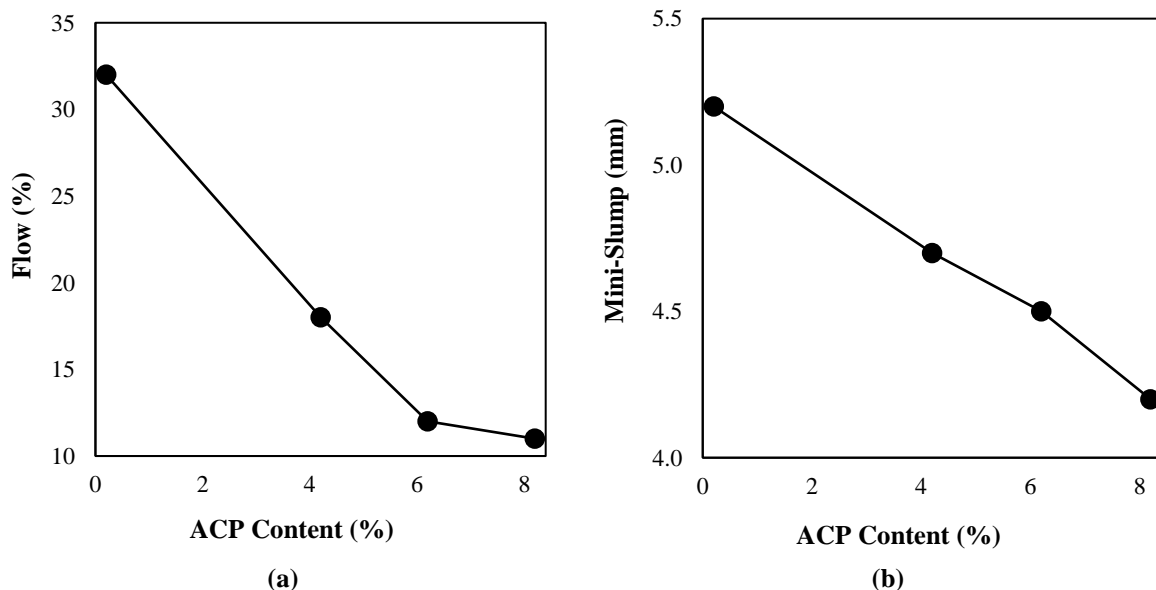


Fig. 3. a) The flow table results; and b) The mini-slump results

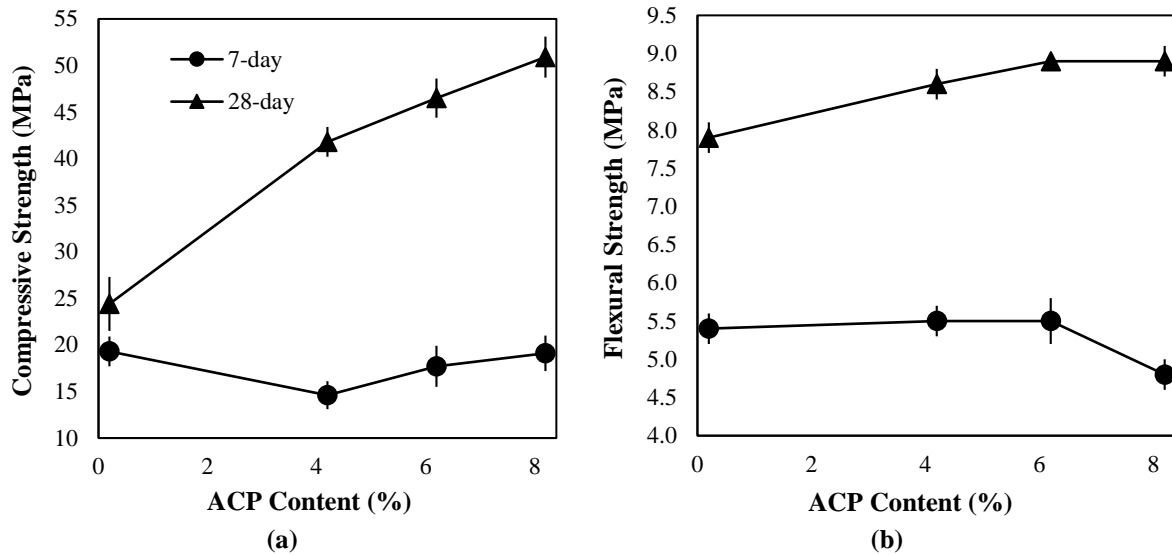


Fig. 4. a) The compressive; and b) flexural strength, of specimens

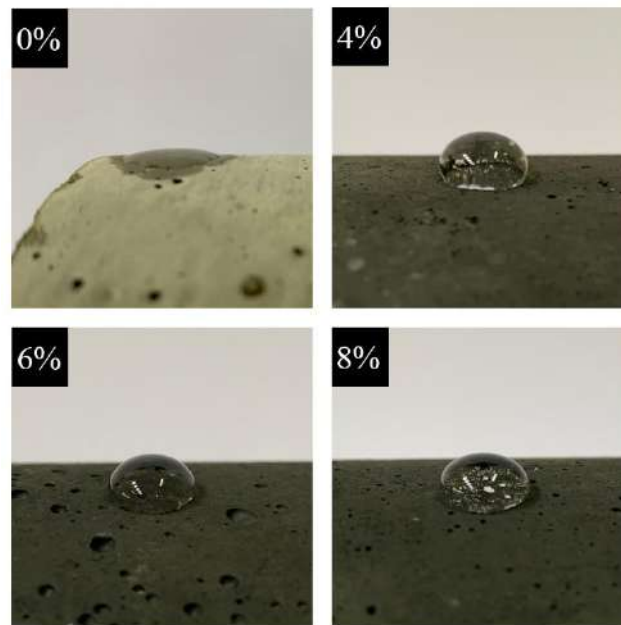


Fig. 5. Effect of AC powder on surface hydrophobicity of cement mortar

4.4. Water Absorption

The absorption rate of the 8 samples including 0%, 4%, 6%, and 8% AC powder, has been plotted versus the square root of time, as shown in Figure 6a. Results illustrate the expected general behaviour in which the rate of absorption, the slope of the graph, decreases as time passes. This was because samples became wetter and the speed of water uptake declined. As can be seen, water ingress has been limited when comparing the control sample to the sample containing 8% of AC powder throughout the whole graph. For instance, the

absorption index of samples containing 4, 6 and 8% ACP, which resembles the mass gain of the sample because of capillary water uptake, has decreased by 14, 17, and 25%, respectively, when comparing to that of the control sample. The results of the volumetric absorption test are depicted in Figure 6b. It is quite clear that AC substantially decreases the total amount of absorbed water dramatically. 54, 56, and 65% reduction in mass gain of the samples with 4, 6, and 8% hydrophobic AC powder was seen.

According to many studies, there is a

direct relationship between water absorbed and the durability parameters such as freeze-thaw cycles (Basheer et al., 2001) and carbonation (Parrott, 1992). Thus, these

results affirm that AC can prepare a hydrophobic medium which may consequently enhance the cement matrix's durability.

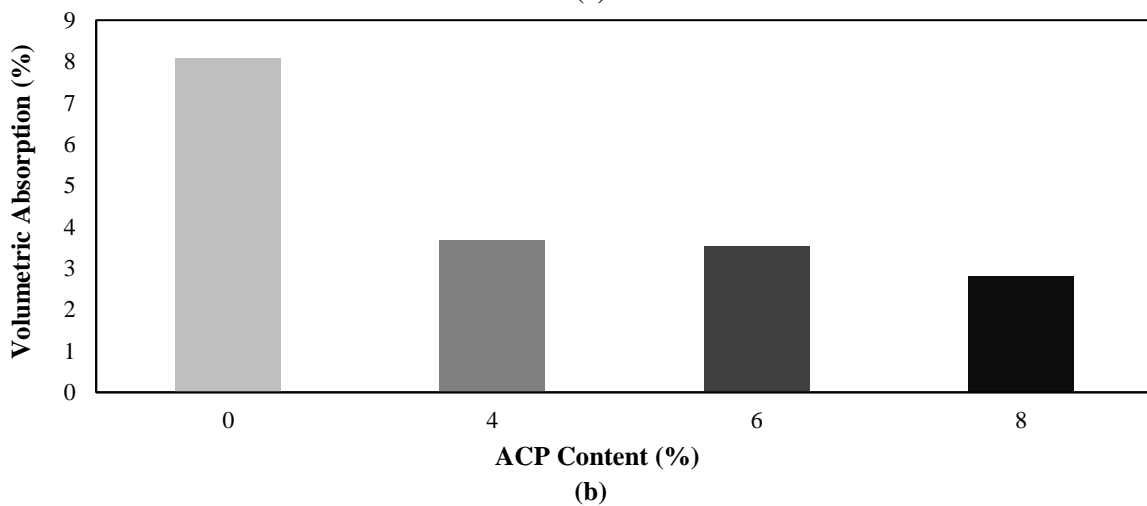
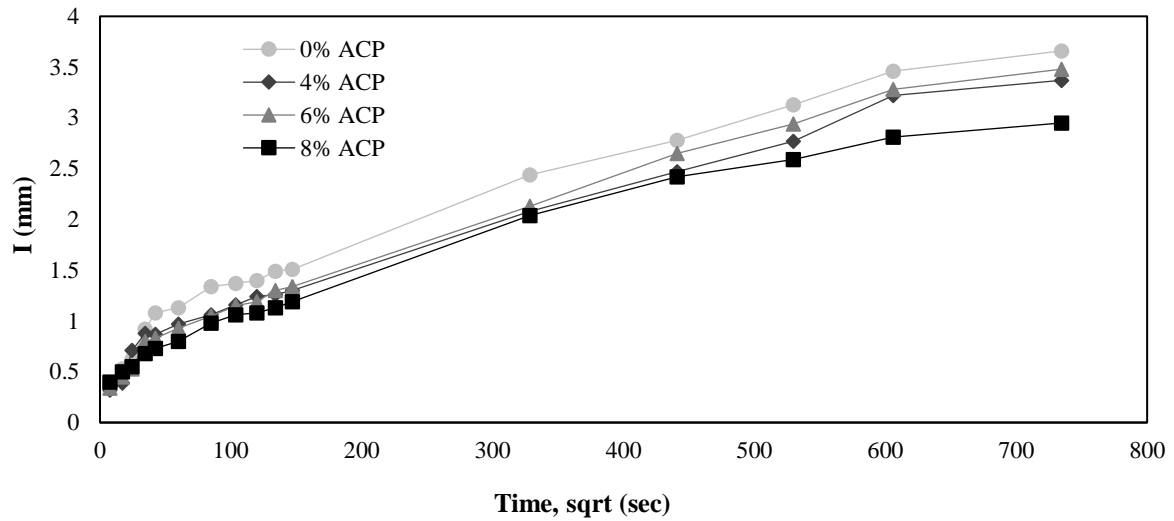


Fig. 6. a) The rate of water absorption; and b) The rate of volumetric absorption

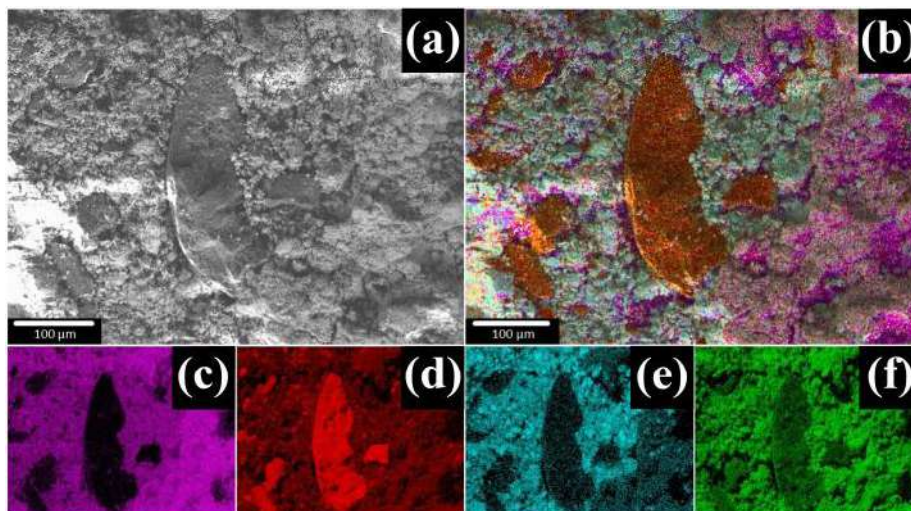


Fig. 7. a-b) SEM and elemental intensity and distribution map of cement mortar with AC; and c-f) Individual intensity and distribution map for predefined elements of calcium, carbon, silicon and oxygen

4.5. Microstructural Analysis

Further investigation on the microstructure of cement mortar with AC powder showed that AC has no chemical reaction with cement when it is used as aggregate. Assuming any chemical reaction, the intensity of calcium must moderately decrease around the carbon particle due to the formation of ITZ by calcium hydroxide molecules. However, it is clear in Figure 7c and 7e that there is no sign of gradual decrease neither for calcium nor silicon intensity near the boundaries of AC powder. This proves the inertia of AC powder in the cement matrix.

5. Conclusions

There is a knowledge gap for recycling AC powder in concrete. This research was done in the first place to enhance the knowledge of mechanical and durability features of concrete with respect to the hydrophobicity of AC. The paper presented the results of the flow table, mini-slump, compressive and flexural strength and water absorption. The following portray the most important findings:

- The inclusion of carbon powder although not affecting the flexural strength remarkably is plausible causation for a sharp increase in 28-day compressive strength.
- ACP 8% mix had the highest increase with a compressive strength of 19.1 and 50.9 MPa in 7 and 28 days, respectively.
- The water absorption rate and total volumetric absorption of the mixtures decreased by increasing the AC content. 8% of AC resulted in a 25 and 65% decline in absorption rate and volumetric absorption, respectively.
- AC powder inclusion resulted in a considerable drop in flow properties. 8% of AC powder was enough to lessen the slump and flow by 88 and 20%, respectively.

The two-way interaction of AC content and compaction energy can be further

investigated by the mean of two-factor factorial design. Furthermore, due to unconformable changes in 7-day and 28-day strengths, the calorimetry tests are essential to analyze the AC effect on the cement hydration. Tests such as sulfate and acid attack, rapid chloride penetration, rapid chloride migration and bulk electrical resistivity can deepen the understandings on exact procedure based on which AC contribute to durability.

6. References

- Abdulrahman, S., Ismail, M., Zaimi, M. and Majid, A. (2014). "Green Bambusa Arundinacea leaves extract as a sustainable corrosion inhibitor in steel reinforced concrete", *Journal of Cleaner Production*, 67, 139-146.
- Al-Kheetan, M.J., Rahman, M.M. and Chamberlain, D.A. (2019). "Fundamental interaction of hydrophobic materials in concrete with different moisture contents in saline environment", *Construction and Building Materials*, 207, 122-135.
- Allen, R., Edwards, S. and Shaw, J. (1993). *The repair of concrete structures*, CRC Press, 2nd Edition, 37-54.
- Ann, K.Y. and Song, H.W. (2007). "Chloride threshold level for corrosion of steel in concrete", *Corrosion Science*, 49, 4113-4133.
- Arabzadeh, A., Ceylan, H., Kim, S., Gopalakrishnan, K. and Sassani, A. (2016). "Superhydrophobic coatings on asphalt concrete surfaces: Toward smart solutions for winter pavement maintenance", *Transportation Research Record*, 2551(1), 10-17.
- Asipita, S.A., Ismail, M., Abd Majid, M.Z., Abdul Majid, Z., Abdullah, C. and Mirza, J. (2014). "Green Bambusa Arundinacea leaves extract as a sustainable corrosion inhibitor in steel reinforced concrete", *Journal of Cleaner Production*, 67, 139-146.
- ASTM C230. (2020). *Standard specification for flow table for use in tests of hydraulic cement*, American Society for Testing and Materials (ASTM), West Conshohocken, PA.
- ASTM C1585. (2020). *Standard test method for measurement of rate of absorption of water by hydraulic-cement concretes*, American Society for Testing and Materials (ASTM), West Conshohocken, PA.
- ASTM C349. (2018). *Standard test method for compressive strength of hydraulic-cement mortars (using portions of prisms broken in flexure)*, American Society for Testing and Materials (ASTM), West Conshohocken, PA.
- ASTM C642. (2013). *Standard test method for*

- density, absorption, and voids in hardened concrete 1, American Society for Testing and Materials (ASTM), West Conshohocken, PA.
- Bamforth, P., Price, W. and Emerson, M. (1997). "International review of chloride ingress into structural concrete", TRL Report, 359.
- Basheer, L., Kropp, J. and Cleland, D.J. (2001). "Assessment of the durability of concrete from its permeation properties: A review", *Construction and Building Materials*, 15, 93-103.
- Berke, N.S. and Hicks, M.C. (2004). "Predicting long-term durability of steel reinforced concrete with calcium nitrite corrosion inhibitor", *Cement and Concrete Composites*, 26, 191-198.
- BS 196-1. (2005). *Methods of testing cement, Part 1: Determination of strength*, British Standard European Norm (BS EN), Chiswick, London.
- Chieng, B.W., Ibrahim, N.A., Daud, N.A. and Talib, Z.A. (2018). "Functionalization of graphene oxide via gamma-ray irradiation for hydrophobic materials", *Synthesis, Technology and Applications of Carbon Nanomaterials*, Chapter 8, 177-203.
- Collepari, M. (2003). "A state-of-the-art review on delayed ettringite attack on concrete", *Cement and Concrete Composites*, 25(4-5), 401-407.
- Coppola, L., Bellezze, T., Belli, A., Bignozzi, M.C., Bolzoni, F., Brenna, A., Cabrini, M., Candamano, S., Cappai, M., Caputo, D., Carsana, M., Casnedi, L., Cioffi, R., Cocco, O., Coffetti, D., Colangelo, F., Coppola, B., Corinaldesi, V., Crea, F. and Yang, F. (2018). "Binders alternative to Portland cement and waste management for sustainable construction, Part 2", *Journal of Applied Biomaterials and Functional Materials*, 16(4), 207-221.
- De Weerd, K., Colombo, A., Coppola, L., Justnes, H. and Geiker, M.R. (2015). "Impact of the associated cation on chloride binding of Portland cement paste", *Cement and Concrete Research*, 68, 196-202.
- FHWA. (1999). *Building more durable bridges*, Federal Highway Administration (FHWA), District of Columbia, WA.
- FHWA. (2019). *FHWA FY 2020 budget, I-3*, Federal Highway Administration (FHWA), District of Columbia, WA.
- Ghasemalizadeh, S. and Toufigh, V. (2020). "Durability of rammed earth materials", *International Journal of Geomechanics*, 20(11), 1-16.
- Glass, G.K. and Buenfeld, N.R. (2000). "Chloride-induced corrosion of steel in concrete", *Progress in Structural Engineering and Materials*, 2, 448-458.
- Habibnejad Korayem, A., Ziari, H., Hajiloo, M. and Moniri, A. (2018). "Rutting and fatigue performance of asphalt mixtures containing amorphous carbon as filler and binder modifier", *Construction and Building Materials*, 188, 905-914.
- Homan, L., Ababneh, A.N. and Xi, Y. (2016). "The effect of moisture transport on chloride penetration in concrete", *Construction and Building Materials*, 125, 1189-1195.
- Hooton, R.D. (2019). "Future directions for design, specification, testing, and construction of durable concrete structures", *Cement and Concrete Research*, 124, 1-17.
- Isteita, M. and Xi, Y. (2017). "The effect of temperature variation on chloride penetration in concrete", *Construction and Building Materials*, 156, 73-82.
- Kooshafar, M. and Madani, S.H. (2017). "Influential mechanisms and potential applications of nano-silicas in cement composites", *Civil Engineering Infrastructures Journal*, 50(2), 375-393.
- Kumar, M.P., Mini, K.M. and Rangarajan, M. (2018). "Ultrafine GGBS and calcium nitrate as concrete admixtures for improved mechanical properties and corrosion resistance", *Construction and Building Materials*, 182, 249-257.
- Lee, S.T. (2009). "Influence of recycled fine aggregates on the resistance of mortars to magnesium sulfate attack", *Waste Management*, 29, 2385-2391.
- Li, K., Zhang, D., Li, Q. and Fan, Z. (2019). "Durability for concrete structures in marine environments of HZM project: Design, assessment and beyond", *Cement and Concrete Research*, 115, 545-558.
- Liu, Z. and Hansen, W. (2016). "Effect of hydrophobic surface treatment on freeze-thaw durability of concrete", *Cement and Concrete Composites*, 69, 49-60.
- Madani, H., Ramezaniapour, A.A., Shahbazinia, M., Bokaeian, V. and Ahari, Sh. (2016). "The influence of ultrafine filler materials on mechanical and durability characteristics of concrete", *Civil Engineering Infrastructure Journal*, 49(2), 251-262.
- Mobasher, B. (2006). *Modeling of stiffness degradation and expansion in cement based materials subjected to external sulfate attack*, Transport properties and concrete quality, Materials Science of Concrete. The American Ceramic Society, John Willy & Sons. New Jersey, 157-171.
- Mora, E., González, G., Romero, P. and Castellón, E. (2019). "Control of water absorption in concrete materials by modification with hybrid hydrophobic silica particles", *Construction and Building Materials*, 221, 210-218.
- Ormellese, M., Berra, M., Bolzoni, F. and Pastore, T. (2006). "Corrosion inhibitors for chlorides induced corrosion in reinforced concrete structures", *Cement and Concrete Research*, 36, 536-547.

- Parrott, L.J. (1992). "Water absorption in cover concrete", *Materials and Structures*, 25, 284-292.
- Qu, Z.Y. and Yu, Q.L. (2018). "Synthesizing super-hydrophobic ground granulated blast furnace slag to enhance the transport property of lightweight aggregate concrete", *Construction and Building Materials*, 191, 176-186.
- Samadi, D., Taghaddos, H., Nilli, M.H. and Noghabaei, M. (2021). "Development of a bridge maintenance system using bridge information modeling", *Civil Engineering Infrastructures Journal*, 54(2), 351-364.
- Schneider, C.A., Rasband, W.S. and Eliceiri, K.W. (2012). "NIH image to ImageJ: 25 years of image analysis" *Nature Methods*, 9(7), 671-675.
- Shahbazi, R., Korayem, A.H., Razmjou, A., Duan, W.H., Wang, C.M. and Justnes, H. (2020). "Integrally hydrophobic cementitious composites made with waste amorphous carbon powder", *Construction and Building Materials*, 233, 1-12.
- Steiger, M. (2005). "Crystal growth in porous materials - II: Influence of crystal size on the crystallization pressure", *Journal of Crystal Growth*, 282, 470-481.
- Taglieri, G., Daniele, V., Rosatelli, G., Sfarra, S., Mascolo, M.C. and Mondelli, C. (2017). "Eco-compatible protective treatments on an Italian historic mortar (XIV century)", *Journal of Cultural Heritage*, 25, 135-141.
- Tatematsu, H. and Sasaki, T. (2003). "Repair materials system for chloride-induced corrosion of reinforcing bars", *Cement and Concrete Composites*, 25, 123-129.
- Tittarelli, F. and Moriconi, G. (2011). "Comparison between surface and bulk hydrophobic treatment against corrosion of galvanized reinforcing steel in concrete", *Cement and Concrete Research*, 41, 609-614.
- Torii, K. and Kawamura, M. (1994). "Effects of fly ash and silica fume on the resistance of mortar to sulfuric acid and sulfate attack", *Cement and Concrete Research*, 24, 361-370.
- Wong, H.S., Barakat, R., Alhilali, A., Saleh, M. and Cheeseman, C.R. (2015). "Hydrophobic concrete using waste paper sludge ash", *Cement and Concrete Research*, 70, 9-20.
- Li, R.Y.M. (2018). *An economic analysis on automated construction safety Internet of Things, Artificial Intelligence and 3D Printing*, Springer.
- Zhou, Y., Cai, J., Chen, R., Hou, D., Xu, J. and Lv, K. (2020). "The design and evaluation of a smart polymer-based fluids transport inhibitor", *Journal of Cleaner Production*, 257, 1-12.
- Zhou, Y., Cai, J., Hou, D., Chang, H. and Yu, J. (2020). "The inhibiting effect and mechanisms of smart polymers on the transport of fluids throughout nano-channels", *Applied Surface Science*, 500, 1-10.
- Ziari, H., Habibnejad Korayem, A., Hajiloo, M., Nakhaei, M., Razmjou, A. and Divandari, H. (2017a). "Evaluating the effect of amorphous carbon powder on moisture susceptibility and mechanical resistance of asphalt mixtures", *Construction and Building Materials*, 152, 182-191.
- Ziari, H., Habibnejad Korayem, A., Hajiloo, M., Nakhaei, M., Razmjou, A. and Divandari, H. (2017b). "Evaluating the effect of amorphous carbon powder on moisture susceptibility and mechanical resistance of asphalt mixtures", *Construction and Building Materials*, 152, 182-191.



This article is an open-access article distributed under the terms and conditions of the Creative Commons Attribution (CC-BY) license.



Collapse Probability Assessment of a 4-Story RC Frame under Post-Earthquake Fire Scenario

Moradi, M.¹, Tavakoli, H.R.^{2*} and Abdollahzade, G.H.R.³

¹ Ph.D. Candidate, Department of Civil Engineering, Babol Noshirvani University of Technology, Babol, Iran.

² Associate Professor, Department of Civil Engineering, Babol Noshirvani University of Technology, Babol, Iran.

³ Professor, Department of Civil Engineering, Babol Noshirvani University of Technology, Babol, Iran.

© University of Tehran 2021

Received: 07 Nov. 2020;

Revised: 10 Jan. 2021;

Accepted: 15 Mar. 2021

ABSTRACT: Post-earthquake fire is a rare event with catastrophic consequences. The occurrence of fire after an earthquake can cause a catastrophe. Structural damage during earthquake loading affects the capacity of the element in the fire following earthquake loading. In this study, the probability of collapse and collapse time probability of a 4 story RC frame under earthquake and post-earthquake fire loading are assessed. At first structural sections are modeled in ABAQUS and heat transfer analysis is performed in them. After the results extraction of heat transfer analysis, the frame is modeled in openSees software base on the Finite Element method. For assessment seismic collapse probability, Incremental Dynamic Analysis (IDA) is conducted and the fragility curve is extracted for three performance levels. Then, seismic and fire loading are applied to frame consecutively and collapse probability is calculated. The probability distribution functions and the cumulative distribution function of the structural collapse time are calculated in the post-earthquake fire analysis. The results show that increasing PGA increases collapse probability and decrease collapse time in the RC frame under post-earthquake fire loading.

Keywords: Collapse Time, Heat Transfer, Post-Earthquake Fire, Probability Assessment, RC Frame.

1. Introduction

Lateral loading has various effects on the structure. Blast and earthquake loading may damage the structural elements (Tavakoli and Kiakojouri, 2015). Each load creates a different response in structures. Some responses are tangible, while most responses are subtle. An earthquake may

cause secondary consequences In addition to the structural damaged (Tavakoli and Afrapoli, 2018).

Earthquake reduces the strength of structures against further loads (Moradi and Abdolmohammadi, 2020). In addition to the damages which are caused by the earthquake itself, it has some subsequent consequences. These consequences in

* Corresponding author E-mail: tavakoli@nit.ac.ir

nature are landslide and tsunami. Moreover, earthquake itself cause some dangers for structures (Moradi et al., 2019). Fire and Post-Earthquake Fire (PEF) are considered to be a serious threat to human societies. This is a rare event with a lot of probable consequences (Moradi et al., 2021). PEF is a real threat in high-density places. This kind of fire has been known as a destructive and severe force in the last century (Albuquerque et al., 2018). Different structural elements lose their strength and stability on exposure to high temperatures. This reduction in strength will increase if the elements are damaged by seismic loads (Elhami Khorasani and Garlock, 2017). Elhami Khorasani (2015) examined the behavior of steel frames under PEF loading probabilistically and deterministically. PEF is a great hazard for the place with a high population density (Ronagh and Behnam, 2012). Structural safety decreases rapidly against natural disasters such as PEF. Many structures such as RC buildings have been damaged by PEF events. The stiffness and capacity of structural members reduce when exposed to extreme heat.

The evaluation of the response of structures under multi-hazard scenarios has been developed in recent years. The damage to gas pipes during an earthquake and gas leak can set the structure on fire after the earthquake. The occurrence of an internal or external explosion may be accompanied by fire. What matters first of all is the safety of the structure for fire prevention and, then, fire resistance of the structure (Behnam et al., 2016). The Post-earthquake fire is known as a destructive force in the last century (Wen et al., 2016). In recent years, the research approaches have increased in the field of multi-hazards events such as PEF. Jelinek et al. (2017) studied the resistance of steel buildings under post-earthquake fire scenarios. Khorasani et al. (2017) studied data-driven probabilistic post-earthquake fire ignition model for a community. Chicchi and Varma (2018) reviewed post-earthquake fire assessment of steel buildings in the United States.

Hutchinson et al. (2018) studied physical damage evolution during earthquake and post-earthquake fire testing of a mid-rise cold-formed steel framed building. Vitorino et al. (2020) studied evaluation of post-earthquake fire capacity of reinforced concrete elements. Tang et al. (2020) studied post-earthquake strength assessment of a steel bridge considering material strength degradation. During Nigatta Earthquake in 2004, the earthquake caused directly 9 fire events (Elhami Khorasani, 2015).

Despite the notable number of studies investigating post-earthquake fire scenarios, the effect of damage caused by earthquake on the structural performance of buildings under the fire loading scenario has not been sufficiently investigated. Such damage may cause notable differences in the behavior damaged reinforced concrete buildings due to the occurrence of cracking and spalling.

In this study, a 4-story RC frame is considered as a structure subjected to post-earthquake fire loading. After seismic loading, the fragility curve is provided and the probability of exceeding performance levels is calculated. Then seismic and fire loads applied to frame and collapse times in post-earthquake fire are extracted. Finally, the fragility curve for post-earthquake loading at Intensity Measures (IM) is provided.

2. Methodology

2.1. Probability

Probability of structural collapse can be calculated from the following equation (Abdollahzadeh and Faghihmaleki, 2018):

$$P[Coll]_{EQ} = P[Coll|EQ] \times P[EQ] \quad (1)$$

where $P[Coll]_{EQ}$: is the annual probability of collapse limit state of the building when the structure is exposed to an earthquake. $P[Coll|EQ]$: is the seismic fragility curve and $P[EQ]$: is the annual rate of seismic activities in the structural site.

If fire to be considered as a calamitous event in a building, the annual probability of structural collapse under fire loading can be deduced from Eq. (2):

$$P[\text{Collapse}]_{\text{Fire}} = P[\text{Collapse}|\text{Fire}] \times P[\text{Fire}] \quad (2)$$

where $P[\text{Collapse}]_{\text{Fire}}$: is the annual probability of collapse limit state of the building when the structure is exposed to a fire loading. $P[\text{Collapse}|\text{Fire}]$: is the fire fragility curve and $P[\text{Fire}]$: is the annual rate of the fire event.

If a PEF to be considered as an event under the following condition, then:

$$P[\text{PEF}] = P[\text{Fire}|\text{Earthquake}] \quad (3)$$

$$P[\text{Earthquake}|\text{Fire}] = 0 \quad (4)$$

The annual probability of structural collapse under PEF loading can be deduced from Eq. (5).

$$P[\text{Collapse}]_{\text{PEF}} = P[\text{Collapse}|\text{PEF}] \times P[\text{PEF}] \quad (5)$$

Substitution Eq. (3) into Eq. (5) results:

$$P[\text{Collapse}]_{\text{PEF}} = P[\text{Collapse}|\text{PEF}] \times P[\text{Fire}|\text{Earthquake}] \quad (6)$$

On the other hand:

$$P[\text{Fire}|\text{Earthquake}] = P[\text{Fire} \cap \text{Earthquake}] \times P[\text{Earthquake}] \quad (7)$$

Substitution Eq. (6) into Eq. (7) results:

$$P[\text{Collapse}]_{\text{PEF}} = P[\text{Collapse}|\text{PEF}] \times P[\text{Fire} \cap \text{Earthquake}] \times P[\text{Earthquake}] \quad (8)$$

Story drift, maximum records acceleration, the stories that fire has been accrued in that story and fire load are the parameters that are considered as engineering parameters. The drift of stories in each PGA under PEF and earthquake

have been calculated and then the probability of exceed of structure from limit state have been calculated.

2.2. Seismic Load

Intact and damaged structures have different responses to fire loading. Earthquakes could cause damage to structures. Damaged and the response of the structure to seismic loads can be expressed as three performance levels base on FEMA 356 (BSSC, 2000). Immediate Occupancy (IO), Life Safety (LS) and Collapse Prevention (CP) are these three performance levels. Structural performance levels can be expressed as maximum story drifts. Based on FEMA 356 (2000), the maximum story drifts equal to 1% under seismic loads represents the IO performance level and cause minor crack and damage in RC sections (Behnama and Ronagh, 2013). The maximum story drifts equal to 2% represent LS performance level and cause major crack and damage in RC sections. In this study, the effect of cracking and spalling caused by a seismic load on heat transfer analysis in reinforced concrete sections is considered (based on Wen et al. (2016) and Behnam and Ronagh (2013)). The effect of the cracks in the heat transfer analysis has been applied in the areas of the plastic hinges (FEMA 356, 2000). These cracks have been created due to the seismic load and its effect has only been observed in the boundary conditions of the heat transfer analysis (Mohammadzade and Jafarzade, 2021).

In this study, incremental dynamic analysis is used to perform seismic load to the RC frame. After each step of the dynamic analysis, the maximum drift of frame is extracted and the performance level of RC frame is evaluated. Based on the performance levels, cracking is applied to sections for each seismic load. Ten ground motion records were selected for applying IDA analysis. Table 1 shows the selected ground motion records characteristics. Each record was scaled from 0.1g to 1g and was applied to frame.

Table 1. Characteristics of ground motion records

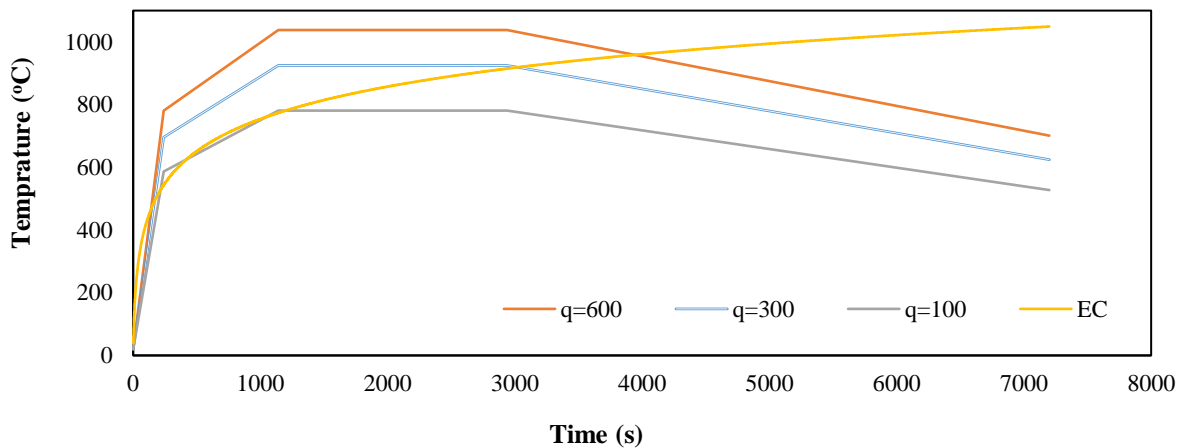
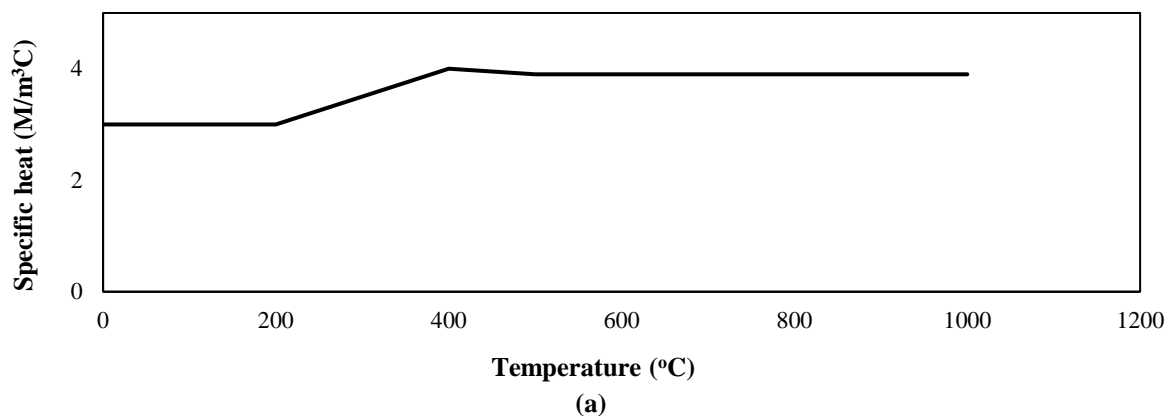
Event	Year	Station	Mag.	Vs (m/s)	PGA (g)
Niigata	2004	NIGH11	6.63	375	0.59
Kobe	1995	Nishi-Akashi	6.9	609	0.48
Loma Prieta	1989	Corralitos	6.93	462	0.645
Northridge	1994	LA Dam	6.69	628	0.426
San Fernando	1971	Lake Hughes #12	6.61	602	0.38
Bam	2003	Bam	6.6	487	0.807
Hector Mine	1999	Hector	7.13	726	0.265
Kocaeli	1999	Arcelik	7.51	523	0.21
Landers	1992	Yermo Fire St.	7.28	353	0.15
Manjil	1990	Abhar	7.37	302	0.13

2.3. Heat Transfer Analysis

Concrete sections (presented in Table 2) were modeled in ABAQUS and thermal properties assigned them. Based on the structural performance presented in Section 3-1-1, minor and major crack were assigned to the concrete section and heat transfer analysis was performed according to fire load (presented in Figure 1). Heat transfer analysis of sections depends on a variety of factors. Density, heat transfer coefficient and specific heat capacity are the most important parameters of heat transfer in various materials. Due to the fire load, the

heat flow transfers from the outermost part of the section were exposed to the heat towards the cooler areas further away from the fire.

In this study, the parameters of thermal conductivity and specific heat capacity are considered as a function of temperature. In Figure 2, the values of thermal conductivity and specific heat capacity of concrete materials are shown. The density of concrete materials is equal to 2.4 g/cm^3 . Standard fire load had been used in most researches as fire loading.

**Fig. 1.** Time-temperature curves of the study

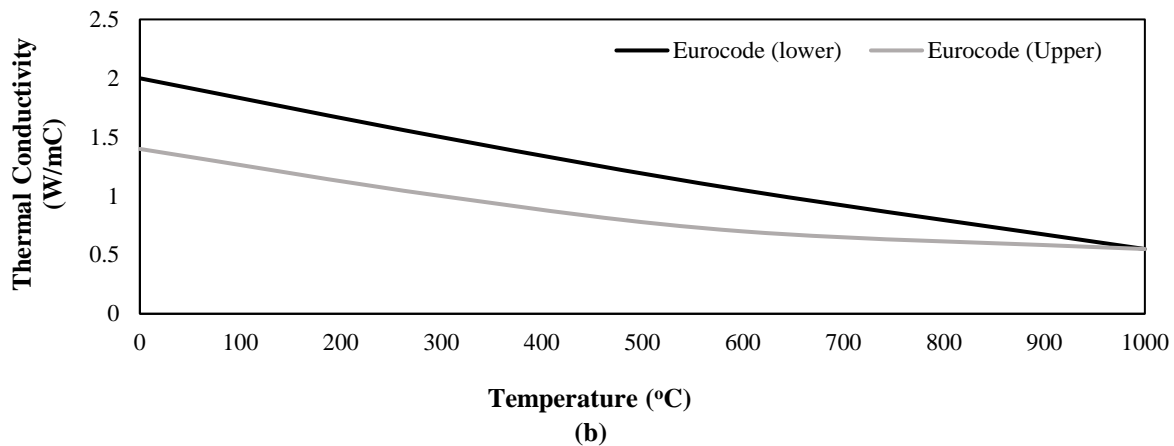


Fig. 2. Changes in the thermal properties of the concrete materials versus an increase in temperature: a) Specific heat capacity; and b) Thermal conductivity coefficient (Moradi et al., 2020)

Although Opensees performs heat transfer analysis, for greater accuracy, ABAQUS software is used to heat transfer analysis. Heat transfer analysis in the reinforced concrete section is the only elementary part of this research. For the thermal modeling of the reinforced concrete sections, the following characteristics have been used:

Special heat and thermal conductivity is shown in Figure 3. The density of concrete materials is equal to 2.4 g/cm^3 . RC section was analysis by film coefficient $25 \text{ W/m}^2\text{C}$ and emissivity 0.7. All of these parameters were extracted from EN 1992-1-2 (2004).

According to Wen (2016) and Behnam and Ronagh (2013) studies, cracking and spalling cause a faster transfer of temperature to reinforcements. Therefore, it is necessary to consider cracking and spalling due to seismic loading effect in modeling the post-earthquake fire. In this research, based on the Wen and Behnam's studies, the spalling effect (caused by the seismic load) is only intended to accelerate heat transfer. In fact, with the transfer of boundary conditions from the cover to the reinforcement, the effect of spalling is considered. Therefore, the effect of spalling due to fire has not been considered in this study.

In this study, the effect of cracking and spalling caused by a seismic load on heat transfer in reinforced concrete sections is considered (based on Wen et al. (2016) and Behnam and Ronagh (2013)). Spalling

makes it possible to separate a piece of concrete from the reinforced concrete section. This allows the boundary conditions to move from the cover to the center of the cross section.

For example, if a member is at the damage level of 4, the thermal load is placed in the boundary conditions of the reinforcements. This causes the temperature in the reinforcement concrete section to be higher than the normal RC section.

The temperature-time curves are extracted for different fire loads (presented in Figure 1) at various concrete section's heights. Figure 3 and 4 show an example of heat transfer in concrete sections with minor and major cracks for the EC fire load. In this figure, H : is the distance from the half of cross-section and d : is the total height of the section. When the thermal analysis is conducted for different concrete sections, the temperature-time curves are extracted and used for the analysis by OpenSees software.

2.4. PEF Scenario

In the second step of the analysis, a 4-story RC frame is modeled in OpenSees. Then the seismic and thermal load is applied to it consecutively. After seismic-thermal loading, the response of frame and collapse times (if there are exist) are evaluated. For applying seismic-thermal analysis after each ground motion a time-temperature curve according to Section 3-1 applied to 4-story RC frame. Four fire loads

were applied to frame in four situations after each seismic loading.

The first situation is applying fire load to the entire fire story (F1). In the second situation, the fire load is applied to the entire first and second stories (F2). In the third and the fourth situations, fire load is applied to entire of stories 1, 2 and 3 and entire of the frame, respectively (F3 and F4). The situations and location of the fire load are shown in Figure 5. Therefore, after each seismic loading, sixteen fire loading scenarios are applied to the frame separately. Fire load is applied to frame in four types and four situations. The seismic load is applied to frame according to IDA analysis.

Each ground motion is scaled from 0.1g to 1g (in the step of 0.1g). Therefore, one hundred ground motions are applied to the RC frame. Generally, one thousand and sixty hundred PEF scenarios were considered for this study. After each PEF

loading, probability of collapse in the structure was assessed and fragility curve for PEF scenario was calculated and presented.

The fire loads were applied to the frame for two hours. Two criteria were considered for structural collapse. First, maximum drift ratio reaches 0.02 during fire loading. Second, the analysis does not converge during fire loading and structural elements loss bearing capacity and failure had been occurred (Moradi et al., 2020).

The Seismic and thermal analysis in the RC frame was applied continuously. So the residual strain effects due to the seismic loading was automatically considered in thermal loading. The time of a sudden increase in the vertical displacement of the middle span of the beam is considered as the failure criterion of the structure under PPF and PEF loads (Behnam and Ronagh, 2013).

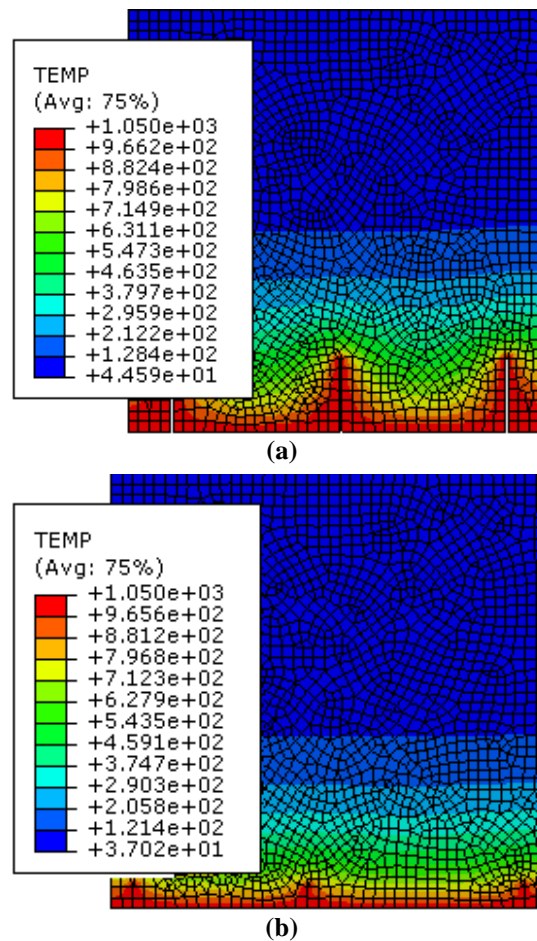


Fig. 3. Heat transfer in the concrete section under fire load proposed by EC: a) Section with major cracks; and b) Section with minor cracks

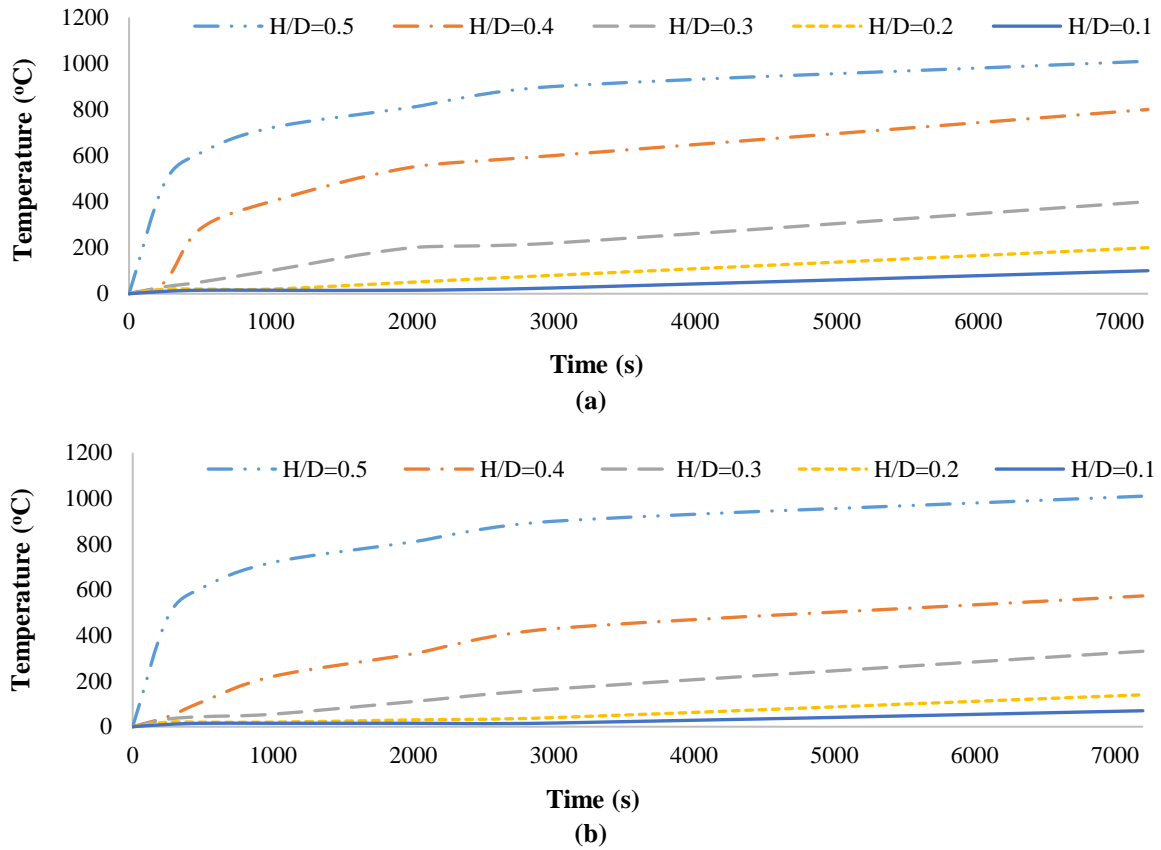


Fig. 4. Temperature-time curves for the depth of cross-section in the concrete section under fire load proposed by EC: a) Section with major cracks; and b) Section with minor cracks

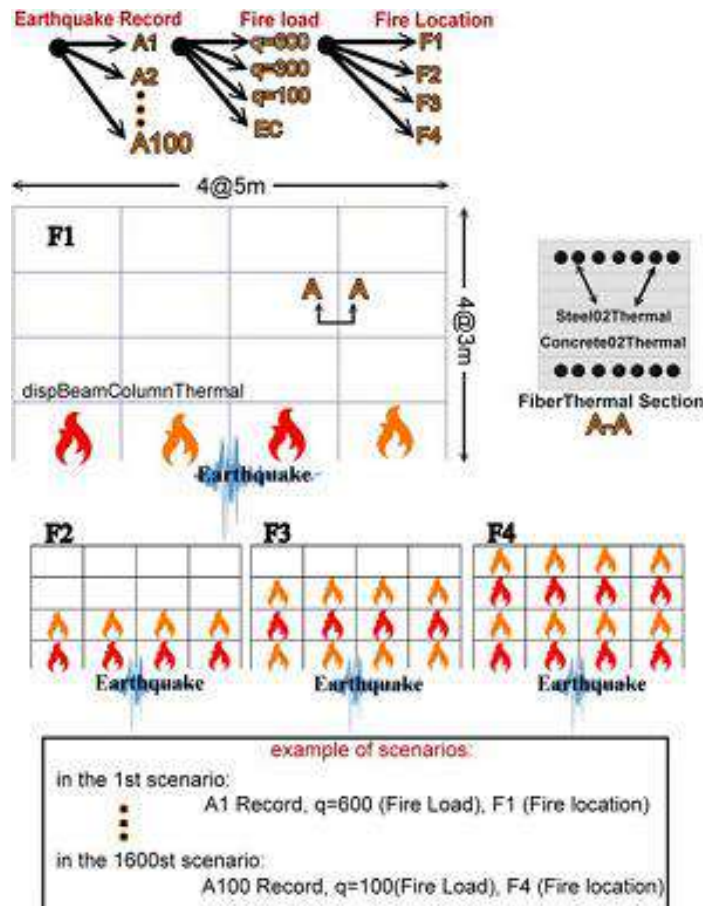


Fig. 5. Schematic figure of structural models and applied loads of the research

2.5. Numerical Modeling

A four-story RC frame is selected for seismic-thermal analysis. The selected case was loaded and designed based on ACI 318-08 (2007) Code. This structure was made using concrete with the compressive strength of $2.8e7 \text{ N/m}^2$ and reinforcement bars with the yield stress of $4.8e8 \text{ N/m}^2$. The dead and live loads were 400 kgf/m^2 and 200 kgf/m^2 , respectively. It was assumed that the frame is loaded with full dead load and 25% live load during the analysis. The frame was considered for residential use, and the soil was of D type. The heights of the story were considered 3 m. It was assumed that frame is in the form of 4-span with 5 m length. Table 2 summarizes the design of the 4-story RC frame.

The nonlinear behavior of the 4-story frame under seismic loading was modeled by using rotational springs. The frame was modeled with `dispBeamColumnThermal` elements that were connected with zero-length elements in the OpenSees environment. Thermal modeling in OpenSees was conducted with the `dispBeamColumnThermal` element. Each beam or column element was divided into ten `dispBeamColumnThermal` elements. Three integration points were assigned to each `dispBeamColumnThermal` elements. The sections of the beam and column were considered as fiber sections. The time-temperature curves were assigned to the fiber for each fire load.

`Concrete02thermal` and `Steel02thermal` were used for concrete and steel material, respectively. Characteristics of `Concrete02thermal` and `Steel02thermal` are shown in Table 3. In this table $f_{sp,\theta}$ is the strength of steel proportional limit at the considered temperature, $f_{sy\theta}$ is the steel yield strength at the considered temperature, f_{yk} is the yield strength at 20

$^{\circ}\text{C}$, $E_{s,\theta}$ is the modulus of elasticity of steel at the considered temperature, $\varepsilon_{c\theta}$ is the concrete strain at the maximum compressive strength, and $f_{c\theta}$ is the maximum concrete compressive strength. Figure 6 shows a schematic representation of the thermal modeling of the elements.

2.6. Verification

The numerical modeling in this study was validated by the comparison between numerical modeling and experimental work by Imani et al. (2014). They exposed a ductile concrete-filled double-skin tube column to cyclic loads as load control and then applied the fire loading. Afterward, they assessed vertical displacements and durability during the thermal loading. Figure 7 graphically illustrates Imani's experimental model.

The mechanical-thermal materials of `Concrete02Thermal` and `Steel02Thermal` were employed as concrete and steel materials for the modeling of this composite column. The `dispBeamColumnThermal` was used for the elements with mechanical-thermal properties. The column was modeled and loaded in accordance with Imani et al. (2014). Figure 8 shows the vertical displacement-time curves for the experimental and numerical models in this study. The results of the numerical modeling study show that the vertical displacement of column falls within the range of vertical displacements in various gauges for the top of the column in the experimental model. The failure time in the numerical model of this study is accurate enough compared to Imani's experimental model. The vertical displacement in the numerical model is close to the mean value of gauges 1 and 2 in the experimental model (Figure 8), which indicates the accuracy of numerical results in this study.

Table 2. Structural sections

Story	Column		Beam		
	Dimensions	Rebar	Dimensions	Top	Bottom
1	50 × 50	20Q20	40 × 40	8Q18	6Q18
2	50 × 50	20Q18	40 × 40	6Q18	5Q18
3	40 × 40	16Q16	35 × 35	5Q16	4Q16
4	35 × 35	16Q14	35 × 35	5Q12	4Q12

Table 3. Changes of concrete and steel material parameters according to different temperatures

	Concrete02thermal			Steel02thermal		
	$f_{c,\theta}/f_{ck}$	$\epsilon_{c,\theta}$	$f_{sy,\theta}/f_{yk}$	$f_{sp,\theta}/f_{yk}$	$E_{s,\theta}/E_s$	
-	1	0.0025	1	1	1	
20	1	0.004	1	0.96	1	
100	0.95	0.0055	1	0.92	0.87	
200	0.85	0.007	1	0.81	0.72	
300	0.75	0.01	0.94	0.63	0.56	
400	0.6	0.015	0.67	0.44	0.4	
500	0.45	0.025	0.4	0.26	0.24	
600	0.3	0.025	0.12	0.08	0.08	
700	0.15	0.025	0.11	0.06	0.06	
800	0.08	0.025	0.08	0.05	0.05	
900	0.04	0.025	0.05	0.03	0.03	
1000	0.01	0.025	0.03	0.02	0.02	
1100						

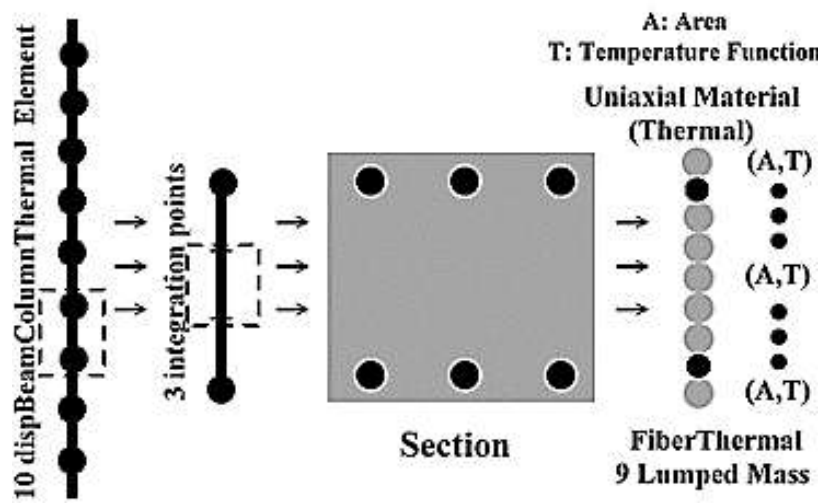


Fig. 6. Schematic figure of mechanical and thermal elements modeling in OpenSees (Moradi et al., 2020)

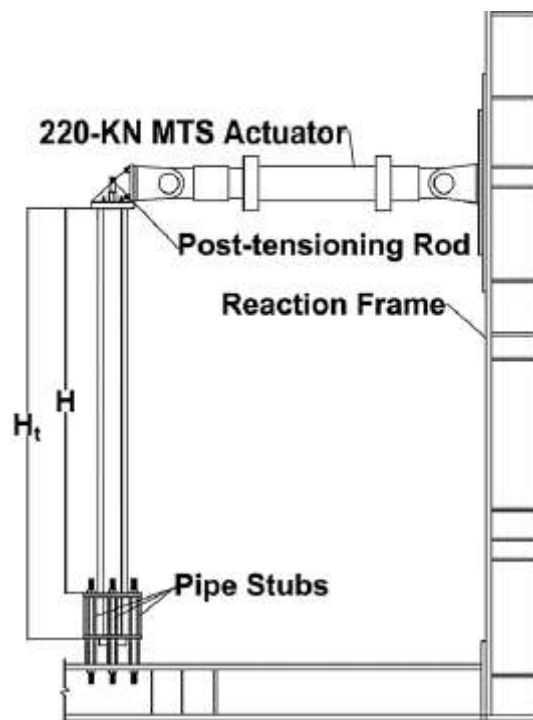


Fig. 7. Imani's experimental model (Imani et al., 2014)

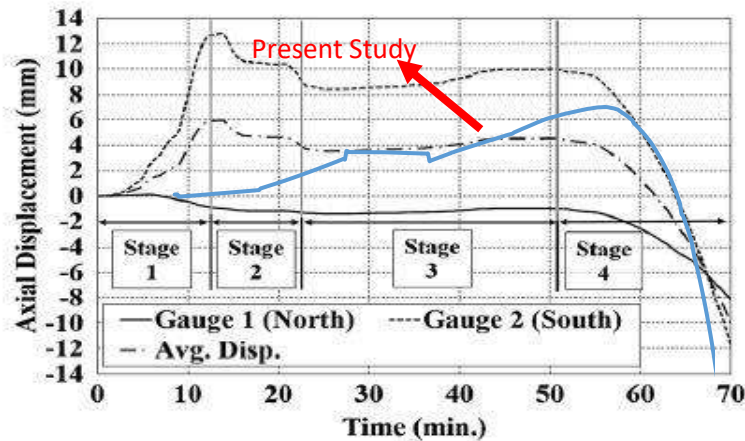


Fig. 8. Vertical displacement-time curve in Imani's experimental model and numerical analysis in this study

3. Analysis of the Results

3.1. Seismic Analysis

In the first step of the study, 4-story RC frame was subjected to seismic loading. IDA analysis was conducted using ten different ground motions scaled to different PGA (0.1g to 1g). After each analysis, the response of the frame was assessed and the maximum story drift was extracted. The probabilistic distribution of maximum frame drift is shown in Figure 9. Based on this figure, the maximum drift values of the RC frame have a quasi-normal distribution. Drift values have an average equal to 0.01401 and a standard deviation equal to 0.00901. Normal distribution for this average and the standard deviation is also shown. It is observed that thirty-four percent of all maximum drift is equal or less than the amount specified in the IO performance level. Forty-one percent of all maximum drift is between IO and LS levels. Twenty-four percent of all maximum drift

of frame under seismic loading is between LS and CP levels and one percent is at CP level. According to Section 2, $P[\text{Collapse}/EQ]$ is the fragility of the frame under seismic loading. The fragility curve of the RC frame is presented in Figure 10 for three different performance levels (IO, LS, and CP).

The limit state for IO, LS and CP performance levels were considered equal to 0.01, 0.02 and 0.04 respectively, and the probability of exceedance over these performance levels was calculated based on the normal distribution function. In this study intensity measure was considered as PGA and fragility curve presented in terms of the PGA. Based on Figure 10 probability of exceedance at $\text{PGA} = 1\text{g}$ is equal to 0.955 for the IO performance level. The corresponding values were equal to 0.74 and 0.08 for LS and CP performance levels respectively. The collapse probability of this frame was equal to 0.02 at $\text{PGA} = 0.9\text{g}$.

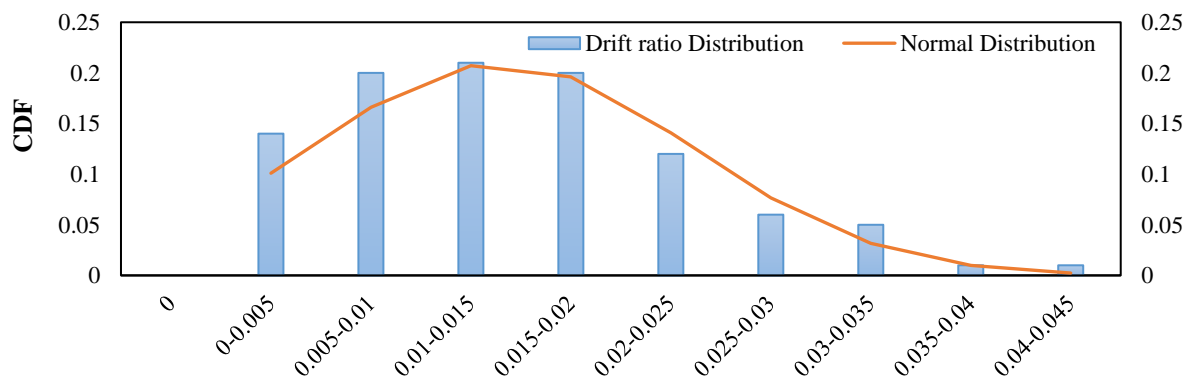


Fig. 9. Probabilistic Distribution Function (PDF) for the maximum drift of the frame in earthquake scenario

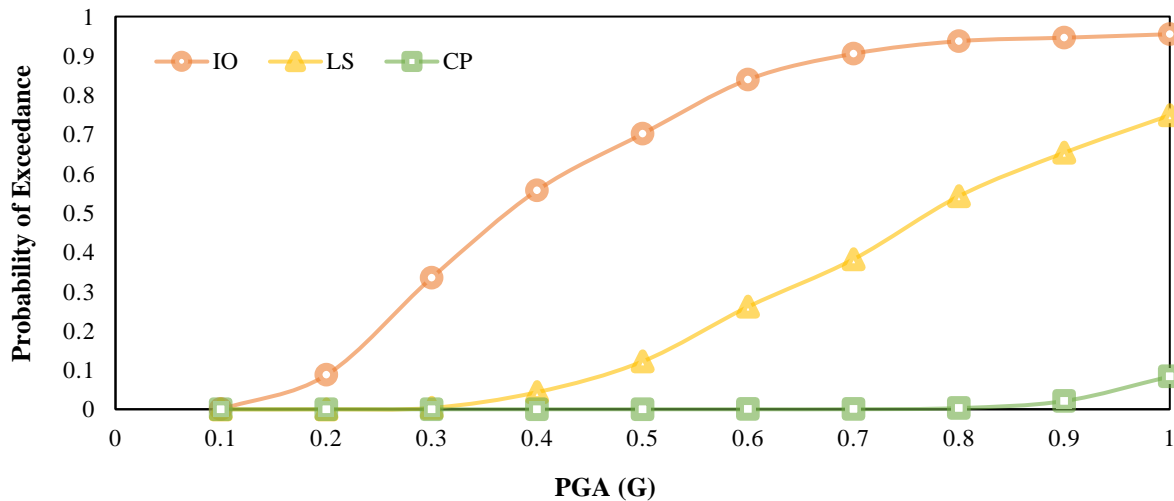


Fig. 10. Fragility curve of the structure under earthquake scenario

3.2. PEF Analysis

After seismic analysis and extraction of fragility curve ($P[\text{Collapse}/EQ]$), the 4-story RC frame was subjected to PEF loading. The frame response under PEF loading was assessment and the probability of collapse for this frame was calculated. Collapse time is the most important parameter in this study. It is assumed that the collapse criterion in the PEF scenario, is reaching the drift values of more than 0.02. In Figure 11, time history curve for the story drift ratio during a PEF scenario (Earthquake: Northridge, PGA = 0.8g, location: F2, Fire load = 100 MJ/m²) is shown.

Based on Figure 11 maximum drift ratio in the earthquake scenario was equal to 0.027. Therefore, the performance of this frame under seismic loading was at LS level. In fire following earthquake loading,

drift ratio in story 1 and 2 increased. Since the drift ratio was less than 0.02, the collapse had not happened during fire loading but permanent drift increased. The result of seismic-thermal analysis showed that fire loading increased the response of the RC frame after seismic loading but may not lead to collapse. Collapse may happen with increasing fire load. In Figure 12, time history curve for the story drift ratio during a PEF scenario (Earthquake: Northridge, PGA = 0.8g, location: F2, fire load = 600 MJ/m²) is shown. Comparison of Figures 11 and 12 shows that increasing load fire increases the response of the RC frame under fire following earthquake loading. Figure 12 indicates the drift ratio in story two was increased from 0.00128 to 0.02 after 1200 seconds during fire loading that means collapse was occurred after about 21 minutes during PEF scenario.

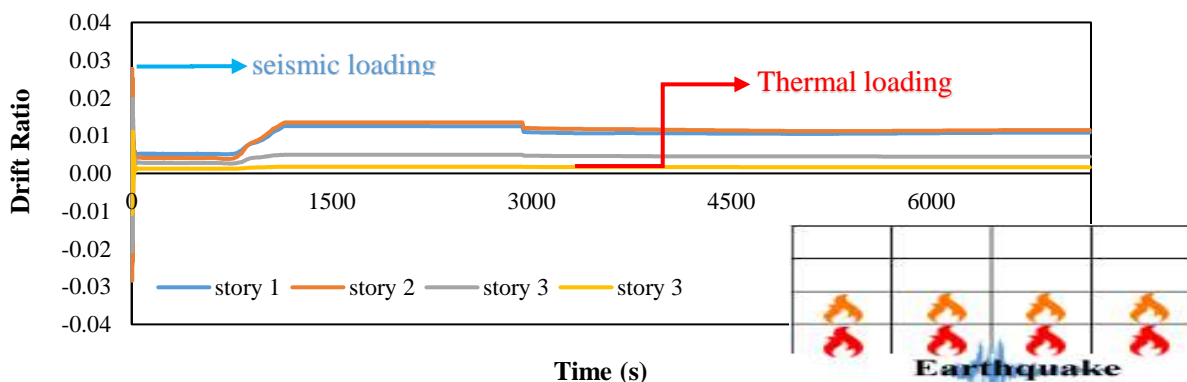


Fig. 11. The time-history curve for the drift of the considered frame in the Northridge earthquake scenario with PGA equal to 0.8g and fire load equal to 100 MJ/m² and F2 situation

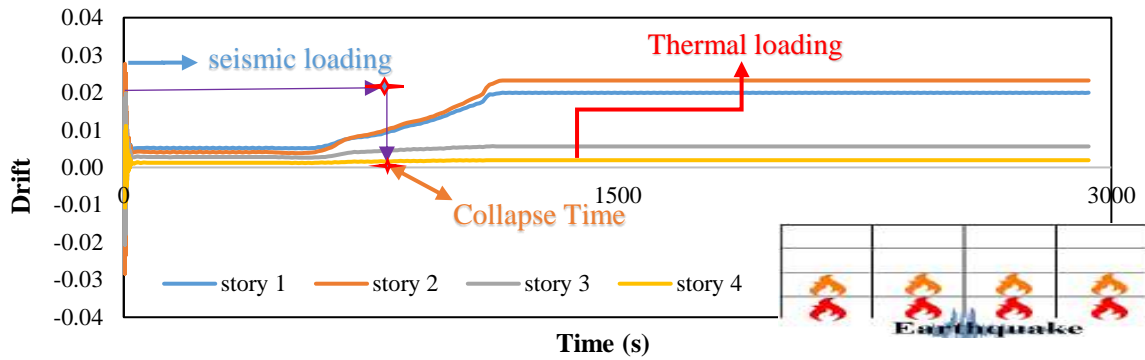


Fig. 12. The time-history curve for the drift of the considered frame in the Northridge earthquake scenario with PGA equal to 0.8g and fire load equal to 600 MJ/m² and F2 situation

In Figure 13, time history curve of axial force for first story middle column under bam ground motion records and fire load of EC in situation F4 is shown. Based on this figure, earthquake and fire following earthquake did not lead to the collapse in PGA = 0.1g to PGA = 0.5g. In PGA equal to 0.6g fire following earthquake was lead to collapse after 5420 seconds. Indeed, considering performance level and corresponding cracking in sections decreased fire resistance time and this reduction is higher in the higher PGA.

In Figure 14 shear-moment curve for the middle beam of the first story under Loma

grand motion record and EC fire load is shown. Based on this figure earthquake and fire following earthquake did not lead to collapse in PGA equal to 0.1 and 0.5g but collapse accrued in PGA equal to 1g at 2600 second after applying fire load. In the ground motions with PGA = 0.1g and 0.5g, shear and moment at first increased under fire loading and then decreased because of high temperature, but this decrease did not lead to collapse. In the ground motions with PGA = 1g cracking, residual displacement and strength loss were lead to collapse during fire loading after 2600 seconds.

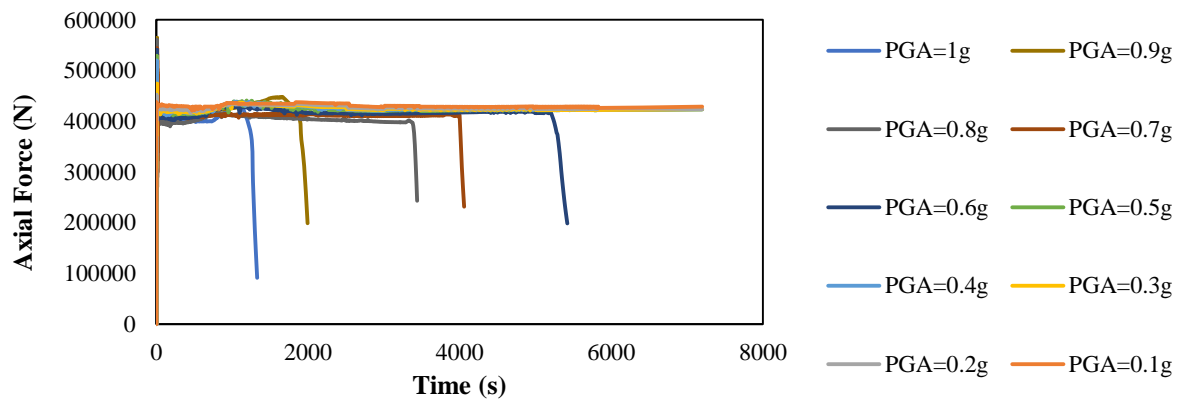


Fig. 13. The time-history curve of axial force in the middle column under PEF scenario

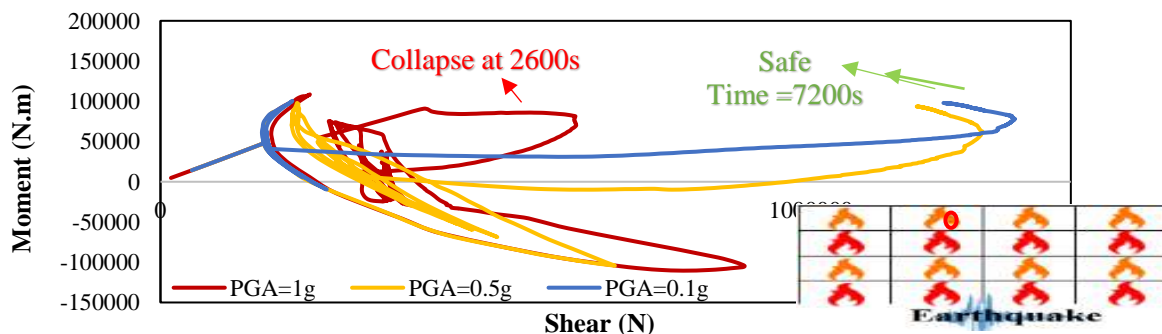


Fig. 14. Shear-Moment curve of Beam in PEF scenarios

Presented PEF scenarios in Section 3-2 were applied to RC frame and durability (collapse mode or safe mode) of the frame under PEF loading was assessed. The probabilistic distribution of the collapse time in the structure was calculated and presented in Figure 14. According to this figure in seventy percent of all PEF scenarios, the post-earthquake fire was not caused to collapse of the RC frame. The fire was lead to the collapse in thirty percent of PEF scenario (collapse time was less than 120 minutes). Probability distribution and cumulative distribution of analysis time were shown in Figures 15 and 16.

Figure 15 shows that in a probabilistic distribution, the collapse time (less than 120 minutes) does not follow a particular trend. Therefore, Bernoulli distribution has been used to assess the probability of collapse and the total number of collapse modes to the total analysis modes is considered as the probability of collapse. In order to evaluate the effect of fire's situation on the collapse time of the RC frame, the PDF and CDF curves are extracted individually for the F1,

F2, F3, and F4 situations (Figures 17 and 18). Probabilistic distribution functions and cumulative distribution probability of the collapse time indicate that in F4 fire situations, the probability of collapse is more than other models.

The results show, number of spans and stories subjected to fire loading effect on strength of RC frame in post-earthquake fire loading. Increasing fire locations increases the probability of collapse under PEF loading. The probability distribution functions show that in almost all cases, the situation F4 and F3 have more probability density at different times. Probability of collapse, in this case study, for F4 and F1 situation was equal to 0.395 and 0.192 respectively. The results of all analysis indicate that the probability of collapse (as a definite event) is equal to 0.3. This value shows 30% of all PEF scenarios were lead to collapse, however, in the earthquake scenarios, 8% of all scenarios were lead to collapse (probability of exceedance from CP performance level).

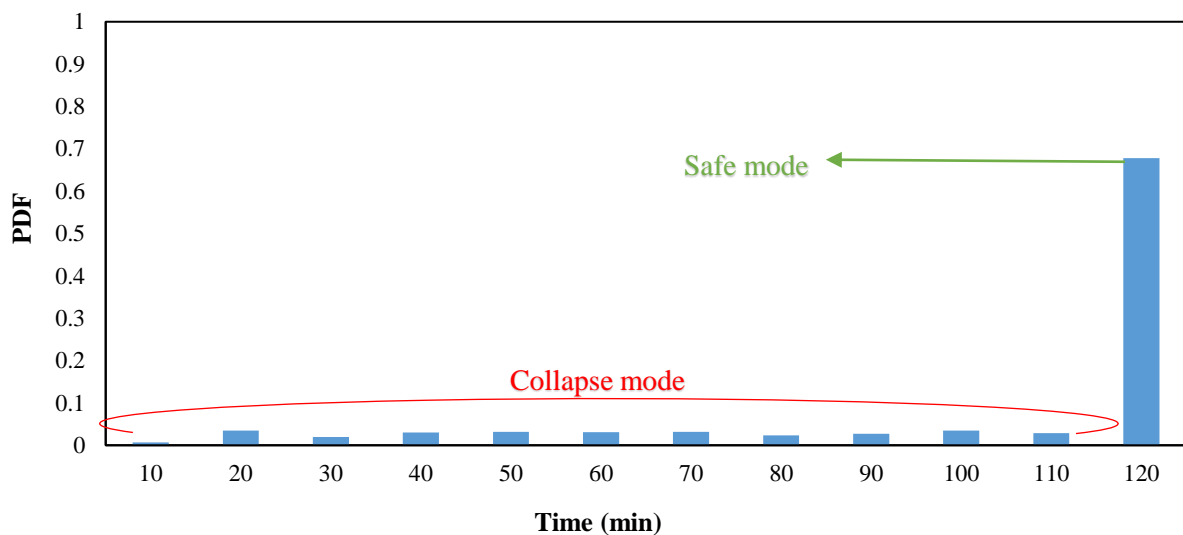


Fig. 15. Probabilistic distribution of the collapse time

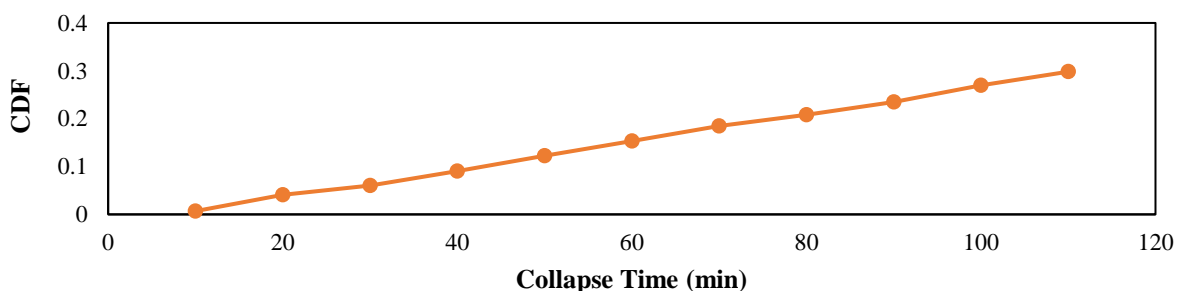


Fig. 16. Cumulative distribution function of collapse time

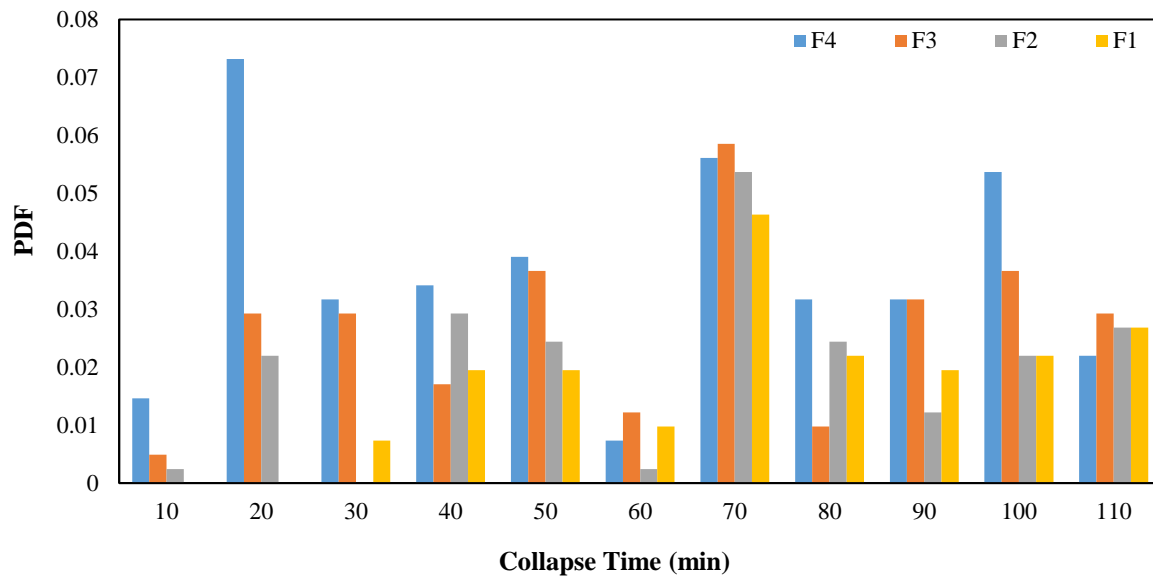


Fig. 17. The probability distribution function of the collapse time in different situations

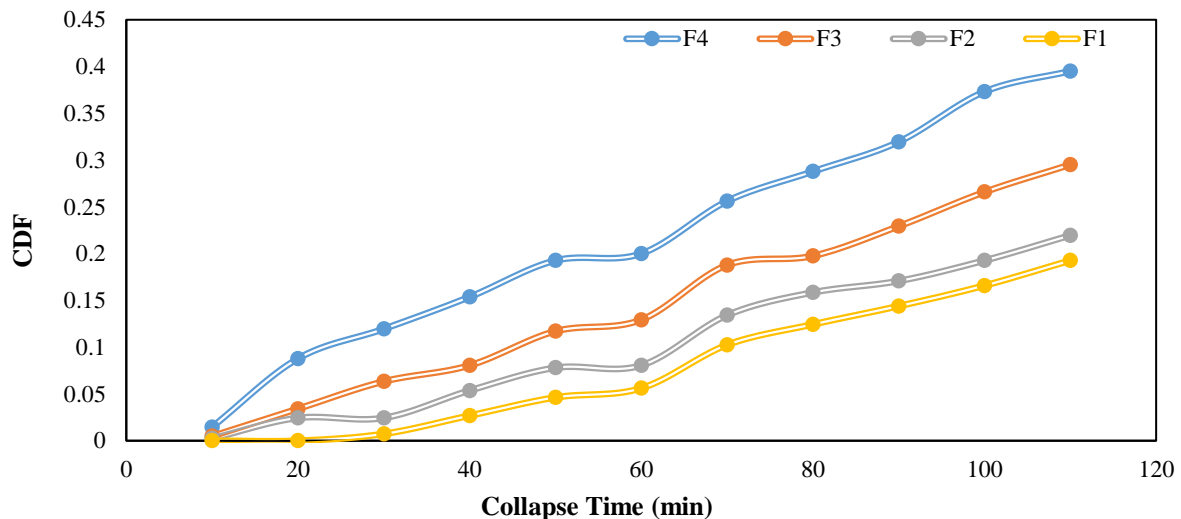


Fig. 18. Cumulative distribution of the probability of collapse time in different situations

The probability of collapse in the PEF scenario is extracted for the different PGA. Collapse probability on condition of PEF occurrence ($P[\text{collapse}|\text{fire} \cap \text{EQ}]$) will be equal to the fragility curve in different intensity measures (PGA). As stated, the probability of collapse in the PEF scenario is calculated by Bernoulli's distribution function. Figure 19 shows the collapse probability curve on the condition of PEF scenario ($P[\text{collapse}|\text{fire} \cap \text{EQ}]$) (fragility curve). Based on this figure, the probability of collapse due to a PEF is zero at a

maximum acceleration of less than 0.3g. As PGA increases, the probability of collapse due to a PEF loading is increased. Based on Figure 19, 9 percent of all fire following an earthquake with PGA = 0.4g loading lead to collapse. The fragility curve of PEF loading shows the probability of collapse in the fire following an earthquake with PGA = 0.8g is equal to 0.625. This value shows in 62.5 percent of fire loading in an RC frame subjected to an earthquake with PGA = 0.8g, the frame will collapse in less than two hours.

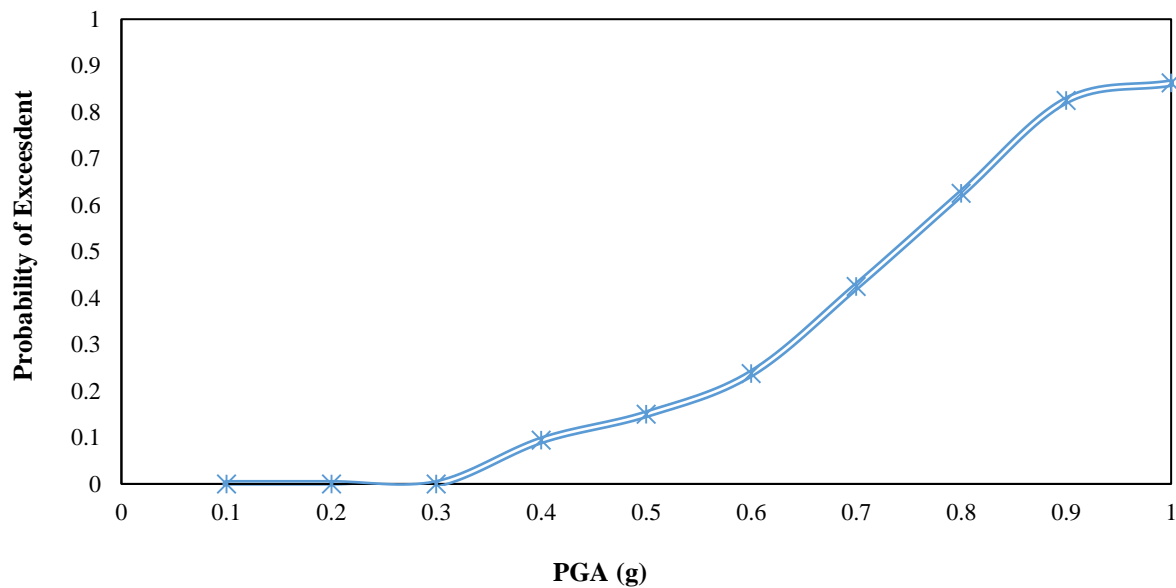


Fig. 19. Fragility curve of the reinforced concrete frame in PEF scenario

Based on Eq. (6), the probability of collapse of structures due to the PEF scenario depends on $P[\text{collapse}|\text{fire} \cap \text{EQ}]$, $P[\text{fire}|\text{EQ}]$ and $P[\text{EQ}]$. $P[\text{fire}|\text{EQ}]$ is a non-engineering parameter that relies on many factors, including structural and population density, safety factors in construction and materials of the structure. According to the researchers conducted in the reference (Khorasani et al., 2016), the possibility of the PEF ($P[\text{fire}|\text{EQ}]$) at a maximum acceleration of 1g in a region with a population density of 10,000 to 40,000 people per square kilometer, can range from about 0.15 to 0.9. This value will be fewer for the smaller maximum acceleration. In this research, assuming a population density of 15,000 km², the probability of a PEF event is 0.2. The annual rate of earthquake occurrence ($P[\text{EQ}]$) usually considered being 10% for conventional structures, during the lifespan of the building. This earthquake usually has an occurrence probability of about 0.0021 per year with a returning period of 475 years, $P[\text{fire}|\text{EQ}] = 0.0021$. So, the maximum probability of collapse because of PEF scenario ($P[\text{collapse}|\text{fire} \cap \text{EQ}]_{\text{max}}$) happens in the maximum acceleration of 1g, which is about 0.86. Therefore, the most probability of annual collapse due to PEF in the 4-story

RC frame can be calculated as follows:

$$P[\text{collapse}] = P[\text{collapse} | (\text{Fire} \cap \text{EQ})] \times P[\text{Fire} | \text{EQ}] \times P[\text{EQ}]$$

$$\rightarrow P[\text{collapse}] = 0.86 \times 0.2 \times 0.0021$$

$$\rightarrow P[\text{collapse}] = 0.00036$$

So, the rate of collapse due to PEF in the intended frame of the research is equal to 0.00036 (0.036 percent). In the following, the probability of collapse of the structure was assessed in the only definite occurrence of earthquake scenario and the definite occurrence scenario of a PEF. Figure 20 indicates the fragility curves for different performance levels in the earthquake scenario and the probability of collapse in the PEF scenario for a 4-story RC frame. According to this figure, the probability of collapse in this research due to the PEF scenario at maximum accelerations of less than 0.7 g is very similar to the fragility curve in the earthquake-only scenario at the performance level of LS. But, the probability of collapse increases in the PEF scenario at higher maximum accelerations. Therefore, the general shape of the fragility curve of the structure in the PEF scenario can be considered to be approximately the same as the fragility curve shape in the earthquake scenario at the LS performance level.

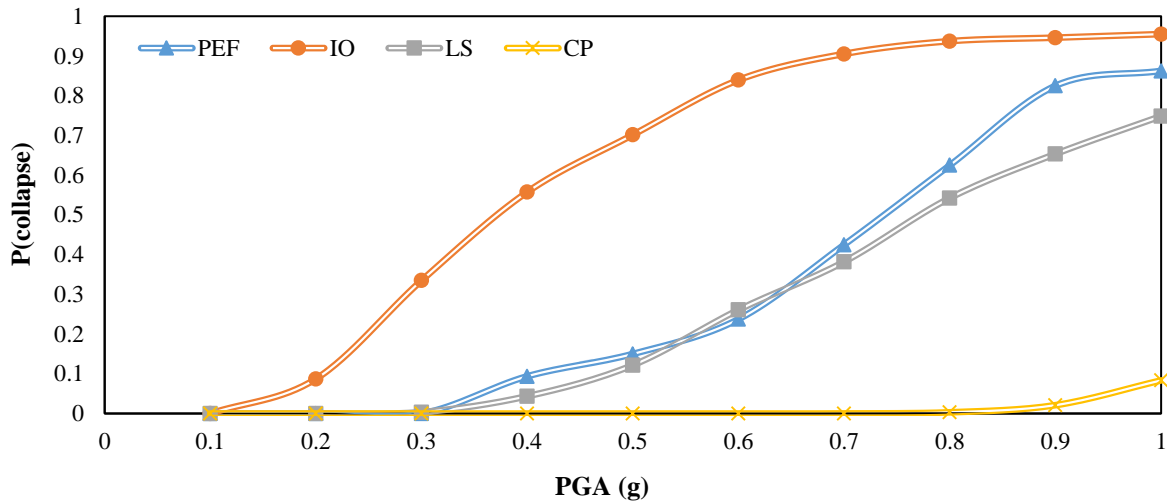


Fig. 20. Fragility curve of the intended frame subjected to the definite events of earthquake and PEF scenarios

4. Conclusions

In the present study, the behavior of a 4-story reinforced concrete frame was surveyed during the PEF scenario based on the probabilistic foundations. The collapse time of the frame during a PEF loading was the most significant parameter of this research. A 4-story reinforced concrete frame has been analyzed based on IDA. Ten grand motions were applied to this frame from 0.1g to 1g. After each seismic load, the thermal load was applied to the frame. For thermal loading, four different fire loads were considered in four different locations and situations of the frame. The results of the analysis showed 70% of loading the structures were able to withstand a durability time equal to or longer than 120 minutes. In 15% of the scenarios, the collapse time in a PEF was shorter than 1 hour. Then the PDF and CDF curve was extracted for a definite event of the post-earthquake scenario. The results showed that PGA and situation of fire loading affected frame resistance under PEF loading. Also, the results of the analysis showed that the fragility curve in the PEF scenario based on the maximum applied acceleration to the structure was very similar to the fragility curve in the earthquake scenario at the LS performance level. The probability of an annual collapse of the structure in the PEF scenario was investigated. For the considered frame, the

annual rate was equal to 0.00036.

The results of this study can be used to assess the probability of rupture of reinforced concrete frames in post-earthquake fire scenario. With seismic fragility curves at the LS level, it is possible to estimate the probability of a break in the loading of a post-earthquake fire at different seismic load intensities. These results can be used to calculate the probability of annual failure due to post-earthquake fire.

5. Acknowledgments

The authors acknowledge the funding support of Babol Noshirvani University of Technology through Grant No. BUT/388011/99.

6. References

- Abdollahzadeh, G. and Faghihmaleki, H. (2018). "Proposal of a probabilistic assessment of structural collapse concomitantly subject to earthquake and gas explosion", *Frontiers of Structural and Civil Engineering*, 12(3), 425-437.
- Albuquerque, G.L., Silva, A.B., Rodrigues, J.P.C. and Silva, V.P. (2018). "Behavior of thermally restrained RC beams in case of fire", *Engineering Structures*, 174, 407-417.
- Behnam, B., Ronagh, H.R. and Lim, P.J. (2016). "Numerical evaluation of the post-earthquake fire resistance of CFRP-strengthened reinforced concrete joints based on experimental observations", *European Journal of Environmental and Civil Engineering*, 20(2), 142-160.

- Behnama, B. and Ronagh, H.R. (2013). "Post-earthquake fire performance-based behavior of reinforced concrete structures", *Earthquakes and Structures*, 5(4), 379-394.
- BSSC, P. (2000). *Commentary for the seismic rehabilitation of building*, FEMA-356, Federal Emergency Management Agency, Washington, DC.
- Chicchi, R. and Varma, A.H. (2018). "Research review: Post-earthquake fire assessment of steel buildings in the United States", *Advances in Structural Engineering*, 21(1), 138-154.
- Elhami Khorasani, N. (2015). *A probabilistic framework for multi-hazard evaluations of buildings and communities subject to fire and earthquake scenarios*, Ph.D. Thesis, Princeton University, USA.
- Elhami Khorasani, N. and Garlock, M.E. (2017). "Overview of fire following earthquake: Historical events and community responses", *International Journal of Disaster Resilience in the Built Environment*, 8(02), 158-174.
- Hutchinson, T., Wang, X., Hegemier, G., Meacham, B. and Kamath, P. (2018). "Physical damage evolution during earthquake and post-earthquake fire testing of a mid-rise cold-formed steel framed building", *Proceedings of the 11th US National Conference on Earthquake Engineering*, Loss Angeles.
- Imani, R., Mosqueda, G. and Bruneau, M. (2014). "Experimental study on post-earthquake fire resistance of ductile concrete-filled double-skin tube columns", *Journal of Structural Engineering*, 141(8), 04014192.
- Jelinek, T., Zania, V. and Giuliani, L. (2017). "Post-earthquake fire resistance of steel buildings", *Journal of Constructional Steel Research*, 138, 774-782.
- Khorasani, N.E., Garlock, M. and Gardoni, P. (2016). "Probabilistic performance-based evaluation of a tall steel moment resisting frame under post-earthquake fires", *Journal of Structural Fire Engineering*, 54(3), 361-374.
- Khorasani, N.E., Gernay, T. and Garlock, M. (2017). "Data-driven probabilistic post-earthquake fire ignition model for a community", *Fire Safety Journal*, 94, 33-44.
- Mohammadzadeh, M.R., and Jafarzadeh, A. (2021). "Comparison of nonlinear dynamic analysis of time history and Endurance Time Method in tall structures with fame-wall system", *Civil Engineering Infrastructures Journal* 54(2), 405-421.
- Moradi, M. and Abdolmohammadi, M. (2020). "Seismic fragility evaluation of a diagrid structure based on energy method", *Journal of Constructional Steel Research*, 174, 106311.
- Moradi, M., Tavakoli, H. and Abdollahzade, G. (2020). "Sensitivity analysis of the failure time of reinforcement concrete frame under postearthquake fire loading", *Structural Concrete*, 21(2), 625-641.
- Moradi, M., Tavakoli, H. and Abdollahzadeh, G. (2019). "Probabilistic assessment of failure time in steel frame subjected to fire load under progressive collapses scenario", *Engineering Failure Analysis*, 102, 136-147.
- Moradi, M., Tavakoli, H.R. and Abdollahzadeh, G.R. (2021). "Comparison of steel and reinforced concrete frames' durability under fire and post-earthquake fire scenario", *Civil Engineering Infrastructures Journal*, 54(1), 145-168.
- Ronagh, H.R. and Behnam, B. (2012). "Investigating the effect of prior damage on the post-earthquake fire resistance of reinforced concrete portal frames", *International Journal of Concrete Structures and Materials*, 6(4), 209-220.
- Tang, Z., Zhang, W., Yu, J. and Pospíšil, S. (2020). "Post-earthquake strength assessment of a steel bridge considering material strength degradation", *Structure and Infrastructure Engineering*, 17(3), 331-346.
- Tavakoli, H. and Afrapoli, M.M. (2018). "Robustness analysis of steel structures with various lateral load resisting systems under the seismic progressive collapse", *Engineering Failure Analysis*, 83, 88-101.
- Tavakoli, H. and Kiakojouri, F. (2015). "Threat-independent column removal and fire-induced progressive collapse: Numerical study and comparison", *Civil Engineering Infrastructures Journal*, 48(1), 121-131.
- Vitorino, H., Rodrigues, H. and Couto, C. (2020). "Evaluation of post-earthquake fire capacity of reinforced concrete elements", *Soil Dynamics and Earthquake Engineering*, 128, 105900.
- Wen, B., Wu, B. and Niu, D. (2016). "Post-earthquake fire performance of reinforced concrete columns", *Structure and Infrastructure Engineering*, 12(9), 1106-1126.



This article is an open-access article distributed under the terms and conditions of the Creative Commons Attribution (CC-BY) license.



Developing Performance Levels for Concrete Bridge Bents with a Focus on the Joint Region

Bahrani, M.K.^{1*}, Nooralizadeh, A.², Sharifi, M.¹ and Karami, N.²

¹ Assistant Professor, Department of Civil Engineering, University of Qom, Qom, Iran.

² Ph.D. Candidate, Department of Civil Engineering, University of Qom, Qom, Iran.

© University of Tehran 2021

Received: 08 Nov. 2020;

Revised: 15 Jun 2021;

Accepted: 12 Jul. 2021

ABSTRACT: Bridges are critical highway structures, and damage to them can result in the loss of vital lifelines. Many bridges reaching the end of their expected lifespans should have their seismic performance evaluated immediately. The study utilized a 1/3 scale model of two-column bridge bents developed within the last 20 years that split from the deck under cyclic loads. The purpose is to investigate seismic performance and define performance levels utilizing experimental observation. The damage estimates from previous studies for each performance level were reviewed and, where necessary, revised. Damage and performance levels for joints were estimated differently than for other components such as cap beams and columns, according to the findings. The present study proposes new performance levels including joint damage. The overall seismic performance of the concrete bridge bents revealed that the anticipated mechanisms did not occur, but that flexural hinges formed in the joint region rather than in the columns, as required by current codes.

Keywords: Concrete Pier, Cyclic Loading, Damage, Performance Level, Seismic Performance.

1. Introduction

Critical infrastructures are essential for post-earthquake maintenance to facilitate response; therefore, they must be available for immediate use after an earthquake (Abudallah Habib et al., 2020; Samadi et al., 2021). Seismic criteria have been stated in the design regulations and seismic design philosophy (AASHTO, 2011; Ghassemieh et al., 2018), and several researchers have studied the seismic and strengthening performance of bridges built to these standards. They proposed various ways to improve the behavior of concrete piers on

bridges in response to earthquakes, including the use of divergent bracing (Rahnavard et al., 2017; Rahnavard and Hassanipour, 2015), non-buckling bracing (Naghavi et al., 2019; Rahnavard et al., 2018), bracing concrete-steel composite walls (Rahnavard et al., 2016), seismic insulators (Radkia et al., 2018, 2019; Rahnavard and Thomas, 2019) and concrete-steel composite connections (Rahnavard et al., 2017).

Extensive research has also been conducted to develop quantitative and qualitative definitions, as well as to determine damage levels for concrete

* Corresponding author E-mail: mkbahrani@ut.ac.ir

frames. Hose et al. (2000) conducted one of the most important studies on the levels of damage to bridge concrete bents. They reviewed previous laboratory studies to determine damage levels as well as performance levels, and they proposed design criteria for use in bridges.

Bahrani et al. (2010, 2017) conducted a series of laboratory investigations at 1/3 scale for multi-column concrete bridge bents subjected to lateral cyclic loads to identify damage and failure modes such as joint failure and longitudinal reinforcement slide at joints. Their findings revealed that the energy dissipation capacity and pinching in the cyclic response had a substantial impact on these damage and failure types. The authors analyzed the members' performance levels and proposed three improvement plans: lowering column shear demand by reducing the effective cross-section of the bars; transverse external post-tensioning; and transverse and longitudinal external post-tensioning in the cap-beam.

Hasaballa et al. (2011) investigated the seismic performance of concrete beam-column exterior joints reinforced with Fiber Reinforced Polymer (FRP) and Glass Fiber Reinforced Polymer (GFRP) rebars. They focused on four laboratory specimens with T-shaped connections and discovered that beam-column connections retrofitted with GFRP rebars and stirrups spared considerable damage under seismic loading.

Vecchio et al. (2014) conducted a series of laboratory studies on beam-column joints retrofitted externally with FRP. They investigated the behavior of non-transverse reinforcement (confinement) of joints that did not comply with current seismic codes as well as the effect of FRP as a strengthening method under constant axial loading and transverse cyclic loading in the as-built and strengthened specimens.

Tukiar et al. (2014) investigated the seismic performance of a beam-column precast corner joint with corbels subjected to up to 1.5 percent drift under lateral

loading. They investigated the seismic performance of exterior reinforced concrete beam-column joints reinforced using various techniques. According to the findings, the proposed strengthening methods increased the seismic capacity of the joints and steel jackets, consequently increasing their load-bearing capacity and ductility.

Lowes and Moehle (1999) conducted an experimental study on beam-column T-joints to investigate common defects in bridges built between 1950 and 1970, such as insufficient column reinforcement development length, a lack of transverse reinforcement in the joint regions (spacing equal to 20 times the diameter of the reinforcement), and cutting 50 percent of the lower reinforcement of the beams near the joint. They also investigated the behavior of joints that had been improved with RC covers. The findings demonstrated that this method was effective in increasing the ductility capacity and shear strength of the joints.

KhanMohammadi et al. (2016) investigated 1/4 scale two-column concrete bridge piers. In primary studies, they discovered significant joint damage and proposed a retrofitting method for the joint. The results showed that the retrofitted specimens had no damage in the joint region and that plastic hinges formed at the ends of both columns in accordance with the mechanism specified in seismic codes.

Bilah et al. (2013) investigated the vulnerability of multi-column bridge bents in near-fault and far-field ground motion. They studied the effects of different retrofitting methods on bridges (steel jackets, concrete jackets, Carbon FRP (CFRP) jackets, and Engineered Cement Composite (ECC) jackets). The ECC and CFRP jackets reduced vulnerability effectively.

Patel et al. (2013) studied the exterior beam-column joints of RC and SFRC structures subjected to cyclic loading in order to reduce confinement reinforcement at the connection zone. Six exterior beam-

column joints were tested at 1/3 scale under cyclic loading. 1.5 percent steel fibers were used in the SFRC beam-column joint. Their findings revealed that the SFRC beam-column joint performed well and that joint behavior improved. Furthermore, the findings indicated that reducing the number of stirrups in a properly reinforced SFRC joint could be considered as an alternative solution to avoid retrofitting the connection zone.

Under cyclic loading, Kaliluthin and Kothandaraman (2017) tested exterior beam-column joint specimens at 1/3 scale using the core strengthening technique. The first set of specimens was detailed as ordinary moment-resisting frames, while the second set was detailed as special moment-resisting frames. The third set followed reinforcement detailing with a new type of reinforcement known as "core reinforcement". According to the experimental results, the strengthened joint performed better in terms of bearing capacity, energy absorption, stiffness coefficient, and ductility. It was discovered that the beam-column exterior joint models with core reinforcement provided adequate stiffness and ductility, and that the stiffness did not decrease significantly when compared to the other joint types.

Deng et al. (2015) studied damaged bridge piers that had been repaired post-earthquake using steel tubes and FRP. The behavior was investigated using both experimental and Finite Element (FE) approaches. Steel tubes, Basalt Fiber Reinforced Polymer (BFRP), or CFRP were used to repair the three damaged circular RC piers. The repaired piers had hysteresis curves similar to the original specimens, and all three repair methods recovered the seismic performance of the damaged earthquake piers, according to FE analysis and experimental observation.

The findings of the preceding research indicate that the seismic cyclic loading performance of a large number of older bridges designed in accordance with codes at the time of construction should be

investigated. The current study performed laboratory testing on one-span concrete piers with two concrete bents at 1/3 scale that were designed in accordance with code in the previous 20 years.

Using experimental observation, the current study investigates seismic performance and defined performance levels. Based on the observations, the types of damage associated with each performance level are defined, and qualitative and quantitative definitions are developed. Furthermore, the seismic behavior and performance of the specimen's components are investigated.

2. Test Program

2.1. Specifications of Specimens

Initially, two as-built one-span specimens (SP-80 and SP-90) were investigated. In the 1980s and 1990s, these specimens were built in accordance with conventional design and construction regulations in Iran. The addition of transverse reinforcement in the joint region is the most significant difference between these two periods.

The specimens were generated at a scale of one-third. The column's arrangement and number of longitudinal reinforcements were the same as in existing codes, and it had full-column cross-section symmetry. Figures 1a and 1b depict the geometry and basic details of existing bridges as well as experimental specimens SP-80 and SP-90.

Tables 1 and 2 show the mechanical properties of the materials used, including the concrete compressive strength in the cap beam and columns, as well as the reinforcement properties. The ratio of longitudinal and transverse reinforcement, joint area details, and cross-section dimensions in these specimens were based on the mean of six bridges with roughly similar conditions (Table 3). Figure 1 depicts the specimen layout and cross-section.

Table 1. Compressive strength of concrete in MPa (fc')

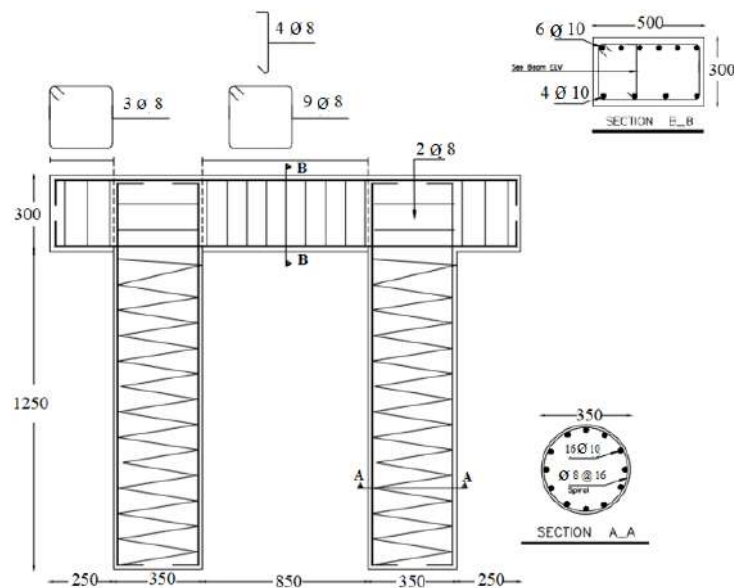
Cap beam	Column
42.1	41.7

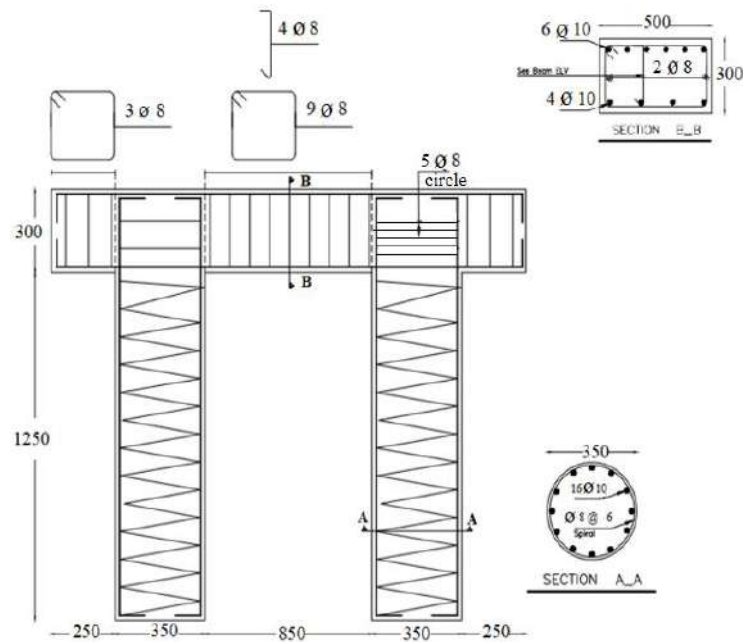
Table 2. Mechanical properties of the longitudinal and transverse reinforcement used in the specimen

Reinforcement type	Yield stress (MPa)	Ultimate stress (MPa)	Ultimate strain (%)
longitudinal	511.4	653.2	12.56
transverse	365.4	540.8	12.34

Table 3. Bridges information for experimental specimen design

Average	Saveh	Kesma	Azadegan	Mohajeran	Aramene	Molasadra	Kashani	Unit	Specifications
18.4	22.5	16	20.5	19	19	15.5	16.5	m	Bridge span
Column information									
1329	1400	1200	1100	2000	1200	1200	1200	mm	Section diameter
7086	10000	4500	7000	7600	6800	7000	6700	mm	Height
4814	5000	4000	4000	5200	6500	5000	4000	mm	Column spacing
	25T25	18T28	32T32	30T28	34T25	16T32	22T26		Longitudinal reinforcement
1.27	0.8	0.98	2.71	0.78	1.48	1.14	1.03	%	Percentage
	T16@10	T14@50	T12@15	T12@75	T12@65	T12@125	T16@70		Transverse reinforcement of hinge region
	spiral	spiral	spiral	spiral	spiral	spiral	hoop	spiral	Type
0.42	1.44	0.26	0.69	0.08	0.14	0.08	0.24	%	Percentage
	T12@100	T14@100	T12@200	T12@100	T12@20	T12@200	T10@150		Shear reinforcement
0.06	0.08	0.13	0.05	0.06	0.05	0.05	0.04	%	Percentage
Capbeam information									
1058		1400	1200	1200	550	1000	1000	mm	Section width
1717		1600	1600	2100	1500	1750	1750	mm	Cross section width
		8T28	12T25	12T32	8T25	12T25	11T28		Top reinforcement
0.35		0.22	0.31	0.38	0.48	0.34	0.39	%	Percentage
		8T22	12T20	8T28	10T25	12T25	7T28		Down reinforcement
		0.14	0.20	0.20	0.59	0.34	0.25	%	Percentage
		4T12@250	6T14@150	6T14@150	6T12@150	6T12@120	6T10@200		Transverse reinforcement
0.26		0.11	0.38	0.29	0.3	0.32	0.13	%	Percentage
Joint information									
				400	500	0	600	mm	Confining reinforcement
				12	12	0	16	mm	Applied length
				75	65	125	70	mm	Diameter
0.46				0.3	0.58	0.00	0.96	%	Percentage
638				400	450	850	850	mm	Anchorage length of column reinforcement
475				400	400	500	600	mm	hook length of column reinforcement

**(a) Details of the laboratory specimen Sp-80**



(b) Details of the laboratory specimen Sp-90

Fig. 1. Details of the studied bridge and experimental specimens

2.2. Test Set-up

Figure 2 shows the components used to install and adjust the specimens as well as provide a rigid base. To achieve the desired hinged support conditions, two high-strength bolts were used at the column's end to connect the concrete bents to the rigid steel beam (Figure 3). Figures 4-7 show the locations of the gauges.

Gravity loading was applied using a cross-shaped steel beam (Figure 8). Figure 9 depicts the overall test setup. The steel beam, which had a joint at each end, was installed to control the jack force. The

distribution of gravity load caused by neoprene at regular intervals between the steel cross-beam and the cap beam. The lateral load was transmitted using a steel shear key (Figure 9). The gravity load was applied using a steel beam installed by a control force jack and a steel element with a joint at both ends. The neoprene causes the gravity load distribution, and is arranged at regular intervals between the steel cross beam and the cap beam. The lateral load was transmitted using a steel shear key (Figure 10).

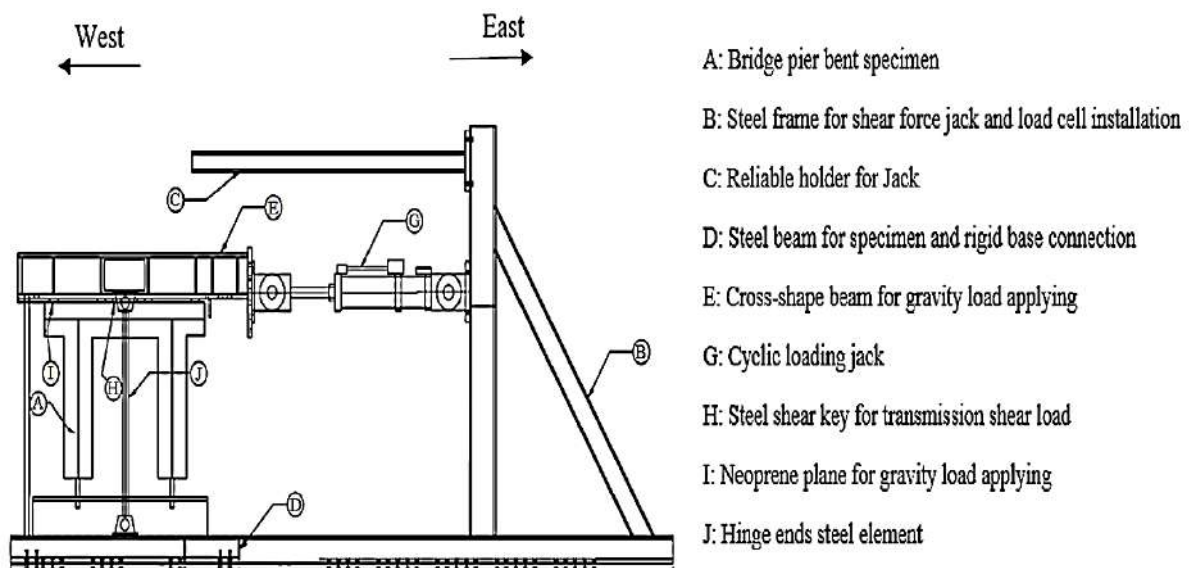




Fig. 2. Set up details



Fig. 3. High strength bars



Fig. 4. Connecting the specimen to a steel beam (rigid floor)



Fig. 5. Displacement control of the end of the cap beam relative to the rigid floor



Fig. 6. Possible slip control of the specimen relative to the steel beam



Fig. 7. Out of plane deformation control (probable rotation control)



Fig. 8. Applying gravity load



Fig. 9. Specimen set up



Fig. 10. Steel shear key between cap beam and cross beam

2.3. Load Pattern

ATC24 (ATC24, 1992) was followed when applying the lateral load. Yield displacement was estimated using observations from the first test as well as early software modeling. The cycles continued until the yield coefficients shifted to the end of testing. Figure 11 represents the lateral load pattern.

3. Results and Observations

3.1. Hysteresis Curves

The response hysteresis curve of the two specimens is presented in Figures 12 and 13. The ultimate failure mechanism is presented in Figures 14 and 15. In all displacements, loss of strength was

observed to follow a similar trend. Throughout the loading process, the loss-of-strength condition in SP-90 was slightly better (less than 5 percent at the same displacement). According to the hysteresis curves, the maximum force applied to the SP-80 and SP-90 was approximately 100 kN, and the maximum force applied in the elastic state occurred at a displacement of 15 mm. As a result, the small change in the connection zone had little effect on the bent strength and stiffness, as expected. The purpose of increasing the number of stirrups in the joint region was to improve the seismic behavior through modification of the failure mechanism by transmitting the hinges to the tops of the columns.

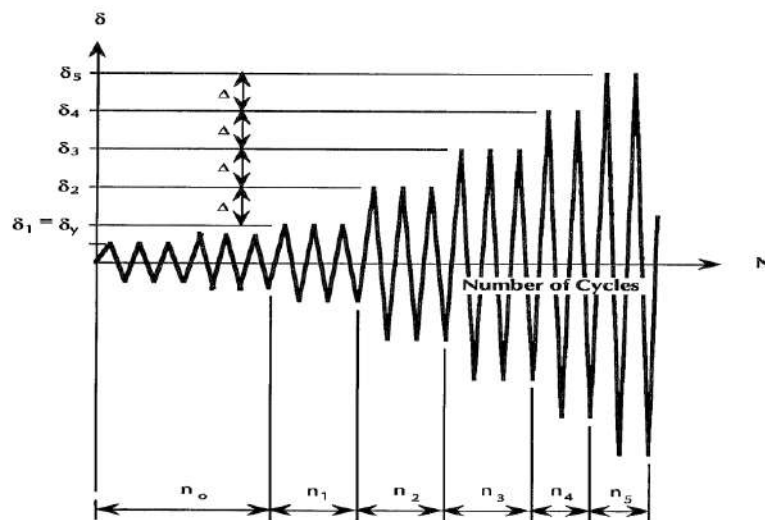


Fig. 11. Quasi-static loading pattern in ATC-24 (ATC24, 1992)

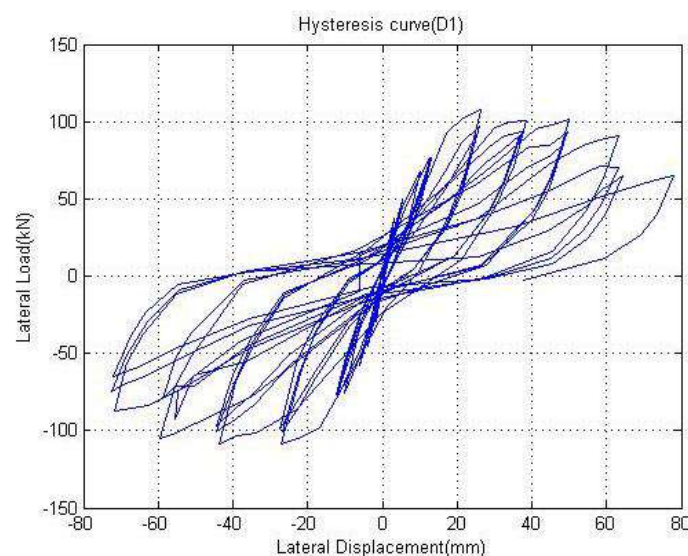


Fig. 12. Hysteresis curve of SP-80

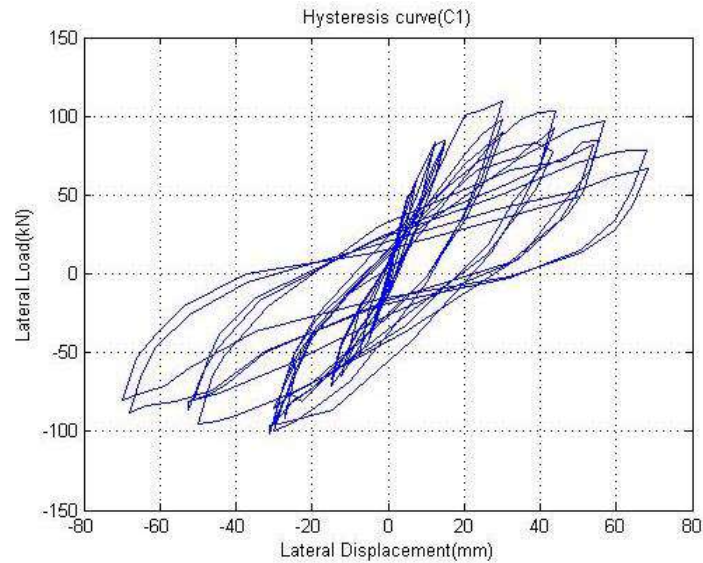


Fig. 13. Hysteresis curve of SP-90



Fig. 14. Ultimate damage mechanism for SP-80



Fig. 15. Ultimate damage mechanism for SP-90

3.2. Damage Development

The results of experimental studies were compared to those of the current study to develop new performance levels. Table 4 shows the qualitative and quantitative definitions of joint performance levels. This classification distinguishes five

performance levels: cracking (I), yielding (II), onset of local mechanism (III), completion of local mechanism (IV), and loss of strength (V). Table 4 shows the qualitative damage types associated with each performance level.

Since in this article, an attempt has been

made to develop quantitative and qualitative definitions of performance levels and damages, with special attention to the connection area, during the test, both specimen must inspect the connection conditions with the head and column beam conditions. Given the improved structural details mentioned for the 1990s example,

generalize to determine whether damage was transferred from the connection to other components in order to approach the appropriate seismic failure mechanism. It is necessary to suggest for the column and cap beam as shown in Table 4 for connection in Tables 5-6.

Table 4. Proposed performance levels for joint

Level	Performance	Qualitative description	Quantitative description
I	Cracking	Diagonal capillary crack in joint; cold joint capillary crack (strain penetration)	Cold joint crack less than 1 mm in width; extension of diagonal crack to 2/3 width of cross-section
II	Yielding	Vertical crack in joint region along column longitudinal reinforcement	Cold joint crack of over 1 mm in width; diagonal crack of over 0.5 mm in width
III	Onset of local mechanism	Reinforcement pullout (slip); extension of diagonal crack (corner to corner); concrete spalling of joint surfaces	Cold joint crack exceeds 3 mm in width; diagonal crack exceeds 1 mm in width; vertical crack exceeds 1 mm in width
IV	Completion of local mechanism	Concrete spalling in joint region; objective view of column longitudinal reinforcement or stirrups through cold joint	Cold joint crack exceeds 5 mm in width; diagonal crack exceeds 2 mm in width
V	Loss of strength	Concrete spalling on upper surface of joint; inadequate anchorage of longitudinal reinforcement in joint region (full slip or stirrup opening); visible permanent deformation in joint region	Core crack in joint exceeds 2 mm; insufficient anchorage of longitudinal reinforcement; fracture of transverse joint reinforcement

Table 5. Define major damages and assign them to performance levels for the column

Level	Performance
I	Bending capillary crack
II	Cracking less than 1 mm Opening of cracks (1 to 2 mm) Full depth cracking
III	Expansion of the diagonal crack Concrete spalling (more than 1/10 section depth) Increase crack width more than 2 mm
IV	The expansion was more than 1.2 section depth Diagonal cracking more than 2/3 section depth visible permanent deformation
V	Reinforcement buckling or failure Cracking of concrete core more than 2 mm

Table 6. Define major damages and assign them to performance levels for the cap beam

Level	Performance
I	Capillary crack - positive bending Capillary crack - negative bending
II	Cracking less than 1 mm Opening of cracks (1 to 2 mm)
III	Expansion of the diagonal crack Sliding column reinforcements Expansion of concrete spalling (more than 1/10 section depth)
IV	Diagonal cracking more than 2/3 section depth Expansion of concrete spalling (more than 2/3 section depth) Increase crack width more than 2 mm Visible permanent deformation
V	Reinforcement buckling or failure Shear and slip failure

The testing results were then compared to the performance criteria in Table 4. The major types of damage sustained by SP-80, which affected the majority of the bridge components, were identified. Level I capillary cracks were observed at all five levels, primarily in flexural members such as the cap beam, and were caused by bending. Such cracks were observed less often in the joint region.

Diagonal cracks generally occur in the joint region due to shear. Capillary cracks in a cold joint, on the other hand, indicate longitudinal column reinforcement slippage in the joint region. Slippage was a major issue in the bents studied in terms of seismic behavior. Cold joint cracking was added to performance level I because it was discovered early on to be caused by strain penetration.

A crack opening exceeding 1 mm, particularly for the cold joint crack, is a criterion at performance level II. According to Bahrani et al. (2010), the 1-mm cold joint crack opening is related to slippage and results in reinforcement yielding. However, the current study found that the reinforcement did not yield and no slippage was observed for a cold joint crack opening. Furthermore, at this performance level, the diagonal crack width criterion was set at 0.5 mm. Furthermore, cold joint cracking was classified as occurring in the joint rather than the column.

In performance level II, Bahrani et al. (2010) reported a cold joint crack width greater than 3 mm as a sign of slippage. Their findings, as well as those of other researchers, have resulted in the inclusion of slippage of longitudinal reinforcement of the column in the joint region at this level of performance. However, because this was not observed in the current experimental study, this item has been classified as performing at the third level.

Items classified as performance level IV include an increase in crack width of more than 2 mm, a cold joint crack opening greater than 5 mm, and concrete spalling that extends up to 50% of the width. These

items will increase nonlinear behavior, which will result in a significant increase in strain.

The lateral load displacement hysteresis curve clearly shows performance level V, loss of strength. At this level of performance, many behaviors can be observed, but one of the most important is permanent deformation. At the end of the experiment, such deformation was clearly visible due to shear strain in the joint region. Furthermore, cracks in the concrete core that were wider than 2 mm were indicators of deterioration. As an indicator of performance level V, severe slippage of the column longitudinal reinforcements was added to this level. Table 7 depicts the various types of major damage and their joint performance levels.

3.2.1. Specimen SP-80

As shown in Table 7, all damages observed in the components and joint region have been described in terms of relative displacement. The first cracks were discovered in the joint region at a relative displacement of 0.73 percent (capillary cracks and diagonal cracks of less than 2.3 mm in width). A diagonal crack exceeding 0.5 mm occurred at the right joint at a relative displacement of 1.83 percent. Strain penetration caused a crack opening greater than 1 mm at the left cold joint. At a relative displacement of 2.73 percent in the joint region, the diagonal cracks extended to more than 1 mm (Figures 16-19).

3.2.2. Specimen SP-90

Table 8 shows the progression of damage in the joints of the SP-80 specimen in terms of relative displacement, which is illustrated in Figures 20-24. At a relative displacement of 0.43 percent, the first crack appeared (capillary and diagonal cracks of less than 2.3 mm in width). A cold joint capillary crack appeared in the interior surface of the left connection at 0.92 percent displacement, and a cold joint capillary crack appeared in the exterior surface of the eastern joint at 0.92 percent displacement.

Diagonal cracks of greater than 0.5 mm were observed at a relative displacement of 1.82% in the left join. At this displacement, the cold joint crack opened wider than 1

mm. At a relative displacement of 3.64%, the width of the cracks in the eastern and left joints exceeded 2 mm.

Table 7. Damage development in joint region (red denotes freight loads and blue denotes return loads)



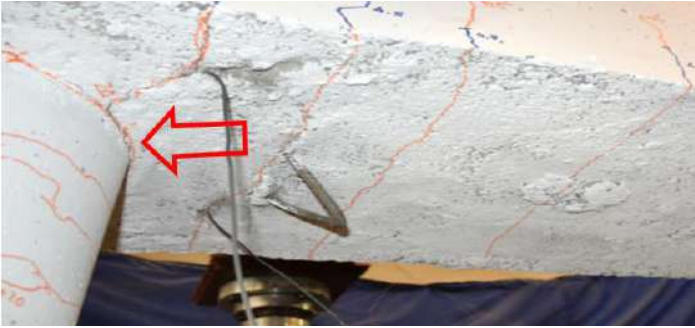






Order	Damage type	Lateral displacement (%)	Figure
1	Capillary cracks and diagonal cracks of less than 2.3 mm in width	0.73	 <p>Fig. 16.</p>
2	Diagonal crack exceeding 0.5 mm at eastern joint; diagonal crack exceeding 1 mm in width at left cold joint crack opening caused by strain penetration	1.83	 <p>Fig. 17.</p>  <p>Fig. 18.</p>
3	Extension of diagonal cracks exceeding 1 mm in length in joint region	2.73	 <p>Fig. 19.</p>

Table 8. Damage development at joints

Order	Damage type	Lateral displacement (%)	Figure
1	Capillary crack and diagonal crack of less than 2.3 mm in width.	0.43	 <p>Fig. 20.</p>
2	Cold joint capillary crack in left joint	0.92	 <p>Fig. 21.</p>
3	Cold joint capillary crack in eastern joint	0.93	 <p>Fig. 22.</p>
4	Diagonal cracks exceeding 0.5 mm observed in left joint	1.82	 <p>Fig. 23.</p>
5	Crack width in eastern and left joints exceeded 2 mm.	3.64	 <p>Fig. 24.</p>

4. Analysis of Results

The performance of the specimens tested was evaluated, compared, and analyzed. The performance of the components, as well as the relative displacements corresponding to their performance levels, have been quantitatively compared and evaluated.

4.1. Qualitative and Quantitative Indices

The quantitative and qualitative damage indices presented by other researchers were compared. A summary of these works was used to create quantitative and qualitative indexes of the joints.

4.1.1. Hose et al.

Tables 9 and 10 present the results based on the flexural behavior of bridge members (cap beams and columns), as well as the damage and performance levels classified by Hose et al. (2000). Table 9 shows the damage levels, which range from capillary cracks at level I to permanent deformation and significant damage at level V. Table 10 shows the performance levels, which range

from cracking in level I to strength degradation in level V.

4.1.2. Bahrani et al.

Bahrani et al. (2010) completed Hose et al. (2000) classifications, indices of performance and damage levels and classified the levels of performance for the joint region and flexural members (Tables 11 and 12). They also created qualitative classifications for damage and observed behavior at each of the five performance levels.

4.1.3. Hassballa et al.

Table 13 summarizes Hasaballa et al. (2011) qualitative and quantitative definitions of joint damage (diagonal shear cracks to shear failure) in terms of the corresponding drift (1 percent to 5 percent).

4.1.4. Vecchio et al.

Based on observations of damage in the joint region, Vecchio et al. (2014) classified joints into four performance levels. The damage characteristics for levels I through IV are shown in Table 14.

Table 9. Bridge damage assessment (Hose et al., 2000)

Level	Damage classification	Damage status	Repair status	Socio-economic status
I	None	Barely visible cracking	No repair	Fully operational
II	Minor	Cracking	Possible repair	Operational
III	Moderate	Open cracks; onset of spalling	Minimum repair	Life safety
IV	Major	Very wide cracks; extensive concrete spalling	Repair	Near collapse
V	Local failure or collapse	Visible permanent deformation; buckling/rupture of reinforcement	Replacement	Collapse

Table 10. Bridge performance assessment (Hose et al., 2000)

Level	Performance level	Qualitative performance level	Quantitative performance level
I	Cracking	Onset of capillary cracks	Barely visible cracking
II	Yielding	First longitudinal reinforcement yielding	Crack width less than 1 mm
III	Onset of local mechanism	Onset of inelastic deformation; onset of concrete spalling; development of diagonal cracks	Crack width of 1 to 2 mm; length of spalled region exceeds 1/10 of cross-section width
IV	Full development of local mechanism	Wide crack widths; spalling over full local mechanism region	Crack widths exceed 2 mm; Diagonal cracks exceed 2/3 of cross-section width; length of spalled region exceeds 1/2 cross-section width
V	Strength degradation	Main reinforcement buckling; Transverse reinforcement rupture; crushing of core concrete	Crack width exceeds 2 mm in concrete core; Measurable dilation exceeds 5% of original member dimension

Table 11. Damage based on performance level of joint (Bahrani et al., 2010)

Level	Performance level	Qualitative description	Quantitative description
I	Cracking	Capillary cracks; cold capillary cracks at joint; onset of longitudinal reinforcement slip	Capillary cracks of less than 0.5 mm
II	Yielding	Concrete cold-joint crack opening	Crack width of less than 1 mm
III	Onset of local mechanism	Full-width cross-section crack; development of diagonal cracks; cap beam reinforcement slip; column reinforcement slip	Crack width of 1 to 2 mm; concrete spalling of less than 1/10 of cross-section
IV	Full development of local mechanism	Concrete spalling; diagonal crack	Crack width exceeds 2 mm; spalling exceeds 1/2 of cross-section width; diagonal cracks over 2/3 of cross-section
V	Strength degradation	Severe column reinforcement slip; visible permanent deformation	Crack of concrete core exceeds 2 mm

Table 12. Damage based on column performance levels (Bahrani et al., 2010)

Level	Performance level	Qualitative performance level	Quantitative performance level
I	Cracking	Flexural capillary cracks	Crack width of less than 0.5 mm
II	Yielding	Extension of flexural cracks	Crack width of less than 1 mm
III	Onset of local mechanism	Onset of concrete spalling; development of diagonal cracks	Crack width of 1 to 2 mm
IV	Full development of local mechanism	Concrete spalling; diagonal cracks	Spalling exceeds 1/2 of cross-section width
V	Strength degradation	Visible permanent deformation; buckling or rupture of longitudinal reinforcement	Crack in concrete core exceeds 2 mm

Table 13. Damage sequence by drift of joint (Hasaballa et al., 2011)

Drift (%)	Damage
1	Diagonal shear cracks
3	Diagonal cracks of 2.6 mm in width
4	Concrete spalling at bottom of joint
5	Specimen failure due to shear failure

Table 14. Performance criteria for joints from Vecchio et al. (2014)

Level	Performance
I	Beam bar yielding
II	Significant cracking of joint
III	Joint shear mechanism
IV	Significant concrete spalling

4.1.5. Tukiari et al.

Tukiari et al. (2014) proposed five levels of performance for members, and Table 15 shows the qualitative descriptions for each level. In the current study, buckling of the reinforcement and collapse are considered separate items; however, Hose et al. (2000) combined them into one item.

4.1.6. Truong et al.

Truong et al. (2017) calculated damage based on a 0.5 to 5% drift in the joint (Table 16). Truong et al. (2017) and Hasaballa et al. (2011) classified damage based on drift,

whereas others reported damage levels based on performance. At performance level 4, Bahrani et al. (2010) reported diagonal crack extension to more than two-thirds of the cross-section, whereas Truong et al. (2017) reported this damage at performance level 1. Full-width cracking did not occur in the current study, but it was observed by Bahrani et al. (2010). Using the findings of other researchers during experimental testing as well as those from the current study, a table was created in which the damage definitions were revised.

4.2. Performance of Specimens

4.2.1. Specimen SP-80

Figure 25 depicts the performance of the specimen SP-80 components in relation to drift. It can be seen that the damage trend and performance level for the joint were level III, level V for the cap beam, and level II for the column. This means that even if the joint is at level III, the column remains at level II. Despite the fact that the joint and cap beam have reached performance level V, the column has not been seriously damaged. This is in direct conflict with the seismic design criteria.

While studying the behavior of concrete bents in bridges, the performance of the joints has been the most important consideration. Figures 26 and 27 show the minimum drift for the SP-80 components

corresponding to the five performance levels. It can be seen that the joint and cap beam performed poorly, and these components were damaged much sooner than the column itself, which received little damage.

4.2.2. Specimen SP-90

Figure 28 depicts the damage trend and performance levels of the bent components in specimen SP-80. As can be seen, the cap beam reached level V, the joint reached level II, and the column reached only level II. This means that while the cap beam advanced to level IV, the column only advanced to level II. The cap beam experienced more damage than any other component, but the column did not sustain serious damage. This does not meet the seismic design criteria.

Table 15. Tukiari functional levels of flexural damage (Tukiari et al., 2014)

Performance level	Damage level
Operational	No damage; fine cracks occur
Immediate occupancy	Slight structural damage; initial spalling of concrete cover; entrance to building only to recover belongings
Life safety	Moderate structural damage; cracks in column and beam-column joint; buckling over reinforcement
Collapse prevention	Large crack in structural elements; fracture of longitudinal bars; loss of stability of structure; structure near collapse and cannot be entered
Collapse prevention	Collapse or imminent danger of collapse

Table 16. Drift and sequence of damage to joint (Truong et al., 2017)

Drift (%)	Damage observed
0.5	Flexural cracks in beam
1	Cracks propagating to neutral axis of beam
1.5	Thin flexural cracks at beam–column interface that spread along beam length
3	Onset of inclined cracks in joint panel zone; shear failure of joint panel zone as loading progresses
5	Several thin vertical and horizontal cracks in joint panel zone; flexural cracks at widened beam-column interface

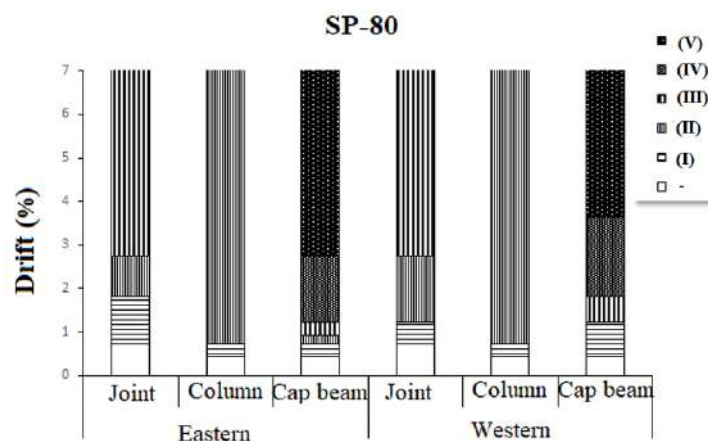


Fig. 25. Performance of components

Figures 29 and 30 represent the minimum drift values for each of the five performance levels. The joint and cap beam performance in specimen SP-90 can be seen to be completely rejected. The cap beam was damaged much earlier than the column,

and the column was only slightly damaged before the joint was damaged. The column eventually reached performance level II, and no damage matching levels III to V were observed. The joint performance, on the other hand, reached level IV.

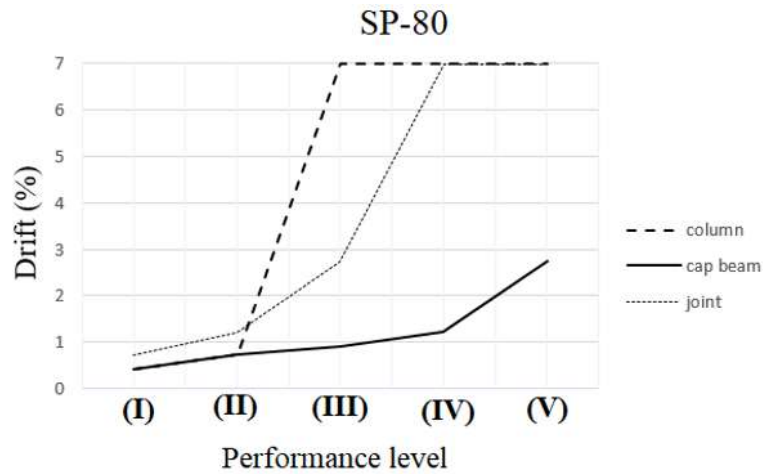


Fig. 26. Comparison of performance of components in SP-80



Fig. 27. Failure mode of SP-80

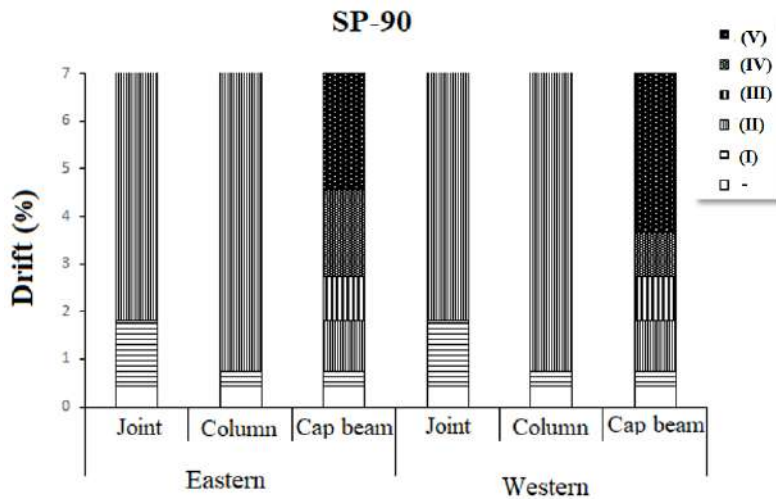


Fig. 28. Performance of components in SP-90

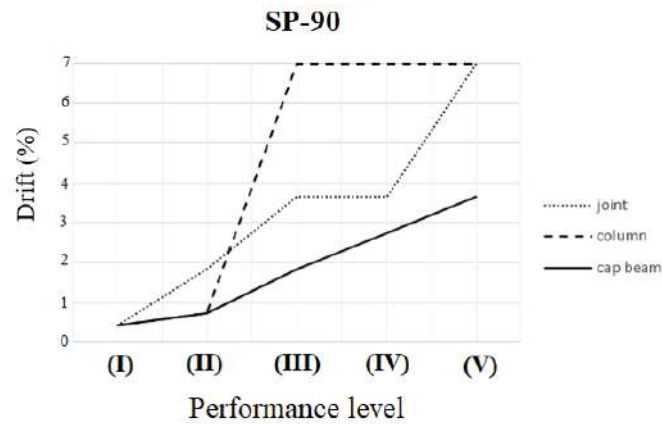


Fig. 29. Comparison of performance of components in SP-90

4.3. Energy Dissipation

The ability to dissipate energy is the most important parameter in structural seismic response. Figure 31 shows the increasing trend of cumulative dissipated energy by specimens. The specimen show relatively low drifts range at the end of test. Hysteresis curves represented little ability to absorbed and dissipate energy. Many reasons can be cited, including the defect of

structural details in older codes, the lack of a desirable failure mechanism, and the early occurrence of damage levels in the beams and connection region. A significant and significant result is the need to strengthen for the tested bents. As a result, more of the structure's capacity can be used for energy dissipation, and more deformation can occur.



Fig. 30. Failure mode of SP-90

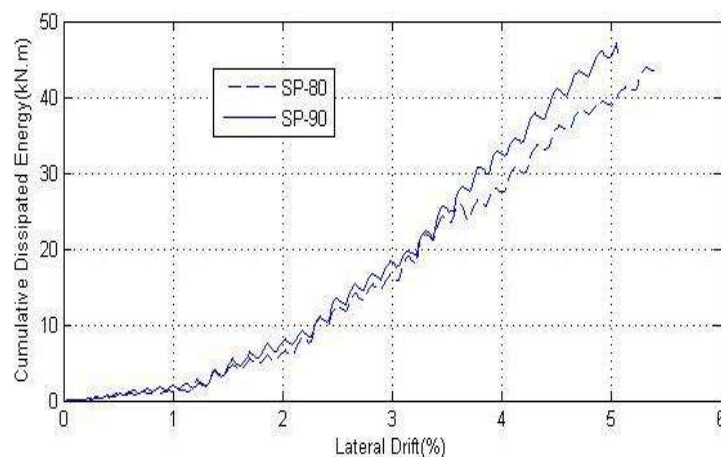


Fig. 31. Increase trend of cumulative dissipated energy

5. Conclusions

The present study performed an experimental evaluation and revised the performance level definitions for two-column concrete bridge bents with joints designed in the 1980s and 1990s. Based on the damage observed, qualitative and quantitative indexes for the performance levels have been presented. The performance of the bent's components was compared, and the following results were obtained:

- The minor change in the connection zone had little effect on bent strength and stiffness, as expected. The goal of increasing the number of stirrups in the joint region was to improve seismic behavior by changing the failure mechanism (moving the hinges to the top of the column). The observed damage revealed no positive change in the failure mechanism or movement of the flexural hinges to the column tops.
- Defining and developing quantitative and qualitative indices with appropriate performance levels for joints in concrete bridge bents is an important aspect of evaluating their seismic behavior and should be regarded as the first step in column strengthening.
- Damage assessment in the joint region revealed the problem of longitudinal column reinforcement embedded in the joint region. Cold capillary cracks were defects in performance level I and were classified as a sign of slippage and complete slippage by Bahrani et al. (2010) in performance levels III and V, respectively. This has not been addressed by Hose et al. (2000) and Tukiari et al. (2014) because they focused only on flexural members.
- The results showed that diagonal cracking was observed in the joint's first cycles and has been classified as performance level I. However, Hose et al. (2000) and Bahrani et al. (2010) based their observations on column damage, so they classified this observation as performance level III. The formation of diagonal cracks in the joint is included in performance level I.
- The findings revealed that the cold joint crack opening is a new qualitative definition in performance level I, with a quantitative definition of less than 1 mm.
- The findings revealed that vertical cracking in a joint that is accompanied by slipping of the column's longitudinal reinforcement, a cold joint crack width greater than 1 mm, and a crack width greater than 0.5 mm were all determinants of yielding. This level of performance is relative to the level of performance in the column.
- It was discovered that concrete crumbling of the joint's upper surface, slippage of the longitudinal reinforcement in the joint region, and permanent visible deformation of the joint due to loss of strength in the joint region all indicate performance level V in the columns. Fracture and buckling of the rebars are signs of this performance level.
- The joint and cap beam in SP-80 achieved performance levels III and V, respectively. However, the column's ultimate performance level was II. In SP-90, the beam and joint achieved performance levels V and II, respectively, despite the fact that the column's ultimate level was II.
- The results showed that the joint and cap beam were damaged before the columns in both experimental specimens. The columns did not meet their final performance levels, which contravened seismic design criteria.
- Test results revealed that the first cracks in the joint were diagonal cracks that occurred at lower drift values.
- Previous reports were based primarily on drift while, they were based on drift as well as performance level for each type of damage reported in the current study.
- Bahrani et al. (2010) reported cap beam and column reinforcement slippage. Only longitudinal column reinforcement

slippage due to strain penetration was observed in the current study.

6. Recommendations

Comparative behavioural evaluation of strengthened bridge pier bent with different spans can be studied. It is important that how bents behave in the similar lateral loading. According to the newer available bridge codes, to achieve the desired seismic behavior of concrete bent, different specimens can be tested and weaknesses should be evaluated.

7. References

- AASHTO. (2011). *AASHTO guide specifications for LRFD seismic bridge design*, AASHTO. Transportation Officials, Subcommittee on Bridges
- Abudallah Habib, I., Wan Mohtar, W.H.M., Muftah Shahot, K., El-shafie, A. and Abd Manan, T.S. (2020). "Bridge failure prevention: An overview of self-protected pier as flow altering countermeasures for scour protection", *Civil Engineering Infrastructures Journal*, 54(1), 1-22.
- Applied Technology Council (ATC24). (1992). "Guidelines for cyclic seismic testing of components of steel structures", Applied Technology Council, California.
- Bahrani, M.K., Vasseghi, A., Esmaeily, A. and Soltani, M. (2010). "Experimental study on seismic behavior of conventional concrete bridge bents", *Journal of Seismology and Earthquake Engineering*, 12(3), 107-118.
- Bahrani, M.K., Vasseghi, A., Nooralizadeh, A. and Zargarani, M. (2017). "Experimental and analytical study on the proposed retrofit method for concrete bent in ordinary highway bridges in Iran", *Journal of Bridge Engineering*, 22(6), 05017004.
- Billah, A.M., Alam, M.S. and Bhuiyan, M.R. (2012). "Fragility analysis of retrofitted multicolumn bridge bent subjected to near-fault and far-field ground motion", *Journal of Bridge Engineering*, 8(10), 992-1004.
- Deng, J., Liu, T., Xie, W., Wei Lu. (2015). "Study on repaired earthquake-damaged bridge piers under seismic load", *Advances in Materials Science and Engineering*, 2015, Article ID 295392, 10 pages.
- Ghassemieh, M., Ghodrati, S.M., Khanmohmmadi, M. and Baei, M. (2018). "A superelastic retrofitting method for mitigating the effects of seismic excitations on irregular bridges", *Civil Engineering Infrastructures Journal*, 51(1), 147-168.
- Hasaballa, M., El-ragaby, A., El-salakawy, E. (2011). "Seismic performance of exterior beam-column joints reinforced with glass fibre reinforced polymer bars and stirrups", *Canadian Journal of Civil Engineering*, 38(10), 1092-1102.
- Hose, Y., Silva, P. and Seible, F. (2000). "Development of a performance evaluation database for concrete bridge components and systems under simulated seismic loads", *Earthquake Spectra*, 16(2), 413-442.
- Kaliluthin, A.K. and Kothandaraman, S. (2017). "Performance evaluation of exterior beam-column joint with core reinforcement technique subjected to reverse cyclic loading", *Arabian Journal for Science and Engineering*, 42(9), 2440-2443.
- Khanmohammadi, M., Abbasloo, A.A. and Valadi, E. (2016). "Enhancing shear strength of cap beam-column joints in existing multicolumn bent bridges using an innovative method", *Journal of Bridge Engineering*, 21(12), 04016086.
- Lowes, L.N. and Moehle, J.P. (1999). "Evaluation of retrofit of beam-column T-joints in older reinforced concrete bridge structures", *ACI Structural Journal*, 96(4), 519-532
- Naghavi, M., Rahnavard, R., Thomas, R.J. and Malekinejad, M. (2019). "Numerical evaluation of the hysteretic behavior of concentrically braced frames and buckling restrained brace frame systems", *Journal of Building Engineering*, 22, 415-428.
- Patel, P.A., Desai, A.K. and Desai, J.A. (2013). "Evaluation of RC and SFRC exterior beam-column joint under cyclic loading for reduction in lateral reinforcement of the joint region", *Magazine of Concrete Research*, 65(7), 405-414.
- Radkia, S., Gandomkar, F.A. and Rahnavard, R. (2018). "Seismic response of asymmetric sliding steel structure with considering soil-structure interaction effects", *Journal of Structural and Construction Engineering*, 6(3), 105-120.
- Radkia, S., Rahnavard, R. and Gandomkar, F.A. (2019). "Evaluation of the effect of different seismic isolators on the behavior of asymmetric steel sliding structures", *Journal of Structural and Construction Engineering*, 6(4), 213-230.
- Rahnavard, R. and Hassanipour, A. (2015). *Steel structures analysis using ABAQUS*, Academic Center for Education, Culture and Research, Publishing Organization of Kerman Branch, Kerman.
- Rahnavard, R., Hassanipour, A. and Mounesi, A. (2016). "Numerical study on important parameters of composite steel-concrete shear walls", *Journal of Constructional Steel Research*, 121, 441-456.
- Rahnavard, R., Hassanipour, A., Suleiman, M. and

- Mokhtari, A. (2017). "Evaluation on eccentrically braced frame with single and double shear panels", *Journal of Building Engineering*, 10, 13-25.
- Rahnavard, R., Naghavi, M., Aboudi, M. and Suleiman, M. (2018). "Investigating modeling approaches of buckling-restrained braces under cyclic loads", *Case Studies in Construction Materials*, 8, 476-488.
- Rahnavard, R., Taghikhajeh, M., Hassanipour, A. and Siahpolo, N. (2019). "Parametric study of seismic performance of steel bridges pier rehabilitated with composite connection", *Journal of Structural and Construction Engineering*, 6(1), 98-113.
- Rahnavard, R. and Thomas, R.J. (2019). "Numerical evaluation of steel-rubber isolator with single and multiple rubber cores", *Engineering Structures*, 198, 109532.
- Samadi, D., Taghaddos, H., Nili, M.H. and Noghabaei, M. (2021). "Development of a bridge maintenance system using bridge information modeling", *Civil Engineering Infrastructures Journal*, 54(2), 351-364.
- Truong, G.T., Hieu Dinh, N., Kim, J.C. and Choi, K.K. (2017). "Seismic performance of exterior RC beam-column joints retrofitted using various retrofit solutions", *International Journal of Concrete Structures and Materials*, 11(3), 415-433.
- Tukiar, M.A., Kay Dora, A.G. and Hamid, N.H. (2014). "Seismic performance and assessment of precast beam-column corner joint subject to reversible lateral cyclic loading", *Applied Mechanics and Materials*, 661(2014), 128-133.
- Vecchio, C.D., Di Ludovico, M., Balsamo, A., Prota, A., Manfredi, G. and Dolce, M. (2014). "Experimental investigation of exterior RC beam-column joints retrofitted with FRP systems", *Journal of Composites for Construction*, 18(4), 04014002.



This article is an open-access article distributed under the terms and conditions of the Creative Commons Attribution (CC-BY) license.



Spatial Transferability of a Daily Activity Type and Duration MDCEV Model

Nohekhan, A.¹, Samimi, A.^{2*} and Zahedian, S.¹

¹ Ph.D. Candidate, Department of Civil and Environmental Engineering, University of Maryland, Maryland, United States of America.

² Associate Professor, Department of Civil Engineering, Sharif University of Technology, Tehran, Iran.

© University of Tehran 2021

Received: 18 Nov. 2020;

Revised: 07 Sep 2021;

Accepted: 20 Sep. 2021

ABSTRACT: This paper explores the transferability of the Multiple Discrete-Continuous Extreme Value (MDCEV) model for activity type and duration using various transfer methods and sample sizes. This study employs the data of travel demand studies in two major cities, Shiraz and Mashhad in Iran. The model is first developed for Shiraz and then transferred to Mashhad. The adopted transfer methods are transfer scaling, Bayesian updating, combined transfer estimation, and joint context estimation. Aggregate and disaggregate transfer measures are adopted to examine the transferred models' general prediction and policy predictability. The results indicate the joint context estimation method's superiority in terms of estimation and policy prediction powers. The available massive data to the authors enabled measuring the value of sample size in this study. The sample size sensitivity analysis revealed a decrease in the marginal gain of the transferred model's performance as the sample size increases. Remarkably, the transferred model outperforms even the locally estimated model when 1) advanced transfer techniques are applied (i.e., the combined transfer estimation and the joint context estimation), and 2) the application context sample size is large enough (i.e., more than 30 percent).

Keywords: Bayesian Updating, Combined Transfer Estimation, Joint Context Estimation, MDCEV Model, Model Transfer, Spatial Transferability, Transfer Scaling.

1. Introduction

The spatial and temporal transfer of travel demand models could undercut obstacles that impede many cities from conducting transportation studies (Ziemke et al., 2015; Lefebvre-Ropars et al., 2017). Since the 70s, several studies have explored traditional travel demand models' transferability with promising results

(Salem and Nurul Habib, 2015). However, the transferability of advanced Activity-Based Models (ABM) is only discussed in a handful of studies (Yasmin et al., 2015), necessitating more research on this topic. Remarkably, the transferability of individual-level activity generation/time-use models is of interest due to the required high-resolution and disaggregated data for model development, an extremely costly

* Corresponding author E-mail: asamimi@sharif.edu

and labor-intensive data to collect (Xiong et al., 2020). Although the application of deep learning models has taken pace in Civil Engineering (Karimae Tabarestani and Zarrati, 2015; Barkhordari and Entezari Zarch, 2015) and, in particular, Transportation Engineering (Zahedian et al., 2020; Nohekhan et al., 2021) to capture the complex interdependencies between the input attributes, the black box structure of these models is the primary obstacle in providing the necessary insights for decision-makers. Therefore, econometrics models capable of delivering such insight while producing accurate estimates for complex behaviors are essential. The MDCEV model, a budget-based approach, is increasingly adopted to model individual-level activity patterns (Wafa et al., 2015) and incorporated in several activity-based travel model systems (Bhat, 2018). Such a growing application of MDCEV models motivated this research to investigate these models' spatial transferability regarding the required sample data and experiment with various well-known transfer methods.

The transferability of transportation model components is widely studied using different methods with varying success levels. Notably, the transferability of activity generation model components is evidenced to be more feasible than those for other travel choices (Bowman and Bradley, 2017) due to the low dependency of individuals' daily activity on the built environment (Sikder and Pinjari, 2013). Arentze et al. (2002), for instance, applied the naïve transfer method and found "substantial evidence for the spatial transferability of Albatross, except for transport mode". Further, Nowrouzian and Srinivasan (2012) used the same method to transfer tour generation models and argued that conventional aggregate transfer metrics are insufficient to ensure acceptable performance for policy assessments. Bowman et al. (2014) adopted a joint context estimation approach and considered two different sample sizes to transfer 14 model components of DaySim. They

determined that the transferred model estimated with a large sample size outperforms the locally estimated model (Bowman et al., 2014).

Yasmin et al. (2015) evaluated the transferability of TASHA (Travel Activity Scheduler for Household Agents), an activity-based model developed for the Greater Toronto Area, Canada, to the Island of Montreal, Canada. The authors explored the spatial transferability of the modeled activity attributes, including frequency, start time, duration, and distance, using a naïve transfer approach. The results illustrated the transferability of the models for work, school, and return to home activities. However, due to differences in behaviors, the transfer models performed poorly on other activities, and a re-estimation step was recommended.

Bowman and Bradley (2017) used the same data and approach to test the transferability of 12 model components of DaySim. They tested similarities in three data segments, namely within-state, similar trip distance, and similar density. They identified "state grouping" as the best criterion, followed by density and trip distance grouping. Tang et al. (2018) explored the spatial transferability of a Neural Network (NN) mode choice model using the naïve transfer and a NN model adaptation method. They train five NN models for five regions of Washington DC and Baltimore and found that while the naïve transfer method is applicable in areas with high similarities, the proposed NN model adaptation method is more suitable for regions with significant differences.

In a more recent study, the spatial transferability of FEATHERS, an ABM model developed for Flanders, Belgium, to Ho Chi Minh City, Vietnam, is explored (Linh et al., 2019). The study found some transferability levels using the naïve method; however, it recommended a recalibration step for all sub-models. In analyzing the potential impacts of the connected and automated transportation technology on travel behavior, Shabanpour

et al. (2019) proposed a transferable framework developed on a small geographic area to generate disaggregate travel data in other regions.

The transferability of MDCEV models has specific gaps, despite the relatively rich literature of model transfer in general. Sikder and Pinjari (2013) introduced one of the earliest papers that studied MDCEV transferability. They used simple transfer methods, namely naïve transfer and constants updating, and argued that the ability to predict aggregate patterns does not necessarily imply good transferability. They determined that updating constants can improve predictions relative to observed patterns. However, this method does not guarantee improved model performance in response to changes in demographic characteristics (Sikder and Pinjari, 2013). Wafa et al. (2015) proposed a latent segmentation approach to endogenously determine appropriate criteria for clustering regions in estimating MDCEV models. This approach had better performance than traditional exogenous identification methods.

The shortcoming in most of these studies is that they have used basic transfer methods. Besides, the effects of sample size and transfer methods on the MDCEV model's predictability have been largely neglected. A summary of the published ABM transferability studies is presented in Table 1 to obtain a broad overview of the literature gaps. This paper fills the gaps by applying four widely-used transfer methods to examine the spatial transferability of the MDCEV models in two major cities, Shiraz and Mashhad, in Iran. The data used for estimating the MDCEV model and its transferability exploration is the household travel behavior surveys conducted in these two cities. The survey in Mashhad is conducted in 1994 and Shiraz in 1999. While these data are old, the study's main contribution is from the methodological aspect of transferability analysis of the MDCEV model, which is independent of the data collection date. At the time of the

survey, Mashhad had roughly 1.8 million and Shiraz 1.2 million residents. In terms of public transportation, both cities at the time of data collection had an extensive network of fixed-route bus lines but no metro lines. Each of these cities has a distinct Central Business District (CBD) comprising mixed land use, with urban neighborhoods situated around the CBD. The present study compares alternative methods of model transfer and analyzes sample size effects on the estimation outcome. The selected transfer procedures are transfer scaling, Bayesian updating, combined transfer estimation, and joint context estimation, each of which is described in detail in the following section.

The structure of the remainder of the paper is as follows. In the second section, the methodology of the study is presented. This section contains a description of the MDCEV model, transfer methods, and transferability metrics. In the third section, the data of the study is introduced and described. This description presents the sociodemographic characteristics and the activity types and time allocations in Mashhad and Shiraz. In the fourth section, the results of estimating the MDCEV model in each region are briefly presented, followed by a detailed description of the transferred models' performance and transferability metrics analysis for each transfer method and various sample sizes of the application context data. In the last section, the findings are summarized and discussed to elaborate on the study's conclusions. Besides, the contributions of this research and recommendations for future studies in transferability analysis are presented in this section.

2. Methodology

This section first presents an overview of the MDCEV model formulation, followed by introducing and discussing the applied transfer methods. Finally, aggregate and disaggregate transferability assessment metrics for comparing the transferred

models' performance are introduced, allowing for a more robust comparison of the transfer methods.

2.1. MDCEV Model

Several travel demand decisions, including activity type and duration, require a simultaneous choice of multiple alternatives (Shamshiripour and Samimi, 2019). Traditional discrete and discrete-continuous models cannot be effectively adopted in such cases, as these models are applicable when only one alternative among a set of alternatives is chosen (Bhat, 2018; Mondal and Bhat, 2021). Unlike the traditional models, the MDCEV model allows choosing different choices with different quantities besides observing diminishing marginal returns with an increase in any specific alternative's consumption (Pinjari and Bhat, 2010). The

MDCEV model estimated in this study adopts the same utility form presented, in Eq. (1), as suggested by Bhat (2008):

$$U(x) = \exp(\varepsilon_1) \cdot \ln(t_1) + \sum_{k=2}^K \gamma_k [\exp(\beta^T z_k + \varepsilon_k)] \cdot \ln\left(\frac{t_k}{\gamma_k} + 1\right) \quad (1)$$

where the first term relates to the utility of allocating time to the activity in which every individual participates (in-home activity in our study), also known as the "outside good", γ_k : is the translation parameter, t_k : is the corresponding allocated time to activity k ($t_k \geq 0$ for all k), β : is a coefficient vector related to activity k , z_k : is a vector of attributes, and ε_k : captures the unobserved characteristics that impact the baseline utility for activity purpose k .

Table 1. Summary of activity-based model transferability literature

Author(s)	Year	ABM studied	Location	Transfer methods	Assessment metrics
Arentze et al.	2002	ALBATROSS	Netherlands	Naïve transfer	Transferred model's aggregate and disaggregate level prediction ability
Nowrouzian and Srinivasan	2012	Original	Florida, USA	Naïve transfer	Elasticity comparisons, Root mean square error between predicted and observed shares
Bowman et al.	2014	DaySim	California, Florida, USA	Joint context estimation (using pooled data of different regions)	Transferability test statistic, t-statistics of difference variables capturing differences in parameters between counties
Sikder and Pinjari	2013	MDCEV	California, Florida, USA	Naïve transfer, Constants updating approach	Transferability test statistic, Root mean square error, Transfer index, Relative aggregate transfer error
Yasmin et al.	2015	TASHA	Toronto, Montreal, Canada	No transfer method implemented	K-S test, Comparison of differences
Wafa et al.	2015	MDCEV	California, Florida, USA	Latent segmentation-based approach	Bayesian information criterion
Bowman and Bradley	2017	Daysim	California, Texas, Florida, and New York, USA	No transfer method implemented	Transferability index, tests of coefficient differences
Tang et al.	2018	NN model	Washington DC, Baltimore, USA	No transfer method implemented	Hit ratio, overall prediction accuracy, mean absolute relative error, root mean square error, relative aggregate transfer error
Linh et al.	2019	FEATHERS	Flanders, Belgium; Ho Chi Minh City, Vietnam	No transfer method implemented	Comparison of differences
Shabanpour et al.	2019	POLARIS	Chicago, Illinois, USA	No transfer method implemented	Comparison of differences

Each person is assumed to maximize his/her utility according to a time budget, formulated as $\sum_{k=1}^K t_k = T$, where T : is the time budget (i.e., 24 hours). Eq. (2) illustrates the probability expression for the time allocation to the first M of the K activities (assuming the first alternative as the “outside good”) (Bhat, 2008):

$$P(t_1^*, t_2^*, t_3^*, \dots, t_M^*, 0, 0, \dots, 0) = \frac{1}{\sigma^{M-1}} \left[\prod_{i=1}^M c_i \right] \left[\sum_{i=1}^M \frac{1}{c_i} \right] \left[\frac{\prod_{i=1}^M t^{v_i/\sigma}}{(\sum_{k=1}^K t^{v_k/\sigma})^M} \right] (M-1)! \quad (2)$$

where σ : is the scale parameter and c_i : is calculated as follows:

$$c_i = \left(\frac{1}{t_i^* + \gamma_i} \right); \quad 1 \leq i \leq M \quad (3)$$

To predict the activity pattern for a given person, Pinjari and Bhat (2010) presented a procedure for predicting the amount of time spent on each activity. This method is used in this study to predict the total amount of time spent for each activity type. Interested readers may refer to Bhat (2008, 2018) and Pinjari and Bhat (2010) for a more detailed description of the MDCEV model structure and the forecasting algorithm.

2.2. Transfer Methods

The spatial model transfer is built upon the notion that the estimated parameters using the data of a region (termed as estimation context) can provide valuable information for estimating the model parameters in another area (termed as application context). There are several levels of model transferability classified as follows Karasmaa (2003):

- The behavioral assertion (e.g., utility maximization),
- Mathematical model class (e.g., a logit formulation),
- Model specifications (e.g., a linear utility function), and
- Model coefficients.

Depending on the type and quality of the data, a model transfer is achievable in at least four approaches: 1) Transfer scaling, 2) Bayesian updating, 3) Combined transfer estimation, and 4) Joint context estimation (Rossi and Bhat, 2014). The following section briefly discusses these well-known model transfer methods.

2.2.1. Transfer Scaling

The primary assumption in transfer scaling is that the model structure is the same across application and estimation contexts. Karasmaa (2003) discussed the four following techniques to apply the transfer scaling approach:

- Naïve transfer: The simplest transfer method is naïve transfer, in which the estimated model is exactly used for the application context (Atherton and Ben-Akiva, 1976).
- Adjusting constant terms: Aggregate data can be utilized to correct the constant terms; therefore, the model imitates existing aggregate data. Therefore, all the model coefficients except for the constant terms are accepted (Atherton and Ben-Akiva, 1976). In this situation, the general utility function of the application context model can be written as follows (Karasmaa, 2003):

$$V_j = C_j + \beta'_i X_i \quad (4)$$

where V_j : is the vector of the general utility function in the application context, C_j : is the vector of constants in the application context, β_i : is the matrix of coefficients in the estimation context, and X_i : is the vector of variables in estimation context.

- Estimating new constants and scale: All or some of the application context's utility function parameters are scaled, in this case. Further, alternative-specific constants are estimated using a sample from application context data assuming that the utility function's remaining parameters are directly transferable from the estimation context (Atherton and Ben-Akiva, 1976). The transfer method formulates the utility function according to Eq. (5) as follows

(Karasmaa, 2003):

$$V_j = C_j + \rho \beta'_i X_i \quad (5)$$

where ρ : is the vector of scale factors for each set of explanatory variables to be scaled.

- Estimating the application context model: A small sample is used, assuming that it represents the choice behavior. In this method, all the estimation context model variables appear in the application context model, and the parameters are estimated solely based on the application context data. This method is identical to transfer scaling if all the coefficients are re-scaled (Karasmaa, 2003).

2.2.2. Bayesian Updating

The primary assumption in the Bayesian updating method is the similarity of individuals' behavior in the estimation and application contexts. This assumption enables combining the parameters estimated from an application context sample data with the estimation context parameter values to update the parameters using a classical Bayesian analysis (Karasmaa, 2003). In its essence, Bayesian updating optimally combines the coefficients estimated on the application and estimation contexts separately, considering the coefficients' estimated variances (Atherton and Ben-Akiva, 1976). This procedure calculates a weighted average of the coefficients in which weights are equal to the inverse of the estimated coefficients' variance, as presented in Eq. (6). It is noteworthy that the weighted average technique is applicable when the coefficient estimates are normally distributed.

$$\hat{\beta}_{transferred} = (\Sigma_i^{-1} + \Sigma_j^{-1})^{-1} (\Sigma_i^{-1} \hat{\beta}_i + \Sigma_j^{-1} \hat{\beta}_j) \quad (6)$$

where $\hat{\beta}_i$ and $\hat{\beta}_j$: are the estimated parameter vectors in the estimation and application contexts, respectively; Σ_i and Σ_j : are the variance-covariance matrices of

estimated parameters for the estimation and application contexts, respectively.

2.2.3. Combined Transfer Estimation

This method is a generalization of Bayesian updating and incorporates transfer scaling (Karasmaa, 2003). The assumption of identical behavioral model parameters between the estimation and application context in Bayesian updating could be quite different from reality in the case of distinct geographical regions where actual differences between parameters of the estimated models might exist (Karasmaa, 2003). The combined transfer estimation method is based on the mean squares error criterion, extending the Bayesian procedure to explicitly account for the transfer bias. The transferred model parameters are determined using Eq. (7):

$$\hat{\beta}_{transferred} = [(\Sigma_i + \Delta \Delta')^{-1} + \Sigma_j^{-1}]^{-1} [\Sigma_i^{-1} \hat{\beta}_i + \Sigma_j^{-1} \hat{\beta}_j + \Delta \Delta'^{-1} \hat{\beta}_i + \Sigma_j^{-1} \hat{\beta}_j] \quad (7)$$

where Δ : is the transfer bias approximated by the estimated bias: $\Delta \approx \hat{\beta}_j - \hat{\beta}_i$.

2.2.4. Joint Context Estimation

The Joint context estimation method involves estimating a new joint model using both the estimation context and application context data (Karasmaa, 2003). The basic idea of merging datasets from different regions is to modify the random variation in the datasets' utility functions (Ben-Akiva and Morikawa, 1990). The following notations are used to develop the joint context estimation technique:

r : superscript denoting context (= 1 for estimation context set; = 2 for application context), ψ_k^r : baseline utility of alternative k in context r , λ_k^r : deterministic baseline utility of alternative k in context r , ε_k^r : random component of the baseline utility for alternative k in context r , ζ : vector of utility function parameters assumed to be constant across the contexts, s_k^r : vector of explanatory variables for alternative k

shared with context r , σ^r : vector of utility function parameters that are assumed to be specific for context r , τ_k^r : vector of context-specific explanatory variables for alternative k within context r , μ : utility function scale for alternative k in context 2. For the sake of simplicity, the context superscript is not written; μ : is the ratio of the context 2 scale to the constant scale 1 for alternative k with unidentifiable absolute values for each of these scales.

The systematic baseline utility for each activity in the two contexts considering the definitions above is as follows:

$$\psi_k^1 = \exp(\sigma^{1T} \tau_k^1 + \zeta^T s_k^1 + \varepsilon_k^1) \quad (8)$$

$$\psi_k^2 = \exp(\sigma^{2T} \tau_k^2 + \zeta^T s_k^2 + \varepsilon_k^2) \quad (9)$$

Therefore, the systematic utility function for each person in each context is as follows:

$$U^1(x) = \sum_{k=1}^K \gamma_k^1 \psi_k^1 \ln \left(\frac{x_k}{\gamma_k^1} + 1 \right) \\ = \sum_{k=1}^K \gamma_k^1 \exp(\sigma^{1T} \tau_k^1 + \zeta^T s_k^1 + \varepsilon_k^1) \ln \left(\frac{x_k}{\gamma_k^1} + 1 \right) \quad (10)$$

$$U^2(x) = \sum_{k=1}^K \gamma_k^2 \psi_k^2 \ln \left(\frac{x_k}{\gamma_k^2} + 1 \right) \\ = \sum_{k=1}^K \gamma_k^2 \exp(\sigma^{2T} \tau_k^2 + \zeta^T s_k^2 + \varepsilon_k^2) \ln \left(\frac{x_k}{\gamma_k^2} + 1 \right) \quad (11)$$

The MDCEV model assumes that the unobserved effects are Independently and Identically Distributed (IID) across different alternatives (Bhat, 2008). The combined transfer estimation method assumes that random terms have IID properties within each of the datasets. Nevertheless, no general reason is to

assume that ε_k^1 and ε_k^2 have an identical distribution, or to be more specific, have equal variances, as the effect of unobserved factors may be different for the two datasets. To equalize the variances of ε_k^1 and ε_k^2 , the utility functions in the second context are scaled by μ (Badoe and Miller, 1995):

$$\mu^2 = \frac{\text{var}(\varepsilon_1)}{\text{var}(\varepsilon_2)} \quad (12)$$

If the random components in each dataset follow the IID Gumbel distribution, and the second context's baseline utility is powered by μ , the combined data follows the IID Gumbel distribution (Karasmaa, 2003). Thus, the application context's baseline utility function will be:

$$(\psi_k^2)^\mu = [\exp(\sigma^{2T} \tau_k^2 + \zeta^T s_k^2 + \varepsilon_k^2)]^\mu \\ = \exp(\mu \sigma^{2T} \tau_k^2 + \mu \zeta^T s_k^2 + \varepsilon_k^1) \quad (13)$$

It is now possible to estimate the model using both contexts' merged data as the error terms variance in both contexts are equal (Train, 2009). Here $\mu = e^{\delta D}$, where D : is a dummy variable equal to one, if the observation belongs to the application context and zero otherwise. Thus, μ : equals to one for the estimation context and e^δ for the application context. This exponential form also guarantees the positivity of the utility function scale. Table 2 summarizes the assumptions made in each of the above transfer methods. As can be seen, the joint context estimation method is a more generic method than the others since it relaxes the transferability of the model specification assumption in addition to model coefficients transferability assumption relaxation of others.

2.3. Transferability Metrics

An empirical assessment of transferability is essential to evaluate the performance of the transferred models. This study implicitly assumes that the underlying

behavioral assertion and mathematical model structure are transferable. The appropriate transferability metrics considering this assumption are presented in Table 3 (Sikder et al., 2013). The first measure, the t-test of individual parameters, shows whether the model is transferrable without any modifications between the two contexts. Next, the transferability test statistic is a log-likelihood-based test used to examine whether the transferred model's predictions are equal to the locally estimated model's predictions in the application context. The other log-likelihood-based measures are ρ_T^2 and Transfer index. The ρ_T^2 describes the goodness-of-fit of the transferred model in

the application context, relative to a reference model such as a constants-only model (Atherton and Ben-Akiva, 1976; Abdelwahab, 1991).

The transfer index measures the transferred model's goodness-of-fit relative to the same model specification estimated in the application context (Koppelman and Wilmot, 1982). Among the aggregate-level prediction metrics, the relative error measure compares the estimated and observed share of selected choices (Koppelman and Wilmot, 1982). The Root-mean-square error measures a weighted average of the relative error measure based on each choice's observation share (Abdelwahab, 1991).

Table 2. Comparison between the assumptions of transfer methods

Transfer method	Transferability			
	Behavioural	Mathematical	Specifications	Coefficients
Naïve transfer	✓	✓	✓	✓
Adjusting constant terms	✓	✓	✓	
Estimating new constants and scale	✓	✓	✓	
Estimating the application context model	✓	✓		
Bayesian updating	✓	✓	✓	
Combined transfer estimation	✓	✓	✓	
Joint context estimation	✓	✓		

Table 3. Summary of transferability assessment metrics

Test type	Test name	Expression
Statistical test of equivalence of individual parameter parameters	t-tests of Individual Parameter Equivalence	$\frac{(\beta_i) - (\beta_j)}{\sqrt{SE(\beta_i)^2 + SE(\beta_j)^2}}$
Statistical test of equivalence of parameters	Transferability Test Statistic (TTS)	$-2[LL_i(\beta_j) - LL_i(\beta_i)]$
Measure of disaggregate-level predictive ability	Transfer rho-square (ρ_T^2)	$1 - \frac{LL_i(\beta_j)}{LL_i(C_i)}$
	Transfer Index (TI)	$\frac{LL_i(\beta_j) - LL_i(C_i)}{LL_i(\beta_i) - LL_i(C_i)}$
	Relative Error Measure (REM)	$(PS_k - OS_k)/OS_k$
Measure of aggregate-level predictive ability	Root-Mean-Square Error (RMSE)	$(\sum_k PS_k \times REM_k^2)^{1/2}$
	Relative Aggregate Transfer Error (RATE)	$\frac{RMSE_i(\beta_j)}{RMSE_i(\beta_i)}$
	Aggregate Prediction Statistic (APS)	$\sum_k \frac{(PS_k - OS_k)^2}{PS_k}$

Notation: LL : stands for log-likelihood value, and β : for a vector of parameters, while i, j : are subscripts for locally estimated and transferred models, respectively. $LL_i(\beta_i)$: is log-likelihood of the local model applied to application context data, $LL_i(\beta_j)$: is log-likelihood of the transferred model applied to application context data, $LL_i(C_i)$: log-likelihood of a constants only model for application context data, OS_k and PS_k : are the observed and predicted shares, respectively, for alternative k .

The relative aggregate transfer error is used to determine the transferred model's aggregate-level predictive performance relative to a model estimated using the application context data (Abdelwahab, 1991; Koppelman and Wilmot, 1982). Finally, the aggregate prediction statistic tests the null hypothesis, where the observed alternative shares are generated by the transferred model in the application context (Abdelwahab, 1991). A more detailed discussion of the pros and cons of different assessment metrics are made elsewhere (Sikder and Pinjari, 2013).

3. Data

This study's data sources are extracted from the comprehensive transportation master plans of Mashhad, Iran (1994) as the application context and Shiraz, Iran (1999) as the estimation context. The selection of this dataset was primarily due to the following reasons:

- The same research team conducted both studies and implemented quite similar data collection methods;
- The entire data with tens of thousands of observations were available to the authors, thus allowing for testing the out-of-sample predictive power of the transferred model without data limitations;
- A wide range of context data sample sizes, from 1 to 50 percent, was available to evaluate the transferred model's performance sensitivity; and
- Methodological evaluation of the MDCEV model transferability, the primary purpose and contribution of the current study, is regardless of the data collection date.

The surveys collected detailed information on all out-of-home activities undertaken by the respondents. At the time, Mashhad and Shiraz, respectively, had almost 1.8 and 1.2 million inhabitants.

The sample sizes were 73,304 (4.1 percent of the population) in Mashhad and 51,212 (4.3 percent of the population) in

Shiraz. These studies did not collect the activities of children younger than six years of age. Further, respondents residing out of the city limits were omitted from the database. This yields to 61,036 individuals in Mashhad and 42,969 individuals in Shiraz. The activities of the respondents were classified into ten groups as follows: 1) In-home, 2) Work, 3) Education, 4) Shopping, 5) Personal business, 6) Health care, 7) Visiting relatives, 8) Recreation, 9) Travel, and 10) Other activities.

Table 4 summarizes several statistics on the demographics, activity participation, and time allocation patterns in each region. Figure 1 illustrates the cumulative time allocations for each of the ten activity types among individuals from both contexts based on their gender. Each point represents the percentage of individuals who participated in the activity more than the point's duration. For example, in part (a) of this figure, 37 percent of males and 68 percent of Shiraz females spent more than 1,200 minutes on in-home activities.

4. Results and Discussions

4.1. Original Models

In the first analysis step, two MDCEV activity patterns (type and duration) models are estimated for Shiraz and Mashhad, with 80 percent of the individuals randomly selected from each dataset. The 20 percent remaining observations of each city were reserved to determine the transferred models' out-of-sample prediction accuracy. The estimating and evaluation of the MDCEV model and later transferring the models is implemented in the STATA software (StataCorp, 2015, Stata Statistical Software: Release 14, College Station, TX: StataCorp LP). While complete model estimation results are provided in the appendix (Tables A1 and A2), Table 5 summarizes these results. These results indicate that the models' performance in their estimation region is comparable. The takeaway from the coefficient estimates, which can be justified by looking at the

Tables A1 and A2 of the appendix, is that individual and household characteristics have rational signs and are similar in both models. For instance, senior citizens tend to participate more in healthcare and in-home activities than younger people, and individuals in smaller families spend more time shopping. The same happens with the geographical zones' specifications. As the proportion of commercial areas in the residence zone increases, individuals tend to participate more in shopping activities. The detailed results of performing t-tests between individual models' parameters are presented in the appendix (Table A3). This test revealed that almost 80 percent of the coefficients are statistically different across the two contexts. Thus, each of the models can hardly be used in another context. However, using a context's model in another context does not necessarily result

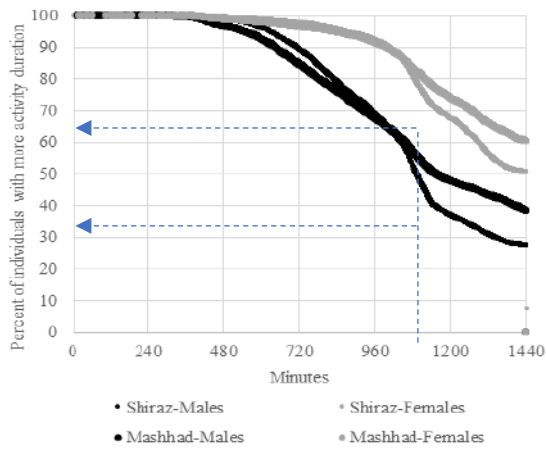
in wrong predictions since a combination of various parameters determines the model's prediction accuracy.

4.2. Transferred Models Assessment Metrics

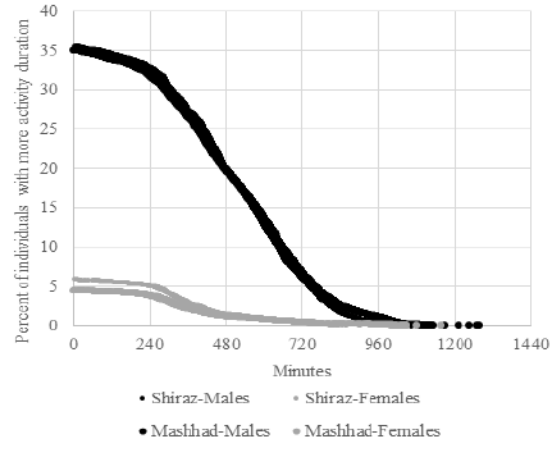
This section presents the results of applying the introduced model transfer methods on the estimated models. Different sample sizes (1, 5, 10, 20, 30, 40, and 50 percent of the entire data) are drawn with replacement to determine the effect of the application context's sample size on the transferred models' prediction accuracy. For each size category, five subsamples are drawn, leading to 35 different subsamples. For each subsample, all the transfer methods are performed along with calculating the transferability assessment metrics.

Table 4. Descriptive statistics of demographics, activity type and duration

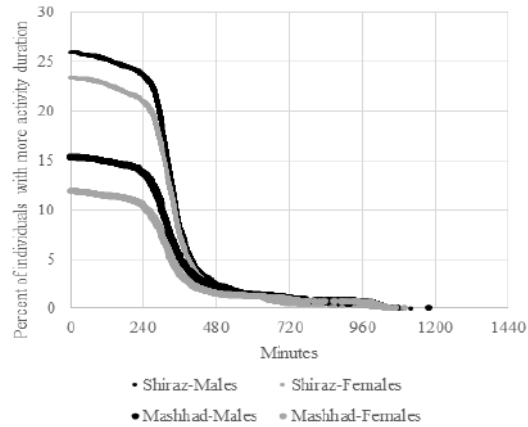
City	Mashhad	Shiraz		
Sample size	61,036	42,969		
Number of TAZs	141	156		
Socio-demographic characteristics				
Male	52.0%	51.1%		
Age: 6 - 12 years	26.9%	17.5%		
Age: 13 - 18 years	21.3%	23.7%		
Age: 19 - 24 years	9.4%	13.1%		
Age: 25 - 35 years	17.2%	17.2%		
Age: 36 - 45 years	13.8%	16.1%		
Age: 46 - 60 years	8.7%	9.6%		
Age: > 60 years	2.7%	2.8%		
Clerk, Teacher, Army	9.2%	11.0%		
Labour, Farmer, Workman	8.9%	6.6%		
Driver	1.7%	1.9%		
Seller	4.5%	5.5%		
Student	45.6%	44.2%		
Unemployed	27.8%	28.6%		
Average household size	4.98	4.00		
Bikes per capita	0.09	0.07		
Motorcycles per capita	0.06	0.04		
Cars per capita	0.06	0.10		
Pickups per capita	0.01	0.01		
Aggregate activity participation (% who participated) and average activity duration (among those who participated)				
Activity types	Participated (%)	Duration (min)	Participated (%)	Duration (min)
In-home activities	100	1208	100	1179
Work	20.3	515	21.3	502
Education	13.7	371	24.7	350
Shopping	7.3	123	9.4	129
Personal business	1.2	154	2.0	154
Healthcare	1.9	148	2.8	164
Visiting relatives	8.9	199	7.0	200
Recreation	5.5	142	3.3	152
Travel	46.3	68	60.9	36
Other	6.1	106	3.5	178



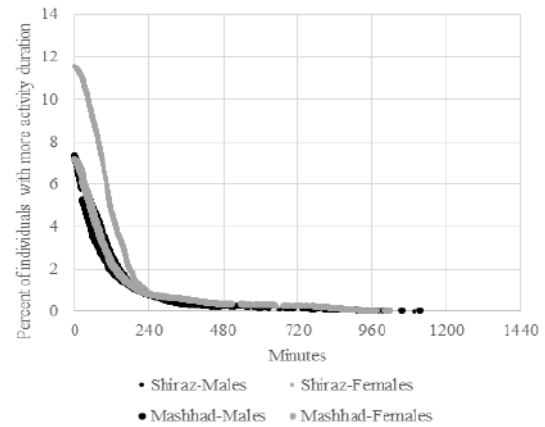
(a) In-home



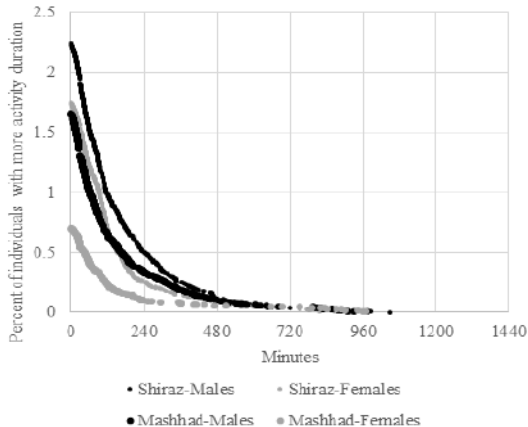
(b) Work



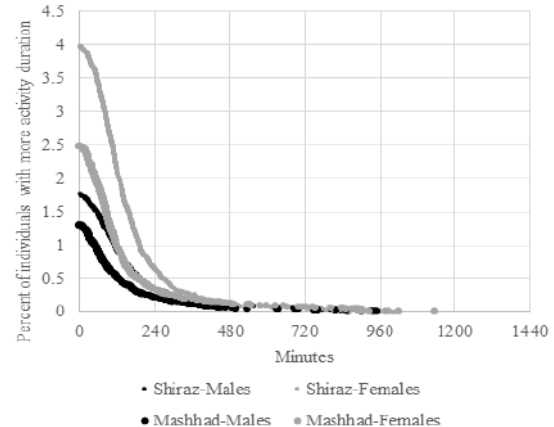
(c) Education



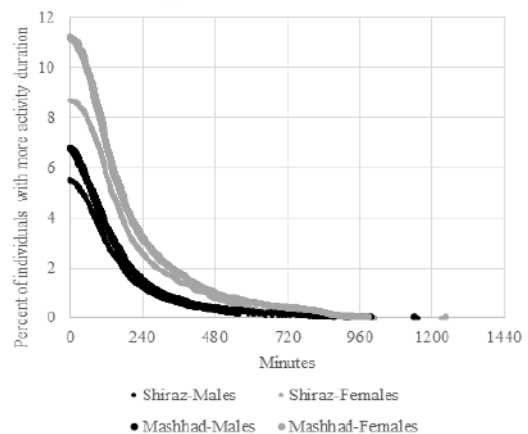
(d) Shopping



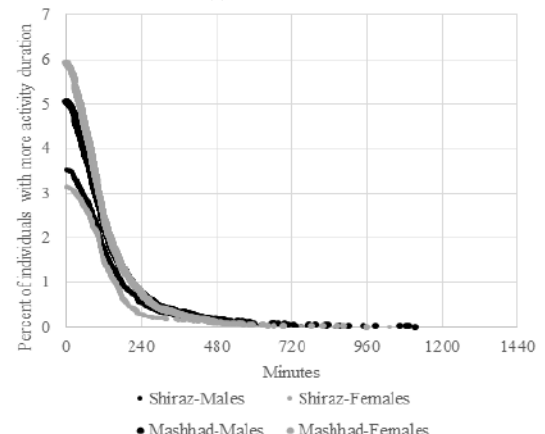
(e) Personal business



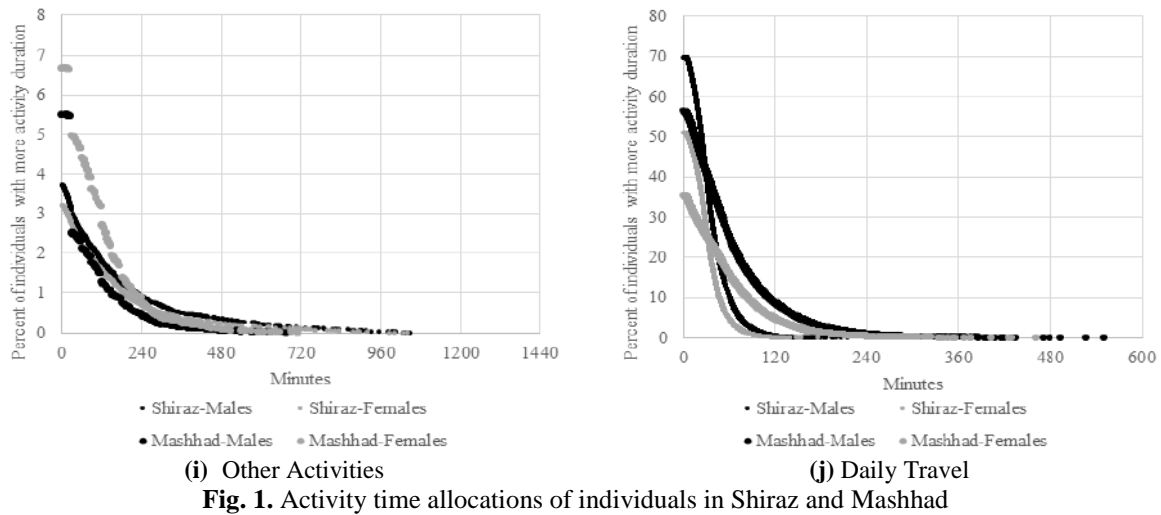
(f) Healthcare



(g) Visiting Family/Friends



(h) Entertainment/Religious

**Table 5.** Summary of model estimation results

Context	Shiraz	Mashhad
Number of observations used in model estimation	34,469	49,036
Log-likelihood value (in convergence)	-8,422,053	-10,878,470
Log-likelihood value (constants-only model)	-9,006,066	-11,621,623
ρ^2	%6.48	%6.40
Run time (hours)	27.20	43.85

The detailed results of the transferability assessment metrics are presented in the appendix (Table A4). However, the distribution of selected transferability assessment metrics for each sample size and transfer method is presented in Figures 2 to 5. As expected, the larger the application context's sample size, the better the transferred model's prediction performance. Likewise, switching from simple transfer methods to more advanced techniques result in better prediction performance of the transferred model.

The Transferability Test Statistic (TTS) assessment metric results are presented in Table A4 of the appendix. The critical value for χ^2 distribution with degrees of freedom equal to the number of model parameters is 242.767. The numbers illustrate that transferred model parameters are statistically equal to the application context model parameters in higher sample sizes for the Bayesian updating, *combined transfer estimation*, and joint context estimation methods.

The locally estimated model in Mashhad using the entire data has ρ^2 -Transferred equal to 6.00 percent. None of the transfer scaling methods obtain this value in any

sample size. While Bayesian updating reaches this value in a 50 percent sample size, the combined transfer estimation method achieves this value in a 40 percent sample size. The critical point is that the joint context estimation method reaches a higher value than 6.00 percent in 20 percent of the application context sample size. Thus, the joint context estimation method outperforms other methods in fitting application context data relative to a reference model.

Transfer Index (TI) measures the goodness-of-fit of a transferred model with respect to a similar model specification in the application context. Based on the TI values, only joint context estimation in 20 percent and combined transfer estimation in 30 percent of the sample size reach that of the Mashhad model.

Root-Mean-Square Error (RMSE) and Relative Aggregate Transfer Error (RATE) show that estimating the application context model and Bayesian updating methods exceed the Mashhad model's values in a 40 percent sample size. Therefore, using data from two regions with somehow similar characteristics improves the model's predictive power. The joint context

estimation reaches the local model's value in RMSE and RATE measures, with a 30 percent sample size. These measures show that the joint context estimation method outperforms other methods in aggregate-level prediction performance of the transferred model, expectedly. The detailed average values of transferability assessment metrics calculated over the 20 percent reserved data for each transfer method are accessible in the appendix.

4.3. Transferred Models Forecasting Power

Since travel behavior models are mainly used for forecasting and policy analysis, comparing the model results under different scenarios is highly recommended (Sikder

and Pinjari, 2013). In this study, a hypothetical scenario is assumed to increase each individual's age by ten years and a 50 percent increase in car ownership. Table 6 illustrates the prediction of aggregate time allocation to each activity type for the locally estimated model using the complete sample and the transferred models with a 10 percent sample size. The results show that the closest predictions to the local model result from a joint context estimation method indicating this method's superiority to other methods. Combined transfer estimation, Bayesian updating, and estimating the application context model methods also provided close aggregate predictions to the local model.

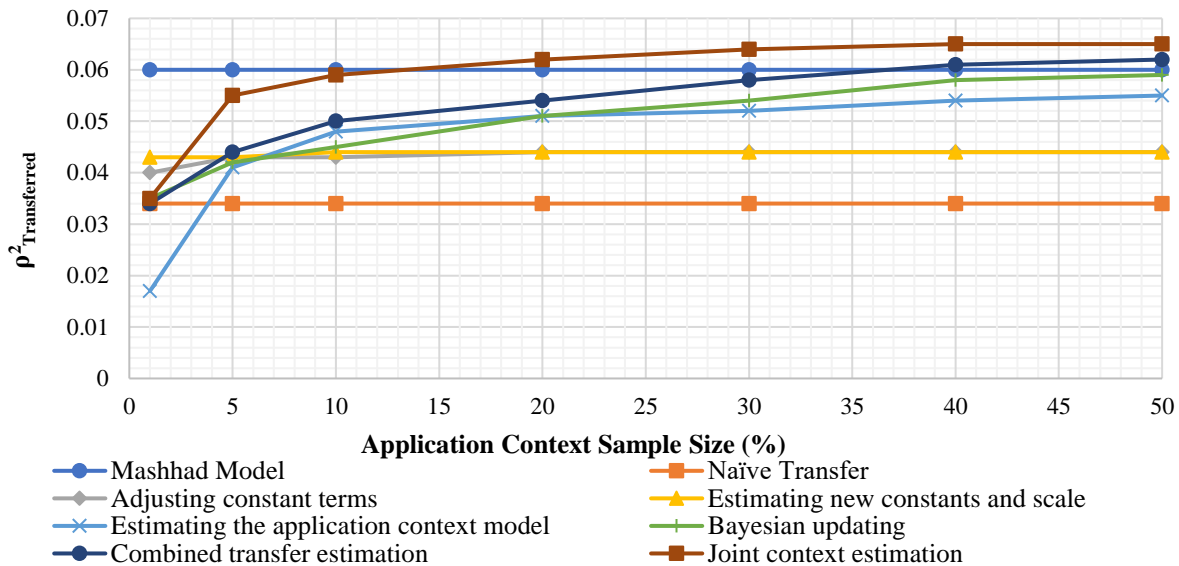


Fig. 2. $\rho^2_{\text{Transferred}}$ of each transfer method against application context sample sizes

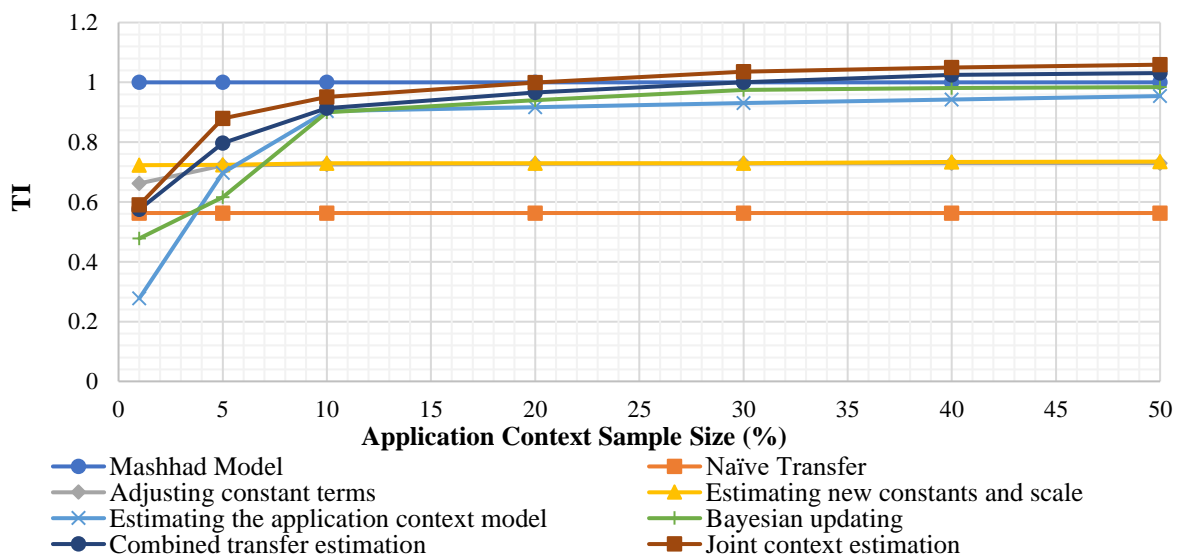


Fig. 3. Transfer Index of each transfer method against application context sample sizes

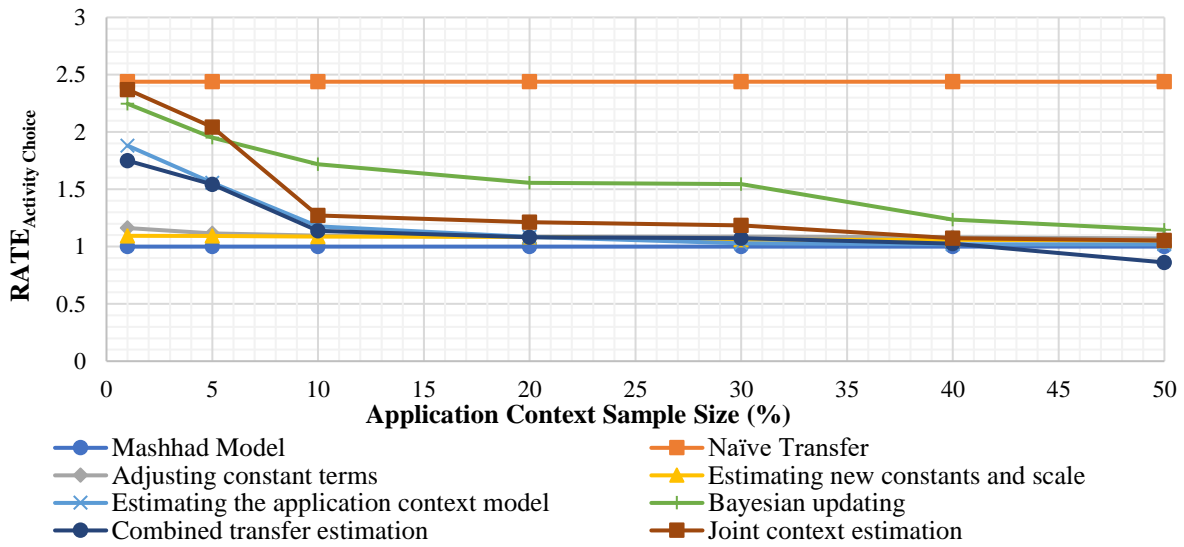


Fig. 4. RATE index of activity choices of each transfer method against application context sample sizes

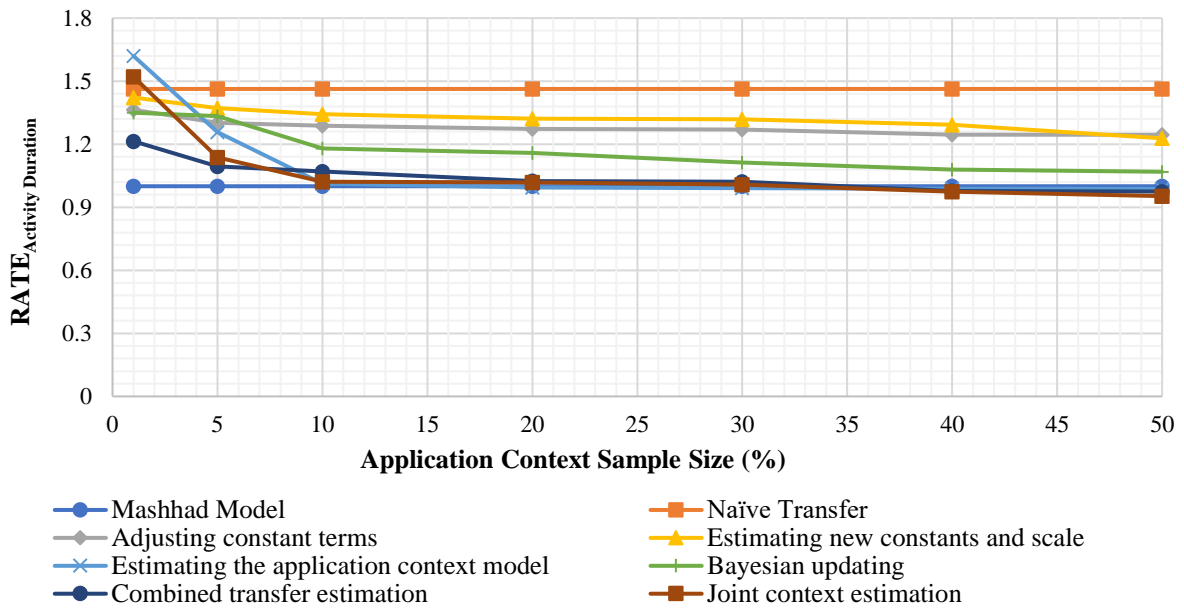


Fig. 5. RATE index of activity durations of each transfer method against application context sample sizes

Table 6. Activity time (min) allocation in local versus transferred models for a hypothetical scenario*

Model	In-home	Work	Education	Shopping	Personal business	Health care	Visiting relatives	Recreation	Travel	Other
Mashhad model (100% sample size)	1074	111	44	23	9	12	23	18	16	54
Naïve transfer	1220	80	37	9	7	8	10	10	13	44
Adjusting constants	1197	83	44	10	7	10	10	10	14	40
Estimating new constants and scale	1123	89	50	12	7	10	26	17	15	33
Estimating the Application context model	1135	160	27	10	8	9	14	17	12	41
Bayesian updating	1113	129	30	14	7	9	18	15	13	40
Combined transfer estimation	1109	132	39	14	7	8	21	17	13	42
Joint context estimation	1102	107	47	18	8	11	21	17	15	45

* 10 years increase in age and 50 percent increase in car ownership

Table 7 provides sample size effects on the joint context estimation method's predictions in the same previous scenario. The larger the estimation context sample, the closer are the predictions to the locally estimated model. The average absolute difference between the local and the transferred model outputs was 3.6 percent for the 50 percent sample, 4.3 percent for the 40 percent sample, 5.5 percent for the 30 percent sample, 6.8 percent for the 20 percent sample, 8.9 percent for the 10 percent sample, 15.0 percent for the 5 percent sample, and 29.8 percent for the 1 percent sample. According to the results, the prediction accuracy improvement rate starts diminishing when the sample size passes the 10 percent value. For the 10 percent sample, however, the average absolute difference between the local and the transferred model outputs was 2.6 percent for in-home, 3.7 percent for work, 5.0 percent for education, 5.6 percent for travel, 5.8 percent for recreation, 6.3 percent for visiting relatives, 8.8 percent for personal business, 17.7 percent for other, and 22.5 percent for shopping. Mandatory activities, understandably, are more convenient to transfer than irregular activities. Another observation is that as the sample size increases, predicted activity durations also increase, except for in-home activity. In other words, all the activity durations are underestimated in small samples, except for in-home activity.

5. Summary and Conclusions

This paper presented an empirical assessment of the spatial transferability of MDCEV models for activity type and duration in two major cities of Iran, Shiraz and Mashhad. The transfer methods used were transfer scaling, Bayesian updating, combined transfer estimation, and joint context estimation. Then, transferability assessment metrics were presented for each approach. Transferability was evaluated using log-likelihood-based measures and aggregate and disaggregate predictability of

the transferred model. The policy predictability of the models was also evaluated and discussed for a hypothetical policy.

The results shed light on the prediction properties of the transferred MDCEV model using different transfer methods and different sample sizes of the application context data. The findings of this study are as follows:

First, joint context estimation and combined transfer estimation are the most appropriate transfer methods if limited data from the application context is available. Nonetheless, the combined transfer estimation provided closer outputs for the presented scenario compared to the local model. Second, although the increase in application context data improves the transfer model's predictability, a sample size of 10 percent of the application context data provides encouraging results. Third, combined transfer estimation had encouraging policy predictability when a hypothetical scenario was tested on age and car ownership increase. Therefore, the transferred model can have a comparable prediction to the locally estimated model for policy analysis and forecast. Besides, an appropriate model transfer can significantly reduce the costs of conducting household travel surveys, shorten the time interval between transportation studies in a given city, and result in more accurate travel behavior models. However, determining the proper application sample size depends on the data collection costs and the desired performance level. This research and other similar studies could lead to the accumulation of empirical evidence in transferring travel demand models and provide a picture of sample size and accuracy trade-offs.

The current study can be extended in several ways:

Table 7. Activity time (min) allocation for different sample sizes in a hypothetical scenario*

Model	Sample size (%)	In-home	Work	Education	Shopping	Personal business	Health care	Visiting relatives	Recreation	Travel	Other
Mashhad model	100	1074	111	44	23	9	12	23	18	16	54
	1	1187	79	38	11	6	8	14	11	11	43
	5	1119	86	43	17	7	9	21	15	14	44
Joint context estimation	10	1102	107	47	18	8	11	21	17	15	45
	20	1087	107	47	18	8	11	22	18	15	48
	30	1078	110	47	18	8	11	22	18	15	48
	40	1075	111	47	19	8	12	22	18	16	48
	50	1072	111	47	19	8	12	23	18	16	49

* 10 years increase in age and 50 percent increase in car ownership

- The cities considered in this study have almost the same demographics. An interesting approach could be transferring an estimated model from a large city to a small city since small cities have a more limited budget to conduct comprehensive travel surveys and can greatly benefit from transferring models to their jurisdictions.
- Other model specifications in the MDCEV family should be specifically investigated since more evidence is required for generalization of this study's findings to other modeling specifications, data sources, or contexts.
- The scale of the random utility components was presumed to be similar across both contexts.
- Scale differences across both regions can potentially shed more light on model transferability.
- Although segmentation of the data by individual characteristics can benefit, this study did not consider such a procedure since the aim here is to analyze the transferability of the MDCEV model as a whole package considering different transfer methods and sample sizes. A future study can investigate the impacts of data segmentation and exploration of each segment's activity type and time allocation similarities and dissimilarities.

6. References

Abdelwahab, W.M. (1991). "Transferability of intercity disaggregate mode choice models in

Canada", *Canadian Journal of Civil Engineering*, 18(1), 20-26.

Arentze, T., Hofman, F., Van Mourik, H. and Timmermans, H. (2002). "Spatial transferability of the Albatross model system: Empirical evidence from two case studies", *Transportation Research Record*, 1805, 1-7.

Atherton, T.J. and Ben-Akiva, M.E. (1976). "Transferability and updating of disaggregate travel demand models", *Transportation Research Record*, 610, 12-18.

Badoe, D.A. and Miller, E.J. (1995). "Comparison of alternative methods for updating disaggregate logit mode choice models", *Transportation Research Record*, 1493, 90-100.

Barkhordari, K. and Entezari Zarch, H. (2015). "Prediction of permanent earthquake-induced deformation in earth dams and embankments using artificial neural networks", *Civil Engineering Infrastructures Journal*, 48(2), 271-283.

Ben-Akiva, M. and Morikawa, T. (1990). "Estimation of switching models from revealed preferences and stated intentions", *Transportation Research Part A: General*, 24(6), 485-495.

Bhat, C.R. (2008). "The multiple discrete-continuous extreme value (MDCEV) model: Role of utility function parameters, identification considerations, and model extensions", *Transportation Research Part B: Methodological*, 42(3), 274-303.

Bhat, C.R. (2018). "A new flexible multiple discrete-continuous extreme value (MDCEV) choice model", *Transportation Research Part B: Methodological*, 110, 261-279.

Bowman, J.L. and Bradley, M. (2017). "Testing spatial transferability of activity-based travel forecasting models", *Transportation Research Record*, 2669(1), 62-71.

Bowman, J.L., Bradley, M., Castiglione, J. and Yoder, S.L. (2014). "Making advanced travel forecasting models affordable through model transferability", In: *Preseted at the 93rd Annual Meeting of Transportation Research Board*, Washington, DC.

- Karasmaa, N. (2003). "The transferability of travel demand models: An analysis of transfer methods, data quality and model estimation", Ph.D. Thesis, Helsinki University of Technology.
- Karimae Tabarestani, M. and Zarrati, A.R. (2015). "Design of riprap stone around bridge piers using empirical and neural network method", *Civil Engineering Infrastructures Journal*, 48(1), 175-188.
- Koppelman, F.S. and Wilmot, C.G. (1982). "Transferability analysis of disaggregate choice models", *Transportation Research Record*, 895, 18-24.
- Lefebvre-Ropars, G., Morency, C., Singleton, P.A. and Clifton, K.J. (2017). "Spatial transferability assessment of a composite walkability index: The pedestrian index of the environment (PIE)", *Transportation Research Part D: Transport and Environment*, 57, 378-391.
- Linh, H.T., Adnan, M., Ectors, W., Kochan, B., Bellemans, T. and Tuan, V.A. (2019). "Exploring the spatial transferability of FEATHERS, An activity based travel demand model for Ho Chi Minh City, Vietnam", *Procedia Computer Science*, 151, 226-233.
- Mondal, A. and Bhat, C.R. (2021). "A new closed form multiple discrete-continuous extreme value (MDCEV) choice model with multiple linear constraints", *Transportation Research Part B: Methodological*, 147, 42-66.
- Nohekhan, A., Zahedian, S. and Haghani, A. (2021). *A deep learning model for off-ramp hourly traffic volume estimation*, *Transportation Research Record*, 03611981211027151.
- Nowrouzian, R. and Srinivasan, S. (2012). "Empirical analysis of spatial transferability of tour-generation models", *Transportation Research Record: Journal of the Transportation Research Board*, (2302), 14-22.
- Pinjari, A.R. and Bhat, C. (2010). "An efficient forecasting procedure for Kuhn-Tucker consumer demand model systems", Technical Paper, Department of Civil and Environmental Engineering, University of South Florida.
- Rossi, T.F. and Bhat, C.R. (2014). *Guide for travel model transfer*, Report No. FHWA-HEP-15-006, Federal Highway Administration: Washington, DC, USA.
- Salem, S. and Nurul Habib, K.M. (2015). "Use of repeated cross-sectional travel surveys to develop a meta model of activity-travel generation process models: Accounting for changing preference in time expenditure choices", *Transportmetrica A: Transport Science*, 11(8), 729-749.
- Shabanpour, R., Golshani, N., Stephens, T.S., Auld, J. and Mohammadian, A. (2019). "Developing a spatial transferability platform to analyze national-level impacts of connected automated vehicles", In: *The Practice of Spatial Analysis*, pp. 253-272, Springer, Cham.
- Shamshiripour, A. and Samimi, A. (2019). "Estimating a mixed-profile MDCEV: Case of daily activity type and duration", *Transportation Letters*, 11(6), 289-302.
- Sikder, S. and Pinjari, A. (2013). "Spatial transferability of person-level daily activity generation and time use models: Empirical assessment", *Transportation Research Record: Journal of the Transportation Research Board*, (2343), 95-104.
- Sikder, S., Pinjari, A.R., Srinivasan, S. and Nowrouzian, R. (2013). "Spatial transferability of travel forecasting models: A review and synthesis", *International Journal of Advances in Engineering Sciences and Applied Mathematics*, 5(2-3), 104-128.
- Tang, L., Xiong, C. and Zhang, L. (2018). "Spatial transferability of neural network models in travel demand modeling", *Journal of Computing in Civil Engineering*, 32(3), 04018010.
- Train, K.E. (2009). *Discrete choice methods with simulation*, Cambridge University Press.
- Wafa, Z., Bhat, C.R., Pendyala, R.M. and Garikapati, V.M. (2015). "Latent-segmentation-based approach to investigating spatial transferability of activity-travel models", *Transportation Research Record: Journal of the Transportation Research Board*, (2493), 136-144.
- Xiong, C., Yang, D., Ma, J., Chen, X. and Zhang, L. (2020). "Measuring and enhancing the transferability of hidden Markov models for dynamic travel behavioral analysis", *Transportation*, 47(2), 585-605.
- Yasmin, F., Morency, C. and Roorda, M.J. (2015). "Assessment of spatial transferability of an activity-based model, TASHA", *Transportation Research Part A: Policy and Practice*, 78, 200-213.
- Zahedian, S., Sekuła, P., Nohekhan, A. and Vander Laan, Z. (2020). "Estimating hourly traffic volumes using artificial neural network with additional inputs from automatic traffic recorders", *Transportation Research Record*, 2674(3), 272-282.
- Ziemke, D., Nagel, K. and Bhat, C. (2015). "Integrating CEMDAP and MATSim to increase the transferability of transport demand models", *Transportation Research Record*, 2493(1), 117-125.



This article is an open-access article distributed under the terms and conditions of the Creative Commons Attribution (CC-BY) license.

Appendix

Table A1. MDCEV model results for Shiraz

Variable	Activity type									
	In-home	Work	Education	Shopping	Personal business	Health care	Visiting relatives	Recreation	Travel	Other
Constant	4.938	-1.894	-6.446	-3.815	-3.981	-5.841	-3.753	-3.977		-4.440
	323.26	-73.43	-30.09	-126.65	-79.91	-109.51	-123.07	-91.37		-101.62
Individual Characteristics										
Age 6 - 12 years	1.653	-4.048	6.246	-0.189	-2.500	-0.504	0.243	0.840	0.563	
	32.43	-40.66	28.46	-3.15	-21.18	-6.40	4.32	12.84	10.91	
Age 13 - 18 years	0.226	-1.758	5.545	-0.514	-1.674	-1.013	-0.469	0.390	0.110	
	5.68	-39.23	25.53	-11.16	-27.19	-16.92	-10.62	7.43	2.72	
Age 19 - 24 years	-0.565	-0.643	3.895	-0.695	-1.007	-1.002	-0.700	-0.379	-0.621	
	-15.68	-16.37	17.98	-17.34	-19.78	-21.01	-17.30	-8.08	-16.93	
Age 25 - 35 years	-0.548	-0.292	2.853	-0.226	-0.806	-0.717	-0.575	-0.305	-0.438	
	-16.00	-7.87	13.17	-5.98	-16.93	-16.11	-15.04	-6.82	-12.58	
Age 36 - 45 years	-0.570	-0.257	1.737	-0.043	-0.831	-0.660	-0.623	-0.508	-0.331	
	-16.7	-6.81	7.93	-1.13	-17.08	-14.63	-15.99	-10.99	-9.35	
Age 46 - 60 years	-0.700	-0.423	0.704	-0.275	-0.846	-0.622	-0.693	-0.666	-0.410	
	-20.18	-11.22	3.11	-7.23	-17.59	-13.93	-17.89	-14.52	-11.60	
Female	0.545	-0.232	0.517	0.331	-0.154	0.877	0.437	-0.219	0.257	
	35.00	-13.39	31.85	18.39	-6.08	36.65	23.49	-10.28	16.32	
White-collar worker	-0.134	1.419	-2.487	0.113	0.066	0.021		-0.292	0.039	
	-7.57	66.78	-75.28	4.32	1.99	0.49		-8.31	2.17	
Blue-collar worker	0.322	2.087	-3.556	0.336		0.376	0.241	-0.088	0.560	
	12.45	73.64	-59.38	9.82		6.95	7.43	-1.98	21.39	
Driver	-0.209	0.883	-2.948	-0.708	-0.570	0.414	0.074	-0.847	-0.339	
	-5.51	21.95	-32.24	-13.31	-8.49	6.17	1.62	-11.61	-8.80	
Seller	0.198	1.666	-4.257	0.155	-0.235	0.142	-0.027	-0.324	0.258	
	6.91	53.72	-42.77	4.26	-5.01	2.51	-0.80	-6.79	8.88	
Student	-0.353	-1.722	-0.091	0.037	0.268	0.165	-0.368	0.222	-0.350	
	-12.30	-47.19	-3.02	1.00	5.95	3.14	-10.51	5.35	-12.02	
Unemployed	-0.126	-2.242	-3.144	0.759	-0.054	0.595	0.570	0.493	-1.163	
	-5.85	-83.21	-112.86	27.29	-1.54	14.36	26.31	15.09	-52.90	
Household characteristics										
Household size	0.116	0.046	0.004	-0.007	0.052	0.052	-0.040	0.022	-0.009	
	34.65	12.89	1.09	-1.77	9.82	10.75	-9.84	4.57	-2.66	
Living in CBD	-0.073	-0.140	-0.291	-0.365	-0.141	-0.411	0.039	-0.006	-0.335	
	-3.60	-6.53	-13.34	-14.86	-3.99	-12.98	1.68	-0.22	-16.60	
Bike capita	-0.300	-0.147	0.212	0.424		-0.060	0.259	-0.123	0.229	
	-7.78	-3.45	4.93	9.29		-0.93	5.38	-2.03	5.85	
Motorcycle capita	0.559	0.878	0.454	0.632	0.232	0.086	0.790	0.295	0.490	
	8.66	13.00	6.45	8.79	2.27	0.91	10.69	3.32	7.51	
Car capita	-1.051	-0.525	-0.138	-0.955	-1.113	-0.894	-0.358	-0.585	-0.680	
	-27.94	-12.96	-3.26	-21.92	-17.08	-15.63	-8.01	-10.61	-17.87	
Pickup capita	-0.076	-0.075			-0.429		0.702		-0.159	-0.476
	-1.65	-1.11			-2.50		8.83		-3.18	-3.62
Presence of child below 12 years	-0.089	-0.090		-0.076	0.003	-0.125	-0.016	-0.161	-0.052	
	-14.85	-11.23		-7.85	0.20	-8.04	-1.49	-10.99	-8.26	
Residing TAZ characteristics										
Recreation land use share	0.008							-0.321		
	0.64							-5.53		
Commercial land use share	-0.366			3.824						
	-2.82			12.99						
Land use Diversity Index	0.018	0.023	0.033	0.018	0.031	0.469	-0.294	-0.269	-0.113	
	0.43	0.52	0.75	0.37	0.46	7.54	-5.90	-4.53	-2.67	
Translation parameter										
γ	0	266.742	193.187	87.839	111.725	137.603	167.914	131.103	118.559	9.117
	-	1106.63	120.93	791.74	359.07	461.62	749.86	491.72	463.52	830.78
Number of observations							34,469			
Log-likelihood value (in convergence)							-8,422,053.2			
Log-likelihood value (constants-only model)							-9,006,066.1			
ρ^2							6.48%			
Run time (hours)							27.20			

Table A2. MDCEV model results for Mashhad

Variable	Activity type									
	In-home	Work	Education	Shopping	Personal business	Health care	Visiting relatives	Recreation	Travel	Other
Constant	4.839	-1.999	-4.275	-3.163	-4.015	-5.644	-3.714	-3.298		-3.325
	358.93	-91.72	-51.27	-121.16	-72.06	-109.08	-152.57	-120.61		-131.98
Individual characteristics										
Age 6 - 12 years	2.739	-1.299	4.180	0.649	-1.553	0.928	1.456	0.546	0.540	
	108.78	-31.57	48.83	18.98	-13.49	16.95	47.31	16.01	20.53	
Age 13 - 18 years	1.598	0.590	4.364	0.802	-0.748	0.701	0.967	0.736	0.985	
	73.73	22.24	51.55	27.44	-10.93	14.63	35.10	25.3	43.49	
Age 19 - 24 years	0.738	0.889	3.284	0.569	0.892	0.546	0.762	0.313	0.621	
	38.71	37.69	38.93	22.1	18.09	13.52	30.62	12.24	30.94	
Age 25 - 35 years	0.423	1.054	2.149	0.672	0.845	0.731	0.758	0.075	0.662	
	24.90	49.36	25.53	29.11	18.42	19.97	33.62	3.24	36.99	
Age 36 - 45 years	0.130	0.826	1.094	0.561	0.581	0.364	0.625	-0.111	0.550	
	7.51	38.05	12.67	23.82	12.36	9.65	27.12	-4.63	30.10	
Age 46 - 60 years	-0.016	0.595	0.249	0.253	0.487	0.015	0.348	-0.087	0.392	
	-0.96	27.53	2.70	10.87	10.63	0.40	15.25	-3.75	21.73	
Female	0.448	-0.643	0.218	-0.236	-0.996	0.377	0.376	-0.216	-0.124	
	41.93	-49.47	18.44	-16.75	-34.27	16.92	28.34	-14.89	-11.28	
White-collar worker	0.0356	1.514	-1.516	-0.06	0.173	0.334		-0.78	0.307	
	2.91	102.39	-68.17	-0.33	6.22	8.94		-12.42	24.01	
Blue-collar worker	0.120	1.869	-3.488	-0.003		0.681	0.018	-0.166	0.534	
	7.81	107.56	-84.75	-0.15		18.15	0.92	-7.03	33.71	
Driver	-0.050	0.856	-3.684	-0.594	-0.325	0.132	0.060	-0.722	-0.240	
	-1.87	29.87	-31.32	-15.07	-5.94	2.03	1.79	-15.70	-8.75	
Seller	0.227	1.649	-3.591	0.482	0.337	0.148	-0.001	-0.254	0.282	
	11.35	78.83	-51.52	18.98	9.72	2.95	-0.04	-8.4	13.81	
Student	-0.326	-1.054	0.234	-0.490	-0.276	-0.511	-0.435	-0.259	-0.031	
	-12.85	-33.22	8.58	-13.66	-5.18	-7.70	-13.42	-7.10	-1.19	
Unemployed	-0.569	-2.679	-3.798	-0.057	-0.414	0.261	-0.126	0.145	-1.285	
	-40.83	-131.67	-158.32	-2.94	-12.74	7.74	-8.28	7.27	-87.90	
Household characteristics										
Household size	0.075	0.013	-0.065	-0.025	0.003	-0.001	-0.083	0.005	-0.063	
	39.63	5.95	-27.89	-10.02	0.73	-0.15	-33.46	1.72	-31.64	
Living in CBD	-0.012	0.067	0.094	0.092	-0.368	0.128	0.359	-0.141	-0.103	-0.012
	-0.80	3.87	5.02	4.41	-8.58	4.31	19.58	-6.36	-6.49	-0.80
Bike capita	-0.636	-0.197	0.177	0.253		0.026	-0.244	0.265	0.093	
	-23.37	-6.31	5.22	7.09		0.45	-7.05	6.97	3.34	
Motorcycle capita	-0.533	-0.296	-0.808	0.008	-0.494	0.039	0.276	0.261	-0.782	
	-16.60	-8.19	-18.91	0.21	-6.23	0.63	7.20	6.06	-23.54	
Car capita	0.000	0.539	1.515	0.725	1.482	0.485	0.931	0.142	0.022	
	0.01	14.65	37.78	17.58	22.23	7.66	24.06	3.11	0.66	
Pickup Capita	-0.078	0.509			0.259		0.674		-0.024	-0.556
	-1.69	7.88			1.41		9.19		-0.27	-10.74
Presence of child below 12 years	-0.061	-0.024		0.026	0.107	0.027	0.058	-0.078	-0.005	
	-10.24	-3.09		2.62	5.04	1.55	6.21	-7.18	-0.85	
Residing TAZ characteristics										
Recreation land use share	-0.154							-0.063		
	-8.21							-1.24		
Commercial land use share	0.290			3.905						
	29.08			1.60						
Land use diversity index	-0.366	-0.526	-0.885	-0.479	-0.763	-1.284	-0.392	0.066	-0.488	
	-12.26	-16.18	-25.53	-12.70	-11.03	-22.21	-10.87	1.47	-16.40	
Translation parameter										
γ	0	314.891	345.102	71.891	92.938	109.292	152.922	109.988	73.525	19.722
	-	1318.63	1240.00	768.76	315.96	427.26	981.75	752.00	730.91	1219.95
Number of observations							49,036			
Log-likelihood value (in convergence)							-10,878,470.7			
Log-likelihood value (constants-only model)							-11,621,923.3			
ρ^2							6.40%			
Run time (hours)							43.85			

Table A3. t-test of difference between coefficient estimates*

Variable	Activity type									
	In-home	Work	Education	Shopping	Personal business	Health care	Visiting relatives	Recreation	Travel	Other
Constant	4.86	3.11	-9.44	-16.36	0.45	-2.65	-1.00	13.21		-22.11
Individual characteristics										
Age 6 - 12 years	-19.10	-25.52	8.77	-12.13	-5.74	-14.93	-18.92	3.99	0.40	
Age 13 - 18 years	-30.28	-45.09	5.07	-24.13	-10.06	-22.35	-27.59	-5.77	-18.88	
Age 19 - 24 years	-31.96	-33.44	2.63	-26.53	-26.79	-24.77	-30.78	-	-29.70	
Age 25 - 35 years	-25.40	-31.44	3.03	-20.28	-24.97	-25.13	-30.03	-7.55	-28.10	
Age 36 - 45 years	-18.29	-24.88	2.73	-13.50	-20.87	-17.41	-27.57	-7.62	-22.11	
Age 46 - 60 years	-17.77	-23.43	1.86	-11.84	-20.07	-10.92	-23.15	-	-20.21	
Female	5.14	18.98	14.89	24.81	21.84	15.29	2.67	-0.12	19.84	
White-collar worker	-7.88	-3.67	-	0.94	-2.47	-5.51		6.78	-12.15	
Blue-collar worker	6.71	6.56	-0.94	8.55		-4.63	5.89	1.55	0.85	
Driver	-3.43	0.55	4.94	-1.72	-2.83	3.02	0.25	-1.45	-2.09	
Seller	-0.83	0.45	-5.48	-7.37	-9.81	-0.08	-0.62	-1.24	-0.68	
Student	-0.70	-13.81	-8.00	10.23	7.80	7.99	1.40	8.71	-8.16	
Unemployed	17.27	12.94	17.79	24.07	7.53	6.25	26.29	9.09	4.62	
Household characteristics										
Household size	10.66	7.89	15.87	3.85	7.31	6.43	9.03	3.02	13.75	
Living in CBD	-2.42	-7.51	-	-14.18	4.08	-12.42	-10.82	3.84	-9.04	
Bike capita	7.12	0.95	0.64	2.95		-0.99	8.48	-5.42	2.83	
Motorcycle capita	15.15	15.33	15.33	7.67	5.61	0.42	6.17	0.34	17.37	
Car capita	-27.94	-19.44	-	-28.00	-27.84	-16.16	-21.80	-	-13.88	
Pickup capita	0.03	-6.25	28.35		-2.74		0.26		-1.32	0.57
Presence of child below 12 years	-3.31	-5.91		-7.36	-4.00	-6.51	-5.20	-4.55	-5.46	
Residing TAZ characteristics										
Recreation land use share	7.19							-3.34		
Commercial land use share	-5.04									
Land use Diversity Index	7.47	10.00	16.39	8.07	8.22	20.64	1.59	-4.50	7.25	
Translation parameter										
γ		-	-	109.9	43.88	72.08	54.96	69.43	163.8	-
		141.91	93.68	1				5	542.76	

*Statistically different if the value is bigger than 2 with %95 confidence interval

Table A4. Transferability assessment metrics

Transfer method	Percent of application context data	LL_1 (*10 ⁶)	$LL_{Transferred}$ (*10 ⁶)	$LL_{Constants Only}$ (*10 ⁶)	TTS (*10 ³)	$\rho^2_{Transferred}$	TI	$RMSE_{Activity}$ y Type	$RMSE_{Activity}$ y Duration	$RATE_{Activity}$ y Type	$RATE_{Activity}$ y Duration	$APS_{Activity}$ Type	$APS_{Activity}$ y Duration
Mashhad model	100	-2.661	-2.735	-2.830	0	0.060	1.000	0.135	0.296	1.000	1.000	0.085	21.467
Naïve transfer	0	-2.661	-2.661	-2.830	148	0.034	0.563	0.329	0.433	2.439	1.463	0.251	42.291
Adjusting constant terms	1	-2.661	-2.718	-2.830	115	0.040	0.662	0.151	0.404	1.162	1.364	0.088	38.429
	5	-2.661	-2.708	-2.830	94.3	0.043	0.722	0.157	0.385	1.116	1.301	0.085	36.808
	10	-2.661	-2.707	-2.830	93.0	0.043	0.725	0.147	0.381	1.096	1.288	0.074	37.249
	20	-2.661	-2.708	-2.830	92.4	0.044	0.727	0.148	0.377	1.088	1.273	0.073	36.743
	30	-2.661	-2.707	-2.830	92.1	0.044	0.728	0.146	0.376	1.088	1.270	0.072	38.443
Estimating new constants and scale	40	-2.661	-2.707	-2.830	92.0	0.044	0.729	0.145	0.369	1.081	1.246	0.071	36.970
	50	-2.661	-2.707	-2.830	91.5	0.044	0.730	0.147	0.369	1.071	1.245	0.070	35.886
	1	-2.661	-2.705	-2.830	93.7	0.043	0.723	0.143	0.421	1.094	1.422	0.082	36.857
	5	-2.661	-2.708	-2.830	93.1	0.043	0.724	0.143	0.406	1.093	1.372	0.081	36.765
	10	-2.661	-2.707	-2.830	91.7	0.044	0.729	0.143	0.398	1.088	1.343	0.080	36.957
20	-2.661	-2.707	-2.830	91.7	0.044	0.730	0.148	0.394	1.085	1.321	0.076	36.487	
30	-2.661	-2.707	-2.830	91.4	0.044	0.730	0.148	0.391	1.060	1.318	0.076	34.955	
40	-2.661	-2.706	-2.830	90.0	0.044	0.734	0.142	0.390	1.058	1.293	0.075	35.743	
50	-2.661	-2.706	-2.830	90.0	0.044	0.735	0.147	0.383	1.050	1.228	0.071	37.204	

Estimating the application context model	1	-2.661	-2.783	-2.830	245	0.017	0.278	0.294	0.380	1.881	1.620	0.370	96.876
	5	-2.661	-2.678	-2.830	34.8	0.041	0.697	0.254	0.372	1.557	1.258	0.314	95.688
	10	-2.661	-2.660	-2.830	-1.19	0.048	0.904	0.210	0.300	1.176	1.013	0.254	67.432
	20	-2.661	-2.658	-2.830	-5.77	0.051	0.917	0.146	0.294	1.085	0.994	0.092	29.402
	30	-2.661	-2.656	-2.830	-10.6	0.052	0.931	0.139	0.288	1.028	0.991	0.089	26.718
	40	-2.661	-2.654	-2.830	-14.5	0.054	0.943	0.138	0.275	1.021	0.988	0.084	26.260
Bayesian updating	50	-2.661	-2.652	-2.830	-18.3	0.055	0.954	0.129	0.246	1.019	0.987	0.082	25.576
	1	-2.661	-2.733	-2.830	245	0.035	0.478	0.303	0.400	2.246	1.350	0.277	85.955
	5	-2.661	-2.726	-2.830	130	0.042	0.616	0.263	0.395	1.951	1.333	0.245	72.938
	10	-2.661	-2.661	-2.830	29.2	0.045	0.900	0.232	0.350	1.720	1.180	0.239	55.895
	20	-2.661	-2.657	-2.830	20.3	0.051	0.940	0.210	0.343	1.557	1.159	0.194	39.797
	30	-2.661	-2.656	-2.830	0.61	0.054	0.975	0.210	0.330	1.545	1.113	0.172	35.164
Combined transfer estimation	40	-2.661	-2.676	-2.830	-8.40	0.058	0.981	0.167	0.316	1.234	1.080	0.141	27.592
	50	-2.661	-2.671	-2.830	-10.6	0.059	0.984	0.155	0.304	1.146	1.069	0.134	26.225
	1	-2.661	-2.783	-2.830	144	0.034	0.575	0.236	0.360	1.750	1.214	0.234	76.585
	5	-2.661	-2.678	-2.830	34.9	0.044	0.797	0.208	0.324	1.543	1.094	0.145	65.777
	10	-2.661	-2.661	-2.830	0.61	0.05	0.914	0.169	0.304	1.138	1.070	0.123	59.078
	20	-2.661	-2.657	-2.830	-5.44	0.054	0.966	0.146	0.302	1.083	1.025	0.093	30.102
Joint context estimation	30	-2.661	-2.656	-2.830	-8.40	0.058	1.000	0.145	0.295	1.072	1.021	0.090	28.219
	40	-2.661	-2.658	-2.830	-10.6	0.061	1.025	0.138	0.290	1.025	0.978	0.084	26.606
	50	-2.661	-2.652	-2.830	-18.3	0.062	1.031	0.116	0.289	0.862	0.975	0.054	26.434
	1	-2.661	-2.730	-2.830	139	0.035	0.590	0.320	0.426	2.371	1.521	0.287	69.448
	5	-2.661	-2.724	-2.830	114	0.055	0.879	0.226	0.361	2.042	1.138	0.234	57.208
	10	-2.661	-2.720	-2.830	11.8	0.059	0.951	0.187	0.293	1.272	1.022	0.112	39.833
20	-2.661	-2.720	-2.830	1.02	0.062	0.999	0.145	0.278	1.213	1.018	0.103	30.647	
30	-2.661	-2.719	-2.830	0.90	0.064	1.036	0.135	0.261	1.186	1.008	0.095	26.062	
40	-2.661	-2.719	-2.830	-8.85	0.065	1.050	0.123	0.261	1.074	0.974	0.084	24.039	
50	-2.661	-2.718	-2.830	-9.82	0.065	1.059	0.112	0.242	1.053	0.953	0.052	23.637	



Damage Detection in Truss Bridges under Moving Load Using Time History Response and Members Influence Line Curves

Kordi, A.¹ and Mahmoudi, M.^{2*}

¹ Ph.D. Student, Department of Civil Engineering, Shahid Rajaei Teacher Training University, Tehran, Iran.

² Associate Professor, Department of Civil Engineering, Shahid Rajaei Teacher Training University, Tehran, Iran.

© University of Tehran 2021

Received: 23 Nov. 2020;

Revised: 05 Jun. 2021;

Accepted: 28 Jun. 2021

ABSTRACT: In recent years, damage detection has been an important issue in the condition assessment of structures. This research presents a new method for the detection of damaged members in truss bridges under moving load using the time history response and influence line curves of the members. For this reason, two different Finite Element (FE) models of truss bridges under moving load with different damage scenarios have been investigated. The damaged members are detected by adapting the difference curve shape of displacement responses obtained from the intact and damaged models to the axial force influence line curve shape of these members. The results demonstrate that when a member of a truss bridge is damaged, the difference curve of displacement responses is similar in shape to the influence line curve of the damaged member. It should be noted that the proposed method can accurately diagnose the damaged members with the displacement response of only one desired point of the truss bridge.

Keywords: Damage Detection, Displacement, Influence Line Curve, Moving Loads, Truss Bridge.

1. Introduction

All structures such as bridges, buildings, and other kinds of onshore or offshore structures undergoing loads, continuously accumulate damages which are often caused by deterioration of members or connections during their service life. The detection of these damages and their effects on Civil Engineering structures such as bridges have been a problem that has received remarkable considerations from researchers in the last three decades (Doebeling et al., 1996; Mahmoud, 2001;

Sinou, 2009; Rezaifar and Doost Mohammadi, 2016; Samadi, 2021). The great use of trusses in bridge structures led some researchers to investigate damage detection in trusses and truss bridges and the effect of damage on their behavior. Brunell and Kim (2013) used an experimental program to investigate the impact of local damage on the performance of steel truss bridges. Li and Hao (2016) discussed the possibility of using the newly introduced sensors to monitor the health condition of joints in steel truss bridges. De Biagi (2016) investigated the behavior of a

* Corresponding author E-mail: m.mahmoudi@sru.ac.ir

metallic truss under progressive damage and defined a strategy for designing a truss that can withstand damage acting at random on one of its elements.

Kim et al. (2016) presented a numerical algorithm for identifying the locations and extent of multiple damages in the truss structures using the free vibration analysis based on the force method. Moradipour et al. (2017) examined the application of an improved two-stage modal strain energy method to a benchmark truss bridge. Unno et al. (2019) utilized vibration signals obtained from sensors installed on the bridges and the Auto-Regressive model were then applied to the time signals to extract the structure's soundness characteristics. Mousavi et al. (2020) presented a damage detection method for a scaled steel-truss bridge model by using Hilbert–Huang Transform based on complete ensemble empirical mode decomposition with adaptive noise and Artificial Neural Network. Perez-Ramirez et al. (2020) proposed a new methodology based on the multiple signal classification for locating different types of damages in a truss-type structure with five bays under forced dynamic excitations.

As bridge structures continuously carry moving loads, several researchers focused on the dynamic responses of bridges under moving loads. Mrechesiello et al. (1999) presented an analytical approach to the problem of vehicle bridge dynamic interaction. Law and Zhu (2004) studied the dynamic behavior of damaged reinforced concrete bridge structures subject to moving vehicular loads and investigated the effects of moving speed, road surface roughness, and oscillator parameters on the dynamic behavior. Chan and Ashebo (2006) developed a method to identify moving forces on a selected span of interest from a continuous bridge. Yu and Chan (2007) investigated the current papers on important factors in the performance of moving load identification methods. Pakrashi et al. (2010) monitored the evolution of a crack in a beam by using the beam strain response

due to the moving load for investigation of increasing crack-depth ratios and estimated the damage levels using distortions of wavelet coefficients of measured strain data.

Li and Law (2012) proposed a damage identification approach based on a dynamic response reconstruction technique for a target substructure subject to moving vehicular loads. Li et al. (2013) presented a structural damage identification approach based on the dynamic response reconstruction under vehicular loads for bridge structures without knowledge of the time histories of the vehicular loads and the properties of moving vehicles and with improvements in the computation efficiency and accuracy. McGetrick et al. (2015) validated an algorithm for the estimation of global bridge stiffness by using the vehicle response during a laboratory experimental process.

Sun et al. (2016) proposed a method for detecting the damage location and extent utilizing dynamic displacement of a bridge structure and defined dynamic curvature, the second derivative of the dynamic displacement, as a damaged index. Siriwardane (2015) proposed a technique to locate the damage region of railway bridges based on measured model parameters using acceleration response under usual moving train loads. Chang and Kim (2016) conducted a field experiment on an actual simply supported steel Warren-truss bridge with four artificial damage scenarios using acceleration responses under moving load. He et al. (2017) developed a two-stage method to detect the structural damages by using the displacement response of beam bridges under quasi-static moving loads. Liu and Zhang (2018) proposed a method to detect the damage in beam bridges by using a quasi-static strain influence line based on the Brillouin optical time-domain analysis in both numerical and experimental analysis.

Hester et al. (2020) proposed a damage identification method in beam bridges based on bridge rotation response to a

moving load and showed a relation between the damage occurrence and an increase in the magnitude of rotation measurements. Yang et al. (2021) proposed a new damage detection index based on the Difference of Strain Influence Line (DSIL) gained from the long-gauge strains under moving load.

The purpose of this research is to identify the damaged members of truss bridges using influence line curves of members and the time history response of truss bridges under moving load. It should be noted that the displacement response of only one desired point of the truss bridge is needed for the process of damage detection.

2. Methodology

2.1. Preliminary Remarks

As is clear from previous studies in damage detection of bridges, the direct use of time history responses under moving load has been less observed, and often displacement or acceleration responses have been used to determine the modal characteristic changes. In other words, rarely has the damage index been defined based on the displacement or acceleration changes but in this study, FE models displacement response and influence lines are used directly and damage identification of truss bridge members is done by combining influence line and displacement response under moving load. By using accelerations from a planar Finite Element simulation model Gonzalez and Hester (2013) illustrated the relationship between the three response components contributes to establishing if damage has occurred. Zhang et al. (2017) used the distance between multi-type vibration measurements, displacement, velocity, and acceleration of undamaged and damaged

structures to indicate the damage location. In this research, as the time history responses of the bridge-vehicle system are used for the process of damage detection, the system's formulation must be provided. The equation of motion for an Euler-Bernoulli beam under a load with a prescribed velocity $v(t)$, along the beam's axial direction, as depicted in Figure 1, can be written as:

$$\begin{aligned} \rho A \frac{\partial^2 u(x,t)}{\partial t^2} + C \frac{\partial u(x,t)}{\partial t} \\ + \frac{\partial^2}{\partial x^2} \left(EI(x) \frac{\partial^2 u(x,t)}{\partial x^2} \right) \\ = P(t) \delta(x - \hat{x}(t)) \end{aligned} \quad (1)$$

which ρA and C : are the mass per unit length and the damping of the beam. $EI(x)$, $u(x,t)$ and $\hat{x}(t)$: are respectively the flexural stiffness, displacement function, and location of moving load $P(t)$ at time t and $\delta(t)$: is the Dirac delta function. The transverse displacement $u(x,t)$ in modal coordinates is as follows:

$$u(x,t) = \sum_{i=1}^{\infty} \phi_i(x) q_i(t) \quad (2)$$

which $\phi_i(x)$ and $q_i(t)$: are the mode shape function and modal amplitude of i th mode. By substituting Eq. (2) into Eq. (1), multiplying by $\phi_i(x)$, integrating with respect to x between 0 and L and applying the orthogonality conditions, the following equation is obtained:

$$\begin{aligned} \frac{d^2 q_i(t)}{dt^2} + 2\xi_i \omega_i \frac{dq_i(t)}{dt} + \omega_i^2 q_i(t) \\ = \frac{1}{M_i} P(t) \phi_i(\hat{x}(t)) \end{aligned} \quad (3)$$

in which ω_i : is the modal frequency, ξ_i : is the damping ratio and, M_i : is the modal mass of the i th mode obtained as:

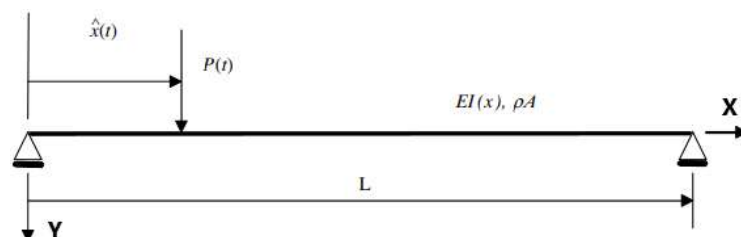


Fig. 1. A simply supported Euler-Bernoulli beam under a moving load

$$M_i = \int_0^L \rho A \phi_i^2(x) dx \quad (4)$$

For a continuous beam with simple supports as shown in Figure 1 with the length L , height h , and width b , the displacement response can be achieved by using the superposition principle in modal analysis and expressed as follows (Zhang et al. 2017):

$$u(x,t) = \sum_{i=1}^{\infty} \frac{\phi_i(x)}{M_i} \int_0^t h_i(t - \tau) P(\tau) \phi_i(\hat{x}(\tau)) d\tau \quad (5)$$

where $u(x,t)$: denotes the displacement of the beam at the location x and time instant t and $h_i(t) = \frac{1}{\omega_i'} e^{-\xi_i \omega_i' t} \sin \omega_i' t$ with $\omega_i' = \omega_i \sqrt{1 - \xi_i^2}$. As the vibration response of a bridge under a moving load is usually dominated by the fundamental frequency, the displacement response can be determined approximately with the first mode shape by using Eq. (5). If a moving constant load is considered and the damping effect is ignored, the displacement response at the mid-span of the beam can be calculated as follows (Zhang et al. 2017):

$$u\left(\frac{L}{2}, t\right) \approx \frac{\phi_1\left(\frac{L}{2}\right)}{M_1} \cdot \frac{P}{\omega_1} \int_0^t \sin(\omega_1(t - \tau)) \phi_1(\hat{x}(\tau)) d\tau \quad (6)$$

Clearly, the damage location x_c is the non-smooth point of the first mode shape (Narkis 1994), which is called a singularity point in mathematics. Considering Eq. (6), the singularity point occurs in the

displacement response.

2.2. Moving Load Modeling

In this study, the Finite Element model of bridges in ABAQUS 6.14-3 Finite Element software (Systèmes, 2014) is used to obtain the displacement responses used for damage detection. As in the next parts of this study, in the process of damage detection, the moving load will be applied to the truss bridges. For verification of the moving load numerical modeling a valid example from a mentioned study (Zhang et al. 2017) is investigated. In this example a $P = 10\text{kN}$ load is moving along a beam with a speed of 2 m/s . The geometric and material properties of the beam are listed in Table 1.

The bridge Finite Element model is built with 20 beam elements, named B22, based on the Euler-Bernoulli beam theory with 1.5 m length. In order to model the moving load in ABAQUS, a 10kN load is applied to a weightless moving cube with dimensions $0.5 \times 0.5 \times 0.5\text{ m}$. According to Figure 3, plane strain shell element with 0.25 m width and height and depth equal to the beam is used to mesh the moving cube. There is no friction between lower area of the moving cube and the beam. The bridge-moving load system has been analyzed in ABAQUS standard solver with an implicit dynamic step with a time period of 20 seconds. The dynamic implicit step, in the process of solving matrices obtained from the Finite Element method, uses the Hilber-Hughes-Taylor Integration operator (Hilber and Hughes 1978).

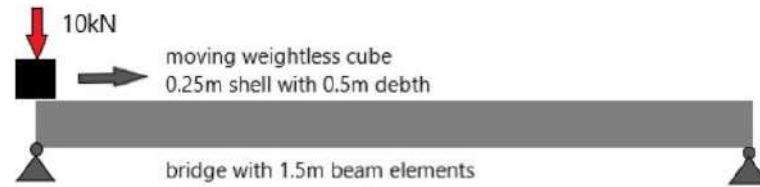
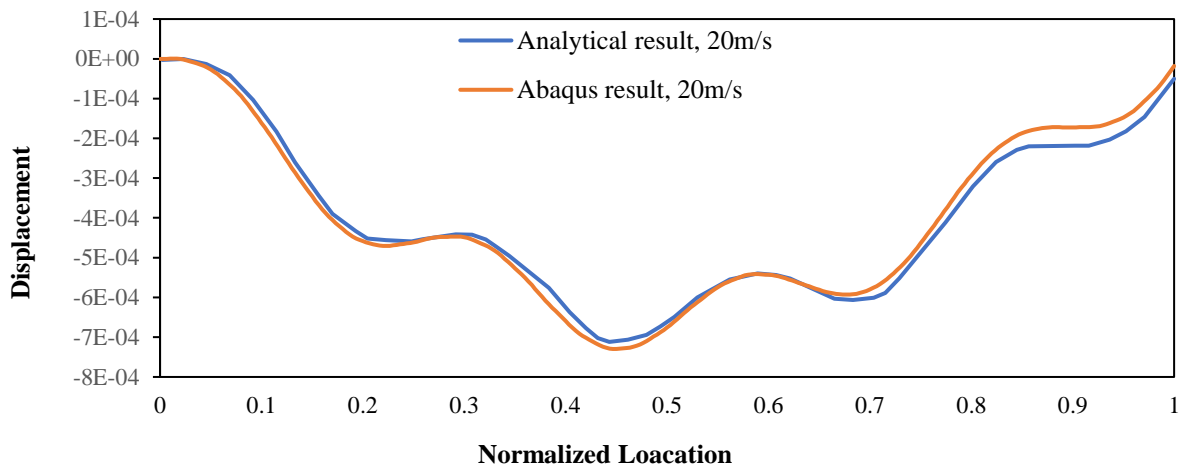
The comparison of finite element analysis and theoretical calculation of the beam for validation of the moving load modeling is shown in Figure 4.



Fig. 2. A simply supported damaged beam under a moving load

Table 1. Properties of geometry and material of the beam structure Zhang et al. (2017)

Material parameters		Geometric parameters	
Density	7800 kg/m ³	Length	30 m
Young's modulus	210 Gpa	Height	1 m
Poisson's ratio	0.3	Width	0.5 m

**Fig. 3.** Moving load modeling in the finite element software**Fig. 4.** Comparison of the numerical and analytical displacement response at the midpoint of the beam

The good agreement demonstrates that the finite element analysis response is finely matched with only the first mode response and this method of moving load modeling is completely usable for the process of truss bridge damage detection.

2.3. The Proposed Method for Damage Detection of Truss Bridges

It should be mentioned first that in this research, the criteria of being known as a damaged member is member's stiffness reduction compared to the initial stiffness. The mentioned damage is applied to the bridge's members by cross-section and Young's modulus reduction in truss and beam elements, respectively. This study aims to detect the damaged members of truss bridges by adapting the displacement responses difference curve obtained from the intact and damaged models and the axial force influence line curve of these members. To reach this aim, the displacement response of the truss bridge's

lower chord, at the midpoint, under moving load is calculated for intact and damaged bridges. The Difference in Displacement responses (DD) is expressed as follows:

$$DD = u_i - u_d \quad (7)$$

where u_i and u_d : stand for the displacement response at the midpoint of the intact and damaged truss bridges, respectively. After obtaining the DD curve for each truss bridge, axial Influence Lines (IL) of truss members are calculated to be compared with the truss bridge DD for identifying the damaged member. It is necessary to mention that only for members on the lower chord, members modeled with beam elements, bending moment influence line is used. The steps of the proposed method for damage detection are as follows:

- Finite Element modeling of intact and damaged truss bridge;
- Obtaining the displacement responses of one point in the truss bridge;

- Denoising the displacement responses by Wavelet toolbox in Matlab program;
- Computing the DD for the truss bridge;
- Calculating the ILs of all or damaged members;
- Comparing the DD curve with ILs curves to identify the damaged member.

In this study, two examples of different truss bridges are modeled numerically in the finite element software to evaluate the proposed method's capability. In addition to these two truss bridge models, Example 3 is provided to demonstrate the ability of this method to detect damage in beam bridges.

2.4. Examples

Example 1: A Pratt Type Truss Bridge with Simple Supports

In this example, a ten-span planner Pratt-type truss, as depicted in Figure 4, is considered. The elements of the lower chord are modeled as beam elements with fixed rectangular cross-sections $B = 8$ cm and $H = 5$ cm and structural mass $m = 10$ kg is attached at each node on the lower chord. The other members have modeled as truss elements sectional area $A = 1$ cm². For all elements, Young's modulus is $E = 2.1 \times 10^{11}$ Pa and material density is $\rho = 7800$ kg/m³ (Lingyun et al., 2005). The truss configuration is depicted in Figure 5.

As in the next part of this study, the

dynamic response of the truss bridge is investigated, the first five natural frequencies of the truss are extracted by applying the frequency analysis. The comparison of reference (Lingyun et al., 2005) measures and those of the present study is shown in Table 2.

In order to evaluate the proposed method for identification of damaged member, in each analysis, one member of the truss is damaged and the displacement response of lower chord midpoint, point 10, under sinusoidal moving load is extracted for intact and damaged models. The sinusoidal load moving the lower chord is as follows:

$$P = 2000(1 + 0.1 \sin(10\pi t) + 0.05 \sin(30\pi t)) \quad (8)$$

In Civil Engineering, vehicle loads are often simulated with the time history of moving load. Since the applied moving load has two high-frequency parts, the displacement response of truss bridges is influenced by excitation frequencies. To eliminate the influences of high frequencies from displacement responses, a filter in the wavelet package of Matlab software is used to convert the displacement responses to some smoother ones (Misti et al., 2007). The displacement response of node 10 in the intact truss bridge under sinusoidal moving load and the denoised form of this curve is illustrated in Figure 6.

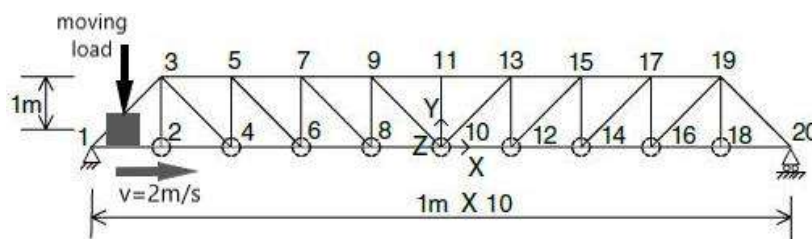


Fig. 5. Pratt simply supported bridge under moving load

Table 2. Natural frequency comparison

Frequency number	Lingyun et al.	Present
1	8.89	8.884
2	28.82	28.699
3	46.92	46.473
4	63.62	62.597
5	76.87	75.056

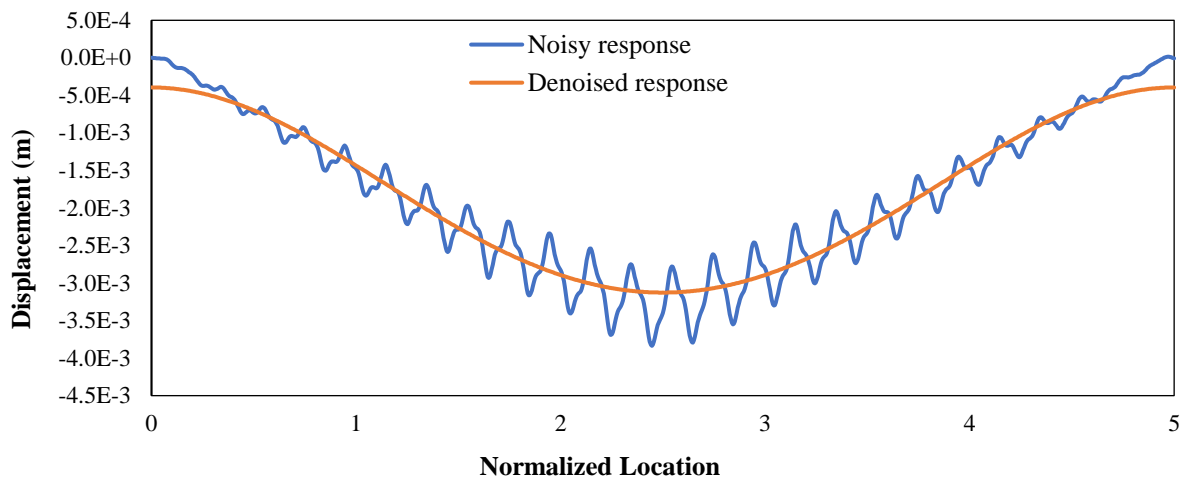


Fig. 6. Pratt truss node 10 displacement response under moving load

In this bridge, for members with truss elements, the damage is modeled by decreasing the sectional area in the whole length of the member and for members with beam elements, by decreasing the elasticity modulus at the center of a member with 0.1 m length. Four different scenarios including all kinds of members such as vertical, diagonal, up and down horizontal, in different parts of the truss are investigated. The damage scenarios and damaged member's features are illustrated in Table 3. Except for M4-6 which is the member between nodes 4 and 6 with beam elements, the other three members are modeled with truss elements.

The IL curves of damaged and some other members are obtained by applying a unit force to the points on the lower chords, 1 up to 20, and calculating each member's axial load or bending moment amounts for truss or beam elements respectively.

Example 2: A Warren Type Truss Bridge with Simple Supports

In the second example, a four-span planner Warren truss with material

properties similar to example number one is investigated. The elements of the lower chord are modeled as beam elements with fixed rectangular cross-sections $B = 2$ cm and $H = 4$ cm. The other members have modeled as bar elements sectional area $A = 4$ cm². The bridge truss is depicted in Figure. 7.

The above truss bridge undergoes a sinusoidal moving load (Eq. (5)), and the displacement response of the lower chord midpoint, point 4, is extracted for intact and damaged models. The sinusoidal load moving the lower chord is as follows:

$$P = 100(1 + 0.1 \sin(20\pi t) + 0.05 \sin(40\pi t)) \quad (9)$$

As is shown in Table 3, three different scenarios are investigated and for each scenario, only one member is damaged. In this table, the selected members' features before and after damage are shown. For example, the M2-5 stands for the member with truss element between nodes 2 and 5, and the M4-6 for the member with beam element between nodes 4 and 6.

Table 3. Damage features

Damage scenarios	Intact members features		Damaged members features	
	cm ²	Mpa	cm ²	Mpa
M6-7	A = 1	E = 2.1E5	A = 0.5	E = 2.1E5
M11-13	A = 1	E = 2.1E5	A = 0.5	E = 2.1E5
M14-17	A = 1	E = 2.1E5	A = 0.5	E = 2.1E5
M4-6	A = 40	E = 2.1E5	A = 40	E = 1.89E5

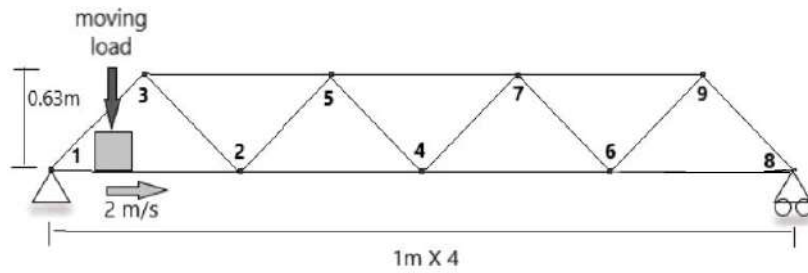


Fig. 7. Warren simply supported bridge under a moving load

Table 4. Damage features

Damage scenarios	Intact members features		Damaged members features	
	cm ²	Mpa	cm ²	Mpa
M2-5	A = 4	E = 2.1E5	A = 2	E = 2.1E5
M5-7	A = 4	E = 2.1E5	A = 2	E = 2.1E5
M4-6	A = 8	E = 2.1E5	A = 8	E = 1.89E5

The good agreement of frequency measures, especially the first mode frequency, illustrates that the truss modeling is correct and its dynamic behavior is valid for the continuation of study and evaluation of the newly proposed method.

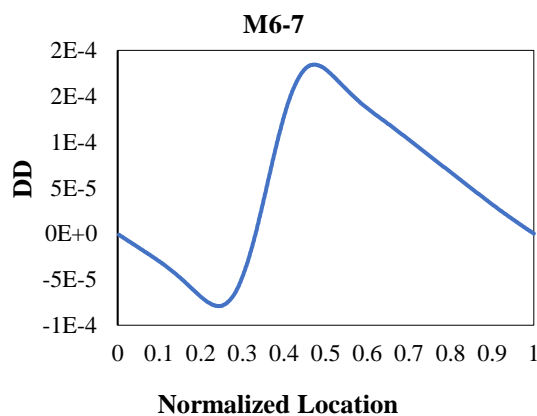
Example 3: A Simply Supported Beam Bridge

In this example, the beam bridge with the geometrical and material properties of Table 1 is modeled in the Finite Element software and the DD and IL curve pattern is presented. The damage is simulated at the location $2L/3$ from the left support of the beam bridge. Damage with 0.1 m length by changing Young's modulus, E , to $E/8$ is created. The filtered displacement responses of intact and damaged beams and DD and IL curves are illustrated in Figures 10 and 11, respectively.

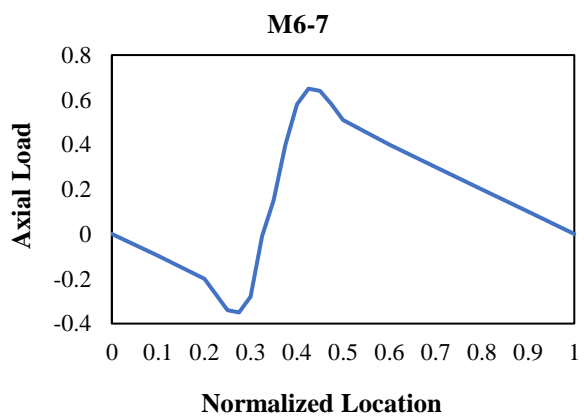
3. Verification of The Proposed Method

As expressed in the previous parts of this study, in the Pratt truss bridge, Example 1, four different scenarios are investigated by damaging vertical, diagonal, upper chord horizontal, and lower chord horizontal member respectively, one by one. In order to evaluate the ability of the new method for the identification of damaged members, the DD curve pattern of the truss bridge for each scenario should be compared with IL curve patterns of damaged members. The comparison of displacement response difference curves and influence line curves of Pratt truss bridge under moving load for each scenario is illustrated in Figure 8.

The left column curves illustrate the displacement difference of the truss bridge lower chord midpoint for each scenario, and the right columns curves show the influence line of damaged members. The results of Example 2 are illustrated in Figure 9.



(a)



(b)

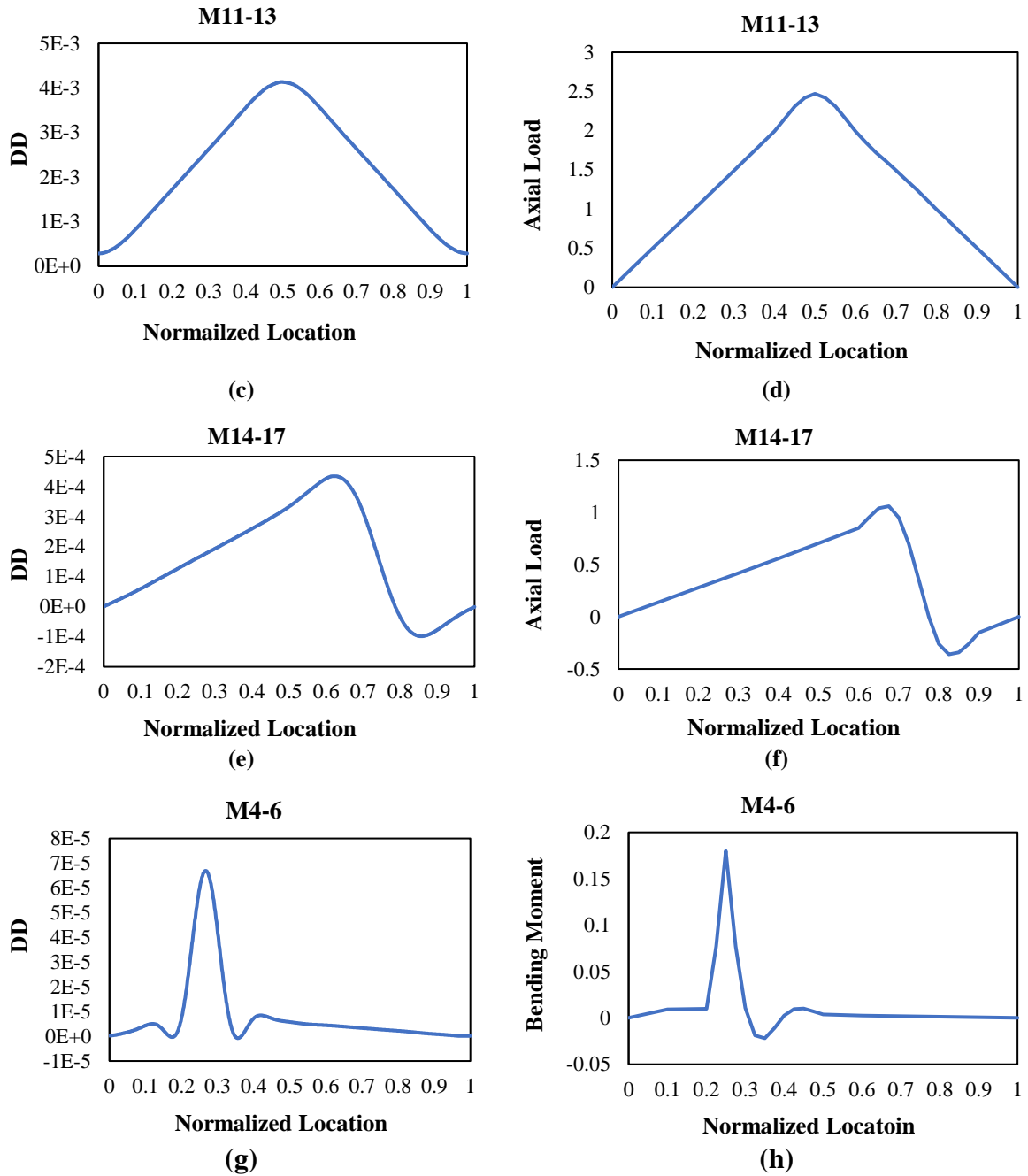
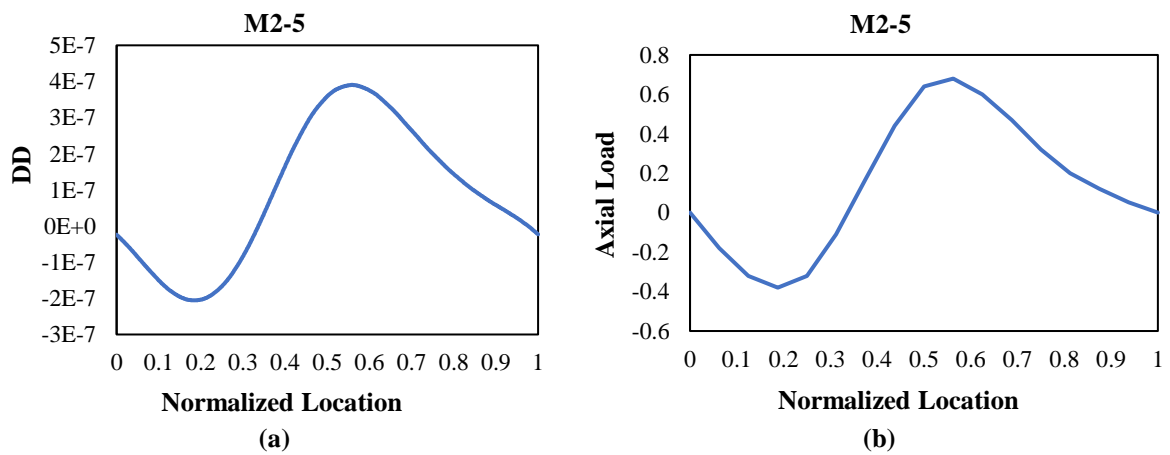


Fig. 8. Adaptation of DDs and ILs: a,b) Vertical; c,d) Up horizontal; e,f) Diagonal; and g,h) Down horizontal



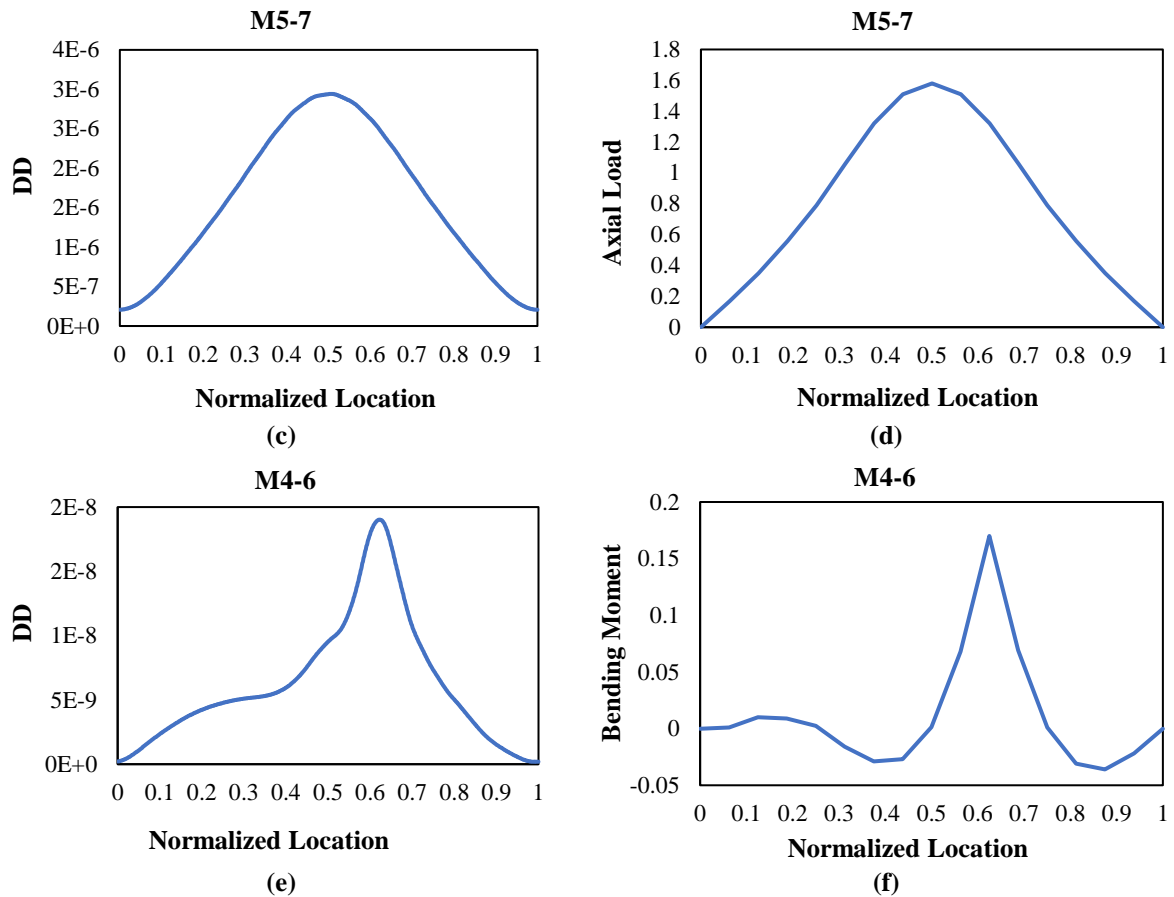


Fig. 9. Adaptation of DDs and ILs: a,b) Diagonal; c,d) Up horizontal; and e,f) Down horizontal

As shown in above figures, in the diagonal and vertical members of truss bridges, the curves experience a jump along an almost constant slope. Although in all horizontal members of truss bridges a peak is seen, in the lower chord members simulated with beam elements, a sharper peak is seen because in these flexural members unlike the upper chord members,

simulated with truss elements, bending moment influence line is investigated, not axial load influence line.

The Figure 11a's curve illustrates the displacement difference of the beam bridge at the midpoint of the beam, and Figure 11b's curve shows the bending moment influence line of the beam.

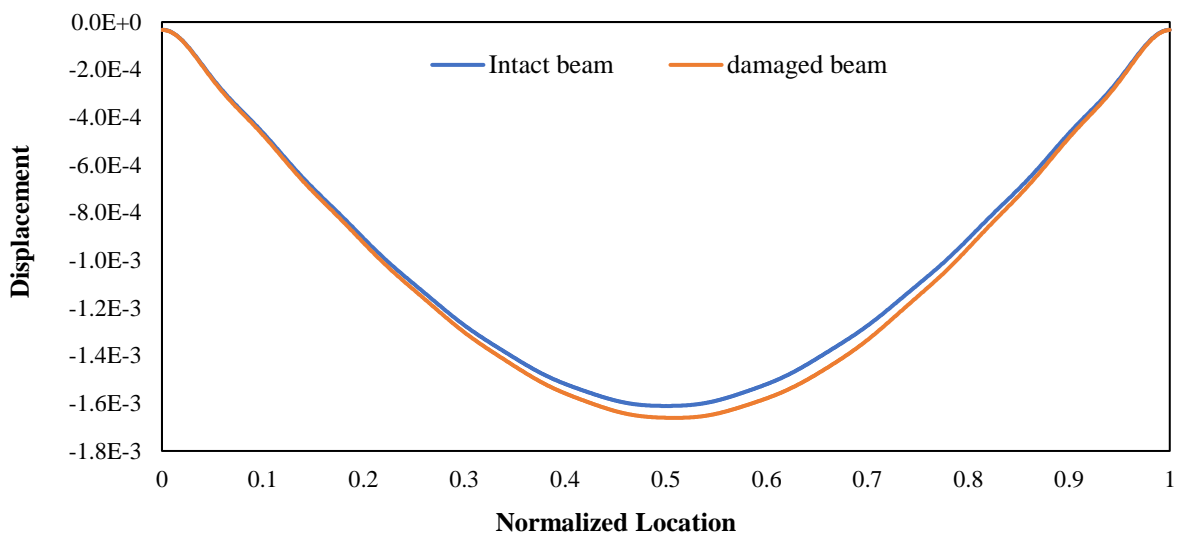


Fig. 10. Filtered displacement response of intact and damaged beam bridges

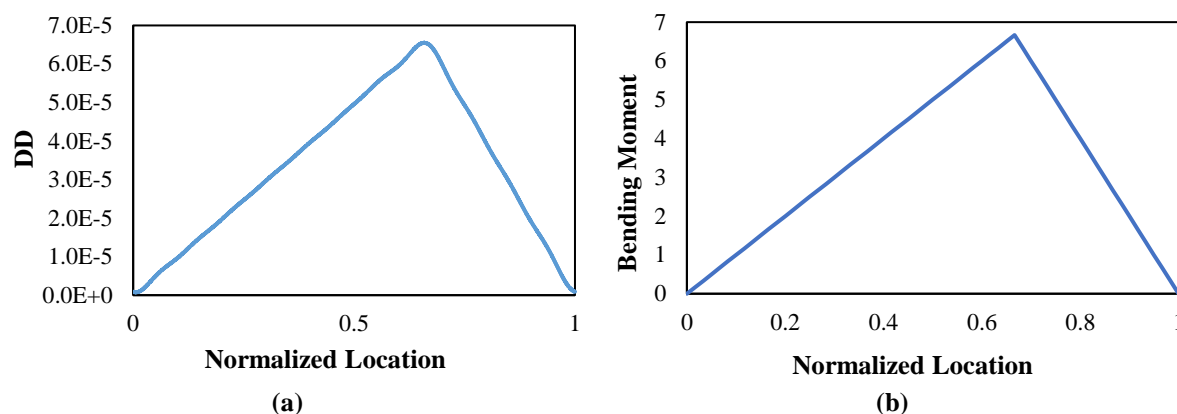


Fig. 11. Adaptation of DD and IL of the 30-meter beam bridge

4. Conclusions

The results presented in this paper indicate that the new proposed method of combining truss bridges members influence line and displacement responses difference is able to simply identify the damaged members. The results demonstrate that when a member in the truss bridge is damaged, the difference curve of intact and damaged truss bridge displacement responses is apparently similar to the influence line curve of the damaged member. In other words, the shape similarity of displacement responses difference curve and the damaged member IL curve is very prominent. It is worth mentioning that the proposed method can accurately diagnose the damaged members with the displacement response of only one point of the truss bridge. Based on the many models investigated, the proposed method is able to identify the members with very minor damages. It is clear that, for intact members, when there is no damage, the DD measure is zero. So there would be no curve for similarity comparison with the IL curves. Obviously, the proposed method is also effective for beam bridges. The third example confirms this. So the peak points of curves in Figure 11, show the location of damage in the beam. Further studies could be required to detect the multiple damages and amount of each member's damage.

5. References

- Brunell, G. and Kim, Y.J. (2013). "Effect of local damage on the behavior of a laboratory-scale steel truss bridge", *Engineering Structures*, 48, 281-291.
- Chan, T.H. and Ashebo, D.B. (2006). "Theoretical study of moving force identification on continuous bridges", *Journal of Sound and Vibration*, 295(3-5), 870-883.
- Chang, K.C. and Kim, C.W. (2016). "Modal-parameter identification and vibration-based damage detection of a damaged steel truss bridge", *Engineering Structures*, 122, 156-173.
- De Biagi, V. (2016). Structural behavior of a metallic truss under progressive damage", *International Journal of Solids and Structures*, 82, 56-64.
- Doebbling, S.W., Farrar, C.R., Prime, M.B. and Shevitz, D.W. (1996). "Damage identification and health monitoring of structural and mechanical systems from changes in their vibration characteristics: A literature review", Los Alamos National Laboratory, Report No. LA-13070-MS, USDOE, Washington, DC.
- González, A. and Hester, D. (2013). "An investigation into the acceleration response of a damaged beam-type structure to a moving force", *Journal of Sound and Vibration*, 332(13), 3201-3217.
- He, W.Y., Ren, W.X. and Zhu, S. (2017). "Damage detection of beam structures using quasi-static moving load induced displacement response", *Engineering Structures*, 145, 70-82.
- Hester, D., Brownjohn, J., Huseynov, F., O'Brien, E., Gonzalez, A. and Casero, M. (2020). "Identifying damage in a bridge by analysing rotation response to a moving load", *Structure and Infrastructure Engineering*, 16(7), 1050-1065.
- Hilber, H.M. and Hughes, T.J. (1978). "Collocation, dissipation and [overshoot] for time integration schemes in structural dynamics", *Earthquake Engineering and Structural Dynamics*, 6(1), 99-117.
- Kim, Y.W., Kim, N.I. and Lee, J. (2016). "Damage identification of truss structures based on force method and free vibration analysis", *Advances in Structural Engineering*, 19(1), 3-13.

- Law, S.S. and Zhu, X.Q. (2004). "Dynamic behavior of damaged concrete bridge structures under moving vehicular loads", *Engineering Structures*, 26(9), 1279-1293.
- Li, J. and Hao, H. (2016). "Health monitoring of joint conditions in steel truss bridges with relative displacement sensors", *Measurement*, 88, 360-371.
- Li, J. and Law, S.S. (2012). "Damage identification of a target substructure with moving load excitation", *Mechanical Systems and Signal Processing*, 30, 78-90.
- Li, J., Law, S.S. and Hao, H. (2013). "Improved damage identification in bridge structures subject to moving loads: numerical and experimental studies", *International Journal of Mechanical Sciences*, 74, 99-111.
- Lingyun, W., Mei, Z., Guangming, W. and Guang, M. (2005). "Truss optimization on shape and sizing with frequency constraints based on genetic algorithm", *Computational Mechanics*, 35(5), 361-368.
- Liu, Y. and Zhang, S. (2018). "Damage localization of beam bridges using quasi-static strain influence lines based on the BOTDA technique", *Sensors*, 18(12), 4446.
- Mahmoud, M.A. (2001). "Effect of cracks on the dynamic response of a simple beam subject to a moving load", *Proceedings of the Institution of Mechanical Engineers, Part F: Journal of Rail and Rapid Transit*, 215(3), 207-215.
- Marchesiello, S., Fasana, A., Garibaldi, L. and Piombo, B.A.D. (1999). "Dynamics of multi-span continuous straight bridges subject to multi-degrees of freedom moving vehicle excitation", *Journal of Sound and Vibration*, 224(3), 541-561.
- McGetrick, P.J., Kim, C.W., González, A. and Brien, E.J. (2015). "Experimental validation of a drive-by stiffness identification method for bridge monitoring", *Structural Health Monitoring*, 14(4), 317-331.
- Misiti, M., Misiti, Y., Oppenheim, G. and Poggi, J.M. (2007). *Wavelet toolbox 4-user's guide*, The MathWorks. Inc., Massachusetts, USA.
- Moradipour, P., Chan, T.H. and Gallage, C. (2017). "Benchmark studies for bridge health monitoring using an improved modal strain energy method", *Procedia Engineering*, 188, 194-200.
- Mousavi, A.A., Zhang, C., Masri, S.F. and Gholipour, G. (2020). "Structural damage localization and quantification based on a CEEMDAN Hilbert transform neural network approach: A model steel truss bridge case study", *Sensors*, 20(5), 1271.
- Narkis, Y. (1994). "Identification of crack location in vibrating simply supported beams", *Journal of Sound and Vibration*, 172(4), 549-558.
- Pakrashi, V., O'Connor, A. and Basu, B. (2010). "A bridge-vehicle interaction based experimental investigation of damage evolution", *Structural Health Monitoring*, 9(4), 285-296.
- Perez-Ramirez, C.A., Machorro-Lopez, J.M., Valtierra-Rodriguez, M., Amezcua-Sanchez, J.P., Garcia-Perez, A., Camarena-Martinez, D. and Romero-Troncoso, R.D.J. (2020). "Location of multiple damage types in a truss-type structure using multiple signal classification method and vibration signals", *Mathematics*, 8(6), 932.
- Rezaifar, O. and Doostmohammadi, M.R. (2016). "Damage detection of axially loaded beam: A frequency-based method", *Civil Engineering Infrastructures Journal*, 49(1), 165-172.
- Samadi, D., Taghaddos, H., Nili, M.H. and Noghabaei, M. (2021). "Development of a bridge maintenance system using bridge information modeling", *Civil Engineering Infrastructures Journal*, 54(2), 351-364.
- Sinou, J.J. (2009). "A review of damage detection and health monitoring of mechanical systems from changes in the measurement of linear and non-linear vibrations", *Mechanical Vibrations: Measurement, Effects and Control*, 643-702.
- Siriwardane, S.C. (2015). "Vibration measurement-based simple technique for damage detection of truss bridges: A case study", *Case Studies in Engineering Failure Analysis*, 4, 50-58.
- Sun, Z., Nagayama, T., Su, D. and Fujino, Y. (2016). "A damage detection algorithm utilizing dynamic displacement of bridge under moving vehicle", *Shock and Vibration*, 2016(January), 1-9.
- Systèmes, D. (2014). *ABAQUS analysis user's manual 6.14-2*. Dassault Systèmes Simulia Corp., Providence, RI, USA.
- Unno, K., Mikami, A. and Shimizu, M. (2019). "Damage detection of truss structures by applying machine learning algorithms", *International Journal*, 16(54), 62-67.
- Yang, J., Hou, P., Yang, C., Yang, N. and Li, K. (2021). "Damage identification method of box girder bridges based on distributed long-gauge strain influence line under moving load", *Sensors*, 21(3), 915.
- Yu, L. and Chan, T.H. (2007). "Recent research on identification of moving loads on bridges", *Journal of Sound and Vibration*, 305(1-2), 3-21.
- Zhang, W., Li, J., Hao, H. and Ma, H. (2017). "Damage detection in bridge structures under moving loads with phase trajectory change of multi-type vibration measurements" *Mechanical Systems and Signal Processing*, 87, 410-425.



This article is an open-access article distributed under the terms and conditions of the Creative Commons Attribution (CC-BY) license.

AIMS AND SCOPE

Since the College of Engineering (Former Faculty of Engineering, FOE) of the University of Tehran has renewed its policy toward scientific publication, the Civil Engineering transaction of the well- built 45 years old Persian journal of "*Nashrieh Daneshkadeh Fanni*" is to be published in English and as separate independent journal with the name of ***Civil Engineering Infrastructures Journal***.

Civil Engineering Infrastructures Journal is an international journal which publishes high quality scientific papers in all areas of engineering and management of civil infrastructures. The civil infrastructures include, but are not limited to: buildings, bridges, dams, transportation systems, geotechnical structures, underground constructions, water distribution systems, offshore platforms, pipelines, ocean structures, airports and power plants.

The scope of this journal encompasses, but is not restricted to the following aspects of engineering and management of infrastructures:

- Mathematical modeling
- Computational and experimental methods
- Environmental Impact assessment
- Passive defense and security issues
- Monitoring and assessment
- Construction and design for durability
- Deterioration modeling and aging
- Failure analysis
- Field testing
- Financial planning
- Inspection and diagnostics
- Life-cycle analysis and prediction

- Maintenance, rehabilitation, repair and replacement strategies
- Non-destructive testing
- Optimization of maintenance and management
- Specifications and codes
- Reliability and risk management
- Supervisory Control and Data Assimilation (SCADA)
- Automation and Robotics in Construction
- Smart civil infrastructure Systems
- Sustainable civil infrastructure systems
- Case studies

Audiences of *Civil Engineering Infrastructures Journal* are researchers and practitioners as well as people working in infrastructure design, construction, maintenance and operation. Papers considered for publication must contain a clear and well-defined engineering component and make a significant contribution to the engineering and management of civil infrastructures. All articles submitted to this journal will undergo a rigorous peer review by anonymous independent experts.

Additional information can be obtained from:

Civil Engineering Infrastructures Journal

College of Engineering,

University of Tehran

P.O. Box: 11155- 4563

Tehran, Iran

Tel/ Fax: +98-21-88956097

Web Site: www.ceij.ir

Email: ceij@ut.ac.ir



University of Tehran
College of Engineering

Copyright Transfer Agreement

In order to protect the author(s), from the consequences of unauthorized use, the publisher requests that all author(s) sign the appropriate statement below:

The author(s) undersigned hereby approves submission of this work and all subsequent revisions for publication and transfers, assigns, or otherwise conveys copyright ownership to the Civil Engineering Infrastructures Journal (CEIJ). I (we) acknowledge that i) the submitted material represents original material, ii) does not infringe upon the copyright of any third party, and iii) that no part of the work has been published or under consideration for publication elsewhere unless and until it is rejected by Civil Engineering Infrastructures Journal (CEIJ). I (we) agree to indemnify the publisher against any loss or damages arising out of a breach of this agreement. In the event that my (our) submission is not published, copyright ownership shall revert to the author (s).

Manuscript Title:

Corresponding Author

Author:

Date:

Signature;

Author:

Date:

Signature:

Author:

Date:

Signature:

Author:

Date:

Signature:

Please submit the signed agreement with the final manuscript to:

Civil Engineering Infrastructures Journal (CEIJ)

School of Civil Engineering

College of Engineering, University of Tehran

Enghelab Ave., P.O. Box: 11155-4563, Tehran, Iran.

Tel: 88956097

Fax: 66498981

E-mail: ceij@ut.ac.ir

Website: www.ceijournal.com

CIVIL ENGINEERING INFRASTRUCTURES JOURNAL (CEIJ)

is indexed and abstracted in the bibliographical databases including:



Web of Science (ESCI)
<http://science.thomsonreuters.com>



Scopus
<https://www.scopus.com>



Islamic World Science Citation
Center;
<http://www.isc.gov.ir>



Directory of Open Access Journals
(DOAJ)
<https://doaj.org>



Google Scholar
<https://scholar.google.com>



General Impact Factor (GIF)
<http://generalimpactfactor.com>



Scientific Indexing Services (SIS)
<http://www.sindexs.org>



International Institute of
Organized Research (I2OR)
<http://www.i2or.com>



Information Matrix for the Analysis
of Journals (MAIR)
<http://miar.ub.edu>



ROAD: the Directory of Open
Access scholarly Resources
<http://road.issn.org>



Scientific World Index
<http://www.sciwindex.com>



International Innovative Journal
Impact Factor (IIJIF)
<http://www.ijif.com>



Science library index
<http://scinli.com>



Journal Factor
<http://www.journalfactor.org>



Open Academic Journals Index
(OAJI)
<http://oaji.net>



Electronic Journals Library (EZB)
<https://rzblx1.uni-regensburg.de>



Systematic Impact Factor
(SIF)
<http://www.sifactor.org>



COSMOS IMPACT FACTOR
<http://www.cosmosimpactfactor.com>

INDEX COPERNICUS
INTERNATIONAL
Polish Ministry of Science and
Higher Education (MSHE)
<https://journals.indexcopernicus.com>



Magiran
<http://www.magiran.com>



Scientific Information Database
(SID); Iran;
<http://www.Sid.ir>

Ministry of Science, Research and Technology of Iran has granted the Science and Research (Elmi-Pajouheshi) credit to CEIJ according to the letter No. 3/252445 at 25 Feb. 2012.



Civil Engineering Infrastructures Journal

Volume 55, Number 1, June 2022

CONTENTS:

Research Papers

- Predicting Compression Strength of Reinforced Concrete Columns Confined by FRP Using Meta-Heuristic Methods 1
Mohammadzadeh, M.R. and Esfandnia, F.
- A Laboratory Study on the Potentiodynamic Polarization and Transport Properties of Binary Concrete with Silica Fume and Zeolite 19
Sobhani, J., Najimi, M. and Pourkhorshidi, A.R.
- Development of the Fragility Curves for Conventional Reinforced Concrete Moment Resistant Frame Structures in Qods Town, Qom City, Iran 31
Dehghani, E. and Soltanimohajer, M.
- Simulation of Near-Fault Seismic Ground Motions of 03 November, 2022 Denali Earthquake Using Modified Semi-Empirical Approach 43
Rajaram, C. and Pradeep Kumar, R.
- Influences of Polyvinyl Alcohol Fiber Addition on the Specimen Size Effect and Energy Absorption of Self-Consolidating Concrete 59
Abbasi Nattaj Omrani, I., Ardeshir-Behrestaghi, A. and Saeedian, A.
- Reduction Factors for Laterally Loaded Pile Groups Accounting for Pile Cross Sections and Soil Properties 75
Talebi, A. and Derakhshani, A.
- Developing a Hybrid ANN-Jaya Procedure for Backcalculation of Flexible Pavements Moduli 89
Ghanizadeh, A.R., Heidarabadizadeh, N. and Khalifeh, V.
- The Effect of Hydrophobic Amorphous Carbon Powder on the Compressive Strength, Water Absorption and Rheological Attributes of Cement Mortar 109
Haji Hossein, A.R., Bigdeli, H.R., Mokhtari, F., Jahantab, S. and Habibnejad Korayem, A.
- Collapse Probability Assessment of a -4 Story RC Frame under Post-Earthquake Fire Scenario 121
Moradi, M., Tavakoli, H.R. and Abdollahzade, G.H.R.
- Developing Performance Levels for Concrete Bridge Bents with a Focus on the Joint Region 139
Bahrani, M.K., Nooralizadeh, A., Sharifi, M. and Karami, N.
- Spatial Transferability of a Daily Activity Type and Duration MDCEV Model 161
Nohekhan, A., Samimi, A. and Zahedian, S.
- Damage Detection in Truss Bridges under Moving Load Using Time History Response and Members Influence Line Curves 183
Kordi, A. and Mahmoudi, M.